Distributed, Efficient and Secure Transmission for Unmanned Aerial Vehicle-Enabled Wireless Networks

Lead Guest Editor: Guangwei Yang
Guest Editors: Jianying Li and Kun Wei

Distributed, Efficient and Secure Transmission for Unmanned Aerial Vehicle-Enabled Wireless Networks

Distributed, Efficient and Secure Transmission for Unmanned Aerial Vehicle-Enabled Wireless Networks

Lead Guest Editor: Guangwei Yang
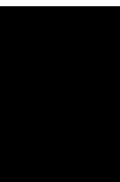Guest Editors: Jianying Li and Kun Wei

Contents

WILEY | Hindawi

Research Article

Smart Grazing in Tibetan Plateau: Development of a Ground-Air-Space Integrated Low-Cost Internet of Things System for Yak Monitoring

Ji Li [1,2] **Min Ling** [1] **Jiangxia Shui** [1] **Shijie Huang** [3] **Junjie Dan** [4] **Biao Gou** [1] **and Yanshuang Wu** [1]

[1]School of Aeronautical Manufacturing Industry, Chengdu Aeronautic Polytechnic, Chengdu 610100, China
[2]School of Aeronautic Science and Engineering, Beihang University, Beijing 100191, China
[3]Sichuan Mister Yak Technology Co., Ltd, Chengdu 610100, China
[4]Chengdu Aircraft Industrial (Group) Co., Ltd, Chengdu 610091, China

Correspondence should be addressed to Min Ling; 18530281@qq.com

This paper analyzes the present situation and difficulties of yak breeding in the "Three Needy Autonomous Regions" of Sichuan Province, integrating the specific natural environments of Qinghai-Tibet Plateau. Research work focuses on the requirements of no network conditions, large-scale application, and ultralow use cost. We propose a smart grazing IoT system, in which collars and ear-tags are designed to collect the positions and physiological signs of yaks, BeiDou Satellite-Base Stations (BDS-BSs) are designed to build local area network and ultralong-distance communication, and what is more, UAV is designed to expand the communication range to hundreds of kilometers. According to the actual needs of grazing monitoring, we propose an effective data reduction method, so that BeiDou Satellite (BDS) short-message technology can be applied to the IoT communication with high efficiency and low cost. The author carried out a significant number of experiments and verification: (1) collar realized positioning and physiological signs collecting of yaks. (2) The local area network (LAN) scheme based on LoRa built a stable communication distance of more than 3 km. (3) Ultralong-distance communication scheme based on BDS short-message technology effectively solved the problem of no network and got excellent zero additional use cost. (4) A plateau mountainous grazing UAV is designed and developed to expand the communication range.

1. Introduction

In the vast northwest of China, especially in Tibet, Qinghai, Northwest Sichuan, Gansu, and Xinjiang provinces as we called "Qinghai-Tibet Plateau areas", where the average altitude is 4000 meters, natural conditions are exceptionally arduous, and people's production and life are challenging. From where the "Three Needy Autonomous Regions" of Ganzi, Aba, and Liangshan in Sichuan Province are the world-known poverty-stricken areas. With typical plateau mountain environments, the vegetation on the top of the mountains is mostly grass and low shrubs, which form nat-ural ranches. Local people who live in the low altitude valleys have to graze on mountain tops, creating a unique habit of "living under the mountain, grazing and production on the mountain" in the Tibetan Plateau for thousands of years. It meanwhile indicates there would be dozens of kilometers' travel distance from residential areas to grazing mountain tops. Generally, isolate mountain pastures may have a radius of more than ten kilometers, and contiguous pastures can reach a radius of hundreds of kilometers, as shown in Figure 1. With the Tibetan Plateau region's unique terrain and climate conditions, only the warm climate from May to October is suitable for grass growth. Yaks mainly fatten
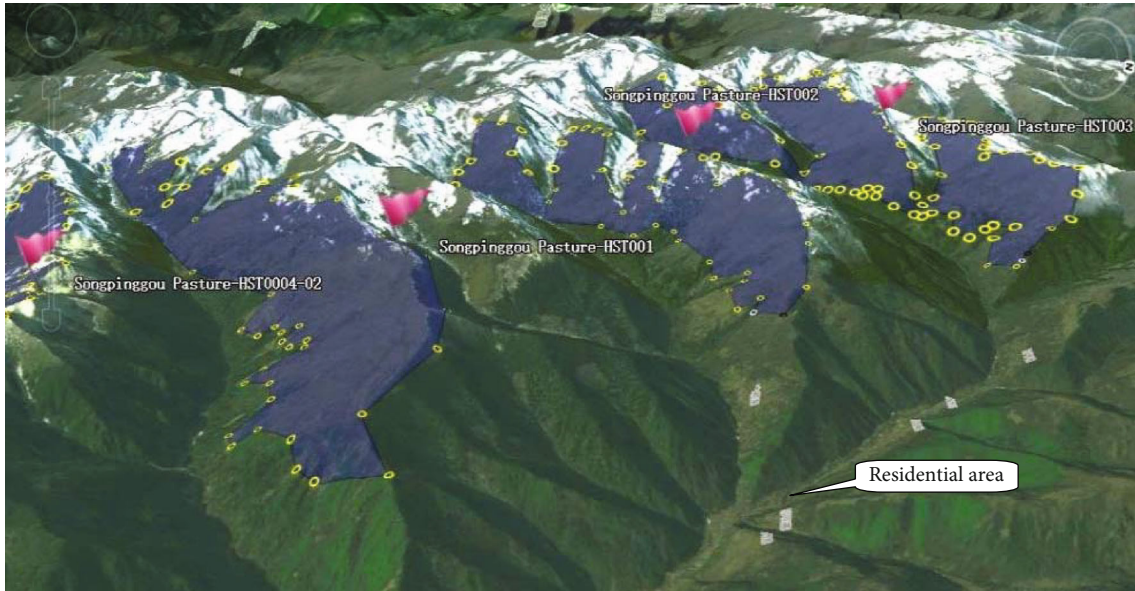
Figure 1: Geographical conditions of plateau mountainous pasture.

up in this period under natural grazing conditions. In other periods, the mountain pastures are capped with snow, which means the food is mainly withered grass. Although yaks can adapt to such climatic conditions, they have to thin down as the effect of limited food gradually. Under these natural conditions, the effective growth cycle of yaks merely maintains half a year. They usually need to grow 5-6 years before being put into the market, brings about the extremely low breeding efficiency.

As the mountain pastures are usually large and far away, the grass is difficult to transport. It is hard for herdsmen to breed yaks. When it comes to snowy winter and spring, it is also challenging to find and cure the weak or sick yaks. What is more, March to April is the most challenging period, as the withered grass is exhausted out, and the green grass has not yet sprouted, and food is extremely scarce. Disease, loss, and unnatural death result in approximately 10% loss rate of yaks per year, which has become the primary risk of grazing and breeding.

Because of the above problems, how to monitor the locations and vital signs of yaks becomes very important. With accurate locations and vital signs, herdsmen could effectively track and locate animals, and weak and sick yaks could be found and cured quickly. With the mountainous plateau's unique grazing conditions, it is urgent to develop long-endurance (more than half a year) and low-cost equipment for monitoring yaks. Under the background of China's Rural Revitalization Strategy, it is important to develop industries with local characteristics according to local conditions. Focusing on characteristic industries, injecting modern science and technology to promote industrial development is a practical solution.

Nowadays, IoT, big data technology, UAVs, and robotics are widely used in our life. These technologies are changing the society deeply, from service industry to manufacturing industry and agriculture. A low-cost and large-scale IoT system is the obvious need of herdsmen in Tibetan Plateau region. Barker and Hammoudeh presented a survey on low power consumption networking for IoT and WSN systems, focused on the power usage of various IoT network protocols, and highlighted the sensor nodes' battery life boosted from hours or days to months and years [1]. Shammar and Zahary studied different disciplines of IoT such as architecture, OS, network stack protocols, software, and application and introduced the IoT technology to be used in tracking and monitoring farm animals to allow real-time surveillance in crucial situations such as the outbreaks of infectious diseases [2]. Xu et al. presented a survey of existing IoT devices/products and classified the commonly used IoT devices into three categories: mobile/wearable devices, smart home/building devices, and network devices, which indicated the wide usage of smart IoT devices in our daily life [3]. Smart city is one of the main mature application fields of IoT technology, like simple daily life of shopping, living payment, transportation, and even in some crucial and complex situations. As COVID-19 is changing our courses of action toward ensuring health security, an IoT network was presented in an airport to monitor the soap levels, room capacity, distances, temperature, and humidity of toilets, basing on different sensors [4]. Cvar et al. extended the concept of Smart Villages (rural settlement) by the use of IoT technologies [5]. An energy harvesting LoRaWAN was deployed and operated in a sampled forest region of Eastern China for environment monitoring [6]. González et al. presented a low-cost, low-power, and real-time monitoring system basing on the development of a LoRa (short for long-range) sensor network for AQM and gas leakage event detection [7]. Davcev et al. presented an innovative, power efficient, highly scalable long-range, and low power consumption IoT agricultural system based on the LoRaWAN

network, which was used to collect air temperature and humidity, leaf wetness, and soil moisture readings in vineyard field [8]. UAVs are rapidly used in the field of agriculture such as weed mapping, soil and crop status monitoring, and pesticide spraying and even being used to monitor large-scale livestock in rural farms [9]. By collecting data from ground WSN, a UAV was utilized to adjust its trajectory for keeping droplet deposition in the target spraying area [10]. A long-term observation was conducted for the yield prediction of maize using an UAV [11]. Minhas et al. presented a reinforcement learning (RL) and UAV-aided multipath routing scheme for public safety networks so as to increase network lifetime [12]. An IoT system can be established to monitor the grazing in mountain pastures of the Tibetan Plateau area.

With the rapid development of IoT technology, satellite positioning, sensor nodes, wearable devices, and communication networking technologies have been vigorously developed and widely used. Satellite navigation devices can be used to determine their positions using a satellite navigation system, such as GPS, Galileo, GLONASS, and BDS. GPS is a well-known and most widely used satellite positioning system, and BDS is the latest deployed navigation system. Li et al. presented an analysis of code bias based on multipath combination observations, which improved the single-point positioning results, and the vertical component decreased by 0.42 m and by 0.28 and 0.1 m in north and east direction [13]. Wei et al. designed a remote monitoring system to track vehicles based on the combination of BDS and GSM, only spent little money on low price hardware and mobile network GSM fees [14]. Yang et al. introduced the basic performance of BDS-3 and presented that the post-processing orbit accuracy of the BDS-3 satellites had been increased to 0.059, 0.323, and 0.343 m, respectively, on radial, tangential, and normal directions [15]. Observation data in approximately 1 month were studied for determining the precise orbit for global positioning system models, and finally, researchers find out the GPS/BDS-3 combined solution got better accuracy performance compared to other solutions [16]. Jin and Su introduced that the BDS will provide highly reliable and precise PNT services as well as unique short-message communication under all-weather, all-time, and worldwide conditions [17]. Although satellite positioning technology has been well applied, researchers are still trying to develop more accurate, lower-cost, and more expandable applications. Especially the short-message technology, not just receiving signals but also sending signals, gives researchers a lot of imagination. Pereira et al. proposed an one M2M system for continuous patient monitoring in emergency wards, using low-cost and low-power WiFi-enabled wearable physiological sensors that connect directly to the internet infrastructure and run open communication protocols [18]. A boat tracking and monitoring system based on LoRa was presented and got the maximum coverage range of 4 km [19]. Sensors, LoRa, and circuits have been integrated into a WQMS system, which was low cost, small size, easy maintenance, continuous sampling, and long-term monitoring for many days [20]. Guidi et al. presented a wearable system comprised of a smart garment and portable electronics;

in fact, it was an elastic smart belt, which was fastened around the chest behind the shoulder area for heart rate variability monitoring in horses [21]. Accelerometer/gyroscope sensors were attached to the ears and collars of sheep, which could continuously survey the eating behavior sampled at 16 Hz and also be used to monitor health and welfare [22].

Advanced technologies should be used to monitor livestock and change the traditional arduous grazing production life of herdsmen in the Tibetan Plateau area. Navigation satellites are used for tracking the position of livestock. Smart sensors and wearable devices could be used to detect the sign information of yaks. Wireless sensor networks (WSNs) and the low-power wide-area network (LPWAN) are potential technologies for establishing the monitoring system and even IoT system.

To solve long-distance and wide-range communication between yaks and herdsmen, mobile communication and satellite communication are the most appropriate ways. However, pastures are usually vast uninhabited areas, and deploying a cellular network will be extremely expensive. The cost of commercial satellite communication services is even higher, which is difficult to adapt to the low-cost and large-scale use in the field of grazing. The BDS-3 short-message communication technology supports long-distance, low-cost, and two-way communication. As the high power consumption of BDS short-message communication technology, in order to meet the needs of long endurance, the device could be large and heavy, which will be difficult to design as a wearable collar. Therefore, it is essential to design independent collars and BDS-BSs, so as to build a yak physiological sign data acquisition and transmission network system. Several BDS-BSs could be enough to provide communication network services for isolated mountain pastures, and for contiguous pastures, UAV equipped with BDS-BS to provide mobile communication network would be the most suitable solution. This paper focuses on using the BDS short-message communication technology to build the communication and data transmission platform, which achieves ultralow-cost communication, as the following points:

(1) Design and develop the ear-tag to collect yaks' body temperature and heart rate data, using Bluetooth technology to send the data to the collar

(2) Design and develop the collar to collect yaks' positioning data, using LoRa technology to send data of position, body temperature, and heart rate to the BeiDou Satellite-Base Station Sender (BDS-BSS) without internet in plateau and mountain areas

(3) Design and develop the BDS-BSS, using LoRa technology to receive the collar's positioning data within a communication distance of more than 3 km, covering a range of 6 km on the mountain pasture

(4) Design and develop the BeiDou Satellite-Base Station Receiver (BDS-BSR), aiming at building long-distance communication for the whole IoT system, which can communicate with the BDS-BSS. With

GPS satellites

BeiDou Satellite

Wide Area Network Communication

BDS-BSS on UAV

BDS-BSS on UAV

Path planning

Aliyun

GPS/BeiDou dual mode
positioning system

LAN Network
Communication

Grazing UAV in plateau
mountain area

Grazing UAV in plateau
mountain area

Path planning

Internet

Internet

Mobile phone app

Mobile
communication
stations

BDS-BSR

The collar

Grazing UAV in plateau
mountain area

Mountain ranch in Tibetan Plateau

Urban residential district

FIGURE 2: Architecture of air-space-ground integrated intelligent grazing system.

Beidou satellite

GPS satellites

Mobile phone APP

BDS short message
communication

BDS short message
communication

Public network base station

GPS + Beidou dual-mode
positioning

BDS-BSR

Aliyun

The collar

LoRa communication
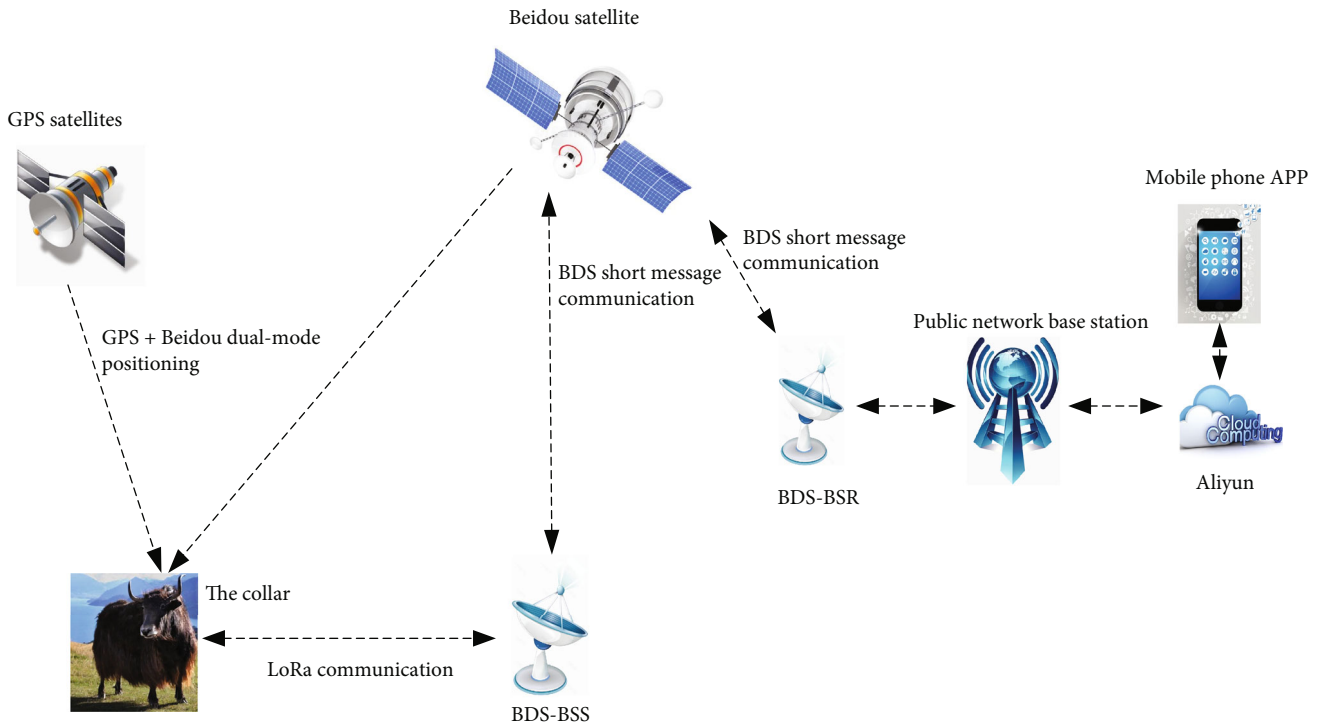
BDS-BSS

FIGURE 3: Subarchitecture of yak monitoring system based on fixed BDS-BSS.
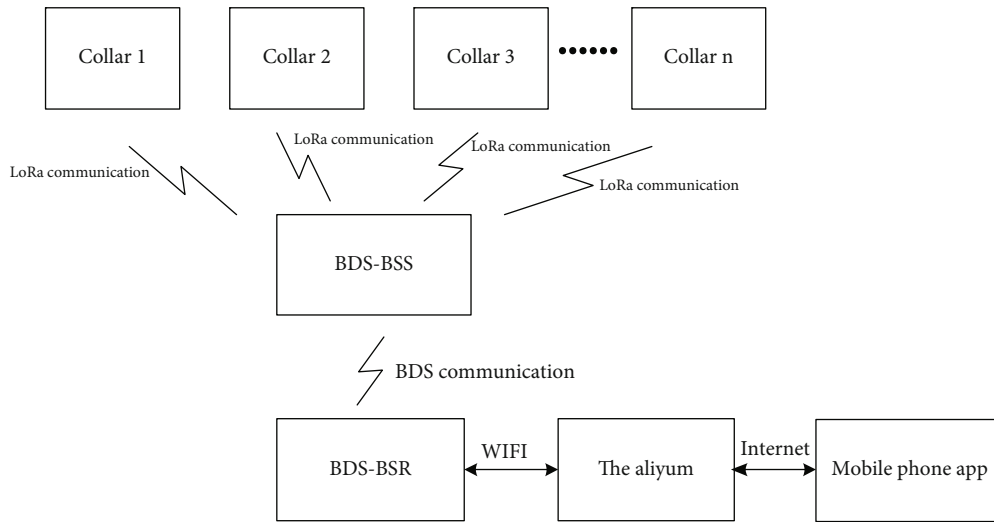
FIGURE 4: Subarchitecture of yak monitoring system diagram.
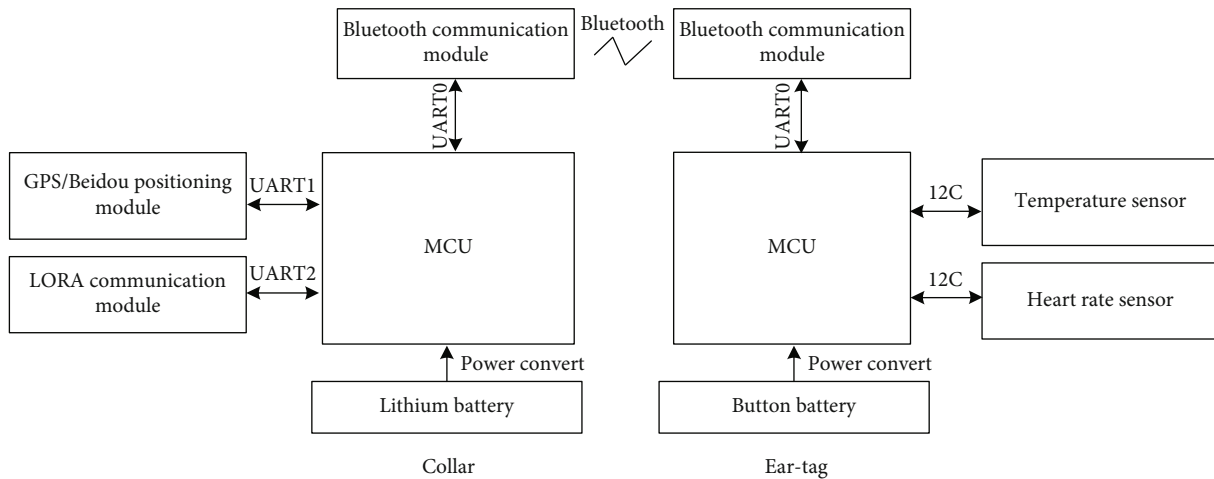
FIGURE 5: Block diagram of the monitoring equipment.

the BDS short-message technology (global communication technique), the BDS-BSR could receive the collar's positioning data and upload it to Aliyun

2. Related Work

Smart grazing concept relates to location-aware devices to monitor the movement of yaks in pastures. Reference [23] used a differentially corrected global positioning system to distinguish grazing and resting activity patterns of cattle based on GPS recordings. Davis et al. developed a low-cost GPS Herd Activity and Well-being Kit (GPSHAWK) to monitor locomotion behavior of cattle, and location data was collected from its own GPS receiver, which was claimed as low-cost device of $500 [24]. In fact, with the price of $500, the GPS receiver would be too expensive to promote a universal application in grazing. By changing the collar/tag ratio, a low-cost IoT system was developed, based on which, some animals were fitted with GPS collars (100-150 € per device) and others were fitted with Bluetooth tags [25]. It is a good method to reduce per animal

cost, but the GPS collar is not cheap. Vázquez-Diosdado et al. proposed a monitoring system with an embedded edge device that includes a triaxial accelerometer and triaxial gyroscope sensors, which accurately classified walking, standing, and lying conditions and represented a potential approach of long-term automated monitoring [26]. Based on combined data of the 3D accelerometer and a GPS sensor fixed on a neck collar, Riabof et al. predicted the behavior of dairy cows on pasture, which is used to better understand the relationship between behaviors and pasture characteristics [27]. Xu et al. developed an efficient and accurate approach to study the social behavior of cattle groups, in which GPS location information was used to build a high-accuracy wireless tracking system [28]. Although a lot of researches on the application of positioning have been taken in the smart grazing field, lower cost and longer service time will be the most unremitting demands, especially for the huge number of yaks.

Positioning is the most important and basic demand in grazing monitoring, and physiological sign detection helps
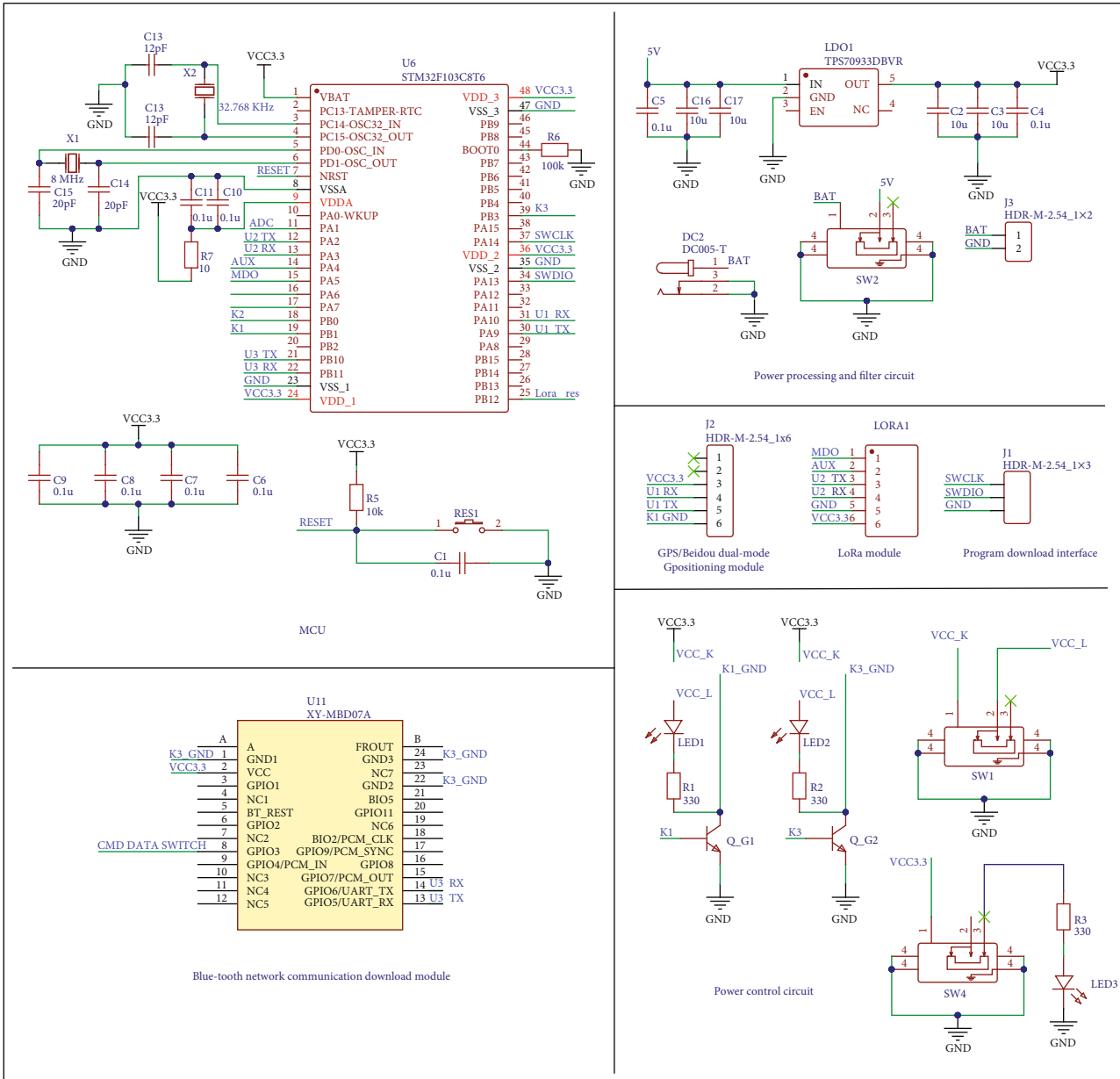
FIGURE 6: Schematic diagram of the collar.

herdsmen to intervene in the healthcare administration of yaks in time. Electrode pads were attached to the left side of the chest of each cow after removing the hair using clippers at three sites, and by this means, Aoki et al. recorded the cows' heart rate variability and applied power spectral analysis of HRV [29]. Various properties and capabilities of HR monitoring techniques were compared to check the potential to transfer the mostly adequate sensor technology of humans to livestock in terms of application. Nie et al. concluded the photoplethysmographic (PPG) technique as a feasible implementation in livestock, which could be integrated into an ear-tag [30]. Nie et al. also emphasized the challenges of transferring the PPG technique from human beings to livestock that whether the PPG theory based on skin blood perfusion is applicable for animals, and the similarities of skin between humans

and animals need to be checked first. Youssef et al. used PPG sensors on a pig's body to test whether it allows the retrieval of a reliable heart rate signal and concluded that the agreement between the PPG-based heart rate technique and the reference sensor was between 91% and 95% [31]. The reference also indicated that locations of the pig's body be chosen to place PPG sensor probe were important, because of their higher cutaneous perfusion and body fat. A number of cited works highlight that physiological sign detections are appealing and challenging for remote livestock monitoring, and there is no public literature on the detection of yak signs.

Smart grazing in Tibetan Plateau pastures is a typical application of long-range WSN and LPWAN systems. Raza et al. introduced and compared all kinds of LPWAN technologies such as SIGFOX, LoRa, INGENU RPMA,

FIGURE 7: Circuit board of the collar.

FIGURE 8: Physical collar and ear-tag.

TELENSA, QOWISIO [32], and NB-IoT [33], which provided the basis for scheme selection. LoRa is the most widely studied and applied technology in similar fields such as remote livestock tracking [34], piggery environment control [35], intelligent agriculture [36], and forestry monitoring [37], and these research works give us clear direction. Janssen et al. investigated a 2.4 GHz LoRa modulated and resulted in a maximum range of 333 km in free space, 107 m in an indoor office-like environment, and 867 m in an outdoor urban context [38], which indicated the great potential LoRa technologies for ultralong-distance grazing. By allocating the spreading factor and timeslot in the frame structure, DG-LoRa could support approximately five times more connections to the LoRa network satisfying a 5% data drop rate [39], which was just a simulation result. Berto et al. presented a peer-to-peer communication between nodes, without the use of gateways, and extend node reachability through multihop communication [40], which was claimed as a beneficial solution of "out-of-internet" communication. However, the so-called peer-to-peer communication only occurs between three nodes, and whether it can be applied on a large scale still needs further research and experiment. By using the LoRaWAN protocol stack, Guerrero et al. estimated the channel conditions and predicted the packet

delivery to ensure wireless networks' dependability [41]. Despite a good number of cited LPWAN system research works, there is no public literature on the real application of out-of-internet conditions similar to Tibetan Plateau pastures. Long-distance, large area, mountainous, and out of mobile network conditions lead to the particularity of communication network construction.

Yak is a very special species, which grows in the form of natural grazing and leads to a super long travel distance, which brings great challenges to the design of the management system. Gaitan proposed and developed a long-distance communication architecture for medical devices based on the LoRaWAN protocol that allows data communications over a distance of more than 10 km [42], which is not long enough for grazing in the Tibetan Plateau. Gaggero et al. developed a prototype based on a quad-copter drone equipped with a LoRaWAN gateway, which verified that a UAV can be suitable for the envisioned purpose [43]. Behjati et al. developed a farm monitoring system that incorporates UAV, LPWAN, and IoT technologies to transform the current farm management approach, which presented the maximum achievable LoRa coverage of about 10 km [9]. The above-cited works cannot meet the actual needs of grazing in Plateau Tibetan areas, long-distance, large area, mountainous, out of mobile network conditions, and real-time monitoring. Satellite communication appears unique advantages under the above conditions, especially the free BDS Short-Message Satellite Communication System service.

3. System Architecture

We propose a ground-air-space integrated grazing system, as shown in Figure 2, which consists of the following two parts:

(1) Subarchitecture of yak monitoring system based on fixed BDS-BSS, as shown in Figure 3. Collar was worn on the neck to collect position, body temperature, and heart rate signs of the yak. LoRa wireless communication technology is used to transmit signs and data between the collar and fixed BDS-BSS. BDS short-message technology is used to transmit signs and data between BDS-BSS and BDS-BSR. And then, the BDS-BSR uploads the relevant data to Aliyun. At last, herdsmen can view the locations and signs of yaks from their mobile phones, which is convenient for monitoring yaks, as shown in Figure 4

(2) *Large-Range Monitoring System Based on Plateau Mountainous Grazing UAV.* The UAV is used to carry a BDS-BSS, which is equipped as an integrated mobile BDS-BSS. With the flight of UVA, the monitoring area of pastures could be extended to more than $100 \, km^2$, which is also used for yak search and rescue.

4. Design and Implementation

4.1. Design and Implementation of Monitoring Equipment. Figure 5 is a block diagram of collar subsystem, which
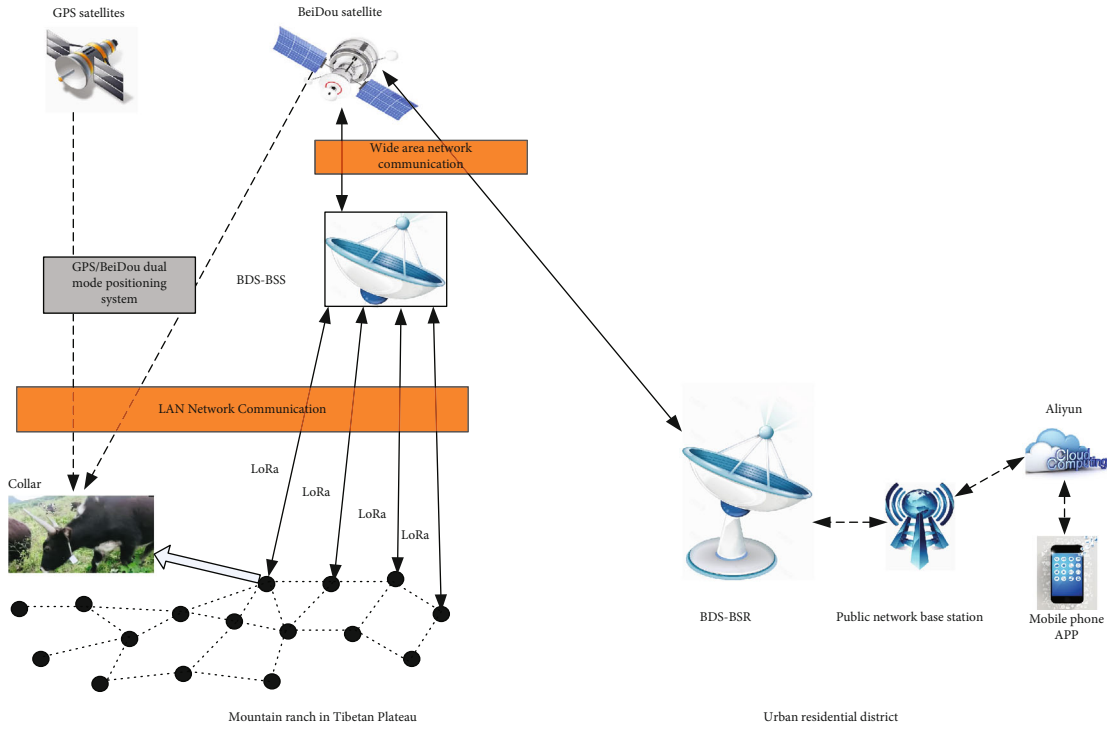
FIGURE 9: Communication network diagram.
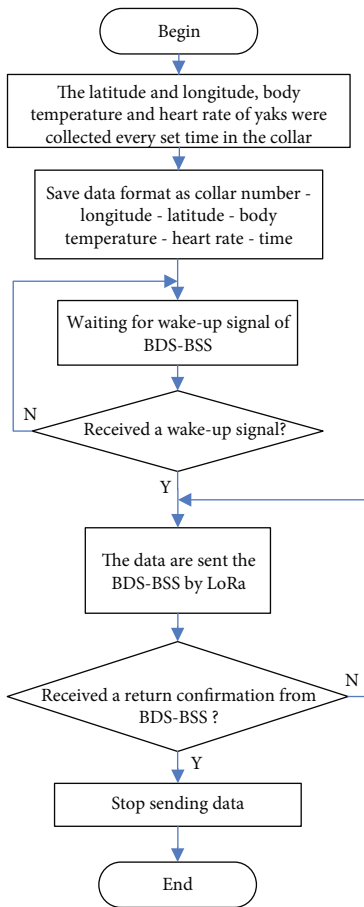
FIGURE 10: Collar communication diagram in LAN.
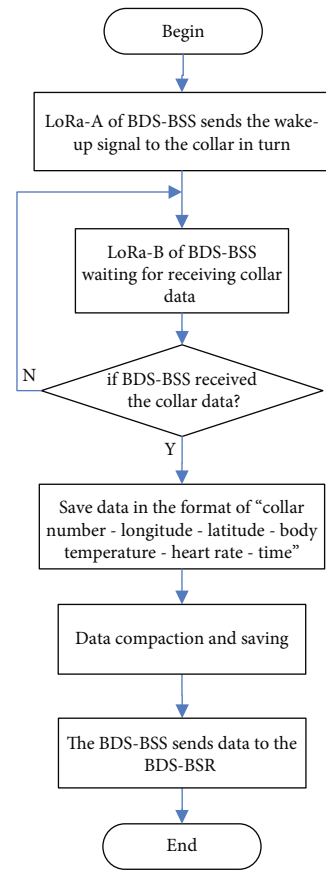
FIGURE 11: BDS-BSS communication diagram in LAN.

TABLE 1: Original data format description.

1-11	12-63	64-114	115-120	121-129	130-140
The collar number (1-2000)	Longitude	Latitude	Body temperature (30°~45°)	Heart rate (30~150/min)	Time (0-1440 minutes a day)

TABLE 2: Simplified data format description.

1-11	12-27	28-37	38-41	42-49	50-60
Collar number (1-2000)	D (0-50000)	Θ (0-628)	Body temperature—30 (0–15)	Heart rate—30 (0–120)	Time (0-1440)

includes a collar and an ear-tag, and the data communication is carried out by Bluetooth. The collar consists of microcontroller unit (MCU), BDS positioning module, LoRa communication module, Bluetooth communication module, and lithium battery. When it is in hibernation, no data is transmitted, which presents the lowest power consumption status. As it is awakened by BDS-BSS, the location and physiological signs will be transmitted to the BDS-BSS through the LoRa communication module. Moreover, the update frequency of location can also be set by the mobile phone APP. The ear-tag needs to be low power and miniaturization, so we selected low power MCU and used RTC settings to change the state of sleep and awakening circularly. The circuit schematic is designed as shown in Figure 6, and the PCB is designed and soldered as shown in Figure 7. Finally, the shell modeling design of the collar and ear-tag is carried out. The physical collar and ear-tag are shown in Figure 8.

4.2. Design and Implementation of Network Communication.
As shown in Figure 9, this communication system includes two parts, LAN and WAN networking. The LAN communication system includes collars and BDS-BSS, and the WAN communication system is composed of numbers of BDS-BSSs and BDS-BSRs.

4.2.1. LAN Communication.
The collar collects and saves positioning, temperature, and heart rate data according to the set time of APP. When collar receives the wake-up signal of BDS-BSS, the saved data are sent to the BDS-BSS through LoRa wireless communication. The BDS-BSS configures two LoRa modules A and B to collaborate with collars. LoRa A sends a wake-up signal to the collar, and LoRa B receives the returned data of collar. The data is consisting of "collar number - longitude -latitude- body temperature - heart rate - time." After receiving the data, the BDS-BSS saves the data and sends a confirmation message to the collar. The data transmitting in LAN communication network is chronologically ordered as shown in Figures 10 and 11.

4.2.2. WAN Communication and Data Compression.
The WAN communication network is based on BDS short-message technology, and data transmits between BDS-BSSs and BDS-BSR. BDS supplies a bidirectional short-message communication service, which is a unique function and the first navigation satellite with message communication in the world. However, the BDS short-message communication service can send only 78 bytes
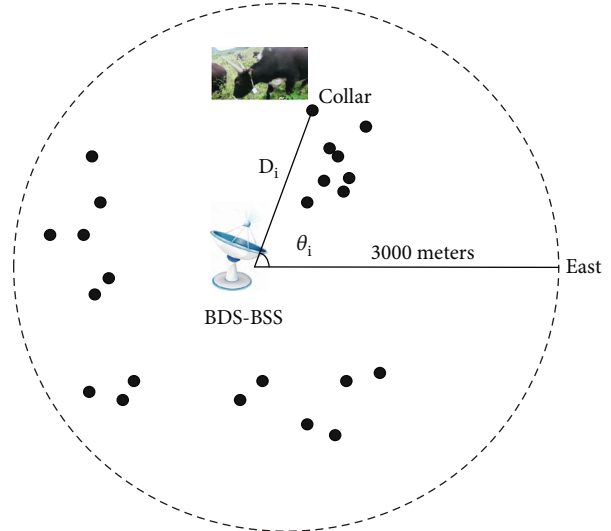
FIGURE 12: Collar azimuth relative to the BDS-BSS.

with maximum transmission frequency of twice a minute, which seriously restricts the application of mass data communication. Therefore, data compression and multicard multiplexing are essential means to improve communication capability.

(1) The Definition of Original Data Format. The data saving format in BDS-BSS is shown in Table 1. A complete piece of collar data is divided into 6 portions that 11 bits are reserved of collar number, 52 bits for longitude, 51 bits for latitude, 6 bits for body temperature, 9 bits for heart rate, and 11 bits for collecting time, in total of 140 bits. BDS short-message information can only send 4 collars' data at one time. The BDS-BSR will take 250 minutes to collect 2000 yaks' data of a common pasture, which seriously affects the real-time monitoring.

(2) Data Simplification. Therefore, it is necessary to simplify and reorganize the data, and we invested considerable energy in data compression in this research project. Firstly, we calculate the distance D between collar and BDS-BSS as Formula (1) described. And then, calculate the azimuth (θ) of the collar relative to the BDS-BSS as Formula (2). With this processing, the decimal point of longitude and latitude is removed and two positive integers are obtained, which compressed D and θ into 16 bits and 10 bits. The yak's body temperature value subtracts 30 (body temperature ranges from 30° to 45°), and the remaining integers occupy 4 bits. The remaining integers

TABLE 3: Data difference format.

11 bits	6~22 bits		5~15 bits		4-8 bits		5-13 bits		3 bits
11	6	0~16	5	0~10	4	0~4	5	0~8	3
Collar number (1-2000)	$D_i - D_{i-1}$ (0-50000)		$\Theta_i - \Theta_{i-1}$ (0-628)		The difference of body temperature (0–15)		The difference of heart rate (0–120)		time

occupy 8 bits after heart rate value subtracts 30 (heart rate ranges from 30 to 150 per minute), as shown in Table 2. BDS-BSS can send out 10 collars' data at one time, which takes 100 minutes to transmit 2000 yaks' data.

As shown in Figure 12, the distance between the collar and BDS-BSS is D_i, and the accuracy is 1 meter. The calculation formula is as follows:

$$D_i = \sqrt{(E_i - E_0)^2 + (N_i - N_0)^2} \bullet 100000. \quad (1)$$

The angle between the collar and BDS-BSS is θ_i, and the accuracy is 0.01 radian. The calculation formula is as follows:

$$\theta \begin{cases} \theta_i = \arccos\left(\dfrac{E_i - E_0}{D_i}\right) \bullet 100, (N_i - N_0) > 0, \\ \theta_i = \arccos\left(\dfrac{E_i - E_0}{D_i}\right) \bullet 100 + \pi, (N_i - N_0) < 0. \end{cases} \quad (2)$$

E represents longitude, N represents latitude, E_0 represents the longitude of BDS-BSS, N_0 represents the latitude of BDS-BSS, E_i represents the longitude of collar, and N_i represents the latitude of collar, $i = 1$-2000.

(3) Data Compression. Through the following data compression method, the transmitted capacity could be increased to 36 yaks per minute, which means 2000 yaks in one pasture could be monitored every hour:

(1) BDS-BSS receives the data of collar $C_{i,0}$ and saves it to array $A_{i,0}$, which is stored in an external memory chip as format of Table 2

(2) BDS-BSS reads out the data of $A_{i,0}$ and sends it to BDS-BSR. BDS-BSR receives the data of $A_{i,0}$ and saves it to array $S_{i,0}$, which is stored in an external memory chip as format of Table 2

(3) BDS-BSS receives the data of collar $C_{i,i+1}$ and saves it to array $A_{i,i+1}$, which is stored in an external memory chip as format of Table 2. Calculate that $A_{i,i+1}$ subtracts $A_{i,i}$ in portions except collar N_0 and time, and the result is saved to array $B_{i,i+1}$ as shown in Table 3. The time is selected as interval time according to the settings of the mobile phone APP, which occupies fixed 3 bits as shown in Table 4. The data in $B_{i,i+1}$ is expressed as fixed digits and variations, and the length of the data is changeable. Under normal conditions, the variations of

TABLE 4: Interval coding.

Interval time (minutes)	Coded signal
1	001
15	010
30	011
60	100
360	101
1440	111
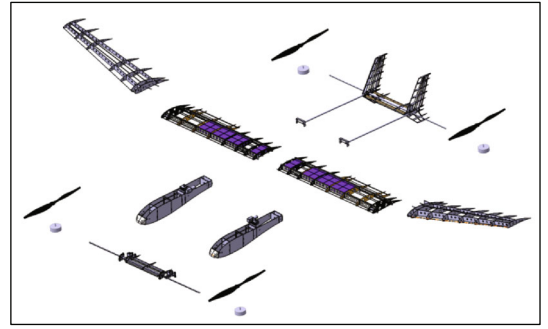
FIGURE 13: Grazing UAV in digital model.

FIGURE 14: Physical prototype of grazing UAV.

movement, temperature, and heart rate could be small. With this method, the transmission data is reduced to 34 bits in minimum and 72 bits in maximum, which promotes transmission efficiency greatly

(4) BDS-BSS reads out the data of $B_{i,i+1}$ and sends it to BDS-BSR. BDS-BSR receives the data of $B_{i,i+1}$ and saves it to array $R_{i,i+1}$, which is stored in an external memory chip as format of Table 3
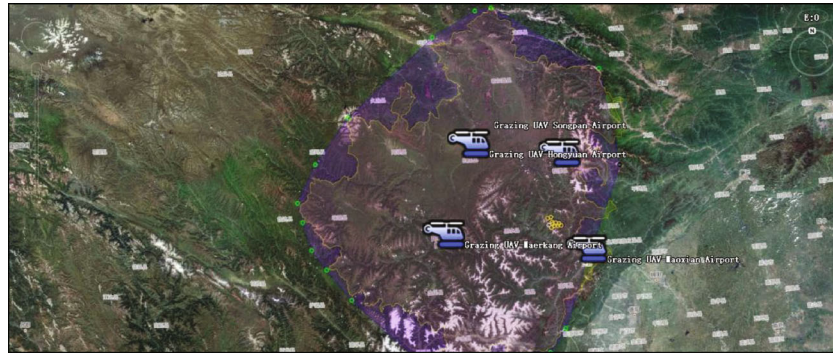
Figure 15: Flying area planning and station setting of mountaintop pasture in Aba Prefecture.
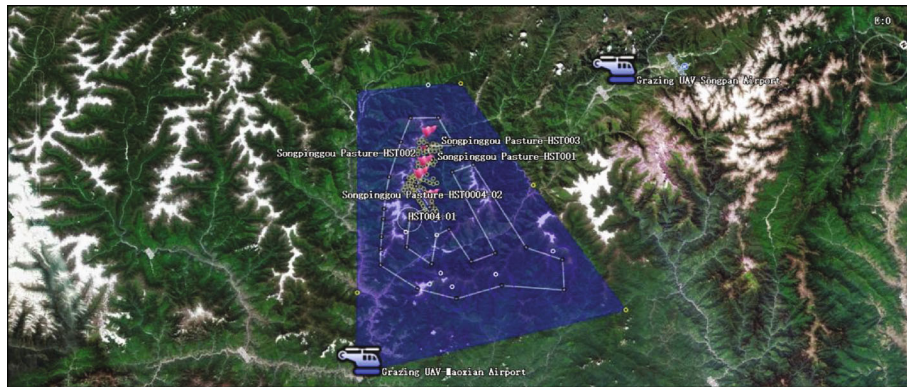
Figure 16: Precise planning of flight route of mountain pasture in the region.

Figure 17: Pasture scene of Songpinggou.

Figure 18: Wear a collar for the yak.

(5) BDS-BSR recovers the data into original format as Table 1 basing on $S_{i,i}$ and $R_{i,i+1}$, and upload it to Aliyun

4.3. Design of UAV for Plateau and Mountainous Grazing

4.3.1. Design of Plateau Mountainous Grazing UAV. Facing the needs of natural grazing application in the geographical environment of Plateau Tibetan areas, we define "plateau mountainous grazing UAV"(PMG-UAV) as a new type of special-purpose UAV, which holds functions of flexible take-off and landing, long-distance flight, and ultralong hang time. At the same time, as the communication network carrier, PMG-UAV is a basic platform, which needs long-term and high-frequency use, and should also have the requirements of high reliability and low cost. To this end, we designed a fixed-wing and multiaxis electric UAV, which could vertically take off and land, and tilt four-rotor for long-distance flight.

With a general design of double fuselage and three-wing layout, the PMG-UAV gets a maximum weight of 37 kg, load

FIGURE 19: Yak with collar.

FIGURE 20: BDS-BSS position on satellite map.

FIGURE 21: BDS-BSS position real scene.
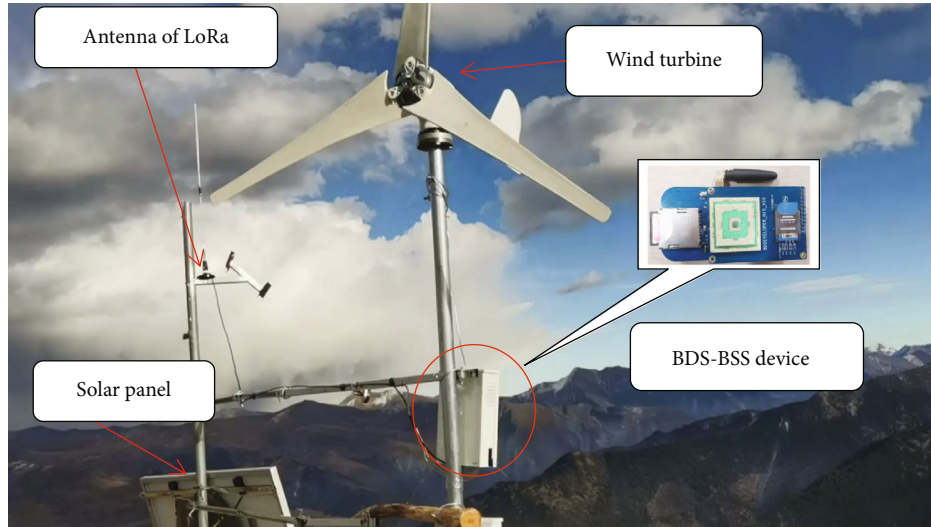
FIGURE 22: BDS-BSS and power generation facilities.

of 5 kg, wing area of 3 m², and a flight distance of more than 200 km. We arranged a 20.5 kg lithium battery in the main wing box to achieve a flight time of more than 6 hours (the currently completed prototype scheme). To further improve the flight time, 12 kg lithium battery and 8.5 kg solar thin-film scheme are designed to achieve a hang time of more than 10 hours (prototype scheme for further promotion). Considering the requirements of low use cost, we designed the aircraft into a detachable fuselage and a four-section detachable wing structure, so that the length of a single component does not exceed 2.5 m, which is convenient for storage and transportation. The digital model and physical prototype of the PMG-UAV design are shown below in Figures 13 and 14.

4.3.2. PMG-UAV Regional Flight Planning. By carrying BDS-BSSs, PMG-UAVs will build a convenient and flexible communication network with collars, so as to realize the data collection of yaks' physiological signs. At present, we have conducted a detailed investigation on the geographical characteristics of Aba Prefecture. There are about 1430 pastures, with a single pasture area of about 6-38 square kilometers, which is a flat, long, and banded. Due to the huge pastoral area in Aba Prefecture, we divide it into four parts and set up a PMG-UAV station in each area, as shown in Figure 15.

As shown in Figure 16, we have made a preliminary plan for the flight route in one of the four areas. Multiple PMG-UAVs are designed to fly in relay mode, so as to meet the needs of timely monitoring and data collection in whole area.

5. Test and Experiment

5.1. Experiment Deployment

5.1.1. Wearing the Collar. Yaks are wearing collars in one of our contracted Aviation Ecological Pasture, in Songpinggou

FIGURE 23: BDS-BSR real scene.

TABLE 5: Test results of different communication distance data.

The distance (m)	LoRa transmission rate (Kbps)	Number of data sent	Number of data received	The packet loss rate
500	0.3	100	100	0%
1000	0.3	100	99	1%
1500	0.3	100	98	2%
2000	0.3	100	96	4%
3000	0.3	100	89	11%

Township, Aba Prefecture of Sichuan Province, as shown in Figures 17–19.

5.1.2. Implementation of BDS-BSS. The BDS-BSS is installed at the top of the pasture, including power supply devices. With abundant solar and wind energy resources in the plateau mountain pasture, the wind and solar power supply
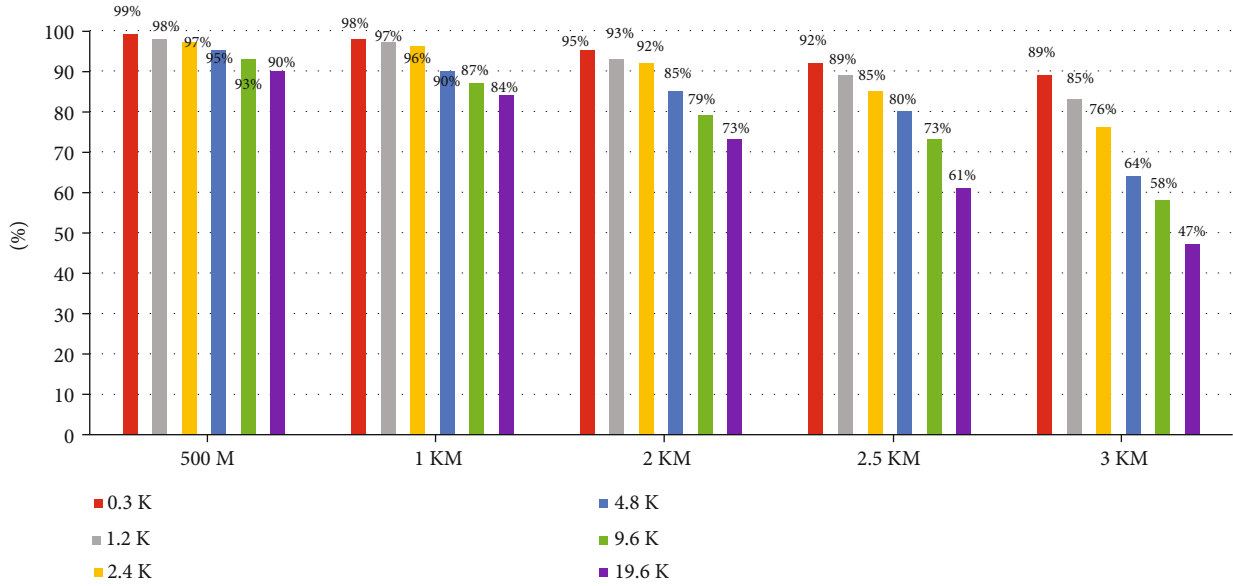
FIGURE 24: The test results of packet loss rate in different transmission rate and distance.

TABLE 6: Test results of maximum stable communication distance.

LoRa data transmission rate (Kbps)	Furthest communication distance (km)
0.3	4.3
1.2	3.2
2.4	2.5
4.8	2.0
9.6	1.4
19.2	0.9
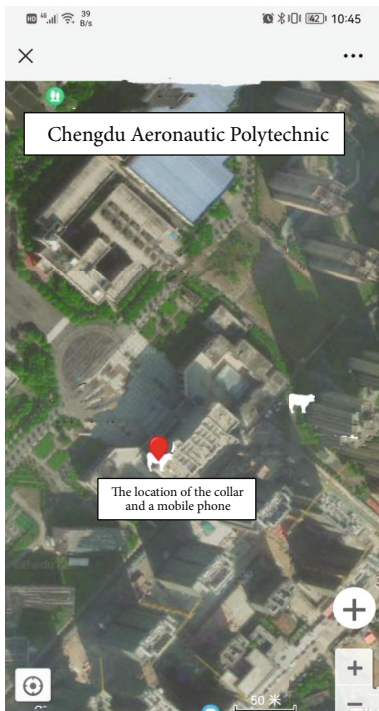
{
  "_id" : ObjectId("5fd2a90430c62457d00326a4"),
  "deviceId" : "5f3ce34ae77e21187fd5c9f9",
  "type" : "LOCATION",
  "time" : ISODate("2020-12-10T23:02:26.773+0000"),
  "location" : {
    "type" : "Point",
    "coordinates" : [
      103.50801434335796,
      32.12452266947445
    ]
  },
  "created_by" : "system",
  "created_date" : ISODate("2020-12-10T23:02:28.218+0000"),
  "last_modified_by" : "system",
  "last_modified_date" : ISODate("2020-12-10T23:02:28.218+0000"),
  "_class" : "com.wingedcare.farm.domain.DeviceTelemetry"
}

{
  "_id" : ObjectId("5fd2a93830c62457d00326a6"),
  "deviceId" : "5f3ce34ae77e21187fd5c9fe",
  "type" : "TEMPERATURE",
  "time" : ISODate("2020-12-10T23:03:19.180+0000"),
  "value" : 39.599998474121094,
  "created_by" : "system",
  "created_date" : ISODate("2020-12-10T23:03:20.865+0000"),
  "last_modified_by" : "system",
  "last_modified_date" : ISODate("2020-12-10T23:03:20.865+0000"),
  "_class" : "com.wingedcare.farm.domain.DeviceTelemetry"
}

{
  "_id" : ObjectId("5fd2a93830c62457d00326a7"),
  "deviceId" : "5f3ce34ae77e21187fd5c9fe",
  "type" : "LOCATION",
  "time" : ISODate("2020-12-10T23:03:19.180+0000"),
  "location" : {
    "type" : "Point",
    "coordinates" : [
      104.03259036124804,
      31.75286313999558
    ]
  },
  "created_by" : "system",
  "created_date" : ISODate("2020-12-10T23:03:20.866+0000"),
  "last_modified_by" : "system",
  "last_modified_date" : ISODate("2020-12-10T23:03:20.866+0000"),
  "_class" : "com.wingedcare.farm.domain.DeviceTelemetry"
}

FIGURE 26: Data received from BDS-BSS..

system is selected to power the BDS-BSS, as shown in Figures 20–22.

5.1.3. Implementation of BDS-BSS. BDS-BSR is placed at a higher place, such as the roof, with WiFi signal coverage, as shown is Figure 23. After BDS-BSR receives the data, it uses WiFi communication to upload all the received data to Aliyun every minute. The location information can be displayed intuitively on the mobile APP which is designed by ourselves independently. Other functions of APP will be enriched and updated gradually in later works.

5.2. Test Result

5.2.1. Communication Distance Test. The communication distance between the collar and BDS-BSS in 0.5 km,

FIGURE 25: Collar position on mobile APP.

Message ID	Tag	Key		
0BC1F3DC7B2B5ACF98003353BB44F30D 11.193.243.220:55752 543 Bytes	MQTT_COMMON	beidou^GID_farm@@@beidou _rd_1^26793552	2020-12-10 23:12:04	2020-12-10 23:12:04
0BC1F3DC7B2B5ACF98003587316 3D30 11.193.243.220:55752 543 Bytes	MQTT_COMMON	beidou^GID_farm@@@beidou _rd_1^26793557	2020-12-10 23:17:14	2020-12-10 23:17:14
0BC1F3DC7B2B5ACF980033 35E1FA19439 11.193.243.220:38045 543 Bytes	MQTT_COMMON	beidou^GID_farm@@@beidou _rd_1^26793563	2020-12-10 23:23:26	2020-12-10 23:23:26
0BC1F3DC7B2B5ACF98003360F636BF70 11.193.243.220:55831 543 Bytes	MQTT_COMMON	beidou^GID_farm@@@beidou _rd_1^26793566	2020-12-10 23:26:32	2020-12-10 23:26:32
0BC1F3DC7B2B5ACF98003366A35A154B 11.193.243.220:38011 543 Bytes	MQTT_COMMON	beidou^GID_farm@@@beidou _rd_1^26793572	2020-12-10 23:32:44	2020-12-10 23:32:44
0BC1F3DC7B2B5ACF980033 6795852370 11.193.243.220:55146 543 Bytes	MQTT_COMMON	beidou^GID_farm@@@beidou _rd_1^26793573	2020-12-10 23:33:46	2020-12-10 23:33:46
0BC1F3DC7B2B5ACF9800336C51AE6854 11.193.243.220:55880 542 Bytes	MQTT_COMMON	beidou^GID_farm@@@beidou _rd_1^26793578	2020-12-10 23:38:56	2020-12-10 23:38:56
0BC1F3DC7B2B5ACF98003383058B8FF0 11.193.243.220:55880 542 Bytes	MQTT_COMMON	beidou^GID_farm@@@beidou _rd_1^26793603	00:03:44	00:03:44
0BC1F3DC7B2B5ACF98003383F798CF10 11.193.243.220:55584 543 Bytes	MQTT_COMMON	beidou^GID_farm@@@beidou _rd_1^26793604	00:04:46	00:04:46
0BC1F3DC7B2B5ACF98003 3BD72915D0D 11.193.243.220:55146 543 Bytes	MQTT_COMMON	beidou^GID_farm@@@beidou _rd_1^26793615	00:15:07	00:15:07

FIGURE 27: Format of data uploaded to Aliyun.
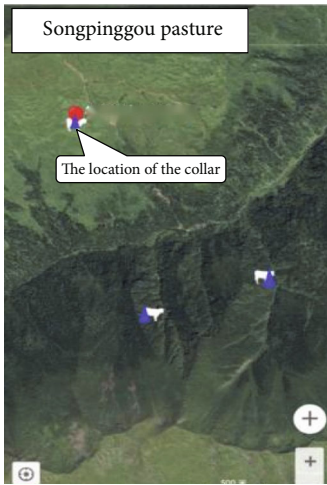
FIGURE 28: Yaks' positions in APP.

TABLE 7: Communication tests at different heights.

Height (m)	Percentage of communication success rate (%)
30	100
40	100
50	100
60	100
70	100
80	100
90	100
100	100

TABLE 8: Communication tests at different speeds.

Different speeds (km/hour)	Percentage of communication success rate (%)
4	100
6	100
8	100

1 km, 2 km, and 3 km is tested and resulted as shown in Table 5.

A packet loss rate of less than 12% is regarded as allowed communication. We can see that the BDS-BSS fixed at the top of the experimental pasture can serve a good LAN communication within the range of 3 km. And the packet loss rate of the LoRa module gets a linear relationship with distance. With further distance, the packet loss rate promotes, and the communication is still successfully established sometimes.

5.2.2. Relationship between LoRa Transmission Rate and Distance. To verify the relevance of packet loss rates in different transmission rates and distances, we took several collars to test the receiving data within the same transmitting power, antenna gain, and frequency and within the same BDS-BSS LoRa module. The test is conducted under different transmission rates, as shown in Figure 24. And the farthest transmission distance under different transmission rates is shown in Table 6, with the condition of less than 12% packet loss rate.

Within the 3 km range, the packet loss rate of data transmission is less than 12%, which is considered effective communication. When the LoRa module's transmission rate is 0.3 Kbps, the reliable communication distance can reach 4.3 km. We selected the LoRa data transmission rate of 0.3 Kbps and built a feasible LAN communication network that ensured effective communication of 3 km.

5.2.3. Data Reception and Presentation. The first step is to test in school, we put the collar and a mobile phone in the same outside place, and a cow pattern and a red dot were displayed on the mobile APP and mobile satellite map

TABLE 9: Equipment cost and usage limitations.

Equipment name	Equipment components	Usage limitations	Price
Collar	A collar and an ear-tag	Temperature is -10~50°C Altitude is below 3500 m	$62.0
BDS-BS	BDS-BSS, BDS-BSR, and power generation facilities	Temperature is -30~60°C Altitude is below 3500 m	$2326.4
PMG-UAV	Aircraft structure, navigation system, and flight control system	Flight speed is 75 km/h Flight altitude is 6000 m	$7528.1

separately. As the collar positioning data is uploaded to Aliyun via the BDS-BSR, it could be displayed correctly on the mobile APP. As shown in Figure 25, the cow pattern represents the measured collar position, the red dot is the calibration point, and the two icons overlap well.

The second step is field test in Songpinggou pasture. The test was implemented in December 10th, 2020. We installed collars on three yaks and obtained the data sent by BDS-BSS, as shown in Figure 26. Then data was uploaded to Aliyun, as shown in Figure 27. The yaks' positioning data was displayed correctly in APP, as shown in Figure 28. The blue triangles were the actual collar position of yaks reflected on the APP, and the red mark was the location of the BDS-BSS.

5.2.4. UAV Extended Communication Experiment. Because of the size and weight limitation of UAVs' low-altitude flight, we only use the four-rotor flight mode for communication verification in low-altitude and low-speed flight states, and the high-altitude and long-distance flight verification needs to be further carried out in pasture. The communication experiment results under low-altitude and low-speed flight are shown in Tables 7 and 8.

The experiment results indicate that the UAV-based LAN communication network can serve excellently under low-altitude and low-speed flight state, which provides potential capabilities of IoT accessing in ultralarge area according to the flight distance of UAVs.

The above test results show that it is feasible to use PMG-UAV to realize BDS data transmission and communication.

5.2.5. Equipment Cost and Usage Limitations. As shown in Table 9, all the equipment cost and the corresponding usage limitations were presented. All the devices meet the low-cost requirements, which can work stably and continuously in Aba Prefecture.

6. Conclusion

We proposed a low-cost grazing IoT system framework for the actual needs of yak breeding in Plateau Tibetan areas and carry out targeted design and experimental verification on terminal equipment (collar and ear-tag), communication base station (BDS-BSS and BDS-BSR), and PMG-UAV. The experimental results show that the scheme can achieve real-time yak sign data collection within 3 km of a single base station, and ultralong-distance data transmission gets zero additional use cost. The smart grazing system framework proved to be effective, feasible, low-cost, and extendable and fully met the needs of yak grazing in the Tibetan Plateau.

BDS short-message technology is applied to the field of IoT for the first time, and a yak sign data compression method based on BDS and the actual situation of grazing is proposed, which improved the short-message communication capacity of four times and makes real-time communication possible.

The specific requirements for plateau mountainous grazing UAV are further clarified, and a feasible low-cost PMG-UAV scheme is presented, which provides a preliminary scheme for the IoT access of large-area pastures over 100 km^2.

In further research, we will promote the following aspects: (1) the flight test of the PMG-UAV in the pasture of Aba Prefecture, (2) flight verification along regional route planning, (3) the study of building communication network with multiple PMG-UAVs, and (4) upgrade the APP and combine it with the whole system so as to realize good application experience.

Abbreviations

BDS: BeiDou Satellite
BDS-BS: BeiDou Satellite-Base Stations
BDS-BSS: BeiDou Satellite-Base Station Sender
BDS-BSR: BeiDou Satellite-Base Station Receiver
PMG-UAV: Plateau mountainous grazing UAV
IoT: Internet of Things
UAV: Unmanned aerial vehicle
MCU: Microcontroller unit
WSNs: Wireless sensor networks
LPWAN: Low-power wide-area network.

Data Availability

The datasets used and/or analyzed during the current study are available from the corresponding author on reasonable request.

Conflicts of Interest

The authors declare that they have no conflicts of interest.

Acknowledgments

References

[1] P. Barker and M. Hammoudeh, "A survey on low power network protocols for the Internet of Things and wireless sensor networks," in *2017 Association for Computing Machinery*, pp. 1–8, Cambridge, UK, 2017.

[2] E. A. Shammar and A. T. Zahary, "The Internet of Things (IoT): a survey of techniques, operating systems, and trends," *Library Hi Tech*, vol. 38, no. 1, pp. 5–66, 2019.

[3] W. Xu, J. Zhang, S. Huang, C. Luo, and W. Li, "Key generation for Internet of Things," *ACM Computing Surveys*, vol. 54, no. 1, pp. 1–37, 2022.

[4] A. Sales Mendes, D. M. Jiménez-Bravo, M. Navarro-Cáceres, V. Reis Quietinho Leithardt, and G. Villarrubia González, "Multi-agent approach using LoRaWAN devices: an airport case study," *Electronics*, vol. 9, no. 9, p. 1430, 2020.

[5] N. Cvar, J. Trilar, A. Kos, M. Volk, and E. Stojmenova Duh, "The use of IoT technology in smart cities and smart villages: similarities, differences, and future prospects," *Sensors*, vol. 20, no. 14, p. 3897, 2020.

[6] Y. Wu, G. Guo, G. Tian, and W. Liu, "A model with leaf area index and trunk diameter for LoRaWAN radio propagation in eastern China mixed forest," *Journal of Sensors*, vol. 2020, Article ID 2687148, 16 pages, 2020.

[7] E. González, J. Casanova-Chafer, A. Romero, X. Vilanova, J. Mitrovics, and E. Llobet, "LoRa sensor network development for air quality monitoring or detecting gas leakage events," *Sensors*, vol. 20, no. 21, p. 6225, 2020.

[8] D. Davcev, K. Mitreski, S. Trajkovic, V. Nikolovski, and N. Koteli, "IoT agriculture system based on LoRaWAN," in *2018 14th IEEE International Workshop on Factory Communication Systems(WFCS)*, pp. 1–4, Imperia, Italy, 2018.

[9] M. Behjati, A. B. Mohd Noh, H. A. H. Alobaidy, M. A. Zulkifley, R. Nordin, and N. F. Abdullah, "LoRa communications as an enabler for internet of drones towards large-scale livestock monitoring in rural farms," *Sensors*, vol. 21, no. 15, p. 5044, 2021.

[10] J. Hu, T. Wang, J. Yang, Y. Lan, S. Lv, and Y. Zhang, "WSN-assisted UAV trajectory adjustment for pesticide drift control," *Sensors*, vol. 20, no. 19, p. 5473, 2020.

[11] Y. Guo, H. Wang, Z. Wu et al., "Modified red blue vegetation index for chlorophyll estimation and yield prediction of maize from visible images captured by UAV," *Sensors*, vol. 20, no. 18, p. 5055, 2020.

[12] H. I. Minhas, R. Ahmad, W. Ahmed, M. Waheed, M. M. Alam, and S. T. Gul, "A reinforcement learning routing protocol for UAV aided public safety networks," *Sensors*, vol. 21, no. 12, p. 4121, 2021.

[13] X. Li, K. Zhang, Y. Yuan, X. Zhang, and X. Li, "BDS code bias periodical mitigation by low-pass filtering and its applications in precise positioning," *The Journal of Global Positioning Systems*, vol. 16, no. 1, 2018.

[14] J. Wei, C.-H. Chiu, F. Huang, J. Zhang, and C. Cai, "A cost-effective decentralized vehicle remote positioning and tracking system using BeiDou Navigation Satellite System and Mobile Network," *EURASIP Journal on Wireless Communications and Networking*, vol. 2019, 2019.

[15] Y. Yang, Y. Mao, and B. Sun, "Basic performance and future developments of BeiDou global navigation satellite system," *Satellite Navigation*, vol. 1, no. 1, 2020.

[16] T. Zeng, L. Sui, R. Ruan, X. Jia, and L. Feng, "Uncombined precise orbit and clock determination of GPS and BDS-3," *Satellite Navigation*, vol. 1, no. 1, 2020.

[17] S. Jin and K. Su, "PPP models and performances from single- to quad-frequency BDS observations," *Satellite Navigation*, vol. 1, no. 1, 2020.

[18] C. Pereira, J. Mesquita, D. Guimarães, F. Santos, L. Almeida, and A. Aguiar, "Open IoT architecture for continuous patient monitoring in emergency wards," *Electronics*, vol. 8, no. 10, p. 1074, 2019.

[19] R. Sanchez-Iborra, I. G. Liaño, C. Simoes, E. Couñago, and A. Skarmeta, "Tracking and monitoring system based on LoRa technology for lightweight boats," *Electronics*, vol. 8, no. 1, p. 15, 2019.

[20] H. C. Yu, M. Y. Tsai, Y. C. Tsai et al., "Development of miniaturized water quality monitoring system using wireless communication," *Sensors*, vol. 19, no. 17, p. 3758, 2019.

[21] A. Guidi, A. Lanata, P. Baragli, G. Valenza, and E. Scilingo, "A wearable system for the evaluation of the human-horse interaction: a preliminary study," *Electronics*, vol. 5, no. 4, p. 63, 2016.

[22] N. Mansbridge, J. Mitsch, N. Bollard et al., "Feature selection and comparison of machine learning algorithms in classification of grazing and rumination behaviour in sheep," *Sensors*, vol. 18, no. 10, p. 3532, 2018.

[23] E. Schlecht, C. Hülsebusch, F. Mahler, and K. Becker, "The use of differentially corrected global positioning system to monitor activities of cattle at pasture," *Applied Animal Behaviour Science*, vol. 85, no. 3-4, pp. 185–202, 2004.

[24] J. D. Davis, M. J. Darr, H. Xin, J. D. Harmon, and J. R. Russell, "Development or and the effect of sample interval on travel distance," *Applied Engineering in Agriculture*, vol. 27, no. 1, pp. 143–150, 2011.

[25] F. Maroto-Molina, J. Navarro-García, K. Príncipe-Aguirre et al., "A low-cost IoT-based system to monitor the location of a whole herd," *Sensors*, vol. 19, no. 10, p. 2298, 2019.

[26] J. A. Vázquez-Diosdado, V. Paul, K. A. Ellis, D. Coates, R. Loomba, and J. Kaler, "A combined offline and online algorithm for real-time and long-term classification of sheep behaviour: novel approach for precision livestock farming," *Sensors*, vol. 19, no. 14, p. 3201, 2019.

[27] L. Riaboff, S. Couvreur, A. Madouasse et al., "Use of predicted behavior from accelerometer data combined with GPS data to explore the relationship between dairy cow behavior and pasture characteristics," *Sensors*, vol. 20, no. 17, p. 4741, 2020.

[28] H. Xu, S. Li, C. Lee et al., "Analysis of cattle social transitional behaviour: attraction and repulsion," *Sensors*, vol. 20, no. 18, p. 5340, 2020.

[29] T. Aoki, M. Itoh, A. Chiba et al., "Heart rate variability in dairy cows with postpartum fever during night phase," *PLoS One*, vol. 15, no. 11, article e0242856, 2020.

[30] L. Nie, D. Berckmans, C. Wang, and B. Li, "Is continuous heart rate monitoring of livestock a dream or is it realistic? A review," *Sensors*, vol. 20, no. 8, p. 2291, 2020.

[31] A. Youssef, A. Peña Fernández, L. Wassermann et al., "An approach towards motion-tolerant PPG-based algorithm for real-time heart rate monitoring of moving pigs," *Sensors*, vol. 20, no. 15, p. 4251, 2020.

[32] U. Raza, P. Kulkarni, and M. Sooriyabandara, "Low power wide area networks: an overview," *IEEE Communications Surveys & Tutorials*, vol. 19, no. 2, pp. 855–873, 2017.

[33] K. Mekki, E. Bajic, F. Chaxel, and F. Meyer, "A comparative study of LPWAN technologies for large-scale IoT deployment," *ICT Express*, vol. 5, no. 1, pp. 1–7, 2019.

[34] Q. M. Ilyas, M. Ahmad, and M. H. Anisi, "Smart farming: an enhanced pursuit of sustainable remote livestock tracking and Geofencing using IoT and GPRS," *Wireless Communications and Mobile Computing*, vol. 2020, Article ID 6660733, 12 pages, 2020.

[35] X. Liu and C. Huo, "Research on remote measurement and control system of piggery environment based on LoRa," in *2017 Chinese Automation Congress (CAC)*, pp. 7016–7019, Jinan, China, 2017.

[36] A. Valente, S. Silva, D. Duarte, F. Cabral Pinto, and S. Soares, "Low-cost LoRaWAN node for agro-intelligence IoT," *Electronics*, vol. 9, no. 6, p. 987, 2020.

[37] M. S. Sardar, Y. Yi, W. Xue-fen et al., "Experimental analysis of LoRa CSS wireless transmission characteristics for forestry monitoring and sensing," in *2018 International Symposium in Sensing and Instrumentation in IoT Era (ISSI)*, pp. 01249–01254, Shanghai, China, 2018.

[38] T. Janssen, N. BniLam, M. Aernouts, R. Berkvens, and M. Weyn, "LoRa 2.4 GHz communication link and range," *Sensors*, vol. 20, no. 16, p. 4366, 2020.

[39] J. Lee, Y. S. Yoon, H. W. Oh, and K. R. Park, "DG-LoRa: deterministic group acknowledgment transmissions in LoRa networks for industrial IoT applications," *Sensors*, vol. 21, no. 4, p. 1444, 2021.

[40] R. Berto, P. Napoletano, and M. Savi, "A LoRa-based mesh network for peer-to-peer long-range communication," *Sensors*, vol. 21, no. 13, p. 4314, 2021.

[41] M. Guerrero, C. Cano, X. Vilajosana, and P. Thubert, "Towards dependable IoT via interface selection: predicting packet delivery at the end node in LoRaWAN networks," *Sensors*, vol. 21, no. 8, p. 2707, 2021.

[42] N. C. Gaitan, "A long-distance communication architecture for medical devices based on LoRaWAN protocol," *Electronics*, vol. 10, no. 8, p. 940, 2021.

[43] G. B. Gaggero, M. Marchese, A. Moheddine, and F. Patrone, "A possible smart metering system evolution for rural and remote areas employing unmanned aerial vehicles and Internet of Things in smart grids," *Sensors*, vol. 21, no. 5, p. 1627, 2021.

WILEY | Hindawi

Research Article

Sparse Covariance Matrix Reconstruction-Based Nulling Broadening for UAV 2D Antenna Arrays

Chuang Han, Haoyang Lei [iD], Yanyun Gong, and Ling Wang [iD]

The School of Electronics and Information, Northwestern Polytechnical University, Xi'an, Shaanxi 710072, China

Correspondence should be addressed to Ling Wang; lingwang@nwpu.edu.cn

Since the antennas on UAVs may have slight vibrations or the interference source is in the state of rapid movement in practice, the interference suppression performance and robustness of the traditional methods may suffer a decline. In this paper, we propose a flexible asymmetric null widening technique, which allows flexible adjustment of the null width to accommodate the variation of the interference source. This method has a good effect of spreading zero trap on the two-dimensional array and can effectively reduce the waste of degrees of freedom. Firstly, the flexible asymmetric null widening method is extended to two-dimensional arrays to accommodate 2D array antennas of UAVs. Secondly, when the SMI algorithm is applied in adaptive beamforming, the desired signal appears in sampling snapshots or using data samples, resulting in a model mismatch. To solve the model mismatch problem of UAV antenna arrays, this paper applies a sparsity-based interference plus noise covariance matrix reconstruction technique. Finally, for the application scenario that the UAV may receive signals from multiple directions, we apply the linear constrained minimum variance criterion (LCMV) to achieve the main beam gain formation in multiple directions. The simulation results show that we can generate a wide null and adjust the null width asymmetrically. The results also show that the model mismatch problem is avoided, and the performance of the adaptive beamforming is almost optimal. For the UAV antenna, we also implemented multiple beams to receive multiple signals .

1. Introduction

In recent years, drones have been widely used in various fields, including aerial photography, target detection, crop condition monitoring, and marine remote sensing [1–4], while in the communication between UAVs or UAVs in receiving the desired target signal, the UAV's receiving antenna needs to process the received signal, i.e., array signal processing, and its core is adaptive array processing also known as airspace adaptive filtering. It is now widely used in military and civilian applications in radar, sonar, seismology, radio astronomy, wireless communications, acoustics, medical imaging, and other fields [5–9]. It is well known that adaptive beamforming techniques are sensitive to model mismatch, especially when the desired signal is present in the training data. In addition, as the absolute stability of UAVs cannot be guaranteed during flight, the antenna may have slight vibration or the unstable interference signal source may have fast movement, resulting in interference

signal deviation. As a result, the adaptive beamforming cannot suppress the deviated interference signal effectively. For these reasons, the performance of traditional adaptive beamformers deteriorates severely. Therefore, robust adaptive beamforming methods have been extensively studied in the past decades, and many robust adaptive beamforming methods have been proposed. In adaptive beamforming, the classic method of minimum variance distortion response (MVDR) [5, 10], also known as Capon beamforming [11], is generally adopted to obtain the weight of beamforming. However, since the ideal sampling covariance matrix cannot be obtained, the sampling covariance matrix inverse algorithm (SMI) [12] is used in practice. Because the SMI algorithm uses sampling data to construct the covariance matrix, it is possible to include information about the desired signal in the covariance matrix. This means that the results are influenced by the expected signal. In the case that the signal-to-noise ratio (SNR) is high, the results can be significantly mismatched, leading to a severe decline in

beamformer performance. Typically, diagonal loading techniques [13] are used to solve these problems, but due to the difficulty of finding the optimum diagonal loading factor for the corresponding beamformer. Worst-case performance optimization [14], on the other hand, can also be considered as a diagonal loading technique. However, the worst-case scenario does not always occur, and the optimization results are still suboptimal. An adaptive tridiagonal loading technique has also been proposed [15], where the unitary matrix is replaced by a Toplitz matrix and the loading factor is determined by a method based on the output power of a low partials beam in the assumed direction of the desired signal. However, since the information of the desired signal is still retained, the performance is improved over other beamformers at large signal-to-noise ratios but still decreases as the signal-to-noise ratio increases. Another solution to the mismatch problem is to deal with the assumed signal guidance vector. Since the mismatch vector and its parametric bound are actually unknown, the actual guidance vector can be estimated in an iterative manner, with each iteration being a quadratic convex optimization problem [16]. In this paper, in order to solve the mismatch problem in UAV antenna beamforming, a better approach is to reconstruct the covariance matrix to remove the information of the desired signal and then directly solve the mismatch problem caused by the desired signal [17]. To reduce the computational effort associated with covariance matrix reconstruction, the sparse nature of the signal source in the observed field in UAV antenna beamforming is used to reconstruct the covariance matrix [18].

Since the UAV cannot be absolutely stable in the flight process and the location of interference sources in the environment cannot be absolutely unchanged, the interference signals to be suppressed by the UAV antenna will deviate slightly. In traditional adaptive beamforming, only a single interference signal cannot produce a zero trap, so it is necessary to broaden the width of the zero trap at the interference. To solve the above problems, the classic zero-trap broadening method is the covariance matrix conization technique (CMT) [19]. It is mainly realized by using a null widening technology independently proposed by Zatman [20] and Mailloux [21], which can obtain a wider zero trap. Much further work has been done based on covariance matrix conization (CMT). A novel null widening method for sidelobe cancellers with high computational efficiency is proposed [22]. The CMT technique can produce a wide zero trap, and it produces the widest zero trap to cover the worst case of interfering signal deviation, which causes it to waste a large number of degrees of freedom [23]. It shows that the cost of degrees of freedom is proportional to the zero-width and aperture of the array. Therefore, [24] proposed a kind of zero-notch width that can be flexibly adjusted and can produce asymmetric zero-notch width to meet different situations. Since the antenna used on UAV is generally a two-dimensional array, we need the zero-trap broadening technology of a two-dimensional array. A null widening technique for the uniform circular array is proposed [25], but it is only limited to the broadening of the uniform circular array.

In this paper, based on Mailloux's zero-notch broadening method, a null widening method for two-dimensional arrays is proposed. The signal received by the drone's two-dimensional array antenna is determined by two dimensions of information. When adding a virtual interference source, you need to add a virtual interference source of equal interval and equal intensity in two dimensions. To produce asymmetrical and flexible zero-notch width, we increase the number of virtual interference sources near the interference signal asymmetrically. The method proposed in this paper can not only obtain a wide zero-trap width and flexibly adjust the width but also produce asymmetric width for the deviation of UAV jamming signal in practice, which does not need to cover the worst deviation to reduce the consumption of freedom. In the realization of zero-trap broadening, the performance of adaptive beamforming is seriously degraded due to the model adaptation in high SNR due to the inclusion of desired signals. In this paper, a sparse covariance matrix reconstruction method [18] is proposed to remove the desired signal information. Finally, given the problem that UAV may encounter in practice in accepting signals from multiple directions, this paper proposes to adopt a linear constrained minimum variance criterion (LCMV) [25] to form a multibeam direction graph. Finally, we simulate a concentric ring array, and the results show that the mismatch problem can be solved well in high SNR, and the asymmetric zero-trap width can be adjusted flexibly.

Section 2 introduces the basic signal model, Section 3 presents the sparse covariance matrix reconstruction method and the zero-trap spreading technique proposed in this paper, Section 4 presents the model of the concentric circular array and gives some simulation results, and finally, Section 5 gives our conclusions.

2. The Signal Model

2.1. Array Signal Model.
Assume that signals emitted from radiation sources at far-field sources include the desired signal with direction θ_0 and M narrowband interference signals with direction $\theta_k (k = 1, 2, \cdots, M)$ and the inevitable noise signal. The array signal model is at this point [26].

$$X(t) = AS(t) + n(t), \tag{1}$$

where $S(t) = [s_0(t), s_1(t), \cdots, s_M(t)]^T$ is the complex envelope of the received signal including desired signal and interfering signals, $n(t) = [n_1(t), n_2(t), \cdots, n_M(t)]^T$ is the noise that exists during transmission, $A = [a(\theta_0), a(\theta_1), \cdots, a(\theta_M)]$ is a matrix of the steering vectors corresponding to the above signal, and $(\cdot)^T$ is the transpose operation of a matrix. The steering vector [26] is

$$a(\theta) = \left[1, e^{j2\pi d \cos \theta / \lambda}, \cdots, e^{j2\pi (M-1)d \cos \theta / \lambda}\right]^T, \tag{2}$$

where λ is the operation wavelength and d is the distance between elements of the array generally taken as $\lambda/2$. The adaptive beamformer output is given by

$$y(t) = w^H X(t) = s(t) w^H a(\theta), \quad (3)$$

where $w = [w_1, w_2, \cdots, w_M]^T$ is the weight of the beamforming, and the weight is an important parameter in adaptive beamforming, and $X(t) = [x_1(t), x_2(t), \cdots, x_M(t)]^T$ is the signal accepted by each array element. $(\cdot)^H$ is the conjugate transpose operator symbol. To btain weights, the minimum variance distortion response (MVDR) beamforming problem is usually used [27].

$$\begin{cases} \min_w w^H R_{i+n} w, \\ \text{s.t} w^H a(\theta_0) = 1, \end{cases} \quad (4)$$

and the solution is the MVDR beamformer, also referred to as the Capon beamformer. Then, the weights are given by

$$w_{\text{opt}} = \frac{R_{i+n}^{-1} a(\theta_0)}{a^H(\theta_0) R_{i+n}^{-1} a(\theta_0)}, \quad (5)$$

where R_{i+n} is the interference plus noise covariance matrix. In the real system, we cannot obtain the ideal covariance matrix, so the Sampled Covariance Matrix Inverse (SMI) algorithm is used, and the maximum likelihood estimation method is used to estimate the covariance matrix as $\widehat{R}_x(M)$ $= 1/M \sum_{i=1}^{M} X(t_i) X^H(t_i)$. Then, the weights of the SMI algorithm are expressed as $w_{\text{smi}} = \widehat{R}_x^{-1} a(\theta_0) / a^H(\theta_0) \widehat{R}_x^{-1} a(\theta_0)$. Since the SMI algorithm estimates the interference plus noise covariance matrix from the sampled signal, there must be information about the desired signal in it.

For a smooth random signal, the interference plus noise covariance matrix can be obtained based on its output signal power as

$$R_{i+n} = \sum_{l=1}^{L} \sigma_l^2 a(\theta_l) a^H(\theta_l) + \sigma_n^2 I. \quad (6)$$

2.2. Interference-Plus-Noise Covariance Matrix Reconstruction.
Generally, the number of interference sources and their actual steering vectors and power are usually unknown. In addition, the noise power is also unknown. Therefore, to reconstruct the interference plus noise covariance matrix, we need to know the spatial-spectral distribution in all possible directions. In this correspondence, we use the Capon spatial spectrum estimator

$$\widehat{P}(\theta) = \frac{1}{a^H(\theta) \widehat{R}^{-1} a(\theta)}. \quad (7)$$

By substituting back the optimal weights of the MVDR beamformer, the objective function in its problem yields $\widehat{R}$. The covariance matrix of the disturbance plus noise can be reconstructed using the method of Capon's spectral estimation as

$$\tilde{R}_{i+n} = \int_\Theta \widehat{P}(\theta) a(\theta) a^H(\theta) d\theta = \int_\Theta \frac{a(\theta) a^H(\theta)}{a^H(\theta) \widehat{R}^{-1} a(\theta)} d\theta, \quad (8)$$

where Θ is the range $\tilde{\Theta}$ that contains the interfering and noisy signals obtained by removing the desired signal that we can estimate. And their concatenation is the whole spatial domain, and their intersection is the empty set.

2.3. Regular Covariance Matrix Tapers.
The method of covariance matrix taper, also known as the Mailloux–Zatman (MZ) null widening method, is achieved by modifying the original covariance matrix as follows:

$$\widehat{R}_{\text{MZ}} = \widehat{R} \circ T_{\text{MZ}}, \quad (9)$$

where T_{MZ} is a positive definite matrix of real numbers, where $\circ$ is the Hadamard product operation, which is the multiplication of the corresponding elements of two matrices. The cone operation on the covariance matrix is also called a cone matrix, and the corresponding elements of its mnth term are

$$[T_{\text{MZ}}]_{mn} = \sin c \left(\frac{(m-n)\Delta}{\pi} \right), \quad (10)$$

where Δ is the normalized virtual bandwidth by whose size and the width of the zero trap can be varied.

2.4. Multibeam Formation Algorithm.
The LCMV criterion is a generalization of the MVDR criterion with the addition of multiple constraints. Assuming that the desired signal arrives in multiple directions at this time, we can obtain the basic mathematical model of the LCMV criterion as

$$\begin{cases} \min_w w^H R_x w, \\ \text{s.t} w^H C = F^H. \end{cases} \quad (11)$$

According to equation (11), we can then obtain the optimal weights under the LCMV criterion as

$$w_{\text{opt}} = R_x^{-1} C \left(C^H R_x^{-1} C \right)^{-1} F, \quad (12)$$

where $F^T = [c_1, c_2, \cdots, c_L]$ is a vector of constants in dimension $L \times 1 (L \geq 1)$. The constant value c is generally taken as 1, and $C = [a(\theta_0), a(\theta_1), \cdots, a(\theta_{L-1})]$ is the popularity matrix of the A-dimensional oriented vector.

3. The Proposed Algorithm

3.1. Interference-Plus-Noise Covariance Matrix Sparse Reconstruction.
In array signal processing, generally, the number of signals sent by the array accepting radiation sources is much smaller than the number of array elements. That is, the sources are sparse in the observation field. In this case, the reconstruction of the (6) covariance matrix does not need to be integrated over the entire airspace coverage. Thus, sparsity can be exploited to

TABLE 1: Parameters of concentric seven circles.

	Circle 1	Circle 2	Circle 3	Circle 4	Circle 5	Circle 6	Circle 7
Radius (m)	$\lambda/2$	λ	$3\lambda/2$	4λ	$5\lambda/2$	6λ	$7\lambda/2$
Number	7	13	19	26	32	38	44
Angle (rad)	$2\pi/7$	$2\pi/13$	$2\pi/9$	$\pi/13$	$\pi/16$	$\pi/19$	$\pi/22$

reconstruct the covariance matrix. The sparse constrained optimization problem used to determine the source location and its power is obtained by combining the l_0-norm (denoted by $\|.\|_0$) and can be expressed as

$$\min_{P,\sigma_n^2} \left\|\widehat{R}_x - APA^H - \sigma_n^2 I\right\|_F^2 + \gamma \|p\|_0,$$

$$\text{subject to } p \geq 0, \sigma_n^2 > 0, \tag{13}$$

where p is the spatial spectrum of the signal we wish to obtain over the entire range of signal space, P is the diagonal matrix of p, $A = [a(\theta_1), a(\theta_2), \cdots, a(\theta_N)]$ is an array of streamlined matrices, σ_n^2 is the noise power taken as the minimum eigenvalue of the covariance matrix, I is an identity matrix, γ controls the tradeoff between the sparsity of the spectrum and the residual norm, and $\|.\|_F$ is the Frobenius norm of a matrix. The optimization problem (13) is a CS problem. This is a difficult combinatorial optimization problem, but when the problem is sparse enough, we can turn it into a l_1-norm (denoted by $\|.\|_1$) problem. Assuming that the DOA estimate of the desired signal is already known, the problem (13) degenerates to an inequality constrained least squares problem. Thus, (13) can be simplified as

$$\min_{p\left(\widetilde{\theta}_p\right)} \left\|\widehat{R}_x - \widehat{\sigma}_n^2 I - A\left(\widetilde{\theta}_p\right)P\left(\widetilde{\theta}_p\right)A^H\left(\widetilde{\theta}_p\right)\right\|_F^2,$$

$$\text{subject to } p\left(\widetilde{\theta}_p\right) > 0, \tag{14}$$

where $\widetilde{\theta}_p$ is the direction of the signal for which we want to estimate the spatial spectrum. This is a convex optimization problem [28, 29] and can be solved using convex optimization software [30]. There are only Q nonzero results in the derived result, and based on the spatial spectrum of Q-sparse, we can reconstruct the interference plus noise covariance matrix

$$\widetilde{R}_{i+n} = \sum_{\substack{k=1 \\ k \neq q}}^{Q} p\left(\widetilde{\theta}_{p_k}\right)a\left(\widetilde{\theta}_{p_k}\right)a^H\left(\widetilde{\theta}_{p_k}\right) + \widehat{\sigma}_n^2 I. \tag{15}$$

Thus, we can obtain the weights of the adaptive beamformer based on the covariance matrix reconstruction as

$$w = \frac{\widetilde{R}_{i+n}^{-1}a(\theta_0)}{a^H(\theta_0)\widetilde{R}_{i+n}^{-1}a(\theta_0)}. \tag{16}$$

3.2. Null Broadening with Covariance Matrix Reconstruction in 2D Arrays.

We know that the expansion matrix T_{MZ} in (9) is the well-known Mailloux or Zatman method. We use the example based on Mailloux's idea, which is to assume the existence of a set of virtual disturbances around narrowband disturbances. Firstly, in a 1D array, we can obtain the mnth term of the covariance matrix using Mailloux's method as

$$\widetilde{R}_{mn} = [R]_{mn} \cdot \sin c\left[\frac{(m-n)dW}{\lambda}\right] = [R]_{mn} \cdot [T_{MZ}]_{mn}, \tag{17}$$

where T_{MZ} is the tapered matrix. To be able to generate asymmetric zero traps, replace the equally spaced virtual interference range in the vicinity of the disturbance in the Mailloux method with $-I_1$ to I_2. Thus, the tapered matrix T can be obtained

$$\left[\widetilde{T}_{MZ}\right]_{m,n} = \sin c\left(\frac{(m-n)(W_2 + W_1)d}{\lambda}\right) \cdot e^{j\pi d(m-n)(W_2-W_1)/\lambda}, \tag{18}$$

where W_1 and W_2 are the widening factors, and the size of which can be adjusted to obtain asymmetric zero-trap widths on each side of the interference. In a two-dimensional array, the direction of origin of the signal is determined by the azimuth θ and pitch angles φ, where the steering vector is

$$a(\theta, \varphi) = \begin{bmatrix} 1 \\ e^{j(2\pi d/\lambda)\cdot L_1 \cdot B_{\theta,\varphi}} \\ \vdots \\ e^{j(2\pi d/\lambda)\cdot L_{M-1} \cdot B_{\theta,\varphi}} \end{bmatrix}, \tag{19}$$

where $B_{\theta,\varphi} = (\cos\theta\sin\varphi, \sin\theta\sin\varphi)^T$ and L is the coordinate of the all array element of the two-dimensional array. The expression for the covariance matrix of interference plus noise is obtained by substituting the steering vector of the 2D array

$$R_{i+n} = \sum_{i=1}^{Q} \sigma_I^2 a(\theta_i, \varphi_i)a^H(\theta_i, \varphi_i) + \widehat{\sigma}_n^2 I. \tag{20}$$

According to the idea of the Mailloux method, in a one-dimensional array, since the signal emitted by the source is accepted as equivalent to a plane wave, we only
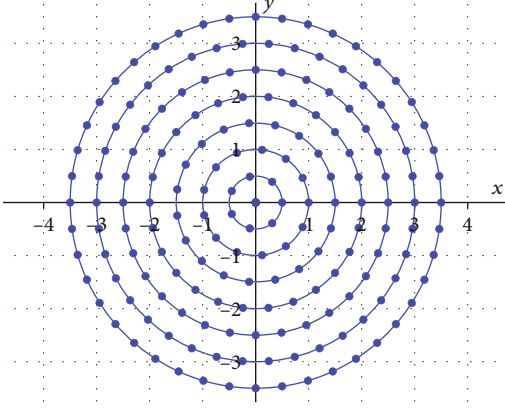
Figure 1: Schematic diagram of the concentric seven-circle array model.

need to add equally spaced virtual interference in one dimension to broaden the zero trap. However, in a two-dimensional array, the signal may be received from all angles in space, and its direction is determined by two angles, the azimuth θ and pitch angles φ, so it is necessary to add virtual interference in two dimensions to form the zero trap.

To derive the tapered matrix for the zero-trap spread of a two-dimensional array, we need to consider the coordinates of the array elements of the two-dimensional array when calculating the covariance matrix. Then, the coordinate matrix of the M array elements is expressed as

$$L = \begin{bmatrix} x_0 & y_0 \\ x_1 & y_1 \\ \vdots & \vdots \\ x_{M-1} & y_{M-1} \end{bmatrix}, \tag{21}$$

where (x, y) is the coordinate of each array element of the two-dimensional array. By substituting the coordinate values into the calculation of the steering vector, we obtain the steering vector as

$$a(\theta, \varphi) = \begin{bmatrix} 1 \\ e^{j2\pi d(x_1 u + y_1 v)/\lambda} \\ \vdots \\ e^{j2\pi d(x_{M-1} u + y_{M-1} v)/\lambda} \end{bmatrix}, \tag{22}$$

where $u = \cos\theta \sin\varphi$ and $v = \sin\theta \sin\varphi$. According to equation (24) we know that the interference-plus-noise covariance matrix R_{i+n} is actually the guided vector multiplied by its transpose matrix, that is, each term of the covariance matrix $[R_{i+n}]_{mn}$ is actually the product of the mth term of a column vector and the nth term of its conjugate transposed row vector, so the mnth term of the covariance matrix can be obtained as

$$\begin{aligned}[R_{i+n}]_{mn} &= \sum_{q=1}^{Q} \sigma_q^2 e^{j2\pi d(x_m u + y_m v)/\lambda} \\ &\quad \cdot \sum_{q=1}^{Q} \sigma_q^2 e^{-j2\pi d(x_n u + y_n v)/\lambda} \\ &= \sum_{q=1}^{Q} \sigma_q^2 e^{j2\pi d[(x_m - x_n)u + (y_m - y_n)v]/\lambda}, \end{aligned} \tag{23}$$

where σ_q^2 is the power of the qth interfering signal. To widen the zero-trap width at the suppressed disturbances, we need to add J equally spaced virtual disturbances in the x and y coordinate dimensions, respectively. Then, the $[\tilde{R}_{i+n}]_{mn}$ equation is expressed as

$$\begin{aligned}[\tilde{R}_{i+n}]_{mn} &= [R_{i+n}]_{mn} \cdot \sin c\left[\frac{(x_m - x_n)dW_x}{\lambda}\right] \cdot \sin c \\ &\quad \cdot \left[\frac{(y_m - y_n)dW_y}{\lambda}\right] = [R_{i+n}]_{mn} \cdot [T_{PA}]_{mn}, \end{aligned} \tag{24}$$

where T_{PA} is a two-dimensional planar array of zero-trapped widened tapered matrices. Thus, we can then obtain the mnth term of the tapering matrix of the zero-trap spread of the two-dimensional array as

$$\begin{aligned}[T_{PA}]_{mn} &= \sum_{p_x=-(J-1)/2}^{(J-1)/2} e^{j2\pi d[(x_m - x_n)p_x \Delta u y\lambda} \cdot \sum_{p_y=-(J-1)/2}^{(J-1)/2} e^{j2\pi d} \\ &\quad \cdot \left[(y_m - y_n)p_y \Delta u\right]/\lambda = \sin c\left[\frac{(x_m - x_n)dW_x}{\lambda}\right] \cdot \sin c \\ &\quad \cdot \left[\frac{(y_m - y_n)dW_y}{\lambda}\right]. \end{aligned} \tag{25}$$

When we use two-dimensional array elements to receive signals may not need to spread the same width at the same time at the interference, which requires us to have the flexibility to adjust the width, we make the equally spaced interference from $-J_1$ to J_2 in x dimension and from $-J_3$ to J_4 in y dimension, and then, the tapering matrix is modified as

$$\begin{aligned}[\tilde{T}_{PA}]_{mn} &= \sum_{p_x=-J_1}^{J_2} e^{j2\pi d[(x_m - x_n)p_x \Delta u]\lambda} \cdot \sum_{p_y=-J_3}^{J_4} e^{j2\pi d[(y_m - y_n)p_y \Delta u]/\lambda} = \sin c\left((x_m - x_n)(W_{x_2} + W_{x_1})d/\lambda\right) \\ &\quad \cdot e^{j\pi d(x_m - x_n)(W_{x_2} - W_{x_1})/\lambda} \cdot \sin c\left((y_m - y_n)(W_{y_4} + W_{y_3})d/\lambda\right) \cdot e^{j\pi d(y_m - y_n)(W_{y_4} - W_{y_3})/\lambda}, \end{aligned} \tag{26}$$

where $J_1 \Delta u = W_{x_1}$, $(J_2 + 1)\Delta u = W_{x_2}$, $J_3 \Delta u = W_{y_3}$, $(J_4 + 1)\Delta u = W_{y_4}$. Equation (26) is an asymmetric two-dimensional array of tapered matrices, and it can not only expand the space for the zero trap but also offset the phase.
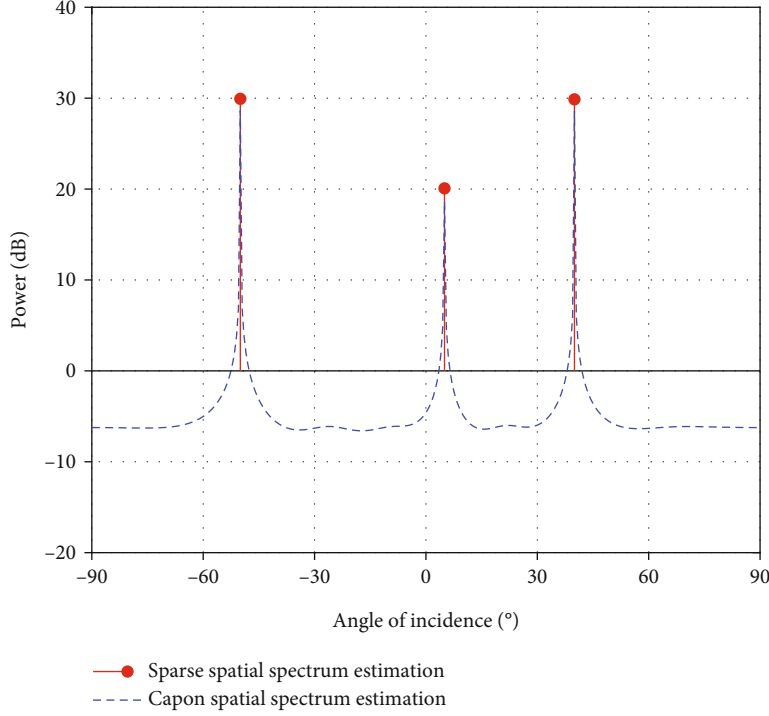
FIGURE 2: Comparison of sparse spatial spectrum estimation and Capon spatial spectrum estimation.

3.3. Concentric Circle Array Model. The concentric ring array consists of a central array element and N circles of concentric rings, with the number of circles set according to requirements. The radius of the ith concentric ring is taken as the half-wavelength multiplied by the number of turns ith which is

$$r_i = \frac{\lambda}{2} \cdot i (i = 1, 2, \cdots, N). \tag{27}$$

The spacing of the array elements on the circle should meet the arc length between two adjacent array elements should be less than or equal to half a wavelength as

$$\frac{2\pi r_i}{k_i} \leq \frac{\lambda}{2} \Rightarrow k_i \geq 2\pi i. \tag{28}$$

Since the number of elements is an integer, we round up to get the number of elements on the ith circle as

$$k_i = \lceil 2\pi i \rceil, \tag{29}$$

where $\lceil \cdot \rceil$ is an upward rounding symbol. Since the array elements on each circle are uniformly equidistant from each other, we can obtain the corresponding angle between the arc lengths of each array element as

$$\alpha_i = \frac{2\pi}{k_i}. \tag{30}$$

Thus, we can get the coordinates of each array element as

$$\begin{cases} x_{k_i} = r_i \cos \alpha_i, \\ y_{k_i} = r_i \sin \alpha_i. \end{cases} \tag{31}$$

In this paper, the concentric seven-ring array model is used, and the corresponding parameters of the array are calculated as shown in Table 1, and the schematic diagram of the array model is shown in Figure 1.

4. Simulation

4.1. Interference-Plus-Noise Covariance Matrix Sparse Reconstruction. In the simulation, a uniform line array model with 10 arrays is considered, the desired signal from 5° directions with a signal-to-noise ratio of 15 dB, interference from -50° and 40° with a signal-to-noise ratio of 30 dB, and the number of sampling snapshots used in the simulation is 300.

A comparison plot of Capon spectral estimation and sparse spectral estimation is shown in Figure 2. From Figure 2, we can see that the spectrum obtained from Capon spectral estimation has valued over the whole range and high spikes at the estimated interference and at the desired signal, while the spectrum obtained from sparse spectral estimation only has an impulse at the interference and at the desired signal with zero values in the other directions. This means that sparse spectral estimation can provide a good estimate of the location and power of our signal of interest.

Figure 3 shows the directional diagram for different methods at a signal-to-noise ratio of 15 dB. We can see that
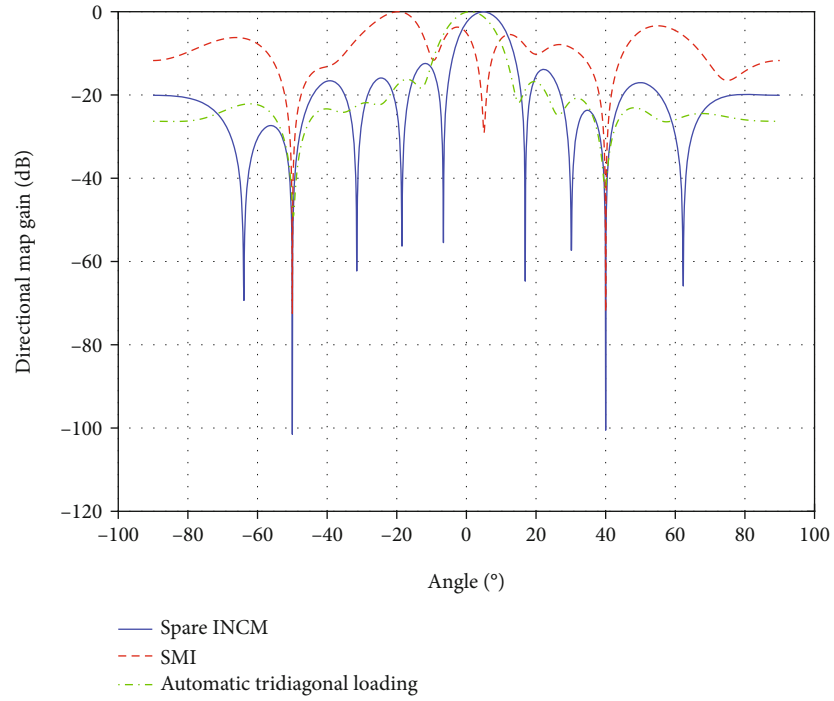
FIGURE 3: Diagram for different methods at a signal to noise ratio of 15 dB.
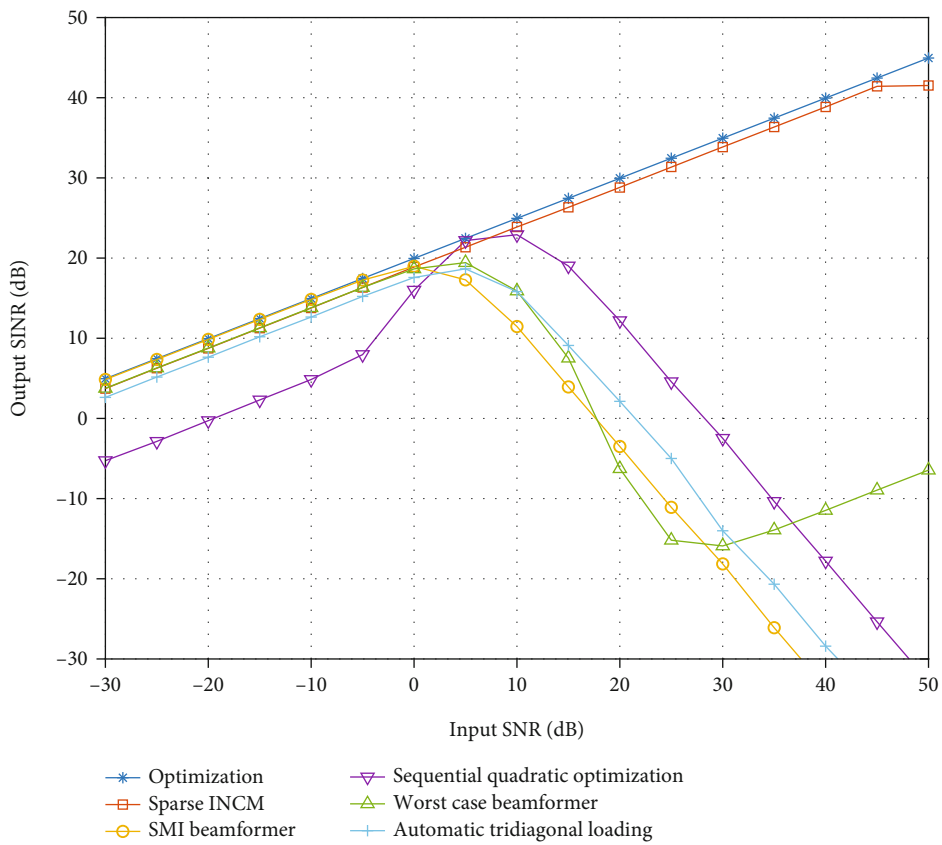
FIGURE 4: The effect of input SNR on output SINR.
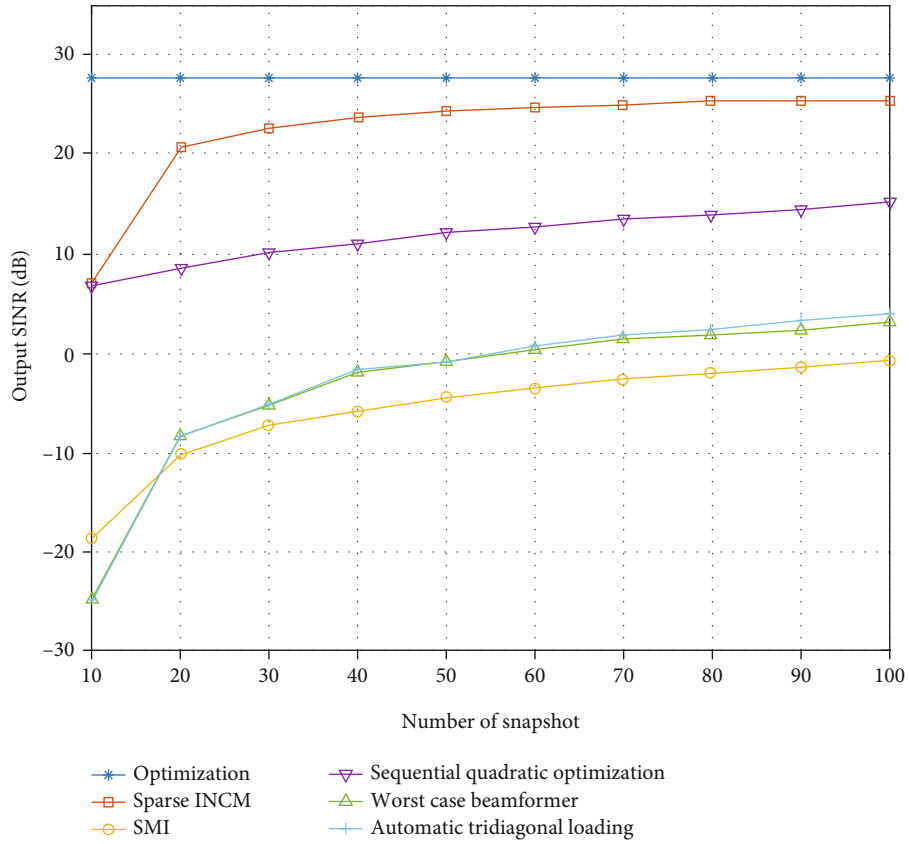
Figure 5: The effect of number of sampling snapshots on output SINR.
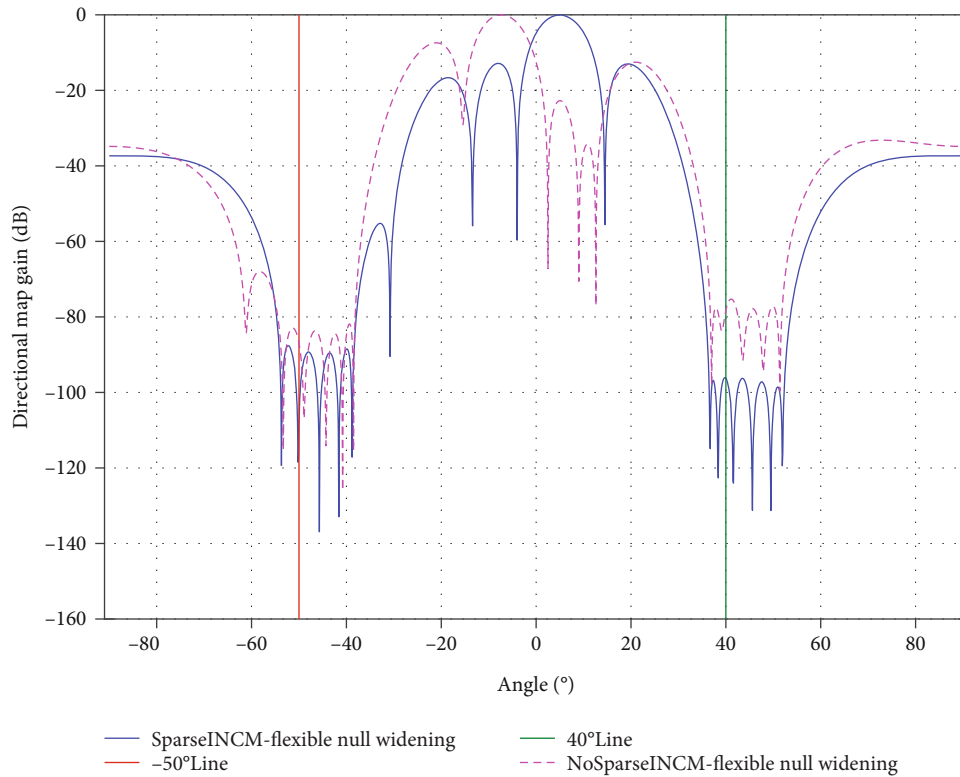
Figure 6: Comparison of flexible nulling widening with and without sparse INCM.
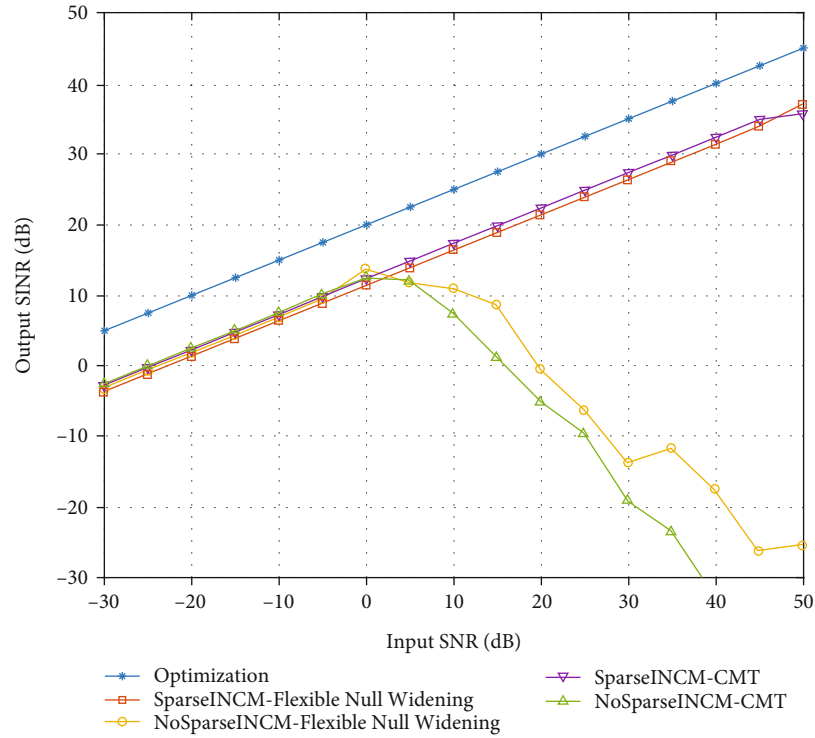
FIGURE 7: Null widening at INCM, for input SNR on output SINR.
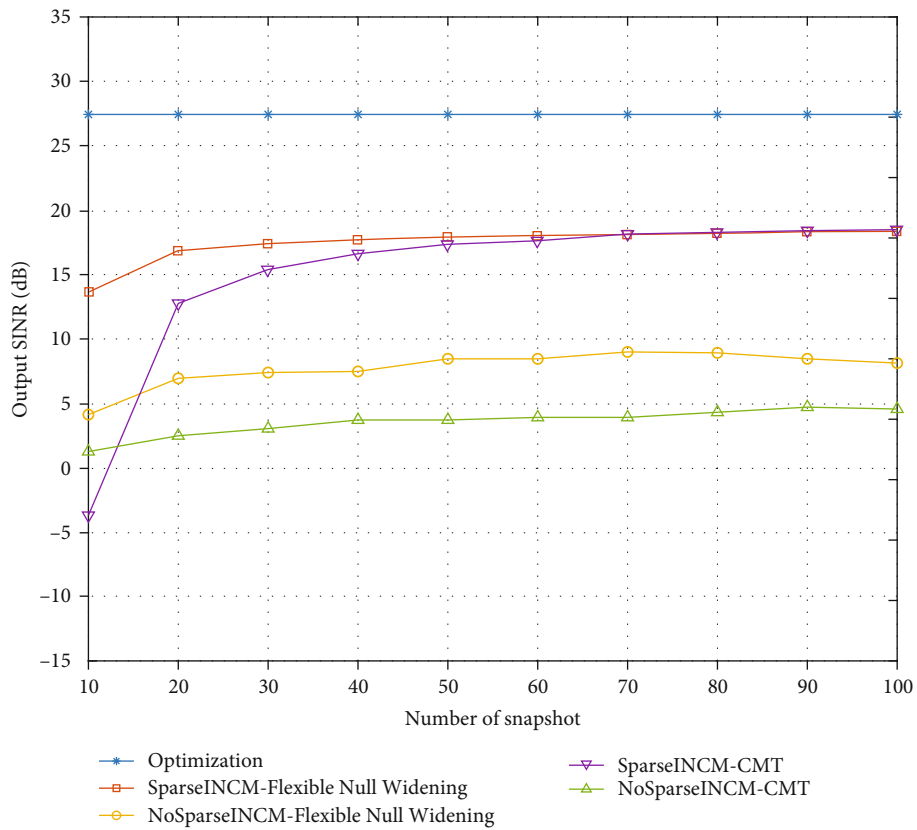
FIGURE 8: Null widening at INCM for number of sampling snapshots on output SINR.
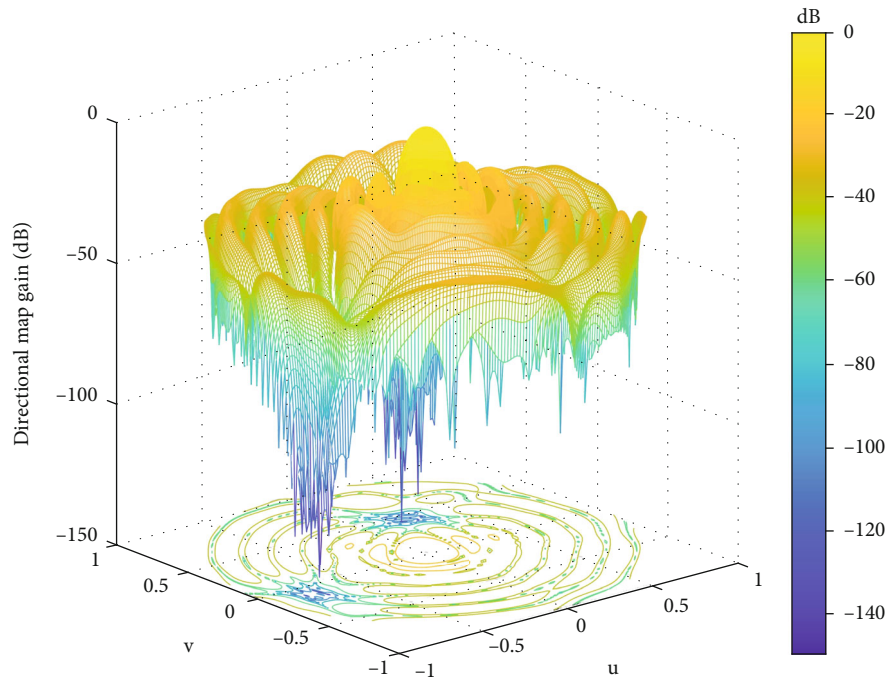
(a) 3D orientation diagram
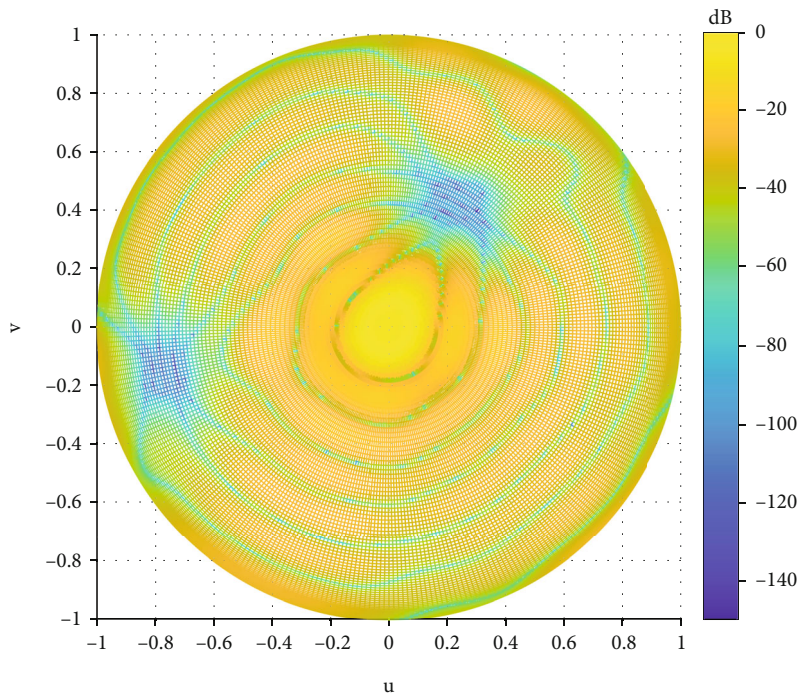
(b) Top view

Figure 9: Continued.
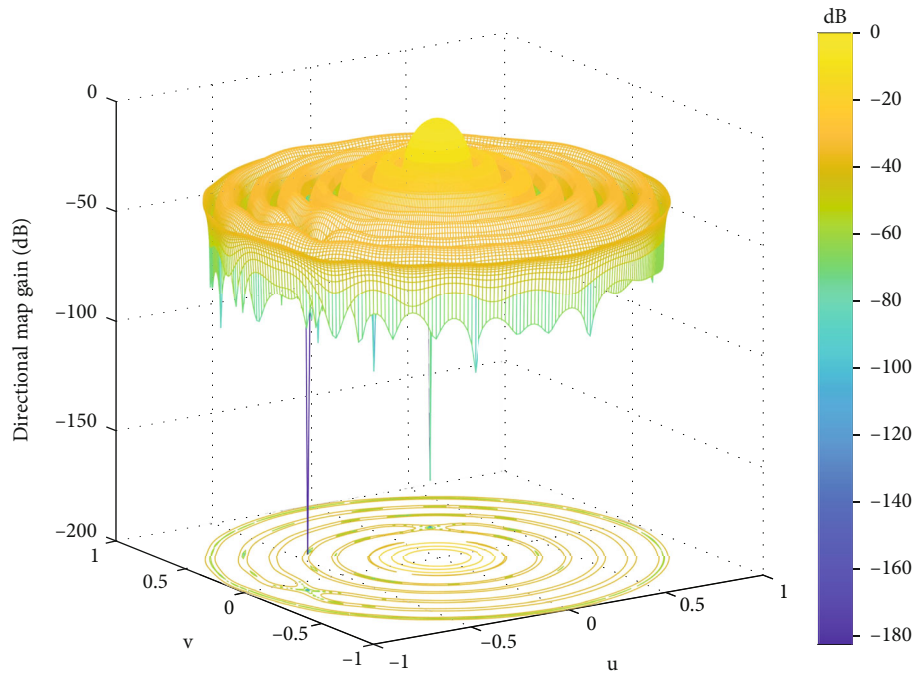
(c) 3D orientation diagram without widening
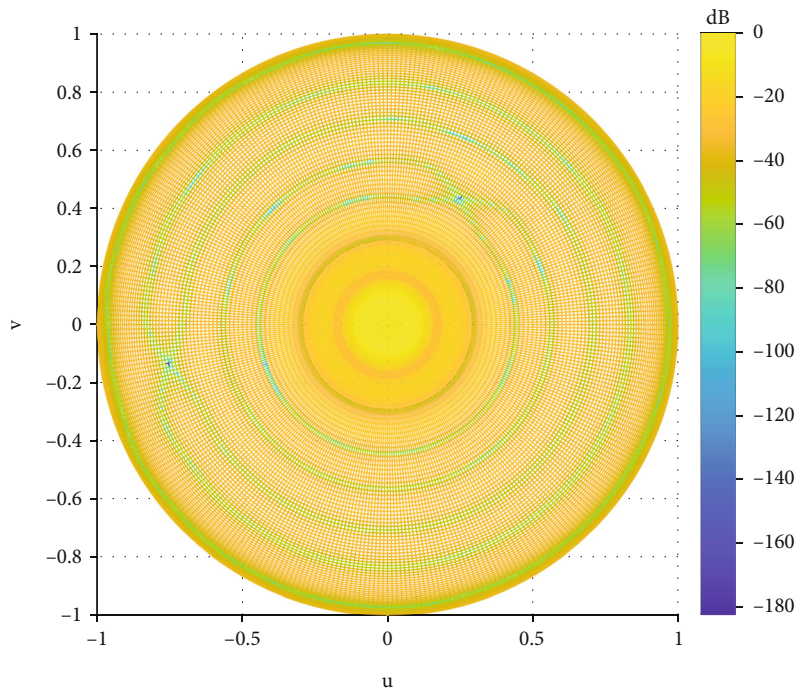
(d) Top view without widening

FIGURE 9: Orientation diagram of the concentric circle.

at large signal-to-noise ratios, the SMI algorithm [12] obtains a directional map with a significant mismatch that does not form the main beam gain. In contrast, sparse interference-noise covariance matrix reconstruction (INCM) [18] gives a stable directional map with good gain in the main beam direction and a deep zero trap against interference. In addition, we also compare an automatic tri-

diagonal loading method [15], which also produces a gain in the main beam but has a wider dominant flap and is much less suppressive of interference than the sparse INCM method [18].

The effect of the input signal-to-noise ratio on the output signal-to-noise ratio is shown in Figure 4, where the input signal-to-noise ratio ranges from -30 dB to 50 dB. We
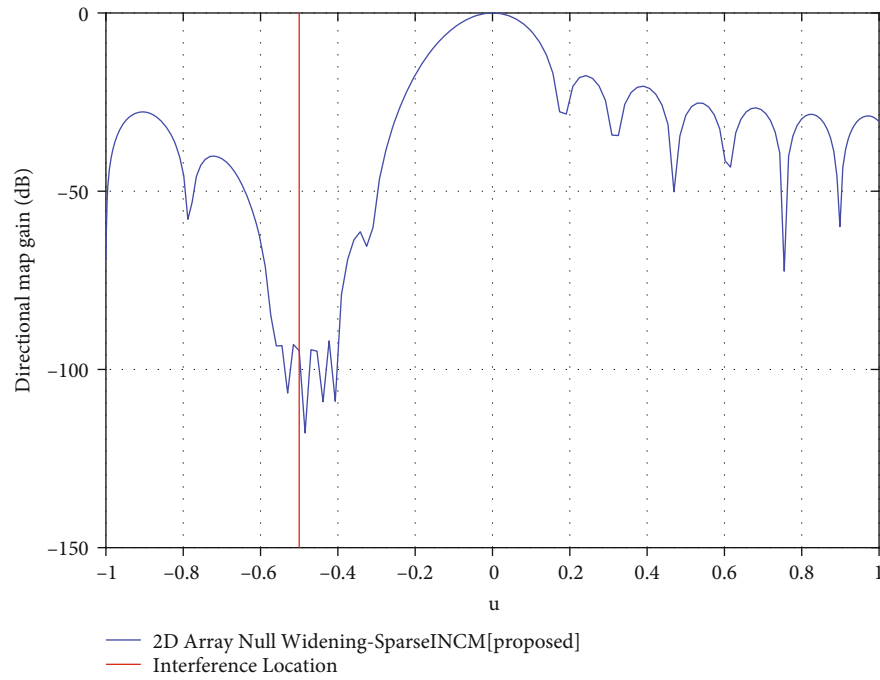
(a) Spread width at $\theta = 60\,^\circ$, $\varphi = 30\,^\circ$
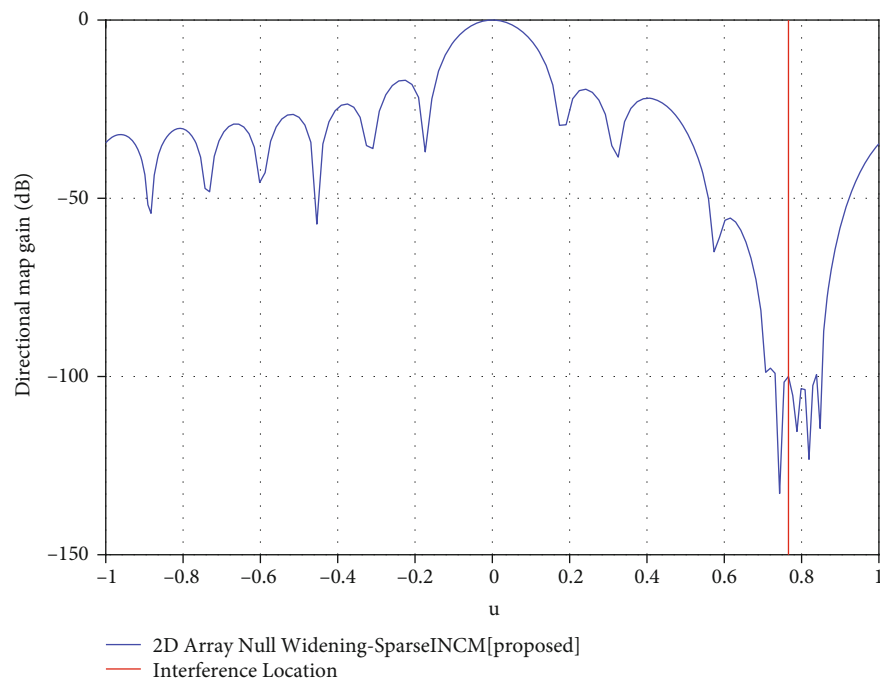
(b) Spread width at $\theta = 190\,^\circ$, $\varphi = 50\,^\circ$

FIGURE 10: Continued.
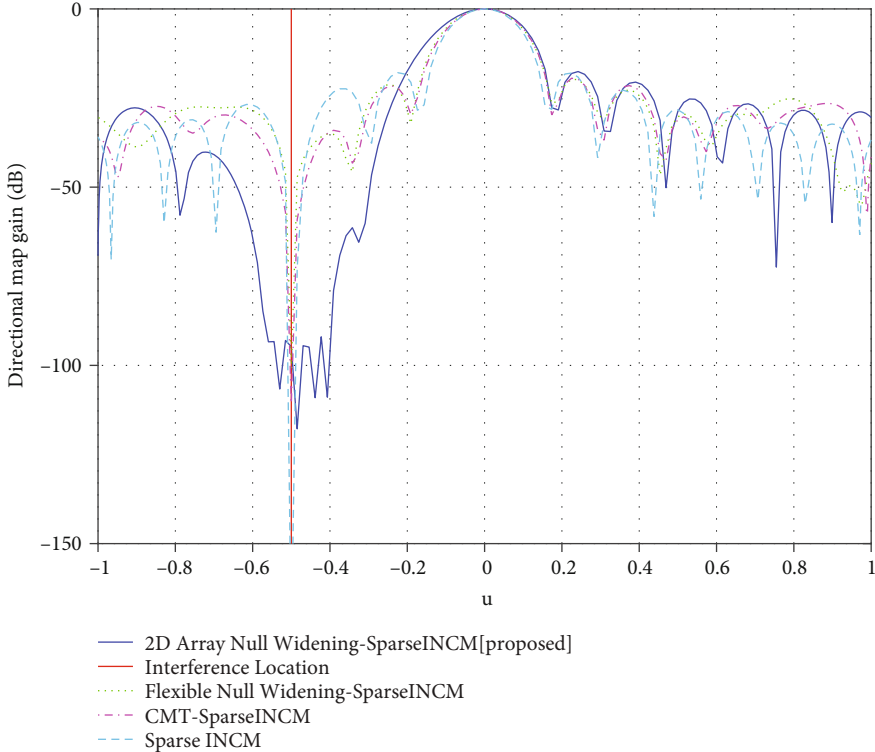
(c) Contrast unexpanded at $\theta = 60°, \varphi = 30°$
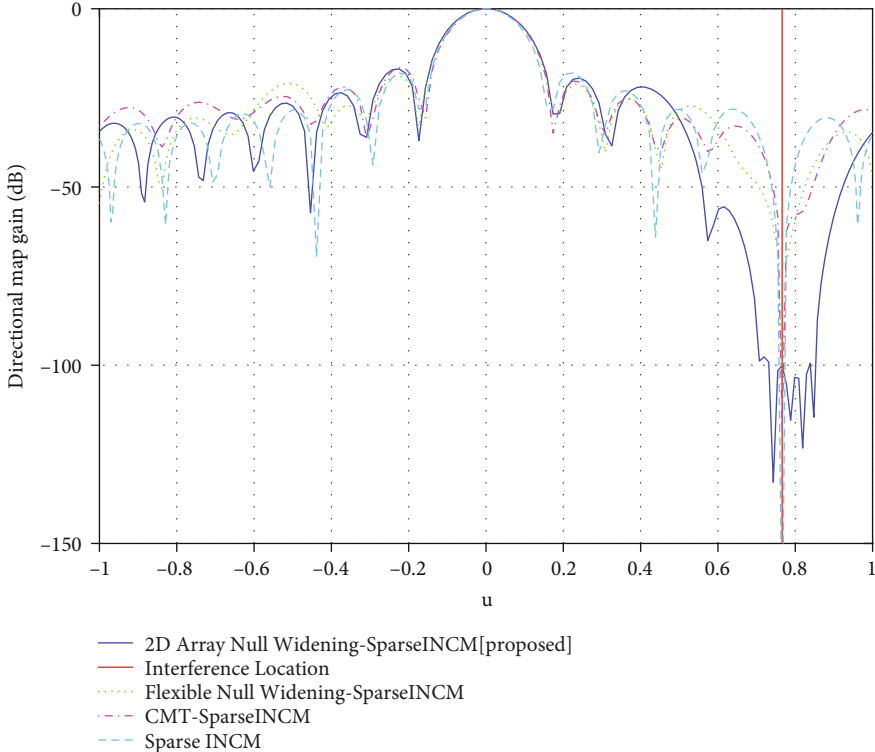
(d) Contrast unexpanded at $\theta = 190°, \varphi = 50°$

FIGURE 10: Cross-sectional view at two disturbances.

(a) SNR = −10 dB

(b) SNR = 10 dB
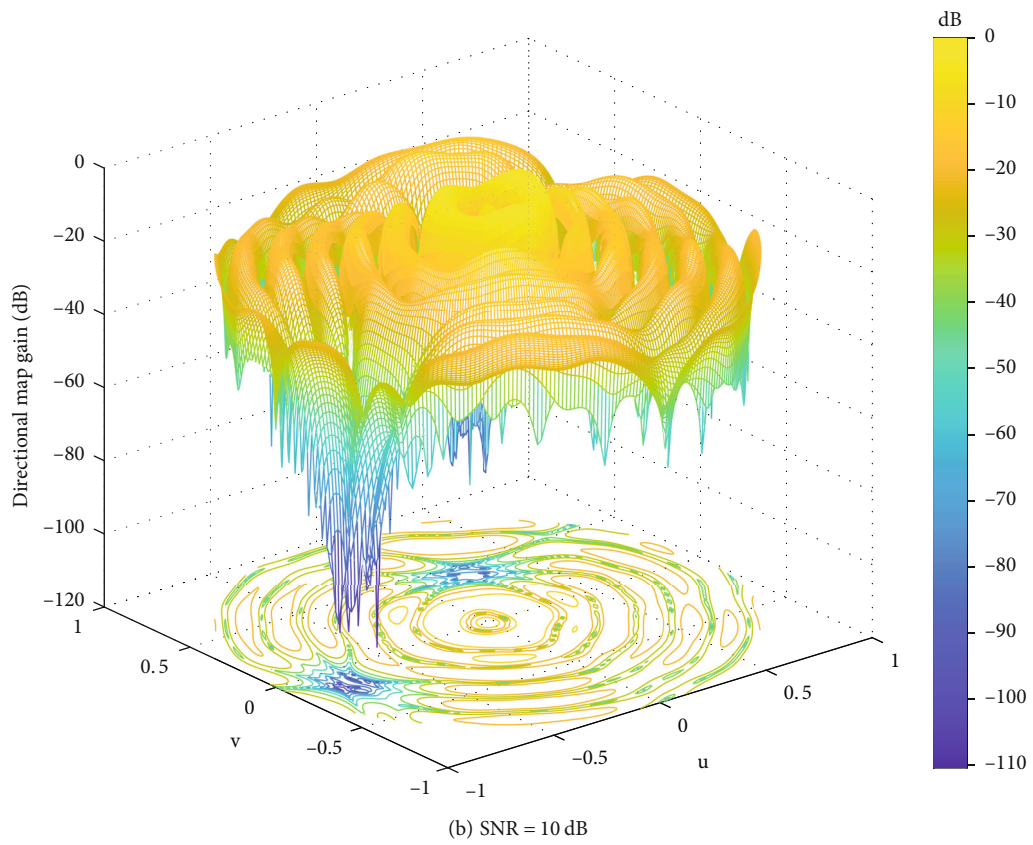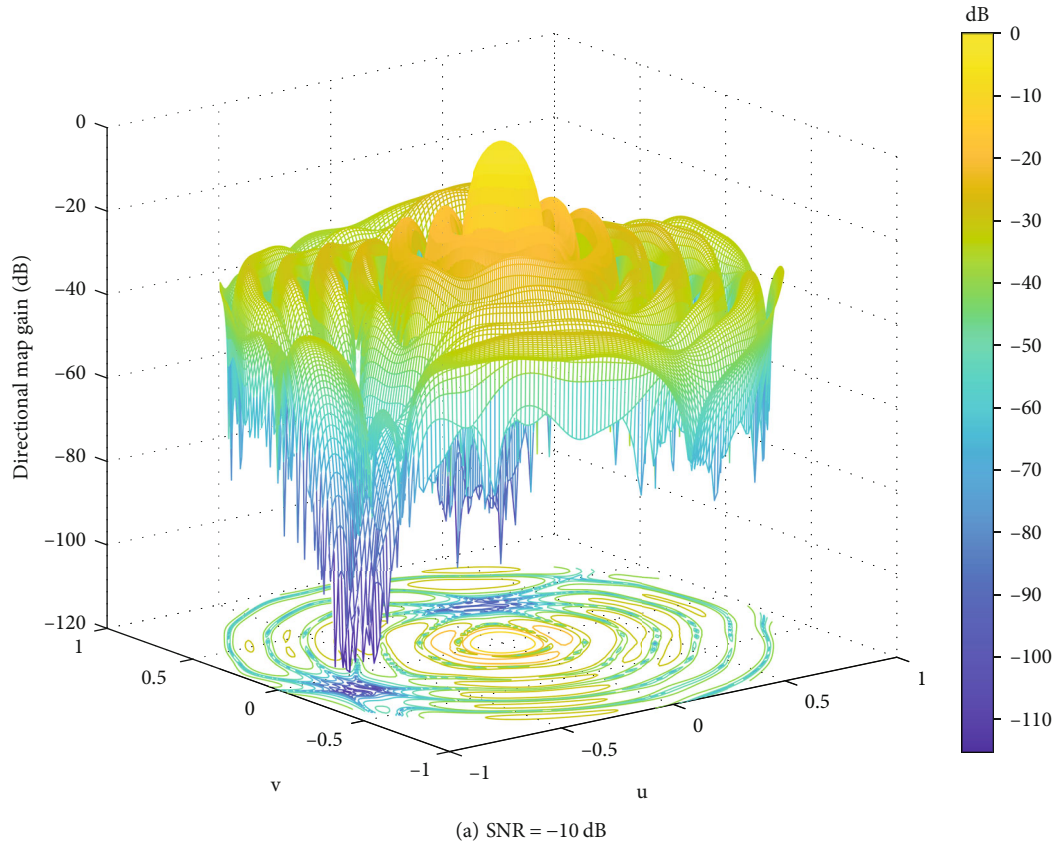
FIGURE 11: Directional map of the SMI algorithm to calculate the covariance matrix.

compare the sparse INCM [18] with several methods including the automatic tridiagonal loading method [15], sequential quadratic beamforming [16], worst-case beamforming [14], the basic SMI algorithm [12], and optimal beamforming without model mismatching. It shows that at low signal-to-noise ratios, the output SINR of the other methods is essentially the same, but as the input signal-to-noise ratio increases, there is an inflection point in the range of 0 dB to 10 dB where the performance starts to deteriorate.

In contrast, the sparse INCM method is not affected by the input signal-to-noise ratio. The effect of the number of sampling snapshots on output SINR is shown in Figure 5, with snapshots ranging from 10 to 100. We still compare several methods and see that the output SINR of the sparse INCM is significantly higher than that of the other methods. And it can be seen that the worst-case beamforming [14], automatic tridiagonal loading method [15], and the basic SMI algorithm [12] perform poorly at large SNRs. Their SINR is basically around 0 dB. Sequential quadratic beamforming [16] is more than 10 dB higher than them, but still more than 10 dB lower than the SINR under sparse INCM. The sparse INCM is basically close to the optimal value.

4.2. Flexible Null Broadening Technology in 1D Arrays. The simulation selects a uniform line array model with 16 elements, the desired angle of the signal is 5°, the corresponding signal-to-noise ratio is 15 dB, the interference signal is coming from the -50° and 40° direction, and its signal-to-noise ratio is 30 dB; the parameters of zero-trap width are set to $W_1 = 0.05$ and $W_2 = 0.15$.

The results of the simulation are shown in Figure 6. From the figure, we can see that the flexible zero-trap widening technique can produce asymmetric zero-trap widths to the left and right of the interference and can result in wider zero traps whether or not the sparse INCM [18] method is used. However, we can see that without the sparse INCM method, there is a clear mismatch in the directional map at large signal-to-noise ratios. With the latter method, not only a good main beam gain but also a deeper zero trap can be obtained.

In addition, we compared the results for the output SINR, using the same parameters for the desired signal as well as for the interference signal as in the directional diagram above and using 100 Monte Carlo experiments. The final result number of sampling snapshots and input signal-to-noise ratio on the output SINR is shown in Figures 7 and 8. In Figures 7 and 8, we compare the output SINR of the two methods using flexible nulling widening (FNW) [24] and covariance matrix tapered technique (CMT) [19] under sparse interference plus noise covariance matrix reconstruction as well as the conventional one. From Figure 7, we can see that as the input SNR increases, the output SINR is more or less the same at low SNR and the CMT and not. This is due to the Maxlloux method [21] of derivation in the FNW, which introduces noise along with virtual interference, so the output SINR is slightly worse. However, it is possible to produce asymmetric zero traps and to save degrees of freedom [23]. Similarly, from Figure 8, we can see that the output SINR of FNW and CMT with sparse INCM [18] is significantly higher as the number of samples
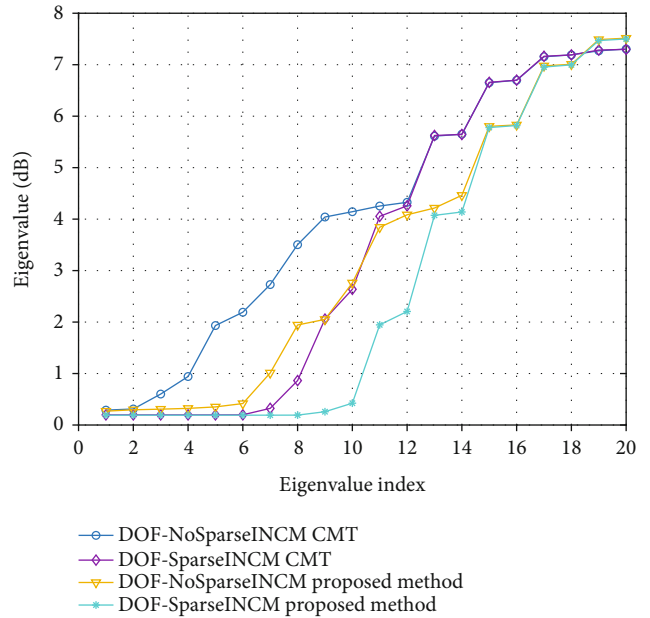

FIGURE 12: The DOF comparison between this method and the CMT method with and without the sparse INCM.

varies with the number of fast samples due to the result of not using it. Moreover, we can see that the two methods based on the sparse INCM converge in the end with an increasing number of beats. However, the results in both Figures 7 and 8 are worse than the optimal case without mismatch, because the other method introduces noise while spreading the zero trap, making the output SINR.

4.3. Null Broadening with Covariance Matrix Reconstruction in 2D Arrays. In this section of the simulation, the concentric circular array model of the seven rings mentioned in A is used to receive the signal with the relevant parameters as shown in Table 1. Assuming that the desired signal has an azimuth of 180°, a pitch angle of 0°, and a signal-to-noise ratio of 10 dB, there are two interfering signals with azimuths of 60° and 190°, pitch angles of 30° and 50°, and a signal-to-noise ratio of 30 dB. The number of sampling snapshots is chosen as 1024. The parameters of zero-trap width are set to $W_1 = 0.05$, $W_2 = 0.10$ and $W_3 = 0.05$, $W_4 = 0.1$. We use the $u - v$ coordinate system when forming the orientation diagram.

The 3D orientation of its simulation is shown in Figure 9(a), and its top view is Figure 9(b). In contrast, Figures 9(c) and 9(d) show the orientation diagrams of the concentric ring array without the zero-trap widening. It can be seen that our proposed method produces a significant width at the interference, whereas without widening, there is only a very narrow zero trap at the interference, which does not suppress the deviating signal well and thus reduces the UAV's immunity to interference when receiving signals.

Next, we have made a cross-sectional plot of Figure 10 for each of the two interference directions, and we can see that we have not only widened the zero trap at the
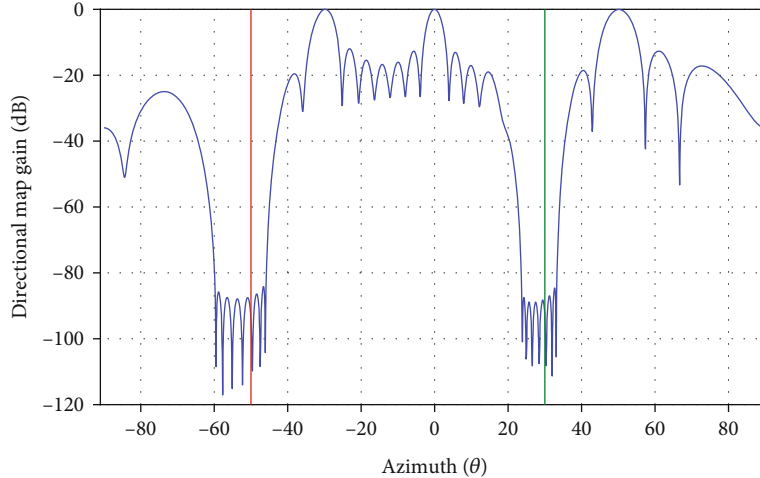
FIGURE 13: Directional map of multiple beamforming for a uniform line array of 32 array elements.

interference but also achieved a flexible asymmetric spreading for the width of the zero trap on both sides of the interference. We can clearly see from Figures 10(a) and 10(b) that our approach yields a wider zero trap and can produce different widths on each side of the interference, allowing the UAV to effectively suppress the deviating interference signal while the asymmetric width reduces the waste of degrees of freedom [22]. Figures 10(c) and 10(d) mainly compare several widening methods with the proposed method including CMT, FNW, and without valence, and we compare the zero-trap widths of several methods at different depths under the interference signal of $\theta = 60°$, $\varphi = 30°$ in Table 2. Here, the width is the u-coordinate as the metric. From the comparison of Figures 10(c) and 10(d) and the data in the table, we can see that although the CMT [19] and FNW [24] methods have a good effect in spreading the zero traps in 1D arrays, they are basically unable to widen the zero traps in 2D arrays, and even the depth of the zero traps is much reduced.

Table 2 shows that the depth and width of the zero traps in the two-dimensional arrays of methods [18, 23] are worse than the method proposed in this paper, while the zero traps that can be obtained by the method in this paper have a deeper depth and wider width. The proposed approach can not only cope with the spreading of zero traps in 2D arrays but can also take into account the depth of zero traps and still have a good spreading effect in deeper zero traps. The covariance matrices we use in the above process are all sparse INCM methods. However, if we use the ordinary SMI algorithm to obtain the covariance matrix, we can only form a good directional map at a low SNR such as Figure 11(a), where the expected signal direction is -10 dB, and when we increase the SNR to 10 dB, the directional map becomes Figure 11(b), which cannot form the main beam.

4.4. Analysis of DOF. Figure 12 shows a simulation comparing the degrees of freedom between the CMT and the widened zero-trap approach proposed in this paper

and incorporating a comparison of the reconstructed interference plus noise covariance matrix and the degrees of freedom without reconfiguration. Here, we have used an array of 20 array elements. The flexible null widening method of the widening factor is $W_1 = 0.05$, $W_2 = 0.10$. The CMT has to cover the worst case, so the widening factor used is 0.2. It can be seen that in Figure 12, the asymmetric widening reduces about 4 DOF. And with the interference plus noise covariance matrix reconstruction, it can be reduced by about 4 DOF.

4.5. Multibeam Formation in 2D Arrays. This section simulates the LCMV-based multibeam directional map formation. Firstly, a 1D uniform line array is simulated, using a 32 array ULA array, with the desired signals from -30°, 0°, and 50°, whose signal-to-noise ratios are 8 dB, 10 dB, and 5 dB, respectively. Two interfering signals are from -50° and 30°, whose signal-to-noise ratios are both 30 dB. The number of sampling snapshots is 1024. The parameters of zero-trap width are set to $W_1 = 0.15$ and $W_1 = 0.05$.

The result is shown in Figure 13. As seen in the figure, the beam is formed in several directions and both the sparse interference plus noise covariance matrix reconstruction we mentioned earlier and the asymmetric zero-trap broadening method are applied. Then, we simulated the concentric seven-circle array model. The expected signals come from azimuth 0°, 40°, 40° and pitch 180°, 80°, 300°, and their respective signal-to-noise ratios are 8 dB, 10 dB, and 5 dB. The interference signals come from two directions: azimuth 60°, 240° and pitch 30°, 30°, and their respective signal-to-noise ratios are 30 dB. The number of sampling snapshots is 1024. The final directional diagram is shown in Figure 14. From Figures 14(a) and 14(b), we can see that for the UAV, the concentric circular array model can form the main beam in multiple directions and also uses a sparse INCM to prevent a model mismatch. The zero-trap spreading can also be achieved for interference signals by applying our proposed widening approach for 2D arrays.

(a) 3D orientation diagram

(b) Top view
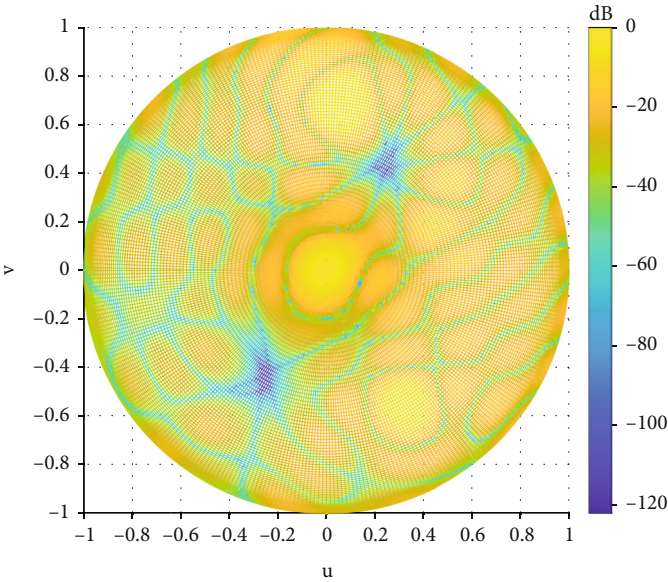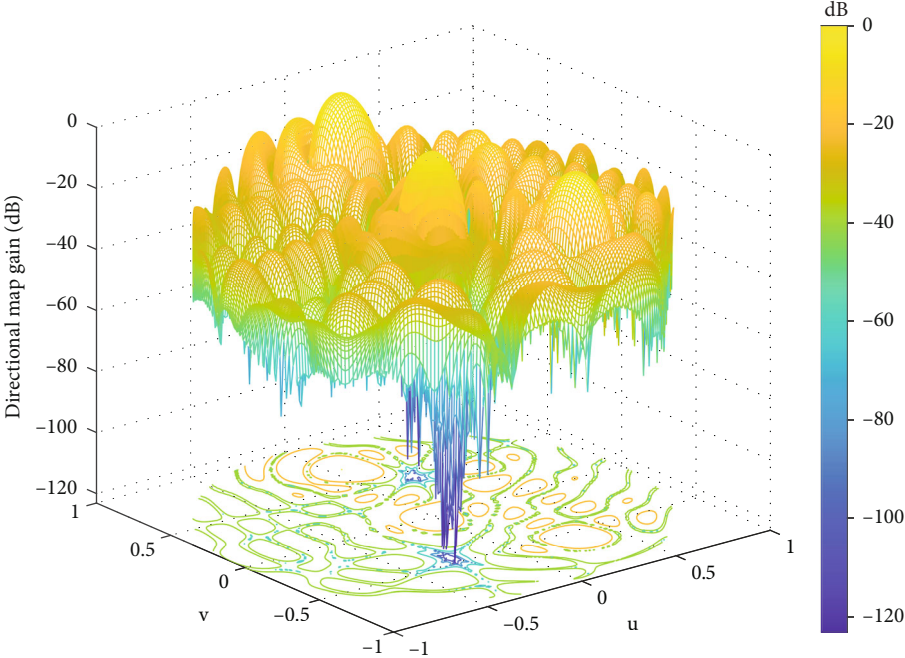
FIGURE 14: Directional map of concentric seven-circle array for multibeam.

TABLE 2: Comparison of zero-trap widths at different depths for different methods.

	-50 dB	-60 dB	-70 dB	-80 dB	-90 dB	-100 dB
No null widening	0.0455	0.0364	0.0271	0.0187	0.0104	0.0056
CMT [18]	0.0213	0.0115	\	\	\	\
FNW [23]	0.0202	0.0103	\	\	\	\
Proposed methods	0.3273	0.2796	0.2212	0.1905	0.1756	0.1591

5. Conclusion

In this paper, we propose a flexible asymmetric zero trap spreading technique for two-dimensional planar arrays in UAVs to prevent the model mismatch caused by high SNR. We use a sparse covariance matrix reconstruction method in constructing to prevent the model mismatch due to the large SNR of the UAV received signals. And a sparse covariance matrix reconstruction method is used to effectively avoid the model mismatch and to improve the performance of the adaptive beamformer. LCMV is applied to form multiple beams for the case that the UAV may receive multiple signals. Simulation results show that for the UAV planar antenna array, we can reduce the waste of DOF and get a good adjustable zero-notch width. At the same time, the performance of the adaptive beam shaper is still good when the SNR is large. And the main beam can be formed in multiple directions. The results also prove that the proposed method works better in a two-dimensional array and avoids the model mismatch problem compared to some zero-trap spreading approaches. The robustness of UAV antenna adaptive beamforming is enhanced, and the antijamming ability of UAV is improved. In future research, we hope to apply the zero-trap broadening technique to more antenna arrays in different dimensions.

Data Availability

The data used to support the findings of this study are included within the article.

Conflicts of Interest

The authors declare that they have no conflicts of interest.

Acknowledgments

References

[1] A. Lucieer, D. Turner, D. H. King, and S. A. Robinson, "Using an unmanned aerial vehicle (UAV) to capture micro-topography of Antarctic moss beds," *International Journal of Applied Earth Observation and Geoinformation*, vol. 27, pp. 53–62, 2014.

[2] S. Minaeian, J. Liu, and Y. J. Son, "Vision-based target detection and localization via a team of cooperative UAV and UGVs," *IEEE Transactions on systems, man, and cybernetics: systems*, vol. 46, no. 7, pp. 1005–1016, 2016.

[3] V. V. Klemas, "Coastal and environmental remote sensing from unmanned aerial vehicles: an overview," *Journal of Coastal Research*, vol. 315, no. 5, pp. 1260–1267, 2015.

[4] J. Bendig, M. Willkomm, N. Tilly et al., "Very high resolution crop surface models (CSMs) from UAV-based stereo images for rice growth monitoring in Northeast China," *The International Archives of the Photogrammetry, Remote Sensing and Spatial Information Sciences*, vol. XL-1/W2, pp. 45–50, 2013.

[5] H. L. Van Trees, *Optimum Array Processing: Part IV of Detection, Estimation, and Modulation Theory*, John Wiley & Sons, 2004.

[6] R. Levanda and A. Leshem, "Synthetic aperture radio telescopes," *IEEE Signal Processing Magazine*, vol. 27, no. 1, pp. 14–29, 2010.

[7] Y. Wang, X. Ma, C. Chen, and X. Guan, "Designing dual-tone radio interferometric positioning systems," *IEEE Transactions on Signal Processing*, vol. 63, no. 6, pp. 1351–1365, 2015.

[8] L. Zhao, W. Z. Song, and Y. X. Fast, "Decentralized gradient descent method and applications to in-situ seismic," in *International Conference on Big Data (Big Data)*, pp. 908–917, Santa Clara, CA, USA, 2015.

[9] C. Yang, H. Zhang, F. Qu, and Z. Shi, "Secured measurement fusion scheme against deceptive ECM attack in radar network," *Security and Communication Networks*, vol. 9, no. 16, 3921 pages, 2016.

[10] K. Buckley, "Spatial/spectral filtering with linearly constrained minimum variance beamformers," *IEEE Transactions on Acoustics, Speech, and Signal Processing*, vol. 35, no. 3, pp. 249–266, 1987.

[11] J. Capon, "High-resolution frequency-wavenumber spectrum analysis," *Proceedings of the IEEE*, vol. 57, no. 8, pp. 1408–1418, 1969.

[12] L. L. Horowitz, H. Blatt, W. G. Brodsky, and K. Senne, "Controlling adaptive antenna arrays with the sample matrix inversion algorithm," *IEEE Transactions on Aerospace and Electronic Systems*, vol. AES-15, no. 6, pp. 840–848, 1979.

[13] B. D. Carlson, "Covariance matrix estimation errors and diagonal loading in adaptive arrays," *IEEE Transactions on Aerospace and Electronic Systems*, vol. 24, no. 4, pp. 397–401, 1988.

[14] S. A. Vorobyov, A. B. Gershman, and Z. Q. Luo, "Robust adaptive beamforming using worst-case performance optimization: a solution to the signal mismatch problem," *IEEE Transactions on Signal Processing*, vol. 51, no. 2, pp. 313–324, 2003.

[15] M. Zhang, X. Chen, and A. Zhang, "A simple tridiagonal loading method for robust adaptive beamforming," *Signal Processing*, vol. 157, pp. 103–107, 2019.

[16] A. Hassanien, S. A. Vorobyov, and K. M. Wong, "Robust adaptive beamforming using sequential quadratic programming: an iterative solution to the mismatch problem," *IEEE Signal Processing Letters*, vol. 15, pp. 733–736, 2008.

[17] Y. Gu and A. Leshem, "Robust adaptive beamforming based on interference covariance matrix reconstruction and steering vector estimation," *IEEE Transactions on Signal Processing*, vol. 60, no. 7, pp. 3881–3885, 2012.

[18] Y. Gu, N. A. Goodman, S. Hong, and Y. Li, "Robust adaptive beamforming based on interference covariance matrix sparse reconstruction," *Signal Processing*, vol. 96, pp. 375–381, 2014.

[19] J. R. Guerci, "Theory and application of covariance matrix tapers for robust adaptive beamforming," *IEEE Transactions on Signal Processing*, vol. 47, no. 4, pp. 977–985, 1999.

[20] M. Zatman, "Production of adaptive array troughs by dispersion synthesis," *Electronics Letters*, vol. 31, no. 25, pp. 2141-2142, 1995.

[21] R. J. Mailloux, "Covariance matrix augmentation to produce adaptive array pattern troughs," *Electronics Letters*, vol. 31, no. 10, pp. 771-772, 1995.

[22] Z. Liu, S. Zhao, G. Zhang, and B. Jiao, "Robust adaptive beamforming for sidelobe canceller with null widening," *IEEE Sensors Journal*, vol. 19, no. 23, pp. 11213–11220, 2019.

[23] H. Su, H. Liu, P. Shui, and Z. Bao, "Adaptive beamforming for nonstationary HF interference cancellation in skywave over-the-horizon radar," *IEEE Transactions on Aerospace and Electronic Systems*, vol. 49, no. 1, pp. 312–324, 2013.

[24] Z. Liu, S. Zhao, C. Zhang, and G. Zhang, "Flexible robust adaptive beamforming method with null widening," *IEEE Sensors Journal*, vol. 21, no. 9, pp. 10579–10586, 2021.

[25] Z. Li, J. You, and X. Cai, "Nulling broadening technology based on circular array adaptive beamforming," in *14th international conference on communication technology*, pp. 1123–1128, Chengdu, 2012.

[26] P. S. Naidu, *Sensor Array Signal Processing*, CRC press, 2009.

[27] M. Grant and S. Boyd, *CVX: Matlab software for disciplined convex programming, version 2.1*, 2014.

[28] S. Boyd, S. P. Boyd, and L. Vandenberghe, *Convex Optimization*, Cambridge university press, 2013.

[29] A. Ben-Tal and A. Nemirovski, "Robust convex optimization," *Mathematics of Operations Research*, vol. 23, no. 4, pp. 769–805, 1998.

[30] C. Stearns and A. Stewart, "An investigation of concentric ring antennas with low sidelobes," *IEEE Transactions on Antennas and Propagation*, vol. 13, no. 6, pp. 856–863, 1965.

WILEY | Hindawi

Research Article

Time-Division Multiarray Beamforming for UAV Communication

Zhengxiang Duan ⓘ **, Xin Yang** ⓘ **, Qian Xu** ⓘ **, and Ling Wang** ⓘ

School of Electronics and Information, Northwestern Polytechnical University, Xi'an 710072, China

Correspondence should be addressed to Xin Yang; xinyang@nwpu.edu.cn

Recently, unmanned aerial vehicles (UAVs) have been widely used in various industries. However, the communication links of UAVs are also threatened by eavesdropping. To enhance physical layer security (PLS) for UAV communications, a time-division multiarray beamforming (TDMB) scheme is proposed. Multiple antenna arrays steer their beamforming vectors based on their position relative to the legitimate user (LU). Thus, angle-distance-dependent directional modulation (DM) can be achieved. Time-division means multiple antenna arrays take turns transmitting different symbols from a same packet. The receiver in undesired directions suffers from intersymbol interference (ISI) because of the path differences between the receiver and different antenna arrays. This paper shows the signal-to-interference-plus-noise ratio (SINR) distribution with the proposed method in a 2-dimensional plane. Also, the improvement of the secrecy rate with the proposed method under different total antennas and artificial noise power is studied. Overall, these results indicate that the security rate has improved more with the proposed method, where the numbers of antennas and the power of AN are limited. Therefore, this method is suitable for UAV security communication.

1. Introduction

The number of unmanned aerial vehicles (UAVs) has experienced explosive growth in the past decade, whether for agriculture, industrial, or civilian use. Wireless communication is a key technique for UAVs. It is used for wireless control and broadcasting data from the sensor network. Nevertheless, information disclosure is inevitable due to the openness of wireless channels. This might lead to property loss. In severe cases, people can be injured. A widely adopted approach to alleviating this problem is encryption. However, it may not be straightforward to use in UAV communications due to the complexity of key distribution and management. In recent decades, physical layer security (PLS) has aroused great research interest among researchers [1]. The basic idea of PLS is to utilize the randomness of the wireless channel to realize secure communication [2]. Since the PLS technique is primarily a signal processing technology, it can be used in conjunction with encryption.

Directional modulation (DM) is one of the most important PLS techniques. It can transmit digital modulated signals to intended spatial directions while twisting the constellations of these signals in all other directions [3]. A method named dual-beam DM was introduced in [4]. In this technique, I and Q data are transmitted by different antennas. However, the synchronization of the I and Q data from different antennas is not taken into consideration. An antenna subset modulation scheme was introduced in [5], where different antenna subsets transmit different symbols from a same packet. However, this method only achieves angle-dependent DM. Artificial noise (AN) can also be employed in DM for a further improvement of the security. The use of AN is to reduce the signal-to-interference-to-noise ratio (SINR) in undesired directions. The AN was used in DM for the first time in [6]. Taking into account the imperfect channel state information (CSI), robust AN-based methods for single-beam and multibeam DM were proposed in [7, 8], respectively. The projection matrix of AN can be

constructed by zero-forcing [9], null-space projection [10], or iteration convex optimization methods [11]. Directional modulation for different types of arrays is also a research hotspot, including the switched antenna array [12], the intelligent reflecting surfaces (IRS) [13], the 4-D antenna array [14, 15], the frequency diverse array (FDA) [16, 17], and the multiple antenna arrays (MAAs) [18]. A spread-spectrum directional modulation technique based on a switched antenna array is proposed in [12]. With the spread-spectrum technique, a low probability of detection is achieved. In [13], a new secure transmission scheme aided by the IRS is proposed. This method can reduce costs and save energy. Another cost-saving method is proposed in [14, 15], which replaces the phase shifter with high-speed RF switches. At the same time, the accuracy of phase shift becomes higher. An FDA scheme is proposed to achieve angle-distance-dependent DM in [16, 17]. In [18], the author also realized angle-distance-dependent DM by MAAs. However, the signals from different arrays will interfere with each other at the receiver, when MAAs transmit in the same frequency band simultaneously. A recent study in [21] proposed a PLS algorithm for UAV communication using linear virtual antenna array (VAA). The random location perturbations of the VAA elements were used to randomize radiation patterns at eavesdroppers (Eves).

In conclusion, despite the various advantages of the aforementioned DM schemes, some problems need to be overcome.

(1) The methods proposed in [4–15] only work when Eves and legitimate users (LUs) are not in the same direction. In other words, when Eves and LUs lie on the same line, the transmission will be unsafe

(2) Most of the above-mentioned methods are complex in the calculation. To improve security performance, the number of antennas and the power of AN need to be increased. It is not suitable for UAV scenarios

Aiming at addressing these problems, we propose a time-division multiarray beamforming (TDMB) scheme to achieve secure and precise transmission. Multiple antenna arrays steer their beamforming vectors based on their position relative to the LU. Time-division means multiple antenna arrays take turns transmitting different symbols from a same packet. The path differences between the receiver and different antenna arrays will cause intersymbol interference (ISI) at the receiver. However, with the knowledge of the LU's precise location, the ISI at LU can be completely removed. Therefore, the received signals of Eves will not only suffer from constellation distortion but also be affected by ISI. In this way, we narrow the unsafe area from "lines" to "points." The main contributions of this paper can be summarized as follows:

(1) We propose a time-division multiarray beamforming scheme, which realizes angle-distance-dependent DM

(2) We improve security performance through ISI rather than increasing the number of antennas or the power of AN

(3) The proposed method has low computational complexity. And it has better security performance with a small number of antennas or low power of AN

Hereafter, the paper is organized as follows. In Section 2, an MAA model is introduced. Section 3 proposes a TDMB scheme. Section 4 analyses the secrecy rate and the symbol error rate (SER). The secrecy performance is evaluated by several numerical results in Section 5. Finally, Section 6 concludes the paper. Tables 1 and 2 summarize the abbreviations and notations of symbols in this paper.

2. System Model

The application scenario of the proposed method is shown in Figure 1. There are three types of UAV, namely, the transmitter, the LU, and Eves. The transmitter sends information through multiple antenna arrays to the LU. Meanwhile, the transmitter transmits AN to interfere with Eves. Eves could be anywhere in the space and try to intercept the information from the transmitter.

We consider the case where a transmitter is equipped with N ($N \geq 2$) non-collocated antenna arrays, of which the spacing is L. Each antenna array is an M-element isotropic uniform linear array (ULA) with spacing $d = \lambda/2(L \gg d)$. λ is the wavelength of the carrier. The MAA system model in the XOY plane is presented in Figure 2. All antennas are on the x-axis. The first antenna of the first array is at the origin of the coordinate axis. Without loss of generality, the first antenna element of each ULA is selected as the reference antenna for that ULA. The coordinates of the receiver are (x, y). r_n and θ_n are the distance and direction angle between the nth transmit antenna array and the receiver, respectively. For the far-field model, it is reasonable to adopt the approximation $r_n \approx r_n - (m - 1)d \sin \theta_n$. As depicted in Figure 2, we can obtain the geometric relationship

$$r_n = \sqrt{[x - (n - 1)L]^2 + y^2}, \quad (1)$$

$$\theta_n = \arctan((x - (n - 1)L)/y). \quad (2)$$

The far-field beam pattern of the MAA model with beamforming factor $w_{n,m}$ in the location (x, y) can be expressed as

$$F(r_1, \theta_1, \cdots, r_N, \theta_N) = e^{j2\pi f_c t} \sum_{n=1}^{N} \sqrt{\rho_n} e^{-j2\pi f_c(r_n/c)} \sum_{m=1}^{M} w_{n,m} e^{2\pi f_c(m-1)d \sin \theta_n/c},$$

$$(3)$$

where c is the speed of light, f_c is the carrier frequency, t is the propagation time, $w_{n,m}$ is the beamforming factor for the mth ($m = 1, 2, \cdots, M$) antenna at the nth ($n = 1, 2, \cdots, N$) transmit antenna array. ρ_n refers to the path loss factor from the nth array to the receiver. The path loss factor

TABLE 1: Abbreviations in the paper.

Abbreviation	Meaning	Abbreviation	Meaning
AA	Antenna array	AN	Artificial noise
AWGN	Additive white Gaussian noise	BER	Bit error rate
CSI	Channel state information	DM	Directional modulation
Eve	Eavesdropper	FDA	Frequency diverse array
FPGA	Field programmable gate array	IRS	Intelligent reflecting surfaces
ISI	Intersymbol interference	LOS	Line-of-sight
LU	Legitimate user	MAA	Multiple antenna array
PLS	Physical layer security	QPSK	Quadrature phase-shift keying
SER	Symbol error rate	SINR	Interference-plus-noise ratio
SNR	Signal-to-noise ratio	TDMB	Time-division multiarray beamforming
UAV	Unmanned aerial vehicle	ULA	Uniform linear array
VAA	Linear virtual antenna array		

TABLE 2: Notations of symbols in the paper.

Symbol	Meaning	Symbol	Meaning
$\mathbb{N}^+$	Positive integer field	$\mathbb{C}$	Complex number field
$(\cdot)^T$	Transpose	$(\cdot)^H$	Hermitian transport
N	Number of antenna arrays	L	Spacing of antenna arrays
M	Number of antennas in an array	d	Spacing of array elements
λ	Wavelength of the carrier	c	Speed of light
f_c	Carrier frequency	P_s	Power for transmitting symbols
P_A	Power for AN	a_i	Normalized QPSK constellation mapping
T	Symbol duration	Q	Total number of symbols in a packet
σ_l^2	The noise variance received by LU	$\mathbf{h}_{l,n}$	Steering vector from LU to the nth antenna array
$\mathbf{h}_{e,n}$	Steering vector from the nth antenna array to Eve	$\sigma_{e,n}^2$	Noise variance received by Eve
R_l	Achievable rates of LU	$\overline{\gamma_e}$	Average SINR of Eve
R_s	Secrecy rate	R_e	Achievable rates of Eve
P_{se}	Symbol error rate	P_b	Bit error rate

decreases slowly when the distance is far enough. Then, we can approximate that $\rho_1 \approx \rho_n$. For simplicity, we define $\rho \triangleq \rho_n$. Equation (3) can be written as

$$F(r_1, \theta_1, \cdots, r_N, \theta_N) \triangleq e^{j2\pi f_c t}\sqrt{\rho}\sum_{n=1}^{N}e^{-j2\pi f_c(r_n/c)}\sum_{m=1}^{M}w_{n,m}e^{2\pi f_c(m-1)d\,\sin\theta_n/c}.$$

(4)

The normalized steering vector of the nth transmit antenna array in position (r_n, θ_n) can be expressed as

$$\mathbf{h}_n(r_n, \theta_n) = \sqrt{\frac{\rho}{M}}\left[e^{j\Phi_n(1)}, e^{j\Phi_n(2)}, \cdots, e^{j\Phi_n(M)}\right]^T,$$

(5)

where $\Phi_n(m)$ is given by

$$\Phi_n(m) = \frac{2\pi f_c(m-1)d\,\sin\theta_n}{c}.$$

(6)

To simplify the expression, we define $\mathbf{h}_n \triangleq \mathbf{h}_n(r_n, \theta_n)$. The far-field beam pattern of the MAA model is actually a superposition of radiation from multiple arrays, i.e.,

$$F(r_1, \theta_1, \cdots, r_N, \theta_N) \triangleq \sum_{n=1}^{N}\mathbf{h}_n^H\mathbf{w}_n e^{-j2\pi f_c(t-(r_n/c))},$$

(7)

where $\mathbf{w}_n = [w_{n,1}, w_{n,2}, \cdots, w_{n,M}]^T \in \mathbb{C}^{M\times1}$ is the transmit beamforming vector.

3. The Proposed TDMB Scheme

In this section, we propose a TDMB scheme, where different antenna arrays take turns to transmit different symbols of a same packet, as illustrated in Figure 3. In this way, the message transmitted by each array is incomplete. Only in the intersection area of different beams can complete information be obtained, while other places suffer from severe ISI.
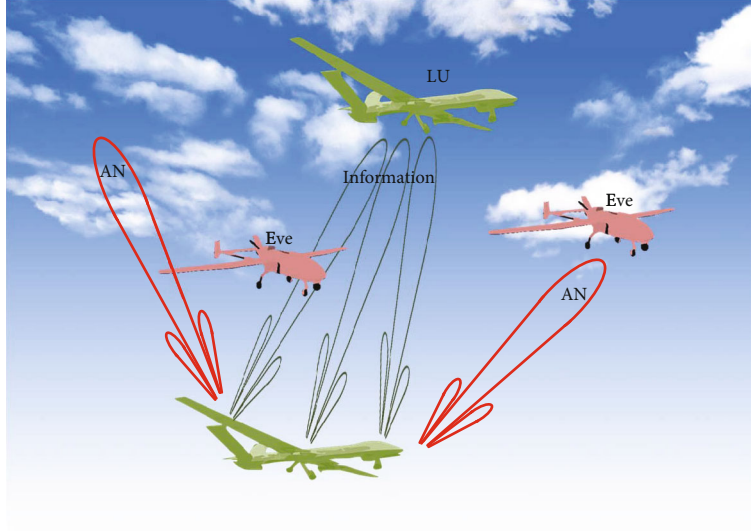
FIGURE 1: The application scenario of the proposed method. There are three types of UAVs, namely, the transmitter, the legitimate user, and eavesdroppers.
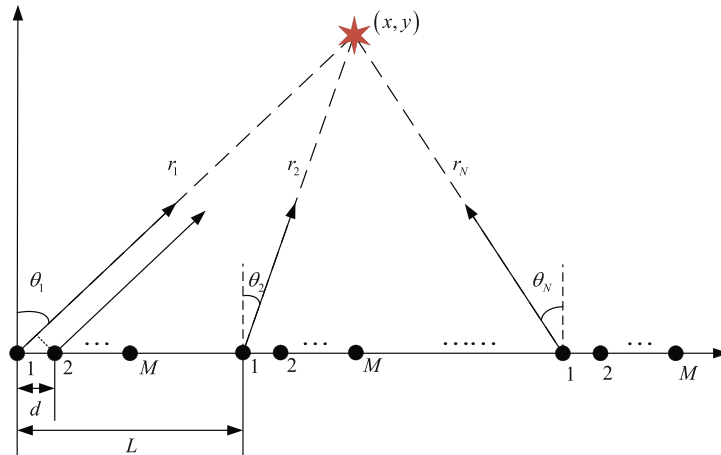
FIGURE 2: System model of MAA.

3.1. Transmitted Signal Model. As shown in Figure 3, the baseband signal of the nth antenna array is given by

$$\mathbf{s}_n(t) = \sqrt{P_s}\mathbf{w}_n x_n(t - (n-1)T + \tau_{l,n})e^{j2\pi f_c \tau_{l,n}} + \sqrt{P_A}\mathbf{n}_{A,n}(t), \tag{8}$$

where P_s and P_A are the power for transmitting symbols and AN, respectively. T is the symbol duration, and $\mathbf{n}_{A,n}(t)$ is the normalized M-tuple AN waveform, which is given by

$$\mathbf{n}_{A,n}(t) = \mathbf{T}_n \mathbf{z}_n(t), \tag{9}$$

where $\mathbf{z}_n(t) \in \mathbb{C}^{M \times 1}$ is a waveform following $\mathscr{CN}(\mathbf{0}_{M \times 1}, \mathbf{I}_M)$ distribution, $\mathbf{T}_n \in \mathbb{C}^{M \times M}$ refers to the projection matrix of AN. Since $\mathbf{z}_n(t)$ obeys a Gaussian distribution at any moment, it can be regarded as a time-independent additive noise. We are more concerned with the statistical properties of $\mathbf{z}_n(t)$ and $\mathbf{n}_{A,n}(t)$ such as variance rather than the exact

value at a given moment. Therefore, the subsequent part of the paper abbreviates $\mathbf{z}_n(t)$ and $\mathbf{n}_{A,n}(t)$ as $\mathbf{z}_n$ and $\mathbf{n}_{A,n}$, respectively. Define (x_l, y_l) as the coordinate of LU, which can be transferred to angle $\theta_{l,n}$ and distance $r_{l,n}$ relative to the nth antenna array. The time difference between the signals transmitted from the nth array and from the first array to LU is denoted as $\tau_{l,n} = (r_{l,n} - r_{l,1})/c$. $x_n(t)$ in (8) represents the quadrature phase-shift keying (QPSK) modulated symbol of the nth array at time instant t, given by

$$x_n(t) = \sum_{k=0}^{Q/N-1} a_{kN+n} g(t - kNT), \tag{10}$$

where k represents the indexes of symbols transmitted by the nth antenna array, e.g., the first antenna array transmits $\{a_1, a_{N+1}, a_{2N+1}, \cdots, a_{kN+1}\}$ with $a_i \in 1/\sqrt{2}\{1 + j, 1 - j, -1 + j, -1 - j\}$, $\forall i \in \mathbb{N}^+$, representing the normalized QPSK constellation mapping, Q is the total number of symbols in a
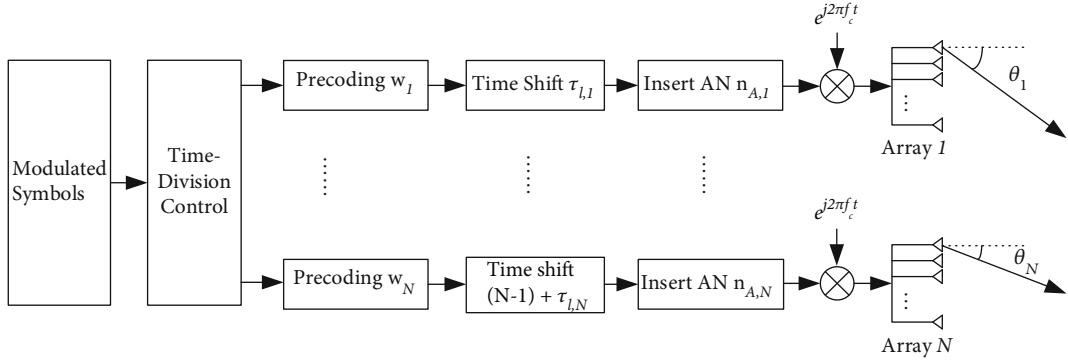
Figure 3: The architecture of the transmitter for the proposed TDMB scheme.

packet. Q is divisible by N. The ideal sinc pulse $g(t)$ is expressed as

$$g(t) = \frac{T}{\pi t} \sin\left(\frac{\pi t}{T}\right). \tag{11}$$

From (10), we can obtain the relationship between the transmitted symbols of each array and the total symbols. This describes how to do time division in the proposed TDMB scheme.

Next, we discuss how to design the transmit beamforming vector $\mathbf{w}_n$ and the projection matrix of AN $\mathbf{T}_n$. After being transmitted through a wireless line-of-sight (LOS) channel, LU will receive mixed signals from different arrays. For notational simplicity, we use $\mathbf{h}_{l,n} \in \mathbb{C}^{M \times 1}$ to denote the steering vector from LU to the nth antenna array, i.e., $\mathbf{h}_{l,n} \triangleq \mathbf{h}_n(r_{l,n}, \theta_{l,n})$. Since the positions of Eves are unknown, to maximize the signal-to-noise ratio (SNR) at LU, the transmit beamforming vector $\mathbf{w}_n$ is designed as

$$\mathbf{w}_n = \frac{\mathbf{h}_{l,n}}{\sqrt{\rho}}. \tag{12}$$

For a further improvement of transmission security, AN is employed. To prevent the LU from being interfered by AN, we project the AN into the null space of the steering vector $\mathbf{h}_{l,n}$. Therefore, the projection matrix of AN $\mathbf{T}_n$ is given by

$$\mathbf{T}_n = \mathbf{I}_M - \frac{1}{\rho}\mathbf{h}_{l,n}\mathbf{h}_{l,n}^H. \tag{13}$$

According to (5), the projection matrix $\mathbf{T}_n$ and the steering vector $\mathbf{h}_{l,n}$ are orthogonal, as shown by

$$
\begin{aligned}
\mathbf{h}_{l,n}^H \mathbf{T}_n &= \mathbf{h}_{l,n}^H \left(\mathbf{I}_M - \frac{1}{\rho}\mathbf{h}_{l,n}\mathbf{h}_{l,n}^H\right) \\
&= \mathbf{h}_{l,n}^H - \frac{1}{\rho}\mathbf{h}_{l,n}^H\mathbf{h}_{l,n}\mathbf{h}_{l,n}^H \\
&= \mathbf{0}.
\end{aligned} \tag{14}
$$

3.2. Received Signal Model. According to (7) and (8), the signal received at LU can be given by

$$
\begin{aligned}
y_l(t) &= \sum_{n=1}^{N} \mathbf{h}_{l,n}^H \mathbf{s}_n\left(t - \frac{r_{l,n}}{c}\right) e^{j2\pi f_c(t-(r_{l,n}/c))} + n_l \\
&= e^{j2\pi f_c(t-(r_{l,1}/c))} \sum_{n=1}^{N} \mathbf{h}_{l,n}^H \mathbf{s}_n\left(t - \frac{r_{l,1}}{c} - \tau_{l,n}\right) e^{-j2\pi f_c \tau_{l,n}} + n_l,
\end{aligned} \tag{15}
$$

where n_l is the additive white Gaussian noise (AWGN) at LU with $n_l \sim \mathscr{CN}(0, \sigma_l^2)$ and σ_l^2 denotes the noise variance received by LU. Supposing the carrier $\exp(j2\pi f_c(t - r_{l,1}/c))$ is perfectly removed and timing synchronization is well done, the received baseband signal is given by

$$r_l(t) = \sum_{n=1}^{N} \mathbf{h}_{l,n}^H \mathbf{s}_n(t - \tau_{l,n}) e^{-j2\pi f_c \tau_{l,n}} + n_l. \tag{16}$$

Substituting (8), (10), and (14) into (16), $r_l(t)$ can be simplified as

$$r_l(t) = \sum_{n=1}^{N} \mathbf{h}_{l,n}^H \left[\sqrt{P_s}\mathbf{w}_n x_n(t - (n-1)T)e^{j2\pi f_c \tau_{l,n}} + \sqrt{P_A}\mathbf{n}_{A,n}\right] e^{-j2\pi f_c \tau_{l,n}} + n_l$$

$$\triangleq \sqrt{\rho P_s} \sum_{k'=0}^{Q-1} a_{k'+1} g\left(t - k'T\right) + n_l, \tag{17}$$

where k' is the index of symbols in a packet. A detailed derivation of the (17) is provided in Appendix. Since the path delay from the antenna arrays to LU is considered at the transmitter, the received symbol interval is equal to symbol duration time T, which means there is no ISI at the LU.

Similarly, the received signal at Eve is given by

$$
\begin{aligned}
y_e(t) &= \sum_{n=1}^{N} \mathbf{h}_{e,n}^H \mathbf{s}_n\left(t - \frac{r_{e,n}}{c}\right) e^{j2\pi f_c(t-(r_{e,n}/c))} + n_e \\
&= e^{j2\pi f_c(t-(r_{e,1}/c))} \sum_{n=1}^{N} \mathbf{h}_{e,n}^H \mathbf{s}_n\left(t - \frac{r_{e,1}}{c} - \tau_{e,n}\right) e^{-j2\pi f_c \tau_{e,n}} + n_e,
\end{aligned}
$$

$$(18)$$

where n_e is the AWGN at Eve with $n_e \sim \mathscr{CN}(0, \sigma_e^2)$ and $\sigma_{e,n}^2$ denotes the noise variance received by Eve; $r_{e,n}$ and $\mathbf{h}_{e,n} \in \mathbb{C}^{M \times 1}$, respectively, refer to the distance and steering vector from the nth antenna array to Eve. The time difference between the signals transmitted from the nth array and from the first array to Eve is denoted as $\tau_{e,n} = (r_{e,n} - r_{e,1})/c$. Under this circumstance, the carrier and delay time are $\exp(j2\pi f_c(t - r_{e,1}/c))$ and $r_{e,1}/c$, respectively. Thus, the baseband signal of Eve is given by

$$
\begin{aligned}
r_e(t) &= \sum_{n=1}^{N} \mathbf{h}_{e,n}^H \left[\sqrt{P_s} \mathbf{w}_n x_n(t - (n-1)T + \tau_{l,n} - \tau_{e,n}) e^{j2\pi f_c \tau_{l,n}} + \sqrt{P_A} \mathbf{n}_{A,n} \right] e^{-j2\pi f_c \tau_{e,n}} + n_e \\
&= \sqrt{P_s} \sum_{n=1}^{N} \mathbf{h}_{e,n}^H \mathbf{w}_n x_n(t - (n-1)T - \Delta\tau_n) e^{-j2\pi f_c \Delta\tau_n} + \sqrt{P_A} \sum_{n=1}^{N} \mathbf{h}_{e,n}^H \mathbf{n}_{A,n} e^{-j2\pi f_c \tau_{e,n}} + n_e \\
&= \underbrace{\sqrt{P_s} \sum_{n=1}^{N} \sum_{k=0}^{Q/N-1} \mathbf{h}_{e,n}^H \mathbf{w}_n a_{kN+n} g(t - (kN+n-1)T - \Delta\tau_n) e^{-j2\pi f_c \Delta\tau_n}}_{\text{ISI}} + \underbrace{\sqrt{P_A} \sum_{n=1}^{N} \mathbf{h}_{e,n}^H \mathbf{n}_{A,n} e^{-j2\pi f_c \tau_{e,n}}}_{\text{AN}} + n_e,
\end{aligned}
$$

$$(19)$$

where $\Delta\tau_n = \tau_{e,n} - \tau_{l,n}$ represents the time differences between the propagation time from the antenna arrays to the Eve and LU. Indeed, the ISI at Eve is caused by $\Delta\tau_n$.

It can be observed from (17) and (19) that symbols received by Eve are disturbed by three factors:

(1) Amplitude and phase of received signals vary because of multiarray DM. $\mathbf{h}_{e,n}^H \mathbf{w}_n$ indicates that the constellation diagram of the received signal in the nondesired direction will be distorted. $\sum_{n=1}^{N} \mathbf{h}_{e,n}^H \mathbf{w}_n$ represents that only in the intersection area of different beams can signals be correctly obtained. These results show that the MAA model can realize angle-distance-dependent DM

(2) Received signals suffer from ISI because of time division. $g(t - (kN+n-1)T - \Delta\tau_n)$ indicates that the interval between adjacent sinc pulses is not equal to T when $\Delta\tau_n \neq 0$. This will cause ISI, as shown in Figure 4. Meanwhile, $\Delta\tau_n$ is determined by the position of receivers

(3) AN. Similar to multiarray DM, only the receiver at the desired location is free from AN

4. Performance Analysis

In this section, the secrecy rate and SER for the proposed beamforming scheme are analysed. To facilitate analysis, we assume that all AWGNs are normalized and have the same distribution with zero mean and variance σ^2 for both LUs and Eves.

4.1. Secrecy Rate. According to (17), the SINR of LU can be expressed as

$$
\gamma_l = \frac{\rho P_s}{\sigma^2}. \tag{20}
$$

In light of (19), the interference of Eve consists of AN and ISI. The power of received AN can be expressed as

$$
P_{r,A} = P_A \sum_{n=1}^{N} \left| \mathbf{h}_{e,n}^H \mathbf{T}_n \right|^2. \tag{21}
$$

Assume that Eves know the positions of LU and antenna arrays, which means Eves can sample at the best time by calculating the path difference, i.e., sample time- $t \in \{(kN+n-1)T + \Delta\tau_n, k = 0, 1, \cdots, Q/N - 1, n = 1, \cdots, N\}$. Since the transmit period can be regarded as NT, we only need to analyse the aliasing of N symbols, i.e., the 2nd symbol to the $(N+1)$th symbol. For simplicity, we only consider the interference from the immediately preceding and following symbols, since that from the rest symbols is negligible. Then, the power of ISI for the lth symbol can be expressed as

$$
P_{l,\text{ISI}} = P_s \left[\left| g(T + \Delta\tau_l - \Delta\tau_{l-1}) \mathbf{h}_{e,l-1}^H \mathbf{w}_{l-1} \right|^2 + \left| g(T + \Delta\tau_{l+1} - \Delta\tau_l) \mathbf{h}_{e,l+1}^H \mathbf{w}_{l+1} \right|^2 \right],
$$

$$
l = 2, \cdots, N+1, \tag{22}
$$
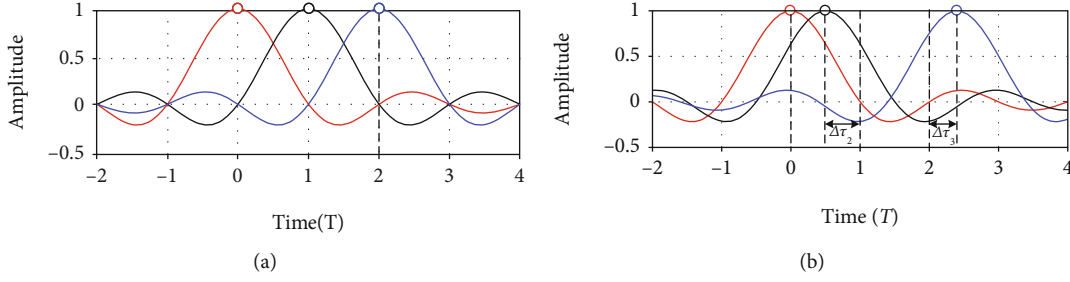
FIGURE 4: The three received symbols of (a) LU and (b) Eve. In (a), each symbol is not disturbed by other symbols. In (b), each symbol suffers from ISI which is determined by $\Delta\tau_n$.
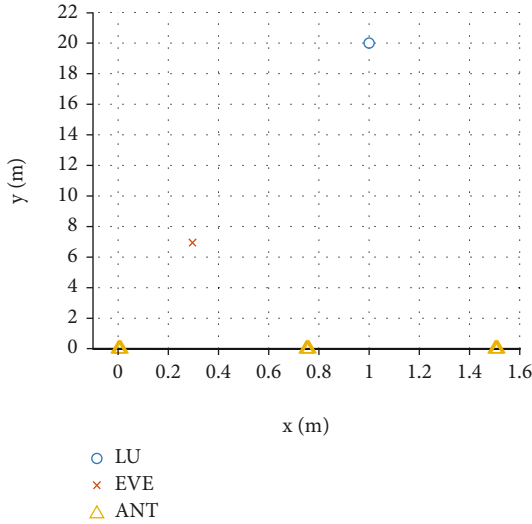
FIGURE 5: The position of LU, Eve, and antenna arrays in a 2-dimensional plane.

where $\Delta\tau_{N+1} = \Delta\tau_1$, $\Delta\tau_{N+2} = \Delta\tau_2$, $\mathbf{w}_{N+1} = \mathbf{w}_1$, $\mathbf{w}_{N+2} = \mathbf{w}_2$, $\mathbf{h}_{e,N+1} = \mathbf{h}_{e,1}$, and $\mathbf{h}_{e,N+2} = \mathbf{h}_{e,2}$, because of cyclicity. Considering that the ISI is different for each symbol, we calculate the average SINR of Eve, which is given by

$$\overline{\gamma_e} = \frac{1}{N^2} \sum_{l=2}^{N+1} \frac{P_s \sum_{n=1}^{N} \left| \mathbf{h}_{e,n}^H \mathbf{w}_n \right|^2}{(P_{l,\mathrm{ISI}} + P_{r,A} + \sigma^2)}. \tag{23}$$

According to (20) and (23), the achievable rates of LU and Eve can be calculated, respectively, by

$$R_l = \log_2(1 + \gamma_l), \tag{24}$$

$$R_e = \log_2(1 + \overline{\gamma_e}). \tag{25}$$

Then, the secrecy rate can be defined as

$$R_s \triangleq \max \{R_l - R_e, 0\}. \tag{26}$$

4.2. SER. To evaluate the communication performance, we are interested in bit error rate (BER) and SER. The BER with the best detection and perfect recovery for QPSK is given by [19]

$$P_b = Q\left(\sqrt{2\gamma_b}\right), \tag{27}$$

where $Q(z) = 1/\sqrt{2\pi} \int_z^{\infty} \exp(-z^2/2)dz$ is the tail distribution function of the standard normal distribution and $\gamma_b = E_b/N_0$ represents the SNR per bit. The relationship between γ_b and the SNR per symbol γ_s for M-PSK modulation leads to the approximations

$$\gamma_b \approx \frac{\gamma_s}{\log_2 M}. \tag{28}$$

Substituting (28) into (27), we get P_b for QPSK as

$$P_b = Q(\sqrt{\gamma_s}). \tag{29}$$

In systems with interference, we use SINR instead of SNR to calculate the BER. Then, we can obtain P_b for LU and Eve, respectively, as

$$P_{b,l} = Q(\sqrt{\gamma_l}), \tag{30}$$

$$P_{b,e} = Q\left(\sqrt{\overline{\gamma_e}}\right). \tag{31}$$

The SER is equal to the error probability of any bit in a symbol, which is given by

$$P_{se} = 1 - (1 - P_b)^2. \tag{32}$$

5. Simulation Results

In this section, the proposed TDMB scheme is evaluated in terms of SINR distribution, secrecy rate, and SER. The carrier frequency is set as $f_c = 30$ GHz. Consider a scenario with limited resources, i.e., UAV, which means large-scale antenna arrays are not permitted. Assume that there is $N = 3$ transmit antenna arrays with $M = 4$ elements for each ULA. The spacing of the array elements and antenna arrays are $d = c/2f_c$ and $L = 150d$, respectively. Thus, the coordinates of arrays are (0 m, 0 m), (0.75 m, 0 m), and (1.5 m, 0 m). The coordinates of LU and Eve are (1 m, 20 m) and (0.3 m, 7 m), respectively, as shown in Figure 5. The baseband modulation is QPSK with symbol rate $R_s = 2$ Gsps, which satisfies the narrow-band assumption. The required SNR for the received signals at LU is 15 dB, which remains unchanged in the simulations. We assume that the noise

TABLE 3: Simulation parameters.

Parameters	Value
Number of antenna arrays, N	3
Number of ULA elements, M	4
Carrier frequency, f_s	30 GHz
Spacing of array elements, d	0.5 cm
Spacing of antenna arrays, L	0.75 m
Coordinates of arrays	(0 m, 0 m), (0.75 m, 0 m), and (1.5 m, 0 m)
Coordinate of LU	(1 m, 20 m)
Coordinate of Eve	(0.3 m, 7 m)
Modulation mod	QPSK
Symbol rate, R_s	2 Gsps
Power for transmitting symbols, P_s	3.07 dBM
Power for AN, P_A	0.06 dBm
Noise power	-100 dBm
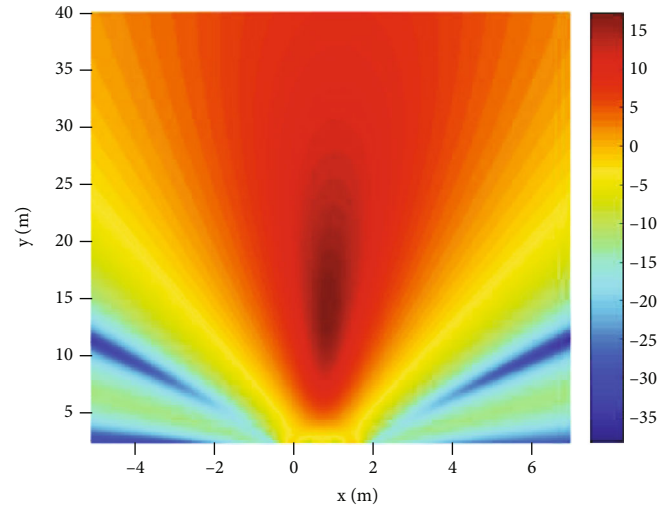
(a)
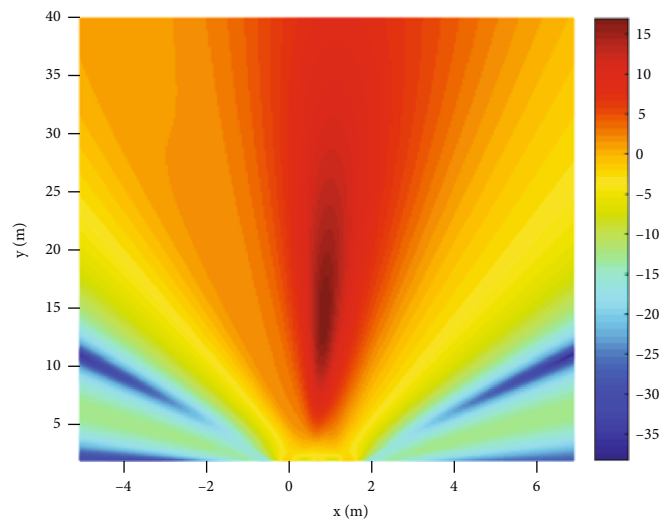
(b)

FIGURE 6: The SINR (dB) distribution in a 2-dimensional plane (a) method in [18] and (b) proposed TDMB scheme.
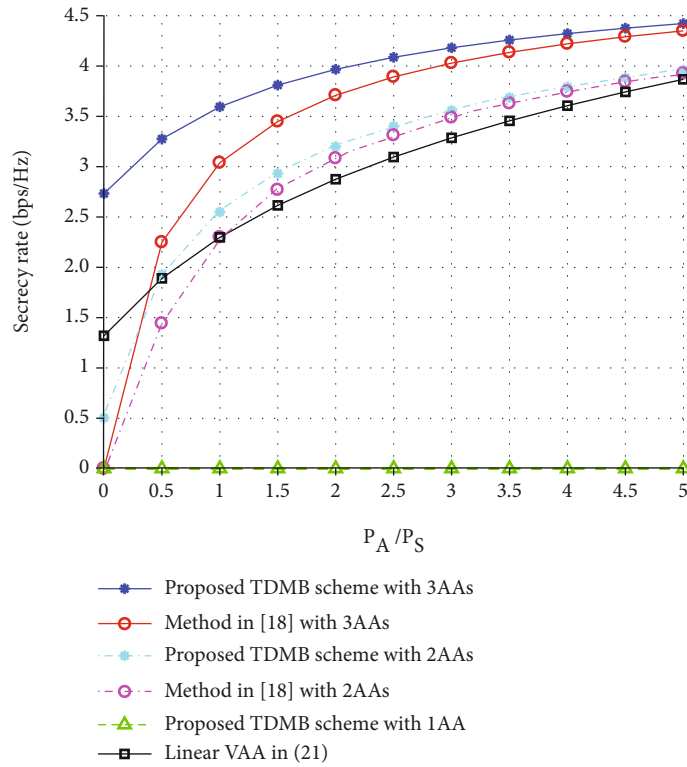
FIGURE 7: The secrecy rate (bps/Hz) versus the power of AN normalized by transmission power for different numbers of antenna arrays and methods, where the total number of antennas $MN = 12$ (applies also to VAA). Transmit power of VAA is $(P_A + P_s)$.
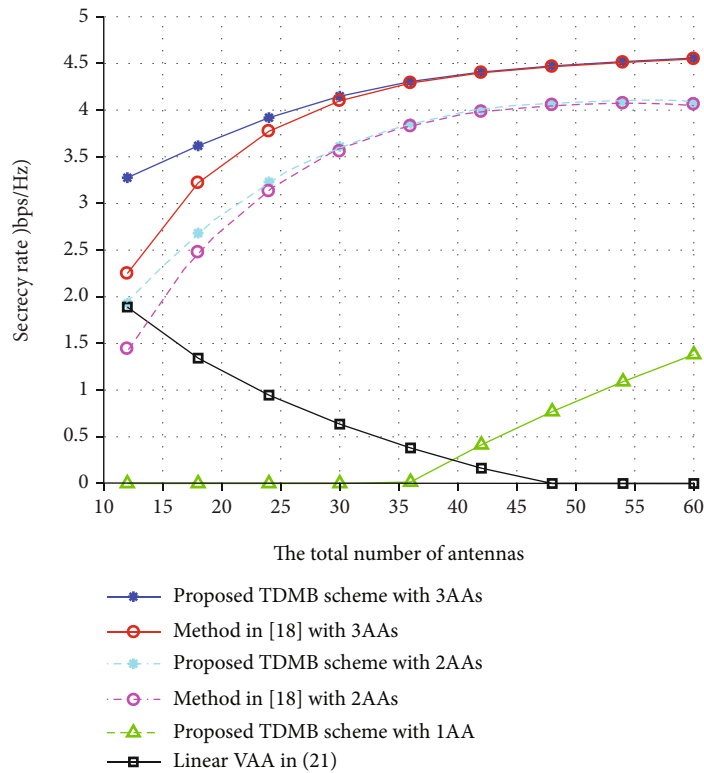
FIGURE 8: The secrecy rate (bps/Hz) versus the total number of antennas for different numbers of antenna arrays and methods, where $P_A/P_s = 1/2$. Transmit power of VAA is $(P_A + P_s)$.
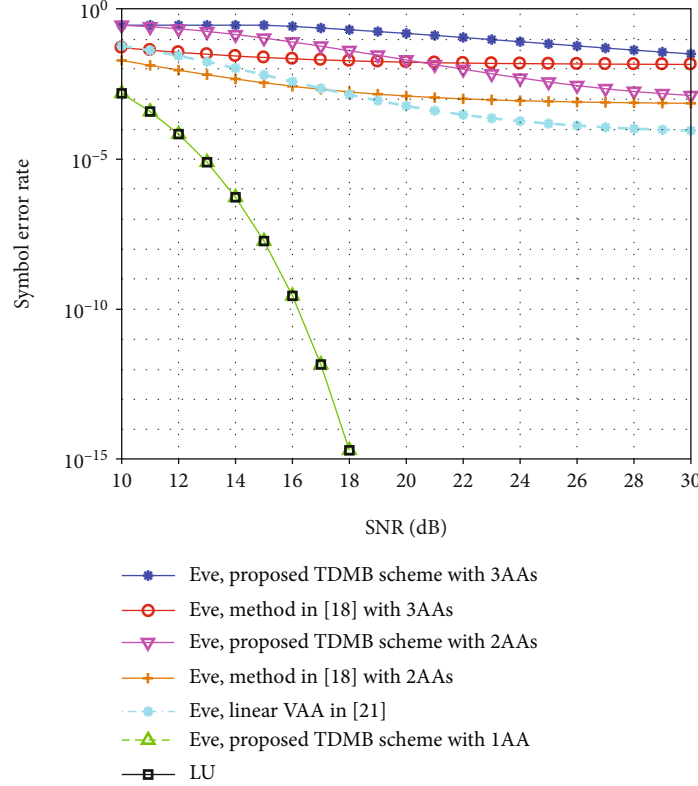
FIGURE 9: The SER versus SNR for different numbers of antenna arrays and methods, where $P_A/P_s = 1/2$.

power is -100 dBm. By means of the radio wave propagation loss in the free space [20], the path loss factor ρ is given by

$$Lfs(dB) = 32.5 + 20 \lg \left[f_c(MHz) \right] + 20 \lg \left[r(Km) \right]. \quad (33)$$

Based on the location of LU, it can be calculated that P_s needs to be 3.07 dBm. Considering that there is not much power for AN, the power of AN is set to be $P_A = 1/2P_s$. Unless otherwise stated, the default simulation parameters are summarized in Table 3.

In Figure 6, we compare the SINR of the proposed scheme with the method in [18]. The signal models in Figure 6 are both three antenna arrays (AAs). Figure 6(b) shows the SINR of the proposed TDMB scheme which exploits the ISI, while Figure 6(a) shows the SINR of the method in [18]. Deeper red indicates higher SINR. As expected, the SINR at LU is 15 dB, which meets our requirement. It can be seen from Figure 6 that the deepest red area is an ellipse rather than a line. This shows that the MAA scheme performs well against eavesdroppers close to the transmitter. In other words, it proves that angle-distance-dependent DM is achieved with MAA. Comparing Figures 6(a) and 6(b), it can be observed that with the help of time-division scheme, the SINR for the region far from LU decreases more significantly; e.g., the area with SINR greater than 10 decreased from 55 m^2 to 29 m^2, which indicates that the proposed scheme can further improve the secrecy performance.

In Figure 7, we investigate the secrecy rate versus the power of AN for different numbers of antenna arrays and methods. We compared the TDMB scheme with the method in [18, 21]. The total number of antennas is set as MN = 12 (applies also to VAA). The position of Eve is chosen as (0.3,7), which has a similar direction angle as LU. The secrecy rate of the method in [21] increases monotonically with increasing distribution length L. So, we set the L of VAA to be 1.5 m in agreement with the 3AAs. Since the method in [21] does not use AN, we assume that the total transmit power is consistent with the TDMB scheme; i.e., the transmit power of VAA is $(P_A + P_s)$. The following simulation of the method in [21] is the same. When the number of antenna arrays is 1, the TDMB scheme is degraded to normal single-beam DM. As shown in Figure 7, the secrecy rate for one antenna array is zero. This indicates that a single array cannot achieve secrecy transmission when the Eves and LU are in the same direction. Conversely, when the number of arrays is greater than one, partial secrecy transmission can be achieved even if Eves and LU are in the same direction of a given array. In addition, it can be observed that the ISI caused by the time-division scheme can significantly improve the secrecy rate when AN is unused. Meanwhile, the interference caused by the random location perturbations of the VAA elements is between the ISI of 3AAs and 2AAs. When P_A/P_s is greater than 0.5, the secrecy rate of the TDMB scheme with 2AAs is greater than the method in [21]. With the increase of the power for AN, the secrecy rate tends to be constant. Because $\Delta\tau_n$ is a variable independent of the power of AN,

(a)

(b)
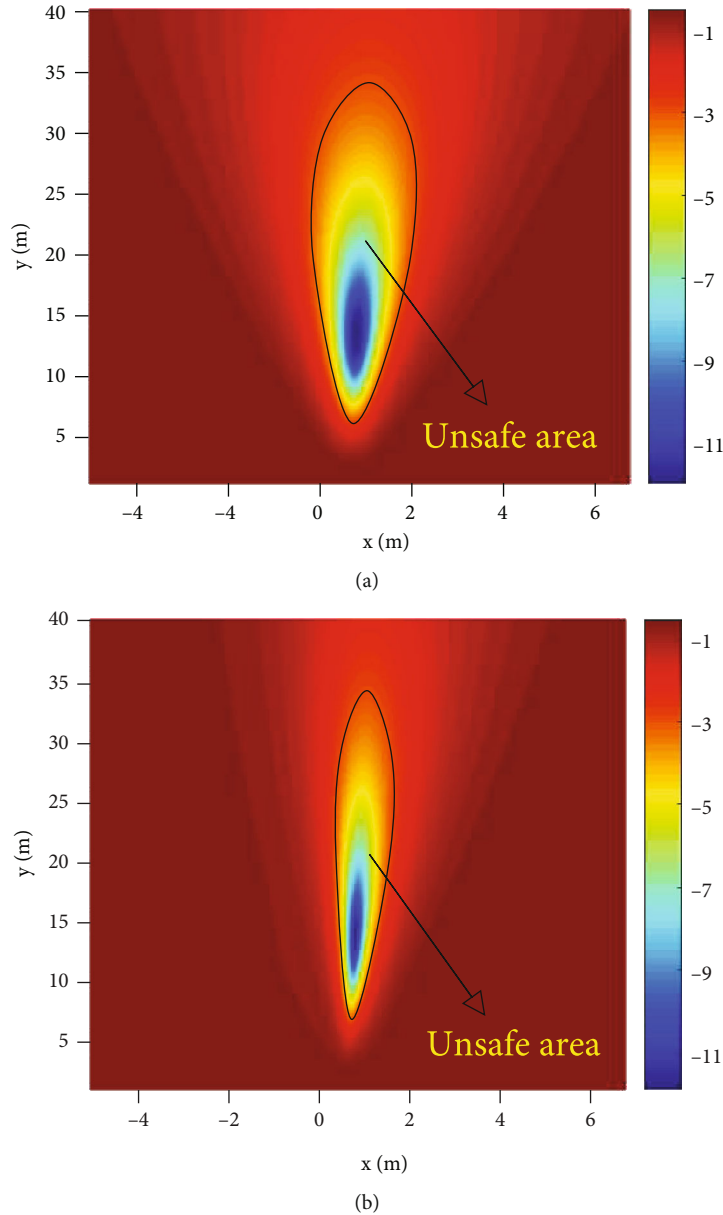
FIGURE 10: The logarithmic SER distribution in a 2-dimensional plane (a) method in [18] and (b) proposed TDMB scheme.

the ISI remains unchanged for the same position. Therefore, with increasing AN power, the impact of ISI on the secrecy rate gradually decreases. Moreover, the upper bound of the secrecy rate improves with the enhancement of the number of antenna arrays. Figure 7 proves that the time-division scheme contributes to the enhancement of the secrecy rate, especially when there is not enough power for AN.

In Figure 8, we investigate the secrecy rate versus the total number of antennas MN for different numbers of antenna arrays and methods. As shown in Figure 8, for a fixed small number of total antennas, the performance gap between the method in [18] and the TDMB scheme is larger for the case "3AAs" than "2AAs". When the total number of antennas is fixed and limited, the number of antennas per array decreases as the number of antenna arrays increases, which means that the beamwidth for each

antenna array becomes wider. With a wider beamwidth, i.e., a larger numerator in (23), ISI plays a more important role in reducing Eve's SINR. When the total number of antennas is the same, the greater the number of arrays, the higher the upper bound of the secrecy capacity. Meanwhile, the greater the number of arrays, the greater the improvement from the time-division scheme. This is because when the number of arrays increases, the scale of MAA will become larger. This results in larger values of $\Delta\tau_n$ as well. With an increasing total number of antennas, the impact of ISI on the secrecy rate gradually decreases. Surprisingly, the secrecy rate using VAA in [21] decreases as the number of antennas increases. According to Equation (24) [21], when the total power is fixed, the SINR of the Eves increase as the number of antennas increases. When the number of antennas reaches

36, the beamwidth of the single antenna array is narrow enough to avoid the Eves. At this point, the secrecy rate starts to be greater than 0. Therefore, the proposed scheme is more suitable for the situation that the number of antennas is limited.

In Figure 9, we investigate the SER versus the SNR for different numbers of antenna arrays and methods. Since we assume the noise power is the same throughout the space, the SNR is determined by the transmit power P_s. The SER level reflects SINR. First, we note that since Eve and LU are basically in the same direction, Eve does not suffer from interference in the case with 1AA. The curve of Eve of the TDMB scheme with 1AA coincides with that of LU. According to Equations (21), (22), (23), and (24) [21], each factor of the numerator and denominator in the SINR formula contains P_s except for the noise power (simplified as $\text{SINR} = aP_s/(bP_s + c)$). This indicates that as P_s increases, the impact of noise power reduces. Eventually, the SINR will converge to a constant a/b. When the number of antenna arrays is the same, the TDMB scheme has a higher SER than the method in [18]. Factor a of the two methods is the same, while factor b of the TDMB scheme is greater than that of the method in [18] because of the ISI caused by the time-division scheme. Similarly, the greater the number of arrays, the higher the SER. The SER of the method in [21] is first higher than 2AAs but eventually less than 2AAs. The reason is that the method in [21] has a greater factor c/b. When P_s is insufficient, factor c plays a more important role. However, the interference caused by random location perturbations of the VAA elements is less than AN and ISI; i.e., the method in [21] has a greater factor a/b. As a result, the method in [21] has a lower SER. Theoretically, the TDMB scheme with 3AAs should have a lower SINR than that with 2AAs, but their SER is the same when the SNR is 10. The reason is that the upper limit of SER, 0.75, is reached.

Figure 10 compares the SER performance surface of the proposed TDMB scheme and the method in [18]. Consistent with the SINR distribution in Figure 6, the regions near LU enjoy a low SER. Note that the effects of path differences on the SER performance are asymmetric, although the path differences are symmetric. The ISI caused by increasing the received symbol interval is less than the ISI caused by decreasing the symbol interval. For example, we can see from Figure 4 that the second symbol moves closer to the first one when $\Delta\tau_2 < 0$. Assuming a new case with $\Delta\tau_2' = -\Delta\tau_2$, the second symbol will be further away from the first. It is easy to find that the first symbol receives more interference in the first case. Suppose that when the SER is greater than 10^{-5}, the Eves cannot eavesdrop on the information normally. Then, we can define an unsafe area, where the SER is lower than 10^{-3}. When the Eves are in an unsafe area, confidential transmission is not possible. We can use some physical methods to ensure that there are no Eves in unsafe areas, such as establishing cordon areas. Finally, as illustrated in Figure 10, the proposed method can improve security performance by utilizing ISI in the undesired directions with only limited resources.

6. Conclusions

In this paper, we investigated the PLS problem for UAV communications using the TDMB scheme. In the TDMB scheme, multiple antenna arrays steer their beamforming vectors based on their position relative to the legitimate user (LU). Meanwhile, multiple antenna arrays take turns transmitting different symbols from a same packet. We studied both analytically and through simulation the secrecy rate and SER of the received signals at different positions. We also simulated the secrecy rate under different total antennas and artificial noise power. These results suggested that the proposed method can achieve angle-distance-dependent DM. Moreover, the path differences between the receiver and different antenna arrays can cause ISI for receivers in undesired directions. Hence, the security performance is further enhanced. These results also suggested that the security rate has a greater improvement with the proposed method, where the number of antennas and the power of AN are limited. Therefore, this method is suitable for UAV security communication. Many UAVs are now equipped with antenna arrays. Although there is a loss in performance, MAAs can be implemented using subarrays. This does not require changes to the structure of the existing UAV, only modifications to the programmable part of the hardware, such as the field programmable gate array (FPGA). Alternatively, clustered UAV systems can be used to achieve MAAs, which requires the cluster to complete the networking first. The proposed method also has some drawbacks. First, it is only effective for phase-shift keying modulated. Second, when resources are sufficient, this method does not improve security performance much.

Further research is needed to investigate the beamforming scheme based on a uniform planar array. It is closer to practical application. The research scene will change from a 2-dimensional plane to a 3-dimensional space. Additional analysis of highly dynamic UAVs or mobile communications is also required.

Appendix

Here, we show the mathematical derivation of (17). By substituting (10), (12), and (14) into (17), we can get

$$
\begin{aligned}
r_l(t) &= \sum_{n=1}^{N} \mathbf{h}_{l,n}^H \left[\sqrt{P_s} \mathbf{w}_n x_n(t - (n-1)T) e^{j2\pi f_c \tau_{l,n}} + \sqrt{P_A} \mathbf{n}_{A,n} \right] e^{-j2\pi f_c \tau_{l,n}} + n_l \\
&= \sqrt{P_s} \sum_{n=1}^{N} \mathbf{h}_{l,n}^H \mathbf{w}_n x_n(t - (n-1)T) + n_l = \sqrt{\rho P_s} \sum_{n=1}^{N} x_n(t - (n-1)T) + n_l \\
&= \sqrt{\rho P_s} \sum_{n=1}^{N} \sum_{k=0}^{Q/N-1} a_{kN+n} g(t - (kN + n - 1)T) + n_l.
\end{aligned}
\tag{A.1}
$$

We expand the double summation

$$
\sum_{n=1}^{N} \sum_{k=0}^{Q/N-1} kN + n,
\tag{A.2}
$$

to obtain each addend

$$
\begin{matrix}
0+1 & 0+2 & \cdots & 0+N \\
N+1 & N+2 & \cdots & 2N \\
\vdots & \vdots & \ddots & \vdots \\
Q-N+1 & Q-N+2 & \cdots & Q
\end{matrix}. \tag{A.3}
$$

It can be seen from (A.3) that (A.2) can be rewritten as

$$
\sum_{n=1}^{N}\sum_{k=0}^{Q/N-1} kN+n \triangleq \sum_{k'=0}^{Q-1} k'+1. \tag{A.4}
$$

Substituting (A.4) into (A.1), (17) can be obtained as

$$
r_l(t) \triangleq \sqrt{\rho P_s} \sum_{k'=0}^{Q-1} a_{k'+1} g\left(t-k'T\right) + n_l, \tag{A.5}
$$

which completes the derivation.

Data Availability

No data were used to support this study.

Conflicts of Interest

The authors declare no conflicts of interest.

Acknowledgments

References

[1] A. Mukherjee, S. A. A. Fakoorian, J. Huang, and A. L. Swindle-hurst, "Principles of physical layer security in multiuser wireless networks: a survey," *IEEE Communications Surveys Tutorials*, vol. 16, no. 3, pp. 1550–1573, 2014.

[2] G. Zheng, I. Krikidis, J. Li, A. P. Petropulu, and B. Ottersten, "Improving physical layer secrecy using full-duplex jamming receivers," *IEEE Transactions on Signal Processing*, vol. 61, no. 20, pp. 4962–4974, 2013.

[3] F. Shu, T. Shen, L. Xu et al., "Directional modulation: a physical-layer security solution to B5G and future wireless networks," *IEEE Network*, vol. 34, no. 2, pp. 210–216, 2020.

[4] T. Hong, M.-Z. Song, and Y. Liu, "Dual-beam directional modulation technique for physical-layer secure communication," *IEEE Antennas and Wireless Propagation Letters*, vol. 10, pp. 1417–1420, 2011.

[5] N. Valliappan, A. Lozano, and R. W. Heath, "Antenna subset modulation for secure millimeter-wave wireless communication," *IEEE Transactions on Communications*, vol. 61, no. 8, pp. 3231–3245, 2013.

[6] O. N. Alrabadi and G. F. Pedersen, "Directional space-time modulation: a novel approach for secured wireless communi-cation," in *In 2012 IEEE International Conference on Communications (ICC)*, pp. 3554–3558, Ottawa, ON, Canada, 2012.

[7] J. Hu, F. Shu, and J. Li, "Robust synthesis method for secure directional modulation with imperfect direction angle," *IEEE Communications Letters*, vol. 20, no. 6, pp. 1084–1087, 2016.

[8] F. Shu, X. Wu, J. Li, R. Chen, and B. Vucetic, "Robust synthesis scheme for secure multi-beam directional modulation in broadcasting systems," *IEEE Access*, vol. 4, pp. 6614–6623, 2016.

[9] T. Xie, J. Zhu, and Y. Li, "Artificial-noise-aided zero-forcing synthesis approach for secure multi-beam directional modula-tion," *IEEE Communications Letters*, vol. 22, no. 2, pp. 276–279, 2018.

[10] F. Shu, L. Xu, J. Wang, W. Zhu, and Z. Xiaobo, "Artificial-noise-aided secure multicast precoding for directional modu-lation systems," *IEEE Transactions on Vehicular Technology*, vol. 67, no. 7, pp. 6658–6662, 2018.

[11] R. M. Christopher and D. K. Borah, "Iterative convex optimi-zation of multi-beam directional modulation with artificial noise," *IEEE Communications Letters*, vol. 22, no. 8, pp. 1712–1715, 2018.

[12] T. Hong, M.-Z. Song, and Y. Liu, "RF directional modulation technique using a switched antenna array for communication and direction-finding applications," *Progress In Electromag-netics Research*, vol. 120, pp. 195–213, 2011.

[13] L. Lai, J. Hu, Y. Chen, H. Zheng, and N. Yang, "Directional modulation-enabled secure transmission with intelligent reflecting surface," in *In 2020 IEEE 3rd International Confer-ence on Information Communication and Signal Processing (ICICSP)*, pp. 450–453, Shanghai, China, 2020.

[14] Q. Zeng, P. Yang, H. Lin, F. Yang, and S. Yang, "Generalized closed-form sidebands radiation expressions for 4-D antenna arrays," *IEEE Transactions on Antennas and Propagation*, vol. 69, no. 2, pp. 1193–1197, 2021.

[15] G. Huang, Y. Ding, and S. Ouyang, "Multicarrier directional modulation symbol synthesis using time-modulated phased arrays," *IEEE Antennas and Wireless Propagation Letters*, vol. 20, no. 4, pp. 567–571, 2021.

[16] B. Qiu, M. Tao, L. Wang, J. Xie, and Y. Wang, "Multi-beam directional modulation synthesis scheme based on frequency diverse array," *IEEE Transactions on Information Forensics and Security*, vol. 14, no. 10, pp. 2593–2606, 2019.

[17] J. Xie, B. Qiu, Q. Wang, and J. Qu, "Broadcasting directional modulation based on random frequency diverse array," *Wire-less Communication and Mobile Computing*, vol. 2019, no. 1, pp. 1–11, 2019.

[18] W. Zhang, M. Le, B. Li, J. Wang, and J. Peng, "Directional modulation-enhanced multiple antenna arrays for secure and precise wireless transmission," *Sensors*, vol. 19, no. 22, p. 4833, 2019.

[19] Q. Cheng, V. Fusco, J. Zhu, S. Wang, and F. Wang, "WFRFT-aided power-efficient multi-beam directional modulation schemes based on frequency diverse array," *IEEE Transactions on Wireless Communications*, vol. 18, no. 11, pp. 5211–5226, 2019.

[20] A. Goldsmith, *Wireless Communication*, Cambridge Univ. Press, Cambridge, U.K., 2007.

[21] H. Jung, S.-W. Ko, and I.-H. Lee, "Secure transmission using linearly distributed virtual antenna array with element posi-tion perturbations," *IEEE Transactions on Vehicular Technol-ogy*, vol. 70, no. 1, pp. 474–489, 2021.

WILEY | Hindawi

Research Article

A UAV Detection and Tracking Algorithm Based on Image Feature Super-Resolution

Bin Li (ID),[1] **Shi Qiu** (ID),[2] **Wei Jiang** (ID),[1] **Wei Zhang** (ID),[1] **and Mingnan Le** (ID)[1]

[1]*School of Information Science and Technology, Northwest University, Xi'an 710127, China*
[2]*Key Laboratory of Spectral Imaging Technology CAS, Xi'an Institute of Optics and Precision Mechanics, Chinese Academy of Sciences, Xi'an 710119, China*

Correspondence should be addressed to Shi Qiu; qiushi215@163.com

UAV is difficult to detect by visual methods at a long distance, so a UAV detection and tracking algorithm is proposed based on image super-resolution. Firstly, a saliency transformation algorithm is built to focus on the suspected area. Then, a generative adversarial network is established on the basis of ROI to realize the super-resolution of weak targets and restore the high-resolution details of target features. Finally, the cooperative attention module is built to recognize and track UAV. Our experiments show that the proposed algorithm has strong robustness.

1. Introduction

Small UAV has the characteristics of portability and strong mobility and also has broad application space in unmanned investigation. However, for long-distance UAV, only a limited number of pixels are displayed on the image, which is of great significance for its accurate discrimination [1]. The research on UAV mainly focuses on target tracking. Ibrahim et al. [2] use UAV to track moving targets. Zhou et al. [3] construct a Kalman filter to realize UAV tracking. Nodland et al. [4] propose the track optimization strategy. Liu [5] introduces prediction points to assist UAV track detection. Ragi and Chong [6] propose an algorithm to dynamically realize multi-UAV tracking. Yoo and Hong [7] realize UAV detection and tracking by visual means. Kadouf and Mustafah [8] analyze the color characteristics of UAV to realize UAV tracking. Yu et al. [9] propose a new coordinate system to analyze the attitude of UAV. Teuliere et al. [10] build a 3D model to track the UAV flying indoors. Choi and Kim [11] use monocular to analyze the UAV track. Quintero et al. [12] use the output-feedback model to predict UAV flight trajectory. Santos et al. [13] build a ground visual tracking system to detect UAV. Zhou et al. [14] construct a Hough transform to detect and track UAV. Vetrella et al. [15] realize

dynamic navigation through a multi-UAV network. Elloumi et al. [16] propose a low-power tracking algorithm from the perspective of UAV energy. Greatwood et al. [17] use parallel means to realize rapid detection and tracking of UAV. Santos et al. [18] propose a 3D model for UAV positioning. Zhang et al. [19] use deep learning to build a coarse to fine detection algorithm to realize UAV detection and tracking. Huang et al. [20] build correlation filters based on deep learning to realize UAV tracking. Rabah et al. [21] build a model based on fuzzy set theory to realize target tracking. Kokunko and Krasnova [22] propose variable constraint mechanism to realize UAV tracking. Li et al. [23] propose augmented memory for correlation filters to realize UAV tracking. Li et al. [24] use deep learning network to extract features and realize UAV object tracking. Moon et al. [25] realize multi-UAV tracking based on deep learning network.

Through the above analysis, main problems of many research studies on UAV detection and tracking are as follows. (1) Traditional target detection algorithms cannot be effectively applied to UAV due to the small size of UAV. (2) The number of pixels on the image of UAV is limited, and its features are not obvious. (3) The flight uncertainty of UAV leads to the construction difficulty of the unified model.

Therefore, on the basis of images, (1) a complete UAV detection and tracking process is proposed, (2) the enhancement algorithm is built to improve the spatial resolution of the target and a new idea of UAV detection is proposed, and (3) according to the principle of visual perception, a depth-based attention model is built to focus on the area, where UAV is located to realize tracking.

2. Algorithm

According to the characteristics of UAV images, a UAV detection and tracking algorithm is proposed based on image super-resolution, as shown in Figure 1. Firstly, the image composition is analyzed and the suspected area extraction module is constructed. Then, a super-resolution model is constructed to highlight local information and increase signal strength. Finally, a deep learning module is constructed to realize UAV tracking based on the attention mechanism.

2.1. ROI Extraction.
The UAV is usually at a long distance, so it presents a limited number of pixels on the image, which leads to difficult detection from the spatial domain. Therefore, the salient area is introduced to extract ROI. First of all, the features are obtained by linear difference:

$$C_f = p_1 + O_b[f_r(R(f_\theta))], \tag{1}$$

where p_1 is the characteristic, O_b is the gradient third-order matrix, f_r is the activation function, and $R(f_\theta)$ is the convolution calculation performed by θ. The salient target area model is constructed by supervised learning, and the image is described as $I_f(y_j = 1 \mid M_t^i)$; then, y_j represents the reliability of pixel j. The corresponding cross-entropy loss function is

$$E_i(C; M_t^i) = -\left[\sum_{j \in X^+} \log I_f(y_j = 1 | C; M_t^i) + \sum_{j \in X^-} \log I_f(y_j = 0 | C; M_t^i)\right], \tag{2}$$

where X^+ and X^- represent the edge and background pixels of the salient target area, respectively. Image segmentation is realized through the edge of the salient target area, but the resolution, affected by the multilayer transmission architecture, will gradually decrease with the change of layers, which needs to be further strengthened:

$$C_i = O_b[C_{e,i}; \theta] + f_h(C_{i+1}), \tag{3}$$

where $f_h(C_{i+1})$ represents the enhancement processing of the features of the previous layer. The cumulative loss function between the corresponding estimation result and the real image is

$$E_T = \sum_i \{E_i(C_{e,i}; M_t^i) + E_i(C_i; M_t^i)\}. \tag{4}$$

The idea of edge enhancement is used to suppress the weakening caused by multiple layers in the process of feature fusion, in order to achieve more accurate salient target area estimation. During the convolution operation, the feedback mechanism is introduced to continuously input the edge features and salient target area features of the image into the convolution operation to obtain a new estimation graph function:

$$I_t = \begin{cases} U(R_1(I(x,y); \theta), R_2(I^P(x,y); \theta); q), & t = 1, \\ U(R_1(I(x,y); \theta), R_2(I^{t-1}(x,y); \theta); q), & t > 1, \end{cases} \tag{5}$$

where $U(.)$ is deconvolution, $I^P(x,y)$ is a priori graph, and q is convolution parameter. Divergence occurs during feedback correction. In order to solve this phenomenon, any two pixels adjacent to each other can be used as a path in $I(x,y)$. Let all paths corresponding to n pixels be expressed as $q =$ $\{q_0, \ldots, q_n\}$. Then, after obtaining the salient target edge, the loss function is calculated as

$$L(x) = \min_{q,x}\left\{\sum_{i=1}^n |C(p_{i-1}) - C(p_i)|\right\}. \tag{6}$$

Let the width and height of $L(x)$ be w and h. The mapping matrix $M = [m_{ij}]_{w \times h}$ can be constructed:

$$m_{ij} = 1 - \frac{\sqrt{(i - 0.5w)^2 + (j - 0.5h)^2}}{\sqrt{(0.5w)^2 + (0.5h)^2}}. \tag{7}$$

According to the mapping matrix, the position of the salient target can be determined. On the basis of a priori information feedback correction, the position of the edge of the salient target can be distinguished to prevent the performance degradation of the feedback correction and realize the suspected area extraction.

2.2. ROI Super-Resolution Reconstruction.
The motion area has been extracted in the previous section. On this basis, the research on ROI super-resolution reconstruction is carried out in this section to further determine whether UAV is included. Because the target area is smaller than the background area, when the target area is enlarged, the background is enlarged at the same time, resulting in coarse-grained information after over division. Therefore, we design the feature super-resolution GAN, transform the weak target features into super-resolution features through super-resolution processing in the feature space, and enhance the feature representation of the weak target. The structure is shown in Figure 2.
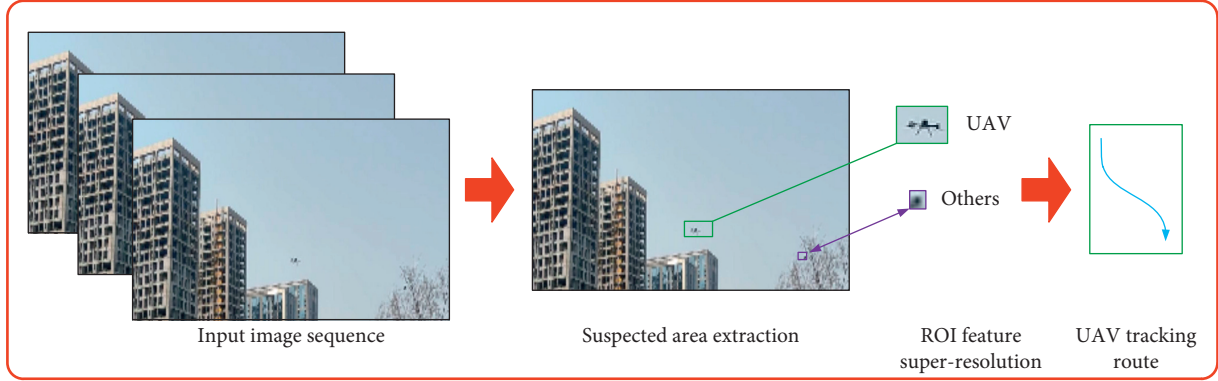
FIGURE 1: Algorithm flowchart.

Let the original input image be $\mathbf{X}_I$. The image $\mathbf{X}_{0.5I}$ is obtained by 2 times downsampling to obtain a pair of low-resolution and high-resolution target features. The output features $\mathbf{F}_I = \{\mathbf{F}_I^1, \mathbf{F}_I^2, \ldots, \mathbf{F}_I^q\}$ and $\mathbf{F}_{0.5I} = \{\mathbf{F}_{0.5I}^1, \mathbf{F}_{0.5I}^2, \ldots, \mathbf{F}_{0.5I}^q\}$ are obtained through the feature network. The weak target features $\mathbf{F}_{0.5I}^q$ are iteratively generated into super-resolution features $\mathbf{S}_{0.5I}^q$ so that the super-resolution features are similar to the features $\mathbf{T}_I^q$ output by the supervisor as much as possible. The feature loss function is defined as

$$L_F = \sum_{q=1}^{C} \left\| T_I^q - S_{0.5I}^q \right\|_2^2.$$ (8)

The generator loss function is defined as

$$L_G = -\sum_{q=1}^{C} \log D\left(S_{0.5I}^q\right).$$ (9)

The feature super-resolution discriminator adopts a three-layer perceptron to train and distinguish $\mathbf{S}_{0.5I}^q$ and $\mathbf{T}_I^q$. The discriminator loss function is defined as

$$L_D = -\sum_{q=1}^{C} \left[\log D\left(T_I^q\right) + \log\left(1 - D\left(S_{0.5I}^q\right)\right) \right].$$ (10)

The feature super-resolution supervisor extracts the high-resolution target feature T_I similar to the low-resolution input feature as the supervision signal for super-resolution model training, in order to enhance the stability of training and improve the quality of super-resolution. In order to avoid the inconsistency between the receptive fields of low-resolution features and high-resolution features, a feature extraction backbone-shared parameter network is designed to extract the qth feature $\mathbf{T}_I^q$ which is more suitable for training the super-resolution model without adding parameters.

2.3. UAV Tracking. Through the online recognition network, we can enhance the discriminative power of the classifier to distinguish the target from other interfering objects in the background, minimize the false detection rate, and complete the rough positioning of the target. We use the depth regression structure to construct the network structure, as shown in Figure 3, which uses two-layer convolution neural network:

$$f(x, w) = \varphi_2\{w_2 * \varphi_1(w_1 * x)\},$$ (11)

where x is the countermeasure network feature graph generated by feature super-resolution, w_1 and w_2 represent the weight of the convolution layer, $*$ is a convolution operation, and φ is the activation function. The loss function is defined as

$$L(w) = \sum_{j=1}^{m} \gamma_j \left\| f(x_j; w) - y_j \right\|^2 + \sum_{k} \lambda_k \|w_k\|^2,$$ (12)

where m is the total number of feature graph samples, γ_j is the learning weight, y_j is the regression classification confidence of every feature sample x_j, and λ_k is a regular term. Gauss–Newton algorithm is used to solve the problem.

We transform the target tracking task into a similarity measurement problem and take the first frame z and the candidate region x of subsequent frames as the input images of template branch and detection branch, respectively. Feature extraction network based on weight sharing $\varphi(.)$ maps to the feature space, and the metric function $f(z.x)$ is learnt to compare the similarity between the template image and the candidate area search image. Finally, return the response graph. In order to highlight the importance of different spaces, a spatial collaborative attention module is designed.

Channel attention models the dependencies between channels, learns the association between features from the semantic level, optimizes features, activates feature channels more related to the target, and removes redundant features. Suppose that the feature diagram extracted by MobileNetV2 network template branch and detection branch is $\varphi(z)$ and $\varphi(x)$. A typical MobileNetV2 network template is shown in Figure 4. The global information of each channel is obtained by global average pooling and condensing spatial dimensions to provide salient target features. Input the results to the input layer, hidden layer, and output layer. We reduce the number of channels in the hidden layer to 1/16 of the input layer. Output channel attention weight $A_c\{\varphi(z)\}$ and $A_c\{\varphi(x)\}$. Finally, the channel attention feature graph is
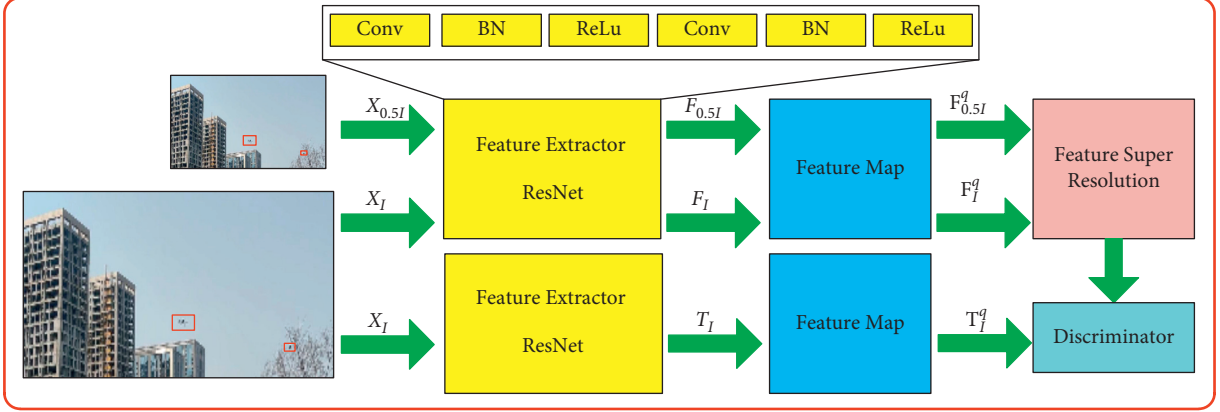
Figure 2: Feature super-resolution countermeasure GAN.

obtained by point multiplication with the input feature $\varphi_c(z)$ and $\varphi_c(x)$.

In the collaborative attention module, each branch code is integrated into another branch to make full use of the background information. In order to facilitate matrix multiplication with features, the output collaborative attention weight $A\{\varphi(x)\}$ and $A\{\varphi(z)\}$. After passing through the channel attention and collaborative attention modules, the weights of the two branches are fused to obtain $\varphi'(z)$ and $\varphi'(x)$.

Spatial attention focus is used to describe the position, which can construct the relationship between different positions in the feature graph, and supplement the channel attention through position weighted fusion. Feature graph $\varphi'(.)$ compresses along the channel dimension to obtain the spatial attention weight $As(.)$ and then obtains the final attention feature graph.

The feature graphs of each layer output by template branch and detection branch in the network are normalized by adjusting the convolution operation of layers, in order to make the feature graph with uniform resolution and the same number of channels.

Let the qth layer adjusted feature graph of classified branch input be $\varphi_{cls}^q(z)$ and $\varphi_{cls}^q(x)$. The adjusted feature diagrams of the qth layer of regression branch input are $\varphi_{reg}^q(z)$ and $\varphi_{reg}^q(z)$. Finally, the output is weighted and fused:

$$\begin{cases} A_{cls}^q = \varphi_{cls}^q(x) * \varphi_{cls}^q(z), \\ A_{reg}^q = \varphi_{reg}^q(x) * \varphi_{reg}^q(z). \end{cases} \quad (13)$$

When classifying the foreground or background of each candidate area, the same target may exist in multiple overlapping rectangular boxes at the same time, so non-maximum suppression (NMS) is used for elimination to accurately track the target.

3. Experiment and Result Analysis

The experimental data include 20 groups of UAV visible light data from far to near, as shown in Figure 5, with an image resolution of 1024×1024.

Based on the network structure, the image is normalized to 512×512 in order to ensure that small targets are not lost. On Win10 operating system with Intel ® Core ™ I5-6500 CPU, 3.20ghz system, the proposed program is run by 8 frames/s, which cannot meet practical requirement. However, due to the continuity of the target, the images can be processed at an interval of 1 frame, which can achieve near real-time operation speed.

3.1. ROI Extraction Algorithm Performance. We introduce the following indicators to measure the algorithm performance [26], as shown in Table 1:

$$\begin{cases} SEN = \dfrac{TP}{TP + FN}, \\[2mm] SPE = \dfrac{TN}{TN + FP}, \\[2mm] ACC = \dfrac{TP + TN}{TP + FP + TN + FN}, \\[2mm] FPF = 1 - ACC, \end{cases} \quad (14)$$

where SEN reflects the detection performance of the algorithm for real targets, SPE reflects the detection performance of the algorithm for false targets, ACC reflects the ratio of correct test results to all samples in the test results, and FPF reflects the ratio of false test results diagnosed as true targets.

The experimental results are shown in Table 2. The color model built in [8] has a good detection effect on UAVs with close range and obvious color characteristics. However, for long-distance UAVs, it is difficult to obtain color information and results in poor effect. Based on the target composition structure, Zhou et al. [14] construct the model through texture features, which is more stable than the color model, and the effect is significantly improved. However, for specific UAVs, the detection rate is limited. Zhang et al. [19] construct a deep learning network based on the deep reinforcement learning (DRL) model to realize ROI detection. It is the current mainstream target detection algorithm, and the effect and performance are further improved. However,
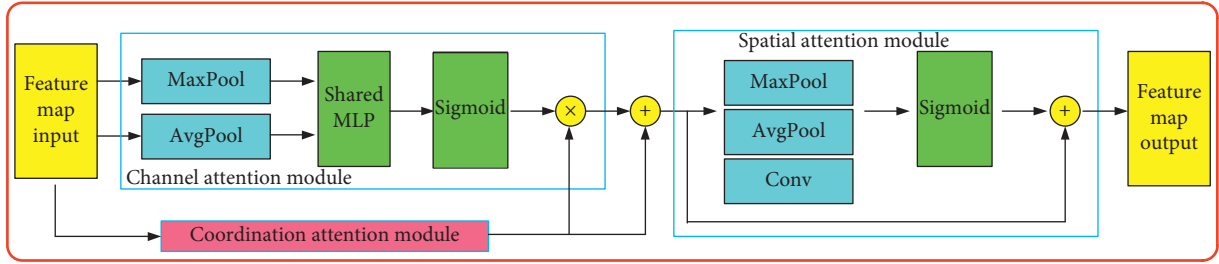
FIGURE 3: Spatial collaborative attention module.
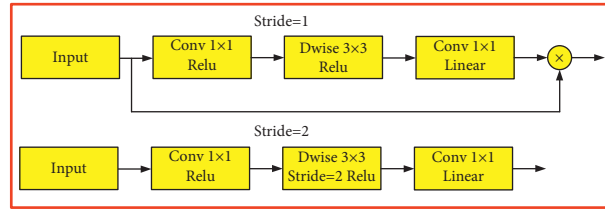
FIGURE 4: Convolution module block diagram.
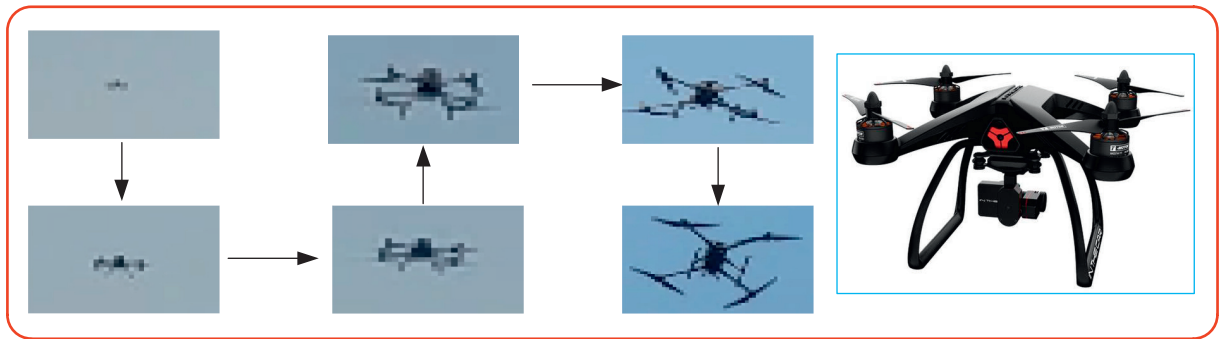
FIGURE 5: UAV data.

TABLE 1: Test result indicators.

TP (True positive)	FP (False positive)
FN (False negative)	TN (True negative)

TABLE 2: Detection effect.

Algorithm	SEN	SPE	ACC	FPF
Color	73	21	76	24
Texture	82	20	86	14
DRL	88	12	90	10
SR	91	9	92	8
SR + UR	93	5	95	5

this process needs to traverse the global image, and the computational cost is high and cannot meet the detection of targets with different scales. Our proposed algorithm introduces saliency region (SR) and focuses on the region of interest step by step. It conforms to the principle of visual perception and uses a priori knowledge to extract ROI. ACC has reached 95. For areas with too small area, there is still a risk of missing detection. On the basis of SR super-resolution module is added to establish the relationship between low-resolution and high-resolution target features, which further improves the detection of small targets.

3.2. UAV Tracking Algorithm Performance. We introduce the tracking success rate curve to intuitively show the algorithm performance, as shown in Figure 6. For short-range UAV tracking, all algorithms have achieved good results because of the high-resolution of the target displayed on the image. With the increase of distance, the performance of the

algorithm decreases. Kalman filter algorithm is the most obvious. Because the size of the target changes greatly in the image, the tracking is easy to be affected by the surrounding environment. According to the difference between UAV and background characteristics, fuzzy set constructs a segmentation algorithm to realize target tracking and has certain robustness to target size. Due to the UAV flying at low speed and uniform speed, the model updating is stable, and all algorithms have good tracking effect. However, in the face of turning flight or sudden acceleration or deceleration, Kalman filter and fuzzy set algorithm will not track due to the limitation of model updating speed. Augmented memory for correlation filters has achieved good results in analyzing short-time flight states. In depth network, UAV information

(a)

(b)

(c)

(d)

(e)
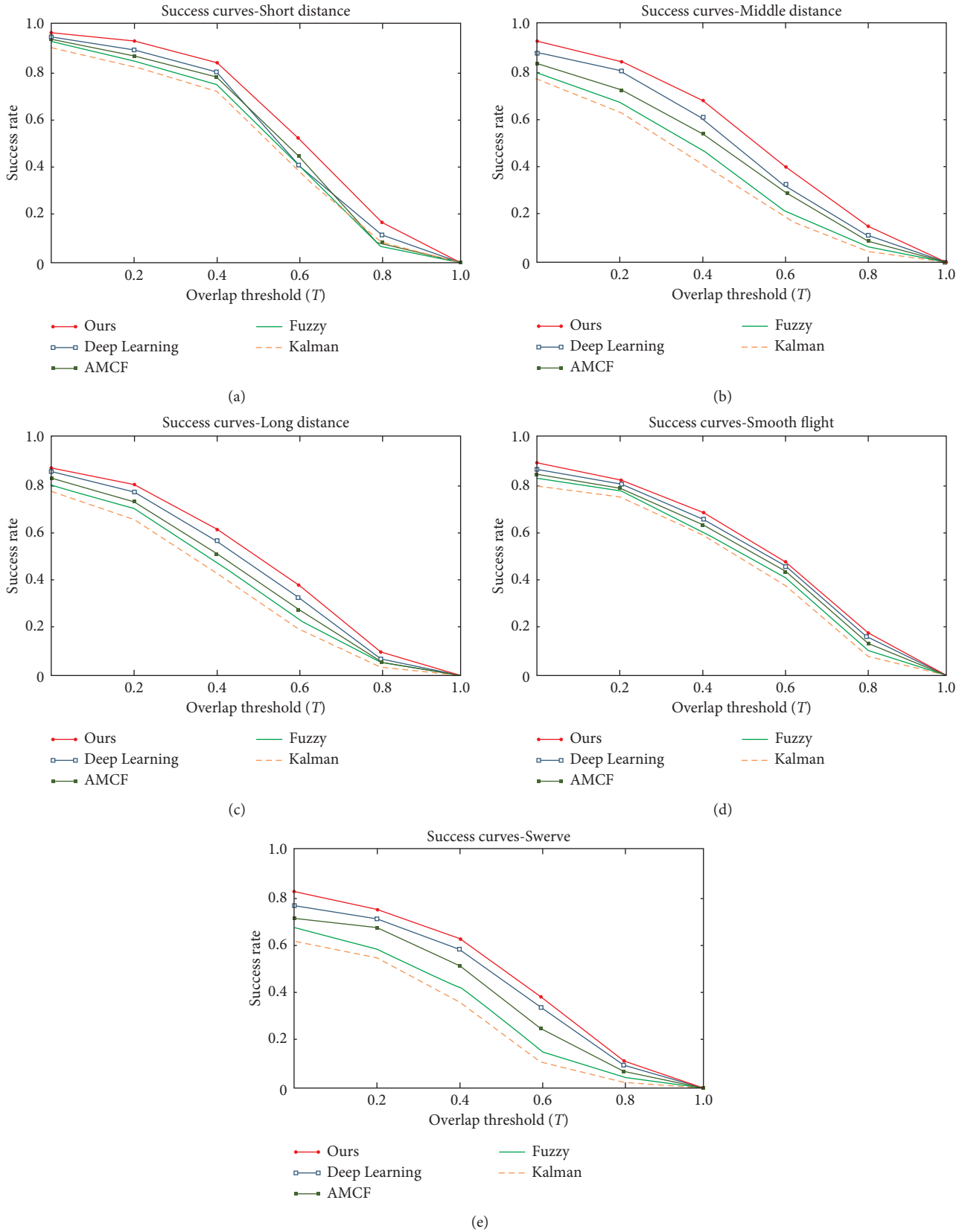
FIGURE 6: Successful ratio curves of different algorithms.

is obtained through a large number of training samples to build the model, but the time dimension information is not used, resulting in some limitations of the algorithm. However, the proposed algorithm introduces the spatial collaborative attention module to focus the target hierarchically to achieve target tracking, which decreases slowly, and the performance is better than other algorithms.

4. Conclusion

Aiming at the difficulty of visual detection and tracking of long-distance UAV, a complete set of weak and small UAV detection process is proposed from the perspective of visual cognition. The ROI area is focused step by step to establish and generate the GAN according to the idea of image super-resolution. The target details are restored to highlight the characteristics of weak targets, and a collaborative attention module is built to identify and track UAVs. The algorithm can be applied to fixed cameras, and the region of UAV can be further determined by the difference between frames. However, the proposed algorithm can also be applied to mobile cameras to focus the UAV area according to the saliency area. It can provide a new idea for the detection and recognition of weak and small targets.

Data Availability

The data used to support the findings of this study are available from the corresponding author upon request.

Conflicts of Interest

The authors declare that they have no conflicts of interest.

Acknowledgments

References

[1] C. Fu, F. Ding, Y. Li, J. Jin, and C. Feng, "DR 2 track: towards real-time visual tracking for UAV via distractor repressed dynamic regression," in *Proceedings of the 2020 IEEE/RSJ International Conference on Intelligent Robots and Systems (IROS)*, pp. 1597–1604, IEEE, Las Vegas, NV, USA, October 2020.

[2] A. Ibrahim, P. Ching, G. Seet, W. Lau, and W. Czajewski, "Moving objects detection and tracking framework for UAV-based surveillance," in *Proceedings of the 2010 Fourth Pacific-Rim Symposium on Image and Video Technology*, pp. 456–461, IEEE, Singapore, November 2010.

[3] Q. Zhou, Y. Zhang, Y. Qu, and C. Rabbath, "Dead reckoning and kalman filter design for trajectory tracking of a quadrotor UAV," in *Proceedings of the 2010 IEEE/ASME International Conference on Mechatronic and Embedded Systems and Applications*, pp. 119–124, IEEE, QingDao, China, July 2010.

[4] D. Nodland, H. Zargarzadeh, and S. Jagannathan, "Neural network-based optimal control for trajectory tracking of a helicopter UAV," in *Proceedings of the 2011 50th IEEE Conference on Decision and Control and European Control Conference*, pp. 3876–3881, IEEE, Orlando, FL, USA, December 2011.

[5] W. Liu, "A UAV route tracking algorithm based on the previewing point and fuzzy PID control," in *Proceedings of the 30th Chinese Control Conference*, pp. 2835–2839, IEEE, Yantai, China, July 2011.

[6] S. Ragi and E. Chong, "Dynamic UAV path planning for multitarget tracking," in *Proceedings of the 2012 American Control Conference (ACC)*, pp. 3845–3850, IEEE, Montreal, QC, Canada, June 2012.

[7] M.-G. Yoo and S.-K. Hong, "Target tracking control of a quadrotor UAV using vision sensor," *Journal of the Korean Society for Aeronautical & Space Sciences*, vol. 40, no. 2, pp. 118–128, 2012.

[8] H. H. A. Kadouf and Y. M. Mustafah, "Colour-based object detection and tracking for autonomous quadrotor UAV," *IOP Conference Series: Materials Science and Engineering*, vol. 53, no. 1, Article ID 012086, 2013.

[9] Y. Yu, X. Ding, and J. J. Zhu, "Attitude tracking control of a quadrotor UAV in the exponential coordinates," *Journal of the Franklin Institute*, vol. 350, no. 8, pp. 2044–2068, 2013.

[10] C. Teuliere, E. Marchand, and L. Eck, "3-D model-based tracking for UAV indoor localization," *IEEE Transactions on Cybernetics*, vol. 45, no. 5, pp. 869–879, 2014.

[11] H. Choi and Y. Kim, "UAV guidance using a monocular-vision sensor for aerial target tracking," *Control Engineering Practice*, vol. 22, pp. 10–19, 2014.

[12] S. Quintero, D. Copp, and J. Hespanha, "Robust UAV co-ordination for target tracking using output-feedback model predictive control with moving horizon estimation," in *Proceedings of the 2015 American Control Conference (ACC)*, pp. 3758–3764, IEEE, Chicago, IL, USA, July 2015.

[13] N. Santos, V. Lobo, and A. Bernardino, "A ground-based vision system for uav tracking," in *Proceedings of the OCEANS 2015-Genova*, pp. 1–9, IEEE, Genova, Italy, May 2015.

[14] C. Zhou, Y. Liu, and Y. Song, "Detection and tracking of a UAV via hough transform," in *Proceedings of the 2016 CIE International Conference on Radar (RADAR)*, pp. 1–4, IEEE, Guangzhou, China, October 2016.

[15] A. Vetrella, G. Fasano, D. Accardo, and A. Moccia, "Differential GNSS and vision-based tracking to improve navigation performance in cooperative multi-UAV systems," *Sensors*, vol. 16, no. 12, p. 2164, 2016.

[16] M. Elloumi, B. Escrig, R. Dhaou, and H. Idoudi, "Saidane Designing an energy efficient UAV tracking algorithm," in *Proceedings of the 2017 13th International Wireless Communications and Mobile Computing Conference (IWCMC)*, pp. 127–132, IEEE, Valencia, Spain, June 2017.

[17] C. Greatwood, L. Bose, T. Richardson et al., "Tracking control of a UAV with a parallel visual processor," in *Proceedings of the 2017 IEEE/RSJ International Conference on Intelligent Robots and Systems (IROS)*, pp. 4248–4254, IEEE, Vancouver, BC, Canada, September 2017.

[18] N. Santos, V. Lobo, and A. Bernardino, "3d model-based estimation for uav tracking," in *Proceedings of the OCEANS 2018 MTS/IEEE Charleston*, pp. 1–9, IEEE, Charleston, SC, USA, October 2018.

[19] W. Zhang, K. Song, X. Rong, and Y. Li, "Coarse-to-fine uav target tracking with deep reinforcement learning," *IEEE*

Transactions on Automation Science and Engineering, vol. 16, no. 4, pp. 1522–1530, 2018.

[20] Z. Huang, C. Fu, Y. Li, F. Lin, and P. Lu, "Learning aberrance repressed correlation filters for real-time uav tracking," in *Proceedings of the IEEE/CVF International Conference on Computer Vision*, pp. 2891–2900, Seoul, Republic of Korea, November 2019.

[21] M. Rabah, A. Rohan, S. A. S. Mohamed, and S.-H. Kim, "Autonomous moving target-tracking for a UAV quadcopter based on fuzzy-PI," *IEEE Access*, vol. 7, pp. 38407–38419, 2019.

[22] Y. Kokunko and S. Krasnova, "Synthesis of a tracking system with restrictions on UAV state variables," *Mathematics in Engineering, Science & Aerospace (MESA)*, vol. 10, no. 4, 2019.

[23] Y. Li, C. Fu, F. Ding, Z. Huang, and J. Pan, "Augmented memory for correlation filters in real-time uav tracking," in *Proceedings of the 2020 IEEE/RSJ International Conference on Intelligent Robots and Systems (IROS)*, pp. 1559–1566, IEEE, Las Vegas, NV, USA, October 2020.

[24] Y. Li, C. Fu, Z. Huang, Y. Zhang, and J. Pan, "Intermittent contextual learning for keyfilter-aware uav object tracking using deep convolutional feature," *IEEE Transactions on Multimedia*, vol. 23, pp. 810–822, 2020.

[25] J. Moon, S. Papaioannou, C. Laoudias, P. Kolios, and S. Kim, "Deep reinforcement learning multi-UAV trajectory control for target tracking," *IEEE Internet of Things Journal*, vol. 8, no. 20, 2021.

[26] S. Qiu, J. Luo, S. Yang, M. Zhang, and W. Zhang, "A moving target extraction algorithm based on the fusion of infrared and visible images," *Infrared Physics & Technology*, vol. 98, pp. 285–291, 2019.

WILEY | Hindawi

Research Article

Priority-Based Hybrid MAC Protocol for VANET with UAV-Enabled Roadside Units

Xin Yang ⓘ**, Yaqi Mao** ⓘ**, Qian Xu** ⓘ**, and Ling Wang** ⓘ

School of Electronics and Information, Northwestern Polytechnical University, Xi'an 710072, China

Correspondence should be addressed to Xin Yang; xinyang@nwpu.edu.cn

Vehicular ad hoc networks (VANETs) connect vehicles with other network units through wireless communication, thus improving traffic efficiency and safety by interacting with traffic information in networks. Roadside unit (RSU) plays an important role in VANETs in connecting vehicles with the transportation centre. With the rapid development of unmanned aerial vehicles (UAV), UAV-enabled RSU (U-RSU) is an effective way to promote the performance of VANETs. In this paper, a novel medium access control (MAC) layer protocol named PHB-MAC is proposed based on the priority setting of transmitted messages. Firstly, the priority-based contention mechanism is presented to ensure the transmission efficiency of the safety message. Then, the proposed MAC protocol combining contention and adaptive scheduled scheme is described in detail. Finally, the numerical analysis and simulation results of PHB-MAC and other existing protocols are presented. It is revealed that the proposed protocol improves throughput by at least 30%. Meanwhile, it reduces packets drop rate and delay by 21% and 22%, respectively. Finally, the numerical analysis and simulation results are given to prove the advancement of the proposed protocol on throughput, packets drop rate (PDR), and delay.

1. Introduction

In recent years, the rapid increase of vehicles around the world has brought about more serious challenges to traffic safety and efficiency. With the rapid development of wireless communication, sensing, mobile computing, and automatic control technology, the vehicular ad hoc network (VANET) has emerged to enhance traffic safety and improve traffic efficiency [1]. VANET is a specific ad hoc network that is composed of many dynamic nodes without any centralized control equipment. In VANET, the vehicle communicates with other vehicles by onboard unit (OBU). Also, vehicles equipped with OBU can build a transmission link with roadside unit (RSU), which is fixed to the side of the road. RSU can communicate with OBUs in its transmission range, including relay and providing traffic information [2]. In this way, the vehicle obtains real-time status information of surrounding vehicles by VANET to avoid road accidents and enhance traffic safety. In addition, with the widespread application of unmanned

aerial vehicles (UAV) in the construction of smart cities, UAV-enabled RSU (U-RSU) is an important way to enhance the performance of VANET. Compared with fixed RSU, U-RSU has the advantages of flexibility, scalability, and connectivity. In addition, U-RSUs can provide effective help to fix RSUs in the case of serious traffic congestion. Unlike other fixed wireless networks, the nodes in VANET are fast-moving vehicles; the primary service of VANET is a safety service [3]. As a result, the key features and performance requirements of VANET are concluded as follows:

(i) The nodes in VANET show a high mobility characteristic.

(ii) The nodes in VANET are vehicles with communication capabilities; unlike traditional fixed wireless networks, they have the characteristics of high mobility as fast as 120 km/h, and the relative speed can achieve more than 200 km/h. Under the circumstances, the VANET needs to handle the

problem of fast and frequent network accessing and switching of vehicles [4].

(iii) The network topology changes frequently.

(iv) Because of the fast-moving of large numbers of vehicles, the topology of VANET changes frequently. In this way, the transmission links between nodes are unstable, which leads to a failed transmission and influences the reliability of networks. What is more, the design of medium access control (MAC) and routing protocol in VANET is more complicated than normal wireless networks [5].

(v) The quality of service (QoS) requirement of VANET is specific.

(vi) The main task of VANET is providing safety services to all vehicles and enhancing traffic safety. Therefore, low latency and packet drop rate (PDR) are both crucial performances to VANET. Besides, high throughput is another important requirement to maintain information transmission in networks. In this way, not only can data information be delivered efficiently, but also the safety message can be transmitted reliably [6].

In the last decade, various MAC protocols were proposed to improve the performance of VANET. In general, these protocols can be divided into three categories, which are contention-based protocols, contention-free protocols, and hybrid protocols, respectively. Contention-based protocols are mainly based on the ALOHA or carrier sense multiple access (CSMA) mechanism, in which there is no predetermined allocation of transmission resources [7]. If the channel is sensed as idle by a node, it accesses the channel and starts transmission directly. Otherwise, if the channel is busy, the node has to pick up a backoff value from the contention window (CW) and start a countdown. When the backoff value reaches 0, the transmission begins. If there is another collision, a larger backoff value is selected randomly. The circulation of backoff does not finish until the transmission is successfully completed. The IEEE 802.11p MAC protocol is a typical protocol based on the CSMA mechanism; like many other contention-based protocols, the QoS cannot meet the performance requirement in high-density VANET. Meanwhile, many contention-free MAC protocols are proposed to improve QoS and efficiency of VANET, especially in a high-density application scenario [8]. Network resources are scheduled in VANET before access and transmission. The main mechanism of the contention-free protocol is based on time division multiple access (TDMA), frequency division multiple access (FDMA), and some other multiple access methods. In this transmission scheme, each node has its own time slot or frequency band to access channel and transmit information [9]. However, when the transmission load of VANET is low, many nodes still occupy the time slots or frequency bands without transmission tasks. In this way, network resources are wasted and lead to a decline in efficiency. To make a tradeoff between contention-based and contention-free protocols, hybrid protocols have been proposed in recent years. The research of hybrid mechanisms focuses on the TDMA-CSMA hybrid protocol to enhance traffic safety and improve transmission efficiency. The difficulty and challenge of the hybrid protocol is how to design specific protocols according to different application scenarios [10]. What is more, the existing MAC protocols seldom make full use of both TDMA and CSMA period to meet the performance requirements in high-density and fast-moving VANET.

In this paper, a novel hybrid MAC protocol named PHB-MAC (priority-based hybrid MAC layer protocol) is proposed for VANET to enhance the transmission efficiency of data information and promote the reliability of safety message transmission. The main contributions of this paper are concluded as follows:

(i) The proposed hybrid protocol is based contending and scheduled hybrid mechanism. Nodes in networks reserve their own transmission slot by a priority-based grouping contention scheme in PHB-MAC. Then, according to the reserved time slots, nodes transmit data in their own slots to avoid contention.

(ii) In the proposed grouping contention scheme, nodes access channels by groups are employed instead of all nodes contending for access. In this way, both efficiency and access fairness are improved simultaneously. In addition, due to the priority setting of PHB-MAC, high-priority information is guaranteed to be timely delivered in its own groups.

(iii) In the adaptive TDMA-based period of the proposed protocol, time slots are allocated not only to transmission between OBUs and U-RSU but also to the information exchanges between adjacent U-RSUs. The trajectory of the vehicle is along the road and predictable, so it is efficient for a U-RSU to transmit information of vehicles in its transmission range to the next U-RSU with which the vehicle will communicate.

(iv) The performance of PHB-MAC on throughput, PDR, and delay is analyzed and simulated in this paper. Simulation results are presented to prove that the PHB-MAC can significantly promote the efficiency and traffic safety of VANET, especially in a high-density scenario.

The rest of this paper is organized as follows. Section 2 gives a brief review of MAC protocol design in VANETs. Next, Section 3 describes the proposed PHB-MAC protocol in detail. Section 4 presents a theoretical analysis of throughput, PDR, and delay of PHB-MAC. Then, the performance evaluation of PHB-MAC in VANET is presented in Section 5. Finally, Section 6 concludes the paper.

2. Related Works

Normally, MAC layer protocols for wireless networks are classified into three types based on access modes, namely, contention-based, contention-free, and hybrid, respectively.

Therefore, a brief and concise review of different types of MAC protocols is described in this section.

In contention-based MAC protocols, the IEEE 802.11p scheme is widely used in VANET, which is derived from IEEE 802.11 scheme and based on the carrier sense multiple access/collision avoidance (CSMA/CA) mechanism [11]. The channel division and modulation method are optimized for VANET in IEEE 802.11p. In CSMA/CA-based VANET, nodes in networks contend for transmission after a channel sensing period. As soon as the channel is sensed as idle, nodes start to access the channel after a distributed inter-frame spacing (DIFS). If the channel switches to busy and collision happens, the node turns to backoff and contends again after a contention window (CW). Each idle slot passes, and the CW counter is reduced by 1. When CW returns to 0, the transmission starts again. In addition, each time a collision happens, the CW increases. The CSMA/CA-based IEEE 802.11p protocol has the characteristics of easy implementation and distribution without a central control node. However, its performance seriously deteriorates in high-density networks. What is more, the safety service of VANET cannot be guaranteed in IEEE 802.11p protocol. A vehicle-to-vehicle protocol named EDF-CSMA is proposed based on IEEE 802.11p to guarantee the QoS of the networks [12]. EDF-CSMA dynamically adjusts the priority of real-time streaming to avoid collision and introduces an admission control policy according to time constraints to provide guaranteed QoS in multichannel environments. But there is still the problem of heavy collisions in high-density VANET when nodes enter and leave the network frequently. In addition, a mobile edge computing- (MEC-) based CSMA mechanism MAC protocol is proposed to promote the performance of VANET [13]. The MEC-based protocol analyzes the average uplink local delay of a vehicle driving on a highway for sending a packet to its serving edge node along the highway. This MEC-based protocol focuses on transmission delay; however, special requirements for safety services are not taken into account.

Also, many contention-free MAC protocols are designed based on a contention-free mechanism, especially on the TDMA scheme. In TDMA, time-domain resources are divided into successive frames. In each frame, nodes access and occupy one or more time slots for transmission as scheduled. TDMA can effectively reduce transmission collision in high-density VANET and enhance efficiency. However, as a scheduled protocol, it will lead to transmission resource waste if a node does not have data to transmit in its own time slot. A prediction-based TDMA MAC protocol named PTMAC is proposed to decrease the number of packet collisions [14]. It is demonstrated to be suitable for VANET in an urban area with unbalanced traffic densities. But in low-density VANET, the predication process can lead to more overhead and increase the delay, especially for safety message delivery. As a result, the QoS of VANET decreases. Meanwhile, another TDMA-based MAC protocol called MoMAC is proposed in [15]. In MoMAC accessing algorithm, the time slot resources are adaptively divided into many subsets according to the road topology. In addition, each node broadcasts safety messages together with the time slot occupying information of neighbors. It improves efficiency and reduces data collision in high-density VANET, but the collision of safety messages is still a problem to solve.

Hybrid MAC protocols combine the advantages of contention-based and contention-free protocols to improve the performance of VANET. A hybrid MAC protocol named HER-MAC is proposed in [16]. The control channel transmission is divided into reserved period and contention period. It allows nodes to transmit a safety message on the control channel and transmit a nonsafety message on the service channel during the interval of the control channel. In this way, the efficiency of transmission is improved. However, there are too many overhead packets that need to be transmitted in HER-MAC, which also increases the collision rate. To solve the problems above with HER-MAC, a hybrid TDMA/CSMA multichannel MAC protocol is presented [17]. It can also enhance broadcasting efficiency and improve the throughput of the control channel by removing unnecessary overhead packets. But the priority of safety message transmission cannot be guaranteed, thus affecting the QoS of VANET. Meanwhile, thanks to the rapid development of fourth-generation (4G) mobile communication technology, VMaSC-LTE is proposed, combining IEEE 802.11p-based multihop clustering and the 4G cellular mechanism [18]. VMaSC-LTE decreases the number of cluster heads and increases the stability of networks, therefore improving efficiency. The clustering algorithm in VMaSC-LTE is easily affected by the changes in node density in VANET, which leads to a waste of channel resources in low-density networks.

As a result, fully considering the application performance requirements of VANET with UAV-enabled RSU, the characteristics of hybrid MAC protocols, and the shortcomings of existing protocols, this study proposes a high efficiency contending and adaptive TDMA hybrid MAC protocol for VANET to improve throughput, delay, and PDR.

3. PHB-MAC Protocol Design

In this section, details of the proposed PHB-MAC protocol for VANET are described. The network under consideration consists of vehicles running two-way on the road. Vehicles are all equipped with OBUs, including global position system (GPS) receivers. Through the OBU, vehicles can communicate with U-RSUs.

3.1. Assumptions. Some assumptions are made for the proposed protocol in VANET as follows:

(1) Every vehicle is equipped with a GPS device and knows its own real-time state information, such as location, speed, and moving direction. This information is broadcast by OBUs at each frame of the group that it belongs to.

(2) The slot information of U-RSU is kept by all vehicles in its transmission range and its one-hop U-RSUs transmission range.
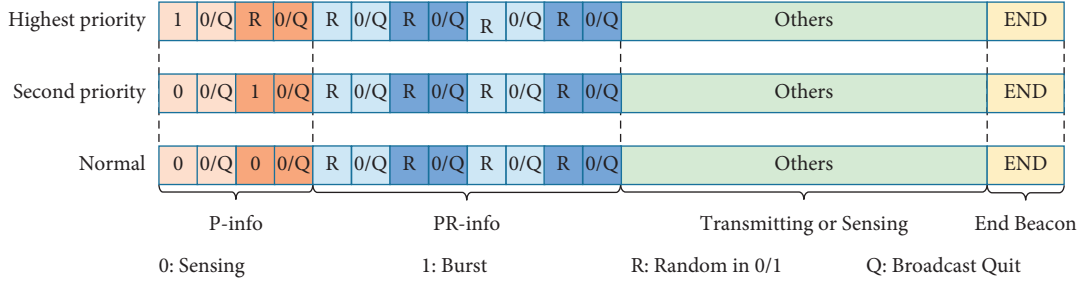
Figure 1: Designing different priority information transmission.

(3) For a newly joined vehicle, it needs to listen to the channel and wait until the next frame starts for its transmission.

(4) The road information, such as road length, traffic congestion, and the number of vehicles, is available for OBUs.

3.2. Message Priority Setting. Designing a transmission scheme according to the priorities of messages is a significantly effective way to enhance transmission performance and traffic safety in VANET. Therefore, it is necessary to set message priority before transmission. In the proposed protocol, transmitted messages are divided into three priorities. First and foremost, safety message is set as the highest priority since it is crucial for all vehicles to run safely. Then, control messages and some messages about important vehicle status information are defined as the second priority. Finally, other messages are set to normal priority. In addition, the ratio of different priority packets is set as $80:16:4$ (normal : second priority : highest priority), which is based on the 80/20 rule.

To ensure that high-priority messages are transmitted successfully, as described in Figure 1, priority information (P-info) and priority random information (PR-info) are set before the transmission period. For easy understanding, it is defined that 0 is denoted as sensing, 1 means burst transmission, R is randomly selected from 0 to 1, and Q means the OBU fails in contention and broadcast a Quit beacon. In the proposed protocol, each slot contains two parts in the contention period. The first part is used for contention; OBUs sent burst or keep silent and sense the channel randomly. In the second part, if the OBU fails in contention, it broadcasts a Quit beacon. Other OBUs keep the sense and listen to the beacon. In case an OBU does not sense anything in the second parts of the slot, it wins contention.

As the rules above, to make sure the highest priority message is transmitted as soon as possible, it is defined that the first slot in P-info of the highest priority is $1-0/Q$. At the same time, if there are some other OBUs that want to transmit a second priority or normal message, they will sense the burst transmission of the highest priority message in the first slot. So, they quit the contention and sense the channel for the next transmitting opportunity. In this way, the highest priority message can be sure to win the contention. Furthermore, if there is no highest priority message to transmit in the first slot, all OBUs sense the channel. Then,

the OBU, which wants to transmit a second priority message, starts a burst in the second slot. Other OBUs that want to send a normal message sense the burst and quit the contention. Otherwise, if all the messages to be sent are normal, the OBUs start the PR-info period to contend for transmitting. Finally, the OBU that wins the contention begins transmitting data to U-RSU in the transmitting period; other OBUs sense the channel until they receive the END beacon and start the next cycle. In addition, the number of slots in the PR-info period is not a constant quantity. It adapts to the degree of traffic congestion and updates every cycle. To describe the message transmission scheme more clearly, the message priority setting and contention processing are presented in Figure 2.

For example, in Figure 3, four OBUs contending to transmit normal messages are described to show the contention process in the same priority. In the P-info period, all of them sense the channel to verify whether there is any higher priority message need to be transmitted. Then, in the PR-info period, every OBU generates a set of random numbers in 0/1 to fill the first part in each slot. The second part of each slot is determined by the first part. In the first part, the random number is 0, and the OBUs switch to a sensing state. If it senses others' burst, which means it fails in contention, the OBU broadcasts Quit and quits the contention. Otherwise, it switches to a sense or burst state according to the corresponding number in the generated random sequence. In the illustration, it is assumed that the generated random sequence of OBU 2 is a 4-bit number 1110, which fills the first part in each slot. As a result, other OBUs failed in the contention because they all sense the burst transmission from OBU 2 and thus quit contention. Meanwhile, the 8-bit contending sequence of OBU 2 is acquired as 10101000. When OBU 2 finishes transmitting data, it broadcasts an END beacon. Then, OBU 4 senses the END beacon and starts transmitting. Generally, as the priority setting above in one contention group, if an OBU senses n Quit beacons in the quit and sensing period, it will begin its transmission period when the $(n+1)$th sensed END beacon finishes. In addition, the slot allocated to the contending sequence is adaptively adjusted to fit the traffic. For each priority level, a collision happens in the contending slot, which means the length of the contending slot is not enough. The U-RSU will increase the length of the next contending time slot by 1 in the corresponding priority level. On the contrary, if all OBUs finish contending with extra contending slots left, the U-RSU will reduce the length of the

FIGURE 2: Message priority setting and contention processing.

FIGURE 3: Group contending in OBU-to-OBU transmission.

next contending time slot by 1 in the corresponding priority level. Specifically, the variation range of the contending slot is confined to integers in $[1, CLx\text{-}m]$, where $CLx\text{-}m$ means the maximum value of CL (contending slot length). In this paper, the length of contending slot for highest priority, second priority, and normal is defined as positive integer CLh, CLs, and CLn, respectively, which are defined as $CLh\text{-}m \geq CLh \geq 1$, $CLs\text{-}m \geq CLs \geq 1$, and $CLn\text{-}m \geq CLn \geq 1$ in the protocol.

3.3. Frame Design of PHB-MAC. According to the proposed assumptions and the definition of message priority, the frame design of the proposed protocol is described in this section. To explain the protocol process more clearly, the general scenario of VANET is presented in Figure 4. Assume that all vehicles are equipped with OBUs and drive on the right side of the road.

U-RSUs are distributed along the road to communicate with OBUs in their transmission range. The distance between each two U-RSUs must be less than the maximum transmission distance of U-RSU. In addition, if an OBU is within the transmission range of two adjacent U-RSUs at the same time, it will select the closer U-RSU for transmission. In the proposed protocol, define that all OBUs communicating with U-RSU-A and U-RSU-B make up group A and group B, respectively. Other groups are defined in the same way. To reduce transmission collision, each group is divided into n subgroups for accessing and transmission separately. That is, the area covered by a group is divided into Ns equal parts; all vehicles in each part form a subgroup. For example, Figure 4 illustrates the subgroups distribution of group A and group B.

To describe the frame design of PHB-MAC in detail, the transmission of U-RSU-A, U-RSU-B, and OBUs in A1 and OBUs in B1 is illustrated in Figure 5 as a one-slot example.
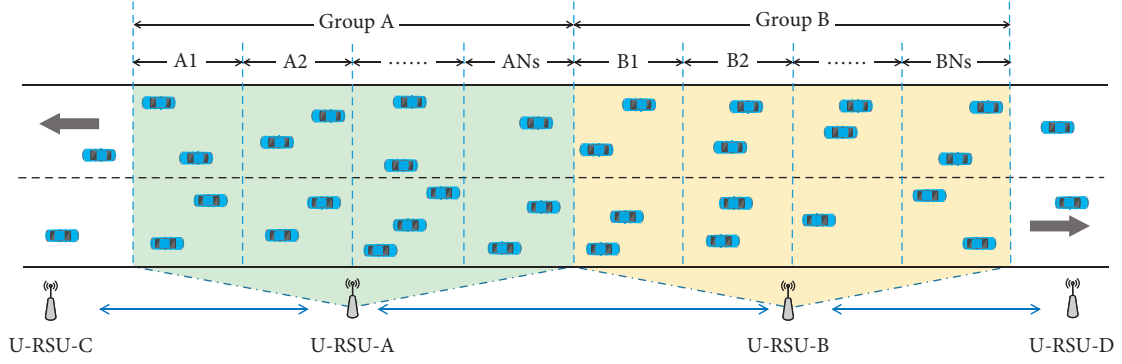
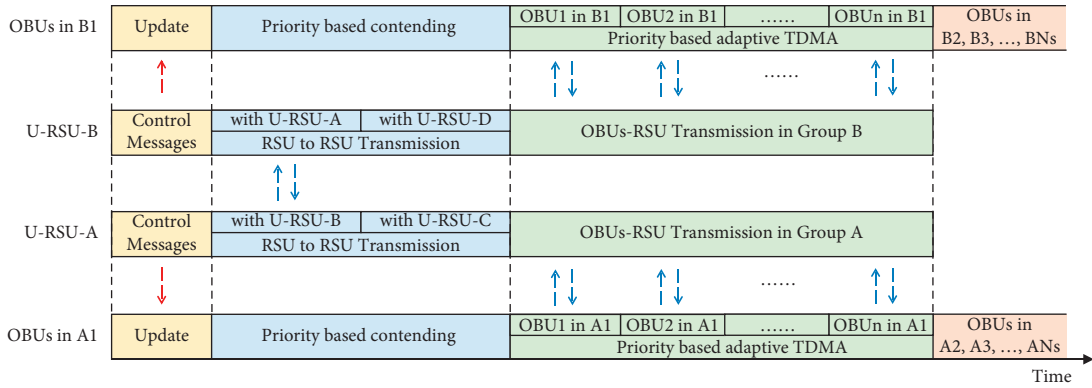FIGURE 4: General scenario of VANET and subgroups distribution.

FIGURE 5: Example of transmission using PHB-MAC.

When the slot begins, RSU-A and U-RSU-B broadcast control messages to OBUs in A1 and B1, respectively. According to the control message, OBUs know when and what states they will switch to in this slot. Meanwhile, OBUs update their own state information as soon as receiving the control message. The next is the priority-based contending period; OBUs in a subgroup A1 or B1 contend based on the priority of messages to reserve transmission in the adaptive TDMA period. The detailed process of the priority-based contending period is shown in Figure 3. At the same time, to take full use of the time slot, U-RSU-A and U-RSU-B both communicate with their adjacent U-RSUs. In this way, key information on road conditions and vehicles is timely transmitted between two groups. The length of time slot for RSU-to-RSU transmission is set equal to the priority-based contending period, in which the transmitting time spent on left U-RSU and right U-RSU is half and half. Then comes to OBUs-RSU transmission period of each group, which follows the priority-based adaptive TDMA scheme in Figure 3. Specifically, in the transmission period between OBUs in A1 and U-RSU-A, all OBUs in A1 communicate with U-RSU-A in their own time slot as the scheduled order of priority-based contending period. When the last OBU finishes communication with U-RSU and broadcasts the END beacon, the mission of the current subgroup is over. The next OBU subgroups start transmission tasks by receiving control messages from U-RSU and updating their own state

information. Then, the process is repeated again as the previous subgroup.

4. Performance Analysis

Based on the assumptions and descriptions of the proposed protocol above, the performance analysis is presented in this section by establishing a Markov model, as shown in Figure 6. The symbols used in the analysis of the proposed protocol are summarized in Table 1.

In the analysis of the proposed protocol, P_c denotes the collision probability of the transmission, P_s is the success probability of packet transmission, P_{tr} denotes the probability that there is a packet to be sent, and the maximum contending slot length of x priority message in the ith slot is defined as CL_{x-mi}, where x represents a kind of message among highest, second, or normal priority. Therefore, the one-step transmission probabilities and steady-state probabilities of the Markov model are calculated as follows:

$$P\{i,k|i,k\} = 1 - P_c, \quad \left(1 \leq k \leq CL_{n-mi}, 1 \leq i \leq n\right), \quad (1)$$

$$P\{i,k+1|i,k\} = P_c, \quad \left(1 \leq k \leq CL_{n-mi}, 1 \leq i \leq n\right), \quad (2)$$

$$P\{i,k|i-1,k\} = \frac{1-P_s}{CL_{x-mn}}, \quad \left(1 \leq k \leq CL_{x-mi}, 1 \leq i \leq n\right), \quad (3)$$
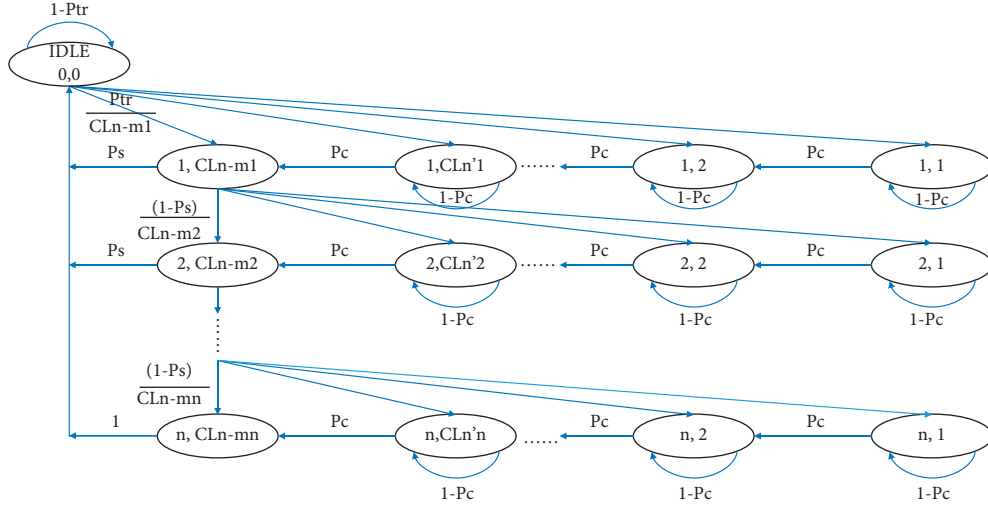
FIGURE 6: Markov model for PHB-MAC protocol.

TABLE 1: Symbols summary for model analysis.

Parameters	Description
N	The number of time slots in priority-based adaptive TDMA period.
P_c	The collision probability of transmission.
P_s	The success probability of packet transmission.
P_{tr}	The probability that there is a packet to be sent.
P_{bus}	The probability that the channel is busy.
τ_{pac}	The probability that a node transmits a data packet in an arbitrary time slot.
N_{cont}	The number of nodes contending for transmission simultaneously.
CL_{x-mi}	The maximum contending slot length of x priority message in the ith slot (x = highest/second/normal).
T_{OBU-h}	The time cost on highest priority message transmission of OBU.
T_{OBU-s}	The time cost on second priority message transmission of OBU.
T_{OBU-n}	The time cost on normal message transmission of OBU.
T_{ctrl}	The time cost on control message transmission.
T_{contx}	The time cost on contending of x priority information.
T_{pac-x}	The time cost on packet transmission of an x priority message.
T_{re-x}	The time cost on retransmission of an x priority message.
S_{Total}	The total throughput of the networks.
S_{RR}	The throughput of RSU-RSU transmission.
S_{OR}	The throughput of OBU-RSU transmission.

$$P\{0, 0|i, CL_{x-mi}\} = \begin{cases} P_s, & (1 \leq k \leq CL_{x-mi}, \quad 1 \leq i \leq n-1), \\ 1, & (1 \leq k \leq CL_{x-mi}, \quad i = n), \end{cases}$$

(4)

$$P\{1, k|0, 0\} = \frac{P_{tr}}{CL_{x-m1}}, \quad (1 \leq k \leq CL_{x-m1}),$$ (5)

$$P\{1, k|i, CL_{x-mi}\} = \begin{cases} \dfrac{P_s P_{tr}}{CL_{x-m1}}, & (1 \leq k \leq CL_{x-m1}, \quad 1 \leq i \leq n-1), \\[3mm] \dfrac{P_{tr}}{CL_{x-m1}}, & (1 \leq k \leq CL_{x-m1}, \quad i = n). \end{cases}$$

(6)

It can be obtained by equations (1)–(5) that

(i) When a message arrives at an idle node, it starts to transmit with a random CL in the first slot. Otherwise, the node continues to remain at an idle state.

(ii) Every time there is a transmission collision, k increases by 1 until it reaches the maximum value CL_{x-mn}.

(iii) If the message is successfully transmitted or reaches its maximum retransmission CL_{x-mi} in all n time slots, the node will reset the CL value and turn to an idle state.

(iv) When a message is not successfully transmitted in the first contending time slot, it will continue to be transmitted in the next slot with a random value of CL.

Let $b_{i,k}$ denote the stationary state probability of the state $\{i, k\}$. Based on the model, the probability that a node transmits a data packet in an arbitrary time slot is represented as

$$\tau_{\text{pac}} = \frac{1 - (1 - P_s)^n}{P_{\text{tr}}} b_{1,\text{CL}x-m1}. \tag{7}$$

Therefore, the busy probability of the channel can be obtained as

$$P_{\text{bus}} = 1 - (1 - \tau_{\text{pac}})^{N_{\text{cont}}}, \tag{8}$$

where N_{cont} means the number of nodes, which are contending for transmission simultaneously. From (7), the collision probability of the transmission is derived as

$$P_c = 1 - N_{\text{cont}}(1 - \tau_{\text{pck}})^{N_{\text{cont}}-1}. \tag{9}$$

Also, the success probability of packet transmission is expressed as

$$P_s = N_{\text{cont}}\tau_{\text{pac}}(1 - \tau_{\text{pac}})^{N_{\text{cont}}-1}. \tag{10}$$

Let T_{ctrl}, $T_{\text{cont}-x}$, $T_{\text{pac}-x}$, and $T_{\text{re}-x}$ be the duration for control message transmission, the duration for contending of x priority message, the duration for packet transmission of x priority message, and the duration for retransmission of x priority message, where x is one of high priority, second priority, and normal priority. As a result, the time cost on the highest, second, and normal priority message transmission of OBU is given as

$$T_{\text{OBU}-h} = T_{\text{ctrl}} + T_{\text{cont}-h} + T_{\text{pac}-h} + T_{\text{re}-h},$$
$$T_{\text{OBU}-s} = T_{\text{ctrl}} + T_{\text{cont}-s} + T_{\text{pac}-s} + T_{\text{re}-s}, \tag{11}$$
$$T_{\text{OBU}-n} = T_{\text{ctrl}} + T_{\text{cont}-n} + T_{\text{pac}-n} + T_{\text{re}-n}.$$

In this paper, the throughput is defined as the ratio of the average transmitted payload length and the average duration in a slot time as follows:

$$S = \frac{E[\text{transmitted payload length in a slot time}]}{E[\text{duration of a slot time}]}. \tag{12}$$

Let S_{Total} be the total throughput of the networks, which can be computed by

$$S_{\text{Total}} = S_{\text{RR}} + S_{\text{OR}}, \tag{13}$$

where S_{RR} and S_{OR} are the throughput of RSU-RSU transmission and OBU-RSU transmission, respectively.

Let $L_{R_{K-1,K}}$ and $L_{R_{K,K+1}}$ be the length of the packet transmitted between two adjacent U-RSUs that is between the (K-1)th U-RSU and the Kth U-RSU, or the Kth U-RSU and the (K+1)th U-RSU. Hence, the throughput of RSU-RSU transmission is derived as

$$S_{\text{RR}} = \frac{L_{R_{K-1,K}} + L_{R_{K,K+1}}}{T_{R_{K-1,K}} + T_{R_{K,K+1}}} = \frac{L_{R_{K-1,K}} + L_{R_{K,K+1}}}{T_{\text{cont}K}}, \tag{14}$$

where $T_{R_{K-1,K}}$ and $T_{R_{K,K+1}}$ represent the duration for transmission between the (K-1)th U-RSU with the Kth U-RSU

and the Kth U-RSU with the (K+1)th U-RSU, respectively. In the proposed protocol, let $T_{\text{cont}K}$ be the duration for the contending period of the Kth U-RSU; we have $T_{R_{K-1,K}} + T_{R_{K,K+1}} = T_{\text{cont}K}$ to support the derivation of (14).

The throughput of OBU-RSU transmission is made up of the throughput of the three-priority information. Let S_{OhR}, S_{OsR}, and S_{OnR} represent the three-priority information, which are highest, second, and normal priority, respectively. Hence, the throughput of OBU-RSU is obtained as

$$S_{\text{OR}} = S_{\text{OhR}} + S_{\text{OsR}} + S_{\text{OnR}} = \frac{P_{\text{trh}}P_{\text{sh}}L_h + P_{\text{trs}}P_{\text{ss}}L_s + P_{\text{trn}}P_{\text{sn}}L_n}{T_{\text{ctrl}} + T_{\text{Tcont}} + T_{\text{Tpac}} + T_{\text{Tre}}}, \tag{15}$$

where T_{Tcont} means the total time of contending in OBU-RSU transmission.

Let P_{conth}, P_{conts}, and P_{contn} denote the contending probability of the highest, second, and normal priority information, respectively. So T_{Tcont} is given as

$$T_{\text{Tcont}} = P_{\text{conth}}T_{\text{conth}} + P_{\text{conts}}T_{\text{conts}} + P_{\text{contn}}T_{\text{contn}}. \tag{16}$$

Let PDR be the packet drop rate of the transmission, which means the probability that a packet will be dropped after the maximum retransmission limit. It is given as

$$\text{PDR} = (1 - P_s)^{M_{\text{mre}}}, \tag{17}$$

where M_{mre} is the maximum number of retransmissions for a packet.

In this paper, the delay is defined as the mean time spent on the successful transmission of information. If a packet is dropped, it can be regarded as an unsuccessful transmission. So, it will not be included in the evaluation of the transmission delay. As a result, the transmission delay is given as

$$\text{Delay} = E[T_{\text{succ}}] = (1 - P_{\text{tr}})T_{\text{slot}} + P_{tr}P_s(T_{\text{ctrl}} + T_{\text{Tpac}})$$
$$+ P_{\text{tr}}(1 - P_s)(T_{\text{Tcont}} + T_{\text{Tre}}), \tag{18}$$

where T_{succ} is the time spent on successful transmission of information and T_{Tpac} and T_{Tre} are the time spent on packet transmission and retransmission, respectively.

5. Simulation Results

In this section, the proposed protocol PHB-MAC is compared with other protocols such as CB-MAC and NC-PNC MAC in the simulation of MATLAB. The simulation scenario is a 2-kilometer long two-way straight road with a number of moving vehicles. The U-RSUs are evenly arranged on the roadside with an interval of 500 meters. The average speed of each vehicle is defined as 60 km/h, with a range of 50 km/s to 70 km/s. It is assumed that the data arrival follows Poisson distribution in the simulations of this paper. The distribution function of Poisson distribution is described as $P(X = k) = \lambda^k/k!e^{-\lambda}$, where k is the number of times that data arrived and $k = 0, 1, 2....$.

In 100 data packets of the simulations, we assume that there are 80 normal priority data packets, 16-second priority

data packets, and 4 highest priority data packets. To simulate the application scenarios of the VANET more realistically, the ratio of different priority packets we set conforms to the 80/20 rule. That is to say, 80 percent of the transmitted data packets belong to normal priority data packets. 80 percent of the remaining 20 percent are second priority data packets; others are highest priority data packets. The main parameters used in the simulations are summarized in Table 2.

Figure 7 presents that the throughput versus different numbers of vehicles varies from 10 to 150. It is easy to find that as the number of vehicles grows, the throughput decreases obviously. Specifically, in Figure 7(a), the proposed PHB-MAC is compared with CB-MAC and NC-PNC MAC in the simulation. The packets arrival rate is set at 100 packets/s. When the number of vehicles is less than 50, the throughput of all three protocols declined rapidly, but by similar values. As the number of vehicles is larger than 50 but less than 100, the throughput provided by CB-MAC is obviously less than the other two protocols. When the number of vehicles is larger than 100, PHB-MAC shows its advantage because the proposed contending and adaptive scheduled hybrid scheme can mitigate transmission collision. As there are 150 vehicles in the simulation, the proposed PHB-MAC can provide nearly 30% and 45% higher throughput than NC-PNC MAC and CB-MAC, respectively. In conclusion, PHB-MAC performs better than other protocols in the simulation, especially in dense networks.

Then, Figure 7(b) presents the simulation results of throughput versus the number of vehicles with different packets arrival rates. The packets with three different priorities (highest, second, and normal priority) accounted for 80%, 16%, and 4%, respectively. Obviously, a lower packet arrival rate leads to a higher throughput due to the fewer transmission collisions in the networks. When the number of vehicles is more than 50, the throughput of 20 packets/s is 2 to 4 times higher than others. However, high data arrival rates are of more concern in the practical application of VANET. In the simulation, we can find that as the data arrival rate increases from 100 packets/s to 500 packets/s, there is no serious drop in throughput (only 8%). That is, the throughput of the proposed protocol does not degrade significantly when the network load increases in a heavy traffic situation. When the number of vehicles continuously grows, the throughput of 100 packets/s and 500 packets/s maintains at nearly 5.1 Mbps and 4.6 Mbps, respectively. The main reason is that the priority-based adaptive TDMA scheme can relieve congestion effectively in heavy payload transmission.

In Figure 7(c), the throughput of safety messages versus the number of vehicles is simulated. The safety message is defined as the highest priority message in this paper, which has a close relationship with traffic safety. The throughput values of all protocols decrease with the increase of vehicles. However, PHB-MAC can mitigate throughput degradation due to its priority-based contending scheme. In this way, safety message transmission and traffic safety are guaranteed to the maximum extent. In contrast, the safety message throughput of NC-PNC MAC and CB-MAC reduces significantly as the vehicles increase. PHB-MAC improves

TABLE 2: Symbols summary in simulation.

Parameters	Value
Carrier frequency	2.4 GHz
Length of the normal priority data packet	1000 bytes
Length of the second priority data packet	200 bytes
Length of the highest priority data packet	50 bytes
Transmission range of OBU and U-RSU	500 m
Length of the control message	512 bits
Length of the END beacon	64 bits
Slot duration	50 ms
SIFS	10 us
DIFS	50 us

safety message throughput by almost 90% and 360% compared to the other two protocols.

Figure 8 shows the simulation results of PDR versus the number of vehicles. The PDR not only reflects the reliability of the protocols but also is an important performance indicator of the network. It can be observed that more vehicles on the road lead to a higher PDR because the transmission collision and congestion occur more frequently as vehicles increase. The PDR of different protocols is shown in Figure 8(a), with the packets arrival rate at 100 packets/s. When the number of vehicles is less than 40, there is little difference in the PDR provided by each protocol. This means that there is not much difference in the reliability among all protocols when the network is not heavily loaded. However, how to reduce the PDR under high transmission load is the concern of the VANET. As the simulation results show, compared with CB-MAC and NC-PNC MAC, when the number of vehicles is greater than 60, PHB-MAC can reduce the packet loss rate by almost 28% and 21%, respectively. In other words, the proposed protocol can reduce PDR effectively in heavy transmission scenarios.

To evaluate the reliability performance of PHB-MAC, the PDR versus the number of vehicles at different packets arrival rates is simulated. Obviously, the higher the data arrival rate, the higher the packet drop rate. When the data arrival rate is 20 packets/s and 100 packets/s, the PDR stays at a relatively low value (less than 20%) when the number of nodes is less than 80. As the number of vehicles increases, the value of PDR increases sharply and reaches 48% (20 packets/s) and 88% (100 packets/s) at 150 vehicles eventually. Meanwhile, with the data arrival rate coming to 500 packets/s, the PDR increases rapidly as the number of vehicles is more than 30. When there are 80 or more vehicles on the road in the simulation, the PDR reaches a relatively high level.

Also, the PDR versus the number of vehicles at safety message transmission is simulated by using different protocols. To provide a strong guarantee for traffic safety, the PDR of safety message is of great importance. On the whole, it is clear to find that the proposed PHB-MAC provides the best PDR among all of the protocols. To be specific, the values of PDR provided by all protocols are at the same level when there are no more than 50 vehicles in the networks. As the number of vehicles increases, the advantage of the proposed protocol on PDR becomes more and more
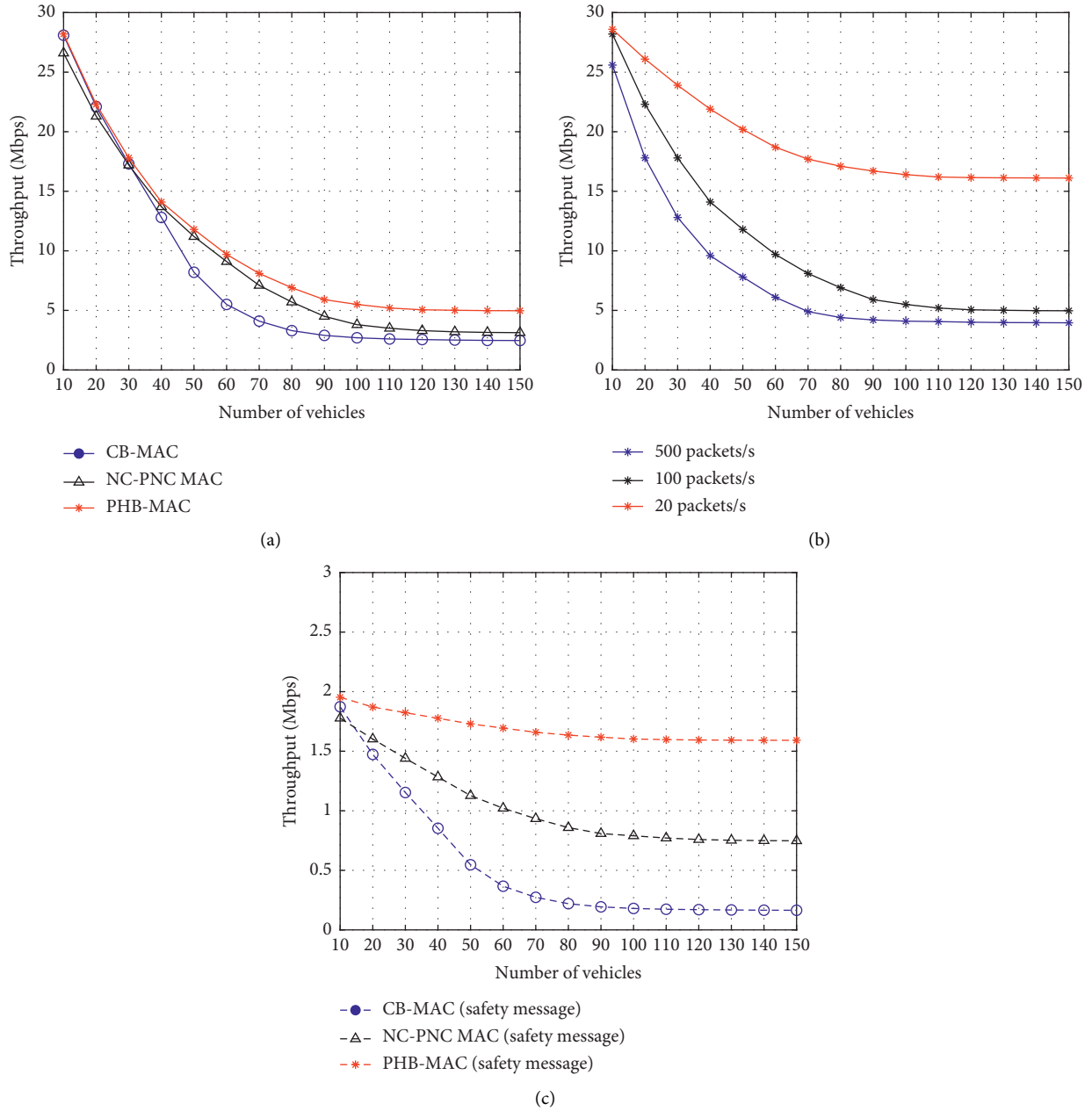
(a)

(b)

(c)

FIGURE 7: (a) Throughput versus the number of vehicles for different protocols. (b) Throughput versus the number of vehicles for different packets arrival rate. (c) Throughput versus the number of vehicles for safety message.

obvious. Compared to CB-MAC and NC-PNC MAC, PHB-MAC reduces the PDR by as much as 81% and 72%, respectively.

As a vital performance, the transmission delay of CB-MAC, NC-PNC MAC, and PHB-MAC is simulated with the results shown in Figure 9 9(a). The packets arrival rate is set at 100 packets/s in the simulation. For all of the protocols, heavier traffic leads to a higher transmission delay. The value of delay shows a swift growth when the number of vehicles is less than 70. Meanwhile, the delay basically remains unchanged when there are more than 100 vehicles in the networks. In particular, when the number of vehicles is less than 40, the three protocols can provide a similar delay

performance. However, with the increase of vehicles, PHB-MAC reveals its advantage because of the adaptive TDMA scheme. The time slot allocation for OBUs can be changed adaptively depending on traffic load to reduce the time cost of queuing and contending. In general, the proposed protocol can provide a 28% and 22% less delay than CB-MAC and NC-PNC MAC in the simulations, respectively.

Meanwhile, the delay of PHB-MAC is simulated under the condition of different packets arrival rates. Therefore, different packets arrival rates represent different traffic conditions. In heavy traffic situations, the frequent generation and forwarding of vehicle and road condition information result in a high packet arrival rate. The simulation
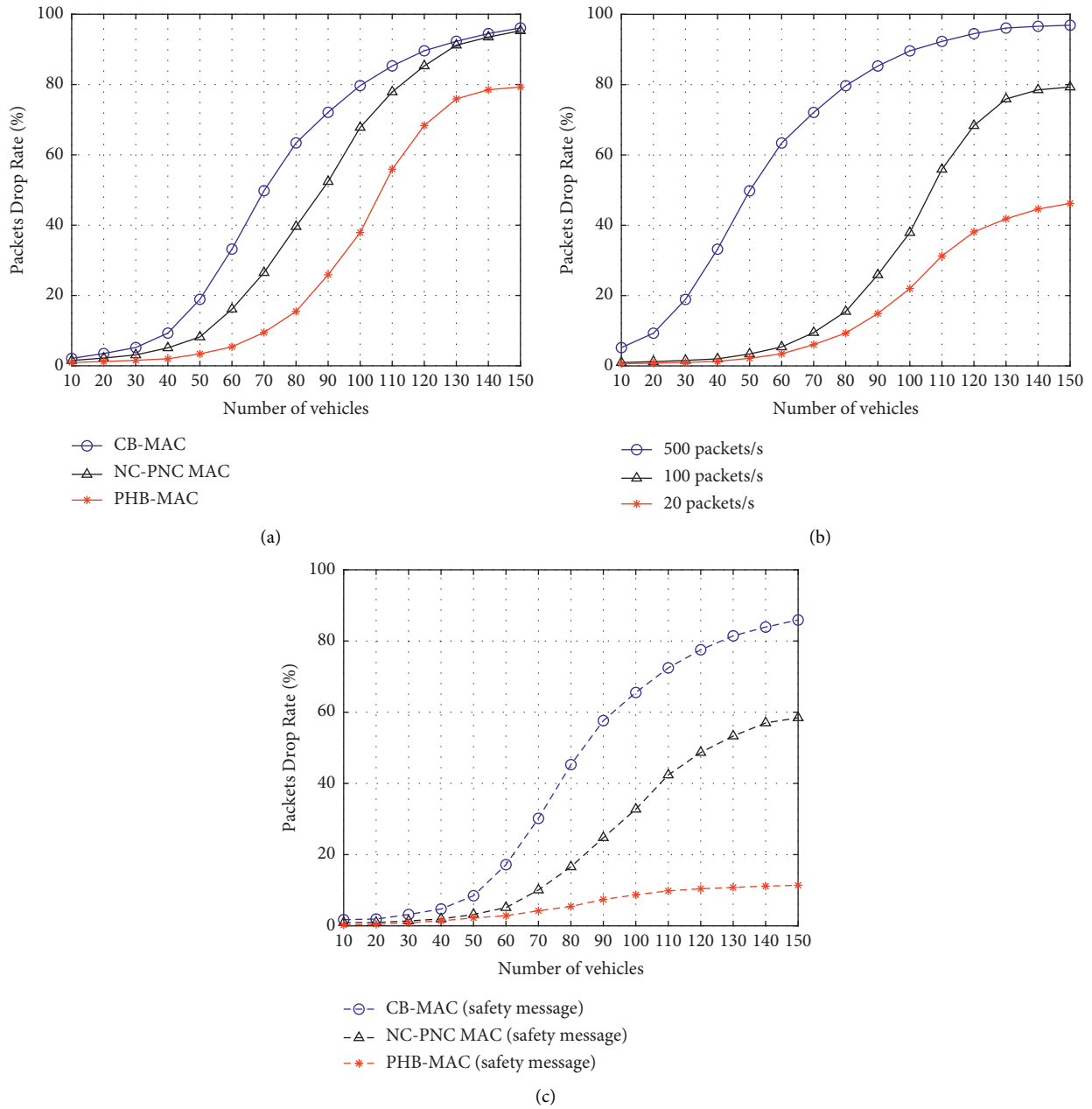
FIGURE 8: (a) PDR versus the number of vehicles for different protocols. (b) PDR versus the number of vehicles for different packets arrival rate. (c) PDR versus the number of vehicles for safety message.

results are shown in Figure 9(b). Obviously, a higher packets arrival rate leads to a significantly higher delay. Specifically, when there are 20 data packets arriving per second, the delay generally remains at a relatively low level. When there are 150 vehicles in the network, the maximum delay is still less than 20 ms. As the packets arrival rate increases to 100 packets/s, the delay shows significant growth and finally arrives at nearly 41 ms. In heavy traffic situations with 500 packets arriving per second, the delay rises rapidly when the number of vehicles is less than 50. However, PHB-MAC can effectively restrain the growth of delay on account of OBUs' subgrouping and adaptive TDMA scheme. The maximum delay arrives at nearly 68 ms, which is acceptable in VANET.

Finally, the safety message transmission delay of the three protocols is simulated, and the results are shown in Figure 9(c). In case there are no more than 50 vehicles in the networks, the delay provided by PHB-MAC and NC-PNC MAC is similar, whereas the delay of CB-MAC increases sharply with the increase of vehicles. When the number of vehicles is larger than 70, the delay of CB-MAC and PHB-MAC maintains steady. But the delay of NC-PNC MAC still grows rapidly. Compared with CB-MAC and NC-PNC MAC in large-scale VANET, PHB-MAC can reduce the delay by almost 38% and 29%, respectively. As a whole, PHB-MAC reveals a prominent advantage in the performance of delay compared to the other two protocols.
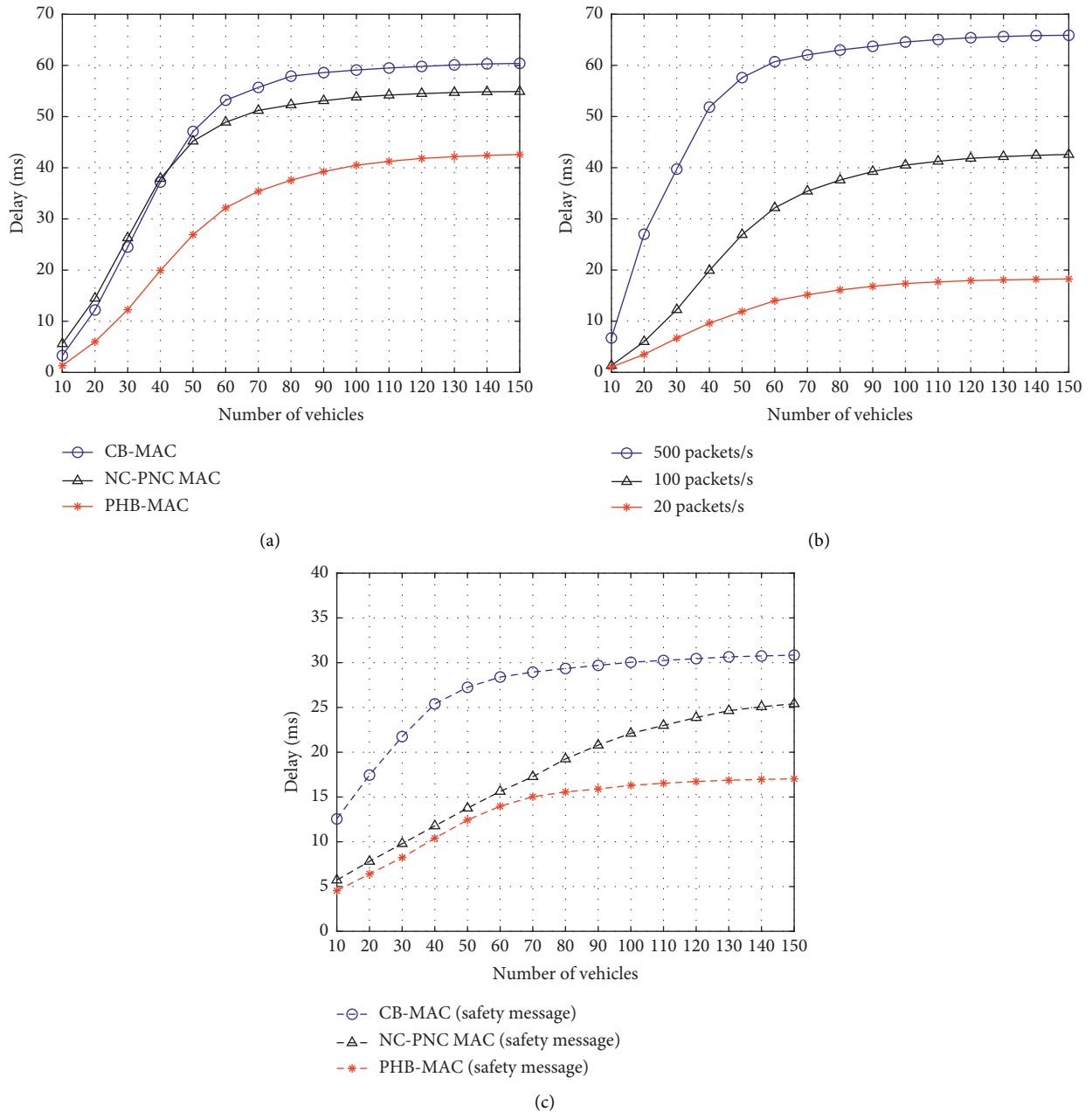
(a)

(b)

(c)

FIGURE 9: (a) Delay versus the number of vehicles for different protocols. (b) Delay versus the number of vehicles for different packets arrival rate. (c) Delay versus the number of vehicles for safety message.

6. Conclusions

In this paper, a hybrid MAC layer protocol based on information priority is proposed for enhancing the transmission performance of VANET with UAV-enabled RSU. In particular, the proposed PHB-MAC protocol significantly promotes the efficient and reliable transmission of the safety message. First of all, all transmitted messages are divided into three categories based on the message priority setting. The fundamental purpose is to ensure that the safety message can be efficiently transmitted, which is critical to traffic safety. Secondly, a hybrid MAC layer-accessing scheme including RSU-to-RSU and OBU-to-RSU transmission link is proposed. In the RSU-to-RSU transmission slot, OBUs in its U-RSU's range are contending based on priority. In addition, the results of the contention can make guidance for the design of the coming adaptive TDMA period. Thirdly, the performance of PHB-MAC on throughput, PDR, and delay is simulated. The simulation results illustrate the advantage of the proposed protocol in VANET, especially for safety message transmission.

Data Availability

The data used to support this study are included in the paper or available from the corresponding author upon request.

Conflicts of Interest

Acknowledgments

References

[1] M. Hadded, P. Muhlethaler, A. Laouiti, R. Zagrouba, and L. A. Saidane, "TDMA-based MAC protocols for vehicular ad hoc networks: a survey, qualitative analysis, and open research issues," *IEEE Communications Surveys & Tutorials*, vol. 17, no. 4, pp. 2461–2492, 2015,.

[2] A. U. Haq and K. Liu, "Review of TDMA-based MAC protocols for vehicular ad hoc networks," in *Proceedings of the IEEE 18th International Conference on Communication Technology (ICCT)*, pp. 459–467, Chongqing, China, October 2018.

[3] S. Ansari, M. Sanchez, T. Boutaleb, S. Sinanovic, C. Gamio, and I. Krikidis, "SAI: Safety application identifier algorithm at MAC layer for vehicular safety message dissemination over LTE VANET networks," *Wireless Communications and Mobile Computing*, vol. 2018, Article ID 6576287, 17 pages, 2018.

[4] L. Hu, Y. Xiao, and Z. Dai, "Beacon transmission rate allocation optimization under synchronized P-persistent repetition MAC protocol for platooning," *Wireless Communications and Mobile Computing*, vol. 2020, Article ID 8887134, 8 pages, 2020.

[5] M. Azizian, S. Cherkaoui, and A. S. Hafid, "A distributed cluster based transmission scheduling in VANET," in *Proceedings of the 2016 IEEE International Conference on Communications (ICC), 2016*, pp. 1–6, Kuala Lumpur, Malaysia, May 2016.

[6] V. Nguyen, O. T. T. Kim, C. Pham et al., "A survey on adaptive multi-channel MAC protocols in VANETs using Markov models," *IEEE Access*, vol. 6, pp. 16493–16514, 2018.

[7] Y. Bouchaala, P. Muhlethaler, O. Shagdar, and N. Achir, "Optimized spatial CSMA for VANETs: a comparative study using a simple stochastic model and simulation results," in *Proceedings of the 2017 14th IEEE Annual Consumer Communications & Networking Conference (CCNC)*, pp. 293–298, Las Vegas USA, January 2017.

[8] A. Bazzi, C. Campolo, B. M. Masini, A. Molinaro, A. Zanella, and A. O. Berthet, "Enhancing cooperative driving in IEEE 802.11 vehicular networks through full-duplex radios," *IEEE Transactions on Wireless Communications*, vol. 17, no. 4, pp. 2402–2416, 2018.

[9] A. T. Giang, A. Busson, A. Lambert, and D. Gruyer, "Spatial capacity of IEEE 802.11p-based VANET: models, simulations, and experimentations," *IEEE Transactions on Vehicular Technology*, vol. 65, no. 8, pp. 6454–6467, 2016.

[10] X. Cao, L. Liu, Y. Cheng, L. X. Cai, and C. Sun, "On optimal device-to-device resource allocation for minimizing end-to-end delay in VANETs," *IEEE Transactions on Vehicular Technology*, vol. 65, no. 10, pp. 7905–7916, 2016.

[11] I. W. Group: IEEE Standard for Information Technology–Telecommunications and Information Exchange Between Systems–Local and Metropolitan Area Networks–Specific Requirements–Part 11: Wireless LAN Medium Access Control (MAC) and Physical Layer (PHY) Specifications Amendment 6, pp. 1–2742, 2011.

[12] C.-Y. Chang, H.-C. Yen, and D.-J. Deng, "V2V QoS guaranteed channel access in IEEE 802.11p VANETs," *IEEE Transactions on Dependable and Secure Computing*, vol. 13, no. 1, pp. 5–17, 2016.

[13] Y. Wu and J. Zheng, "Modeling and analysis of the uplink local delay in MEC-based VANETs," *IEEE Transactions on Vehicular Technology*, vol. 69, no. 4, pp. 3538–3549, 2020.

[14] X. Jiang and D. H. C. Du, "PTMAC: a prediction-based TDMA MAC protocol for reducing packet collisions in VANET," *IEEE Transactions on Vehicular Technology*, vol. 65, no. 11, pp. 9209–9223, 2016.

[15] F. Lyu, H. Zhu, H. Zhou et al., "MoMAC: mobility-aware and collision-avoidance MAC for safety applications in VANETs," *IEEE Transactions on Vehicular Technology*, vol. 67, no. 11, pp. 10590–10602, 2018.

[16] D. N. M. Dang, H. N. Dang, V. Nguyen, Z. Htike, and C. S. Hong, "HER-MAC: a hybrid efficient and reliable MAC for vehicular ad hoc networks," in *Proceedings of the IEEE 28th International Conference on Advanced Information Networking and Applications*, pp. 186–193, Victoria, BC, May 2014.

[17] V. Nguyen, T. Z. Oo, P. Chuan, and C. S. Hong, "An efficient time slot acquisition on the hybrid TDMA/CSMA multi-channel MAC in VANETs," *IEEE Communications Letters*, vol. 20, no. 5, pp. 970–973, 2016.

[18] S. Ucar, S. C. Ergen, and O. Ozkasap, "Multihop-cluster-based IEEE 802.11p and LTE hybrid architecture for VANET safety message dissemination," *IEEE Transactions on Vehicular Technology*, vol. 65, no. 4, pp. 2621–2636, 2016.

WILEY | Hindawi

Research Article

Path Planning for Multi-Vehicle-Assisted Multi-UAVs in Mobile Crowdsensing

Jiancheng Song ⓘ, Liang Liu ⓘ, Yulei Liu ⓘ, Jie Xi ⓘ, and Wenbin Zhai ⓘ

College of Computer Science and Technology, Nanjing University of Aeronautics and Astronautics, Nanjing, China

Correspondence should be addressed to Liang Liu; liangliu@nuaa.edu.cn

Due to the capability of fast deployment and controllable mobility, unmanned aerial vehicles (UAVs) play an important role in mobile crowdsensing (MCS). However, constrained by limited battery capacity, UAVs cannot serve a wide area. In response to this problem, the ground vehicle is introduced and used to transport, release, and recycle UAVs. However, existing works only consider a special scenario: one ground vehicle with multiple UAVs. In this paper, we consider a more general scenario: multiple ground vehicles with multiple UAVs. We formalize the multi-vehicle-assisted multi-UAV path planning problem, which is a joint route planning and task assignment problem (RPTSP). To solve RPTSP, an efficient multi-vehicle-assisted multi-UAV path planning algorithm (MVP) is proposed. In MVP, we first allocate the detecting points to proper parking spots and then propose an efficient heuristic allocation algorithm EHA to plan the paths of ground vehicles. Besides, a genetic algorithm and reinforcement learning are utilized to plan the paths of UAVs. MVP maximizes the profits of an MCS carrier with a response time constraint and minimizes the number of employed vehicles. Finally, performance evaluation demonstrates that MVP outperforms the baseline algorithm.

1. Introduction

In recent years, due to the massive increase in sensor-rich mobile devices, mobile crowdsensing (MCS) [1] has emerged as a new way of sensing, which relies on a crowd of personal mobile phones, tablet computers, and other smart gadgets to perform large-scale tasks. While traditional sensing technologies incur large overheads due to the deployment of lots of sensors, MCS just needs to pay some incentive rewards to attract individuals to perform sensing tasks, which is obviously more cost-effective. Therefore, MCS has been used in a lot of valuable applications recently, such as detecting air quality and collecting traffic information [2, 3].

In addition, tremendous progress in the research of microelectromechanical systems has enabled UAVs to enter the civilian market. Since UAVs are economical, flexible, and easy to operate, they have been widely used in agriculture, geological exploration, military, and other fields [4–6]. Due to the high mobility and fast deployment, UAVs can collect various data anywhere and anytime when equipped with rich sensors. They could also be used to collect data in regions where ground vehicles are difficult to reach, e.g., flood hazard areas. With the increasing popularity of UAVs, more and more researchers began to introduce UAVs into the MCS to get better performance.

Despite the mentioned benefits, the hovering time of UAVs is quite constrained by limited battery capacity, which prevents them from serving a wide area. To solve the problem, in practice, ground vehicles are utilized to transport UAVs to collect data. In addition, UAVs will fly back to a ground vehicle to charge themselves after completing sensing tasks. The so-called vehicle-assisted UAV sensing benefits from both the long driving distance of the vehicle and high flexibility of UAVs [7].

After introducing the ground vehicle, efficient path planning and scheduling of drones and ground vehicle become a key issue. There are lots of researches that are dedicated to optimizing the routing and scheduling of vehicle-assisted UAVs for the transporting of parcels [8–10], wherein

vehicles can also visit the customers to deliver parcels. These works are inappropriate for the vehicle-drone cooperative sensing problem studied in this paper, wherein a vehicle is only used to transport UAVs. In the meantime, only few researches studied the routing of the vehicle-drone cooperative sensing system [11, 12]. [11] assumes that the vehicle has only one drone, and [12] considers one vehicle with multiple drones and proposes algorithms to collect sensing data in multiple target points simultaneously.

However, all the existing researches suppose that there is only one ground vehicle. In real world, we need to employ multiple vehicles with multiple drones to perform sensing tasks simultaneously. Compared with relying on only one ground vehicle, using multiple vehicles can effectively improve the efficiency of the MCS system.

When involving multiple vehicles, path planning of vehicles and drones becomes a more complex problem, which cannot be converted into a classic optimization problem. In this paper, we formalize the joint route planning and task assignment problem (RPTSP). To simplify RPTSP, we divide it into two subproblems: task assignment problem and path planning problem. In our scenario, the second subproblem includes multivehicle path planning and multi-UAV path planning. We propose an efficient heuristic allocation algorithm EHA to determine the paths of multiple vehicles, which actually solves the task assignment problem and multivehicle path planning problem. EHA utilizes an iterative process to assign tasks for each ground vehicle based on the expenses incurred and the time consumed. Besides, to solve the multi-UAV path planning problem, we transformed it into a Multiple Traveling Salesmen Problem (MTSP). After that, the genetic algorithm and reinforcement learning are utilized to solve MTSP. In general, our goal is to maximize the profits of the MCS carrier with a time budget by globally optimizing the assignment of tasks and the route of vehicles and UAVs. Besides, we hope that the number of employed ground vehicles can be minimized.

To the best of our knowledge, we are the first to consider the task assignment and the routing problem for multi-vehicle-assisted multi-UAVs in MCS. The contributions of this work are summarized as follows:

(i) We introduce multiple vehicles to the vehicle-drone cooperative sensing system and formalize the joint route planning and task assignment problem (RPTSP).

(ii) To solve RPTSP, we propose a multi-vehicle-assisted multi-UAV path planning algorithm (MVP), which maximizes the profits of the MCS carrier with a response time constraint

(iii) Extensive experiments are conducted, and the results show that MVP outperforms the baseline algorithm

The remainder of this paper is organized as follows. Section 2 gives an overview of the existing work related to the problem that we are addressing. Section 3 describes the system model and problem formulation. Section 4 illustrates the details of MVP. Section 5 introduces the simulation experiment. Section 6 concludes this paper.

2. Related Work

Recently, a lot of researches have been conducted on MCS. These works take different methods to perform sensing tasks in different application scenarios: (1) the MCS system relies on individuals' smart devices to perform sensing tasks, (2) it utilizes one vehicle and one drone to perform sensing tasks, (3) it utilizes one vehicle and multiple drones to perform sensing tasks. In the following, we will describe these works.

2.1. MCS Utilizing the Smart Devices. For traditional MCS that relies on the smart gadgets possessed by individuals, there have been many studies on assigning sensing tasks to participants.

These studies have different optimization objectives; e.g., He et al. [13] devised an efficient local ratio-based algorithm to maximize the benefits of the MCS carrier under a time budget constraint; Xiong et al. [14] introduced an incentive allocation framework to minimize total incentive payment while ensuring predefined spatial-temporal coverage; and Shi et al. [15] designed a crowdsensing task assignment mechanism to maximize the task completion rate under a predefined incentive budget.

2.2. MCS Utilizing One Vehicle and One Drone. When evolving towards MCS architectures consisting of UAVs and vehicles, route planning should be well designed to minimize the consumed time or rewards in performing sensing tasks.

Chen et al. [16] designed a trajectory segment selection scheme to remove data redundancy and improve the coverage quality. Luo et al. [11] proposed two heuristic algorithms to solve the two-echelon cooperated routing problem for the ground vehicle and its carried drone. Savuran and Karakaya [17] proposed a path optimization method that allows the vehicle to keep moving when the drone is performing tasks. However, the above works all consider the case of only one drone, which makes it impossible for vehicle-assisted UAVs to perform multiple tasks in parallel.

2.3. MCS Utilizing One Vehicle and Multiple Drones. As for the case of using multiple UAVs, Hu et al. [18] proposed a vehicle-assisted multi-UAV routing and scheduling algorithm (VURA). It works by iteratively deriving solutions based on UAV routes picked from the memory that contains flight paths of drones. Through continuous joint optimization of parking spot selection, path planning, and tour assignment, VURA can produce a final appropriate solution. In [12], Hu et al. proposed a novel algorithm (VAMU) based on VURA, which schedules the multiple drones to be launched and recycled in different places. It avoids the time wastage when the vehicle waits for drones to return and thus reduces the time required to complete all tasks.

However, the works mentioned above did not take multiple vehicles into account. In reality, the MCS carrier needs to employ multiple vehicles with multiple drones to perform sensing tasks simultaneously, which significantly improves the efficiency of the MCS system. Therefore, this motivates

us to consider a more general scenario, in which multiple vehicles and multiple drones are used to perform sensing tasks allocated by the MCS system.

3. System Model and Problem Formulation

3.1. System Model. In our model, there are several ground vehicles with different numbers of UAVs. A set of detecting points that UAVs need to visit and collect data are distributed in a target region. Every detecting point needs to be visited once only by a UAV. And a UAV can visit multiple detecting points (i.e., perform sensing tasks) consecutively in a single flight. Due to the limited battery capacity, UAVs cannot serve a wide area. To solve the problem and maximize the efficiency in the meantime, this paper employs multiple ground vehicles to assist UAVs.

As shown in Figure 1, with the aid of ground vehicles, the UAVs can visit detecting points distributed in a very large region. From the starting point, a ground vehicle transports drones to the preselected parking spots sequentially. Once a ground vehicle arrives at a parking spot, the UAVs carried by it are released to perform sensing tasks in nearby detecting points. When the UAVs finish their missions of one single trip, they return to the corresponding ground vehicle to be charged. Notice that it is possible for a UAV to be launched and recycled multiple times in each parking spot. When all detection points near the parking spot have been visited by UAVs, the ground vehicle with multiple UAVs leaves to the next selected parking spot. Once all detecting points are visited, the whole sensing task in the target region is finished.

The consumed time and the generated incentive rewards must be considered when the MCS system assigns sensing tasks and plans the route of vehicles as well as UAVs.

For simplicity, we make the following hypothesis:

(i) The MCS system knows the coordinates of each detecting point

(ii) Each detecting point should be accessed once

(iii) The time consumed by the UAV to perform the sensing task in a detecting point is constant

(iv) Both the ground vehicle and UAVs travel at a constant speed [12, 18]

3.2. Problem Formulation. Let $G = \{V, E\}$ be an undirected graph where V is the set of vertex and E is the set of edge. And V is divided into $V_d = \{d_1, d_2, \cdots, d_{N_d}\}$ and $V_p = \{p_1, p_2, \cdots, p_{N_p}\}$, which represent the set of detecting points and the set of candidate parking spots, respectively. N_d represents the number of detecting points, and N_p represents the number of parking spots. The distance of point n_1 and n_2 is denoted by $\mathrm{dis}(n_1, n_2)$, where the points n_1 and n_2 represent the detecting point or parking spot.

Ground vehicles we employed are expressed as $\mathrm{GV} = \{\mathrm{gv}_1, \mathrm{gv}_2, \cdots, \mathrm{gv}_{N_{\mathrm{gv}}}\}$, where N_{gv} represents the total number of ground vehicles. And $U_{\mathrm{gv}_i} = \{u_1, u_2, \cdots, u_{m_i}\}(\mathrm{gv}_i \in$

GV) denotes the set of UAVs that the vehicle gv_i possesses, where m_i represents the number of drones owned by vehicle gv_i. $V_{\mathrm{gv}_i} = \{d_{k_1}, d_{k_2}, \cdots, d_{k_i}, \cdots, d_{k_n}\}$, where $d_{k_n} \in V_d$ denotes the detecting points that the UAVs possessed by gv_i need to access. Besides, we use V_{vehicle} and V_{uav} to represent the speed of the vehicles and the UAVs, respectively. D_{u_i} represents the maximum flight distance of UAV u_i. In this paper, the main objective is to jointly optimize the sensing task assignment and the path planning of ground vehicles and UAVs such that the incentive rewards produced are minimized with a time budget constraint that is denoted as $\mathrm{Time}_{\mathrm{budget}}$.

We need to address the following issues: first, we should think out how to select the proper parking points from the roads lying on the target region. There are infinite points that can be selected as candidate parking spots in the road network. What we need to do is to select some points as parking spots from this infinite number of points and assign detecting points to these parking spots. The detecting points that are assigned to parking spot p_j are represented as $V_{p_j} = \{d_{k_1}, d_{k_2}, \cdots, d_{k_i}, \cdots, d_{k_n}\}(p_j \in V_p, d_{k_i} \in V_d)$. It should be guaranteed that when the vehicle is parked at these points, the drones carried on the vehicle can access all the detecting points.

Then, we need to plan the flight paths of UAVs when a ground vehicle arrives at parking spot p_j. In our scenario, each drone performs a trip by visiting the detecting points along its route sequentially. Since we employ N_u UAVs to perform tasks in parallel, the flight paths of UAVs possessed by ground vehicle gv_i can be denoted as $\mathrm{FP}_{p_j}^{\mathrm{gv}_i} = \{R_{p_j}^{u_1}, R_{p_j}^{u_2}, \cdots, R_{p_j}^{u_{m_i}}\}$ when the ground vehicle is parking at the parking spot p_j. In detail, the flight path of $u_k(1 \le k \le m_i)$ at parking spot p_j is expressed as $R_{p_j}^{u_k} = \{a_1, a_2, \cdots, a_z\}(a_z \in V_{p_j})$.

We use $C(R_{p_j}^{u_k}, a_z)$ to denote whether the route $R_{p_j}^{u_k}$ contains the detecting point a_z, where $R_{p_j}^{u_k} \in \mathrm{FP}_{p_j}$ and $a_z \in V_{p_j}$. In detail, $C(R_{p_j}^{u_k}, a_z) = 1$ means that the detecting point a_z is included in the route $R_{p_j}^{u_k}$. Furthermore, $\mathrm{Adj}_{R_{p_j}^{u_k}}(d_a, d_b)$ $(d_a, d_b \in V_{p_j})$ is used to express whether the points d_a and d_b are adjacent in the route $R_{p_j}^{u_k}$. For example, $\mathrm{Adj}_{R_{p_j}^{u_k}}(d_a, d_b) = 1$ indicates that d_a and d_b are adjacent in the route $R_{p_j}^{u_k}$. Then, the total flight distance of the UAV u_k at the parking spot p_j can be defined as follows:

$$l\left(R_{p_j}^{u_k}\right) = \sum_{d_a \in R_{p_j}^{u_k}} \sum_{d_b \in R_{p_j}^{u_k}} \mathrm{dis}(d_a, d_b)\mathrm{Adj}_{R_{p_j}^{u_k}}(d_a, d_b). \quad (1)$$

Based on the above equation, the total distance that all UAVs of the ground vehicle gv_i travel at the parking spot p_j is given as follows:

$$l\left(\mathrm{gv}_i, p_j\right) = \sum_{r_z \in \mathrm{FP}_{p_j}^{\mathrm{gv}_i}} l(r_z). \quad (2)$$
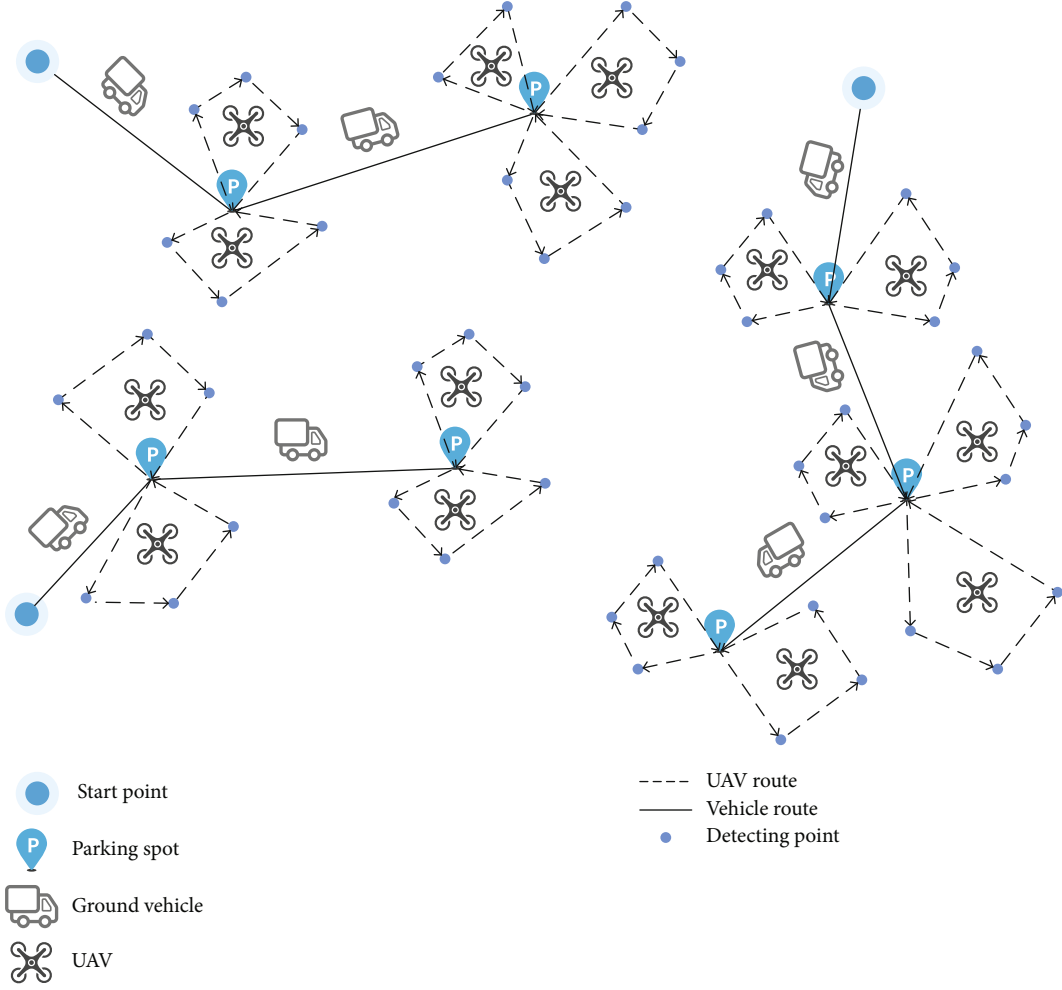
Figure 1: System model.

Besides, a sorted set of parking spots needs to be determined for each vehicle to minimize the generated incentive rewards with a time budget constraint. We use $R_{gv_i} = \{p_{k_i}, p_{k_2}, \cdots, p_{k_i}, \cdots, p_{k_n}\}$ where $p_{k_i} \in V_p$ to represent the route for the ground vehicle gv_i. We use $\text{Adj}_{R_{gv_i}}(p_a, p_b)$ to denote whether the points p_a and p_b are adjacent in the vehicle route R_{gv_i} ($\text{Adj}_{R_{gv_i}}(p_a, p_b) = 1$) or not ($\text{Adj}_{R_{gv_i}}(p_a, p_b) = 0$). Then, the travel distance of the ground vehicle gv_i is expressed as follows:

$$l(gv_i) = \sum_{p_a \in R_{gv_i}} \sum_{p_b \in R_{gv_i}} \text{dis}(p_a, p_b) \text{Adj}_{R_{gv_i}}(p_a, p_b). \quad (3)$$

Since the distance of UAVs and the vehicle that carries them is calculated, we can easily get the time $\text{Time}(gv_i)$ consumed by vehicle gv_i with its UAVs in the whole sensing task:

$$\text{Time}(gv_i) = \frac{l(gv_i)}{V_{\text{vehicle}}} + \sum_{p_j \in R_{gv_i}} \frac{l(gv_i, p_j)}{V_{\text{uav}}}. \quad (4)$$

Thus, the total time $\text{Time}_{\text{final}}$ cost by all vehicles and UAVs is defined as follows:

$$\text{Time}_{\text{final}} = \max \left(\text{Time}(gv_1), \text{Time}(gv_2), \cdots, \text{Time}(gv_i) \right). \quad (5)$$

Finally, the calculation of the incentive rewards generated throughout the execution of all sensing tasks should also be confirmed. In this paper, for a ground vehicle, its revenue depends on the total flight distance of its UAVs and the travel distance of its ground vehicle. Therefore, the final incentive rewards earned by a ground vehicle are calculated as follows:

$$\text{IR}(gv_i) = \text{IR}_{\text{base}} + \alpha l(gv_i) + \beta \sum_{p_j \in R_{gv_i}} l\left(gv_i, p_j\right), \quad (6)$$

where IR_{base} represents the base incentive rewards that a ground vehicle can get if it has accepted the sensing tasks and completed assigned tasks. α and β are the price coefficients for the UAV and the vehicle, respectively, which are used to transform distance to the price.

TABLE 1: Notation and terminology.

Notation	Definition
V_p	The set of parking spots
V_d	The set of detecting points
N_p	The number of parking spots
N_d	The number of detecting points
$\mathrm{dis}(n_1, n_2)$	The distance between two different points
GV	The set of ground vehicles
U_{gv_i}	The set of UAVs that the vehicle gv_i possesses
N_{gv}	The number of ground vehicles
V_{gv_i}	The set of detecting points assigned to the vehicle gv_i
V_{p_j}	The set of detecting points assigned to the parking spot p_j
V_{vehicle}	The speed of ground vehicles
V_{uav}	The speed of UAVs
D_u	The max flight distance of UAVs
$\mathrm{Time}_{\mathrm{budget}}$	The budget of time
m_i	The number of drones of the vehicle gv_i
$R_{p_j}^{u_k}$	The flight path of u_k at the parking spot p_j
$\mathrm{FP}_{p_j}^{\mathrm{gv}_i}$	The flight paths of drones possessed by vehicle gv_i at the parking spot p_j
$C\left(R_{p_j}^{u_k}, a_z\right)$	Binary indicating whether the route $R_{p_j}^{u_k}$ contains the detecting point a_z
$\mathrm{Adj}_{R_{p_j}^{u_k}}(d_a, d_b)$	Binary indicating whether d_a and d_b are adjacent in the route $R_{p_j}^{u_k}$
$l\left(\mathrm{gv}_i, p_j\right)$	The total distance that all drones of the vehicle gv_i travels at the parking spot p_j
R_{gv_i}	The route of the vehicle gv_i
$l(t_i)$	The travel distance of the vehicle gv_i
$\mathrm{Time}(t_i)$	The time consumed by the vehicle gv_i with its drones in the whole sensing mission
$\mathrm{IR}(\mathrm{gv}_i)$	The total incentive rewards earned by the vehicle gv_i with its drones

In our scenario, for the MCS carrier, the income is proportional to the number of detection points. Besides, for an actual sensing task, the income is a fixed value, which means that maximizing profits equals minimizing expenses. Then, our objective can be transformed to minimize the generated incentive rewards. The total incentive reward cost, expressed as $\mathrm{Cost}(s)$, includes all the revenues of each ground vehicle in the solution. The algorithm proposed in this paper is aimed at minimizing the total incentive reward consumption.

$$\min \mathrm{Cost}(s) = \sum_{\mathrm{gv}_i \in \mathrm{GV}} \mathrm{IR}(\mathrm{gv}_i), \tag{7}$$

$$N_t \geq 1, \tag{8}$$

$$m_i \geq 1, \forall i \in [1, N_t], \tag{9}$$

$$0 \leq l\left(R_{p_j}^{u_k}\right) \leq D_u, \tag{10}$$

$$0 \leq \mathrm{Time}_{\mathrm{final}} \leq \mathrm{Time}_{\mathrm{budget}}, \tag{11}$$

$$\sum_{R \in \mathrm{FP}_{p_j}^{\mathrm{gv}_i}} \sum_{a_z \in V_{p_j}} C(R, a_z) = \left| V_{p_j} \right|, \forall p_j \in V_p. \tag{12}$$

Constraint (8) confirms that at least one ground vehicle is employed. Constraint (9) emphasizes the requirement that every ground vehicle has at least one drone. Constraint (10) means that the flight distance of a UAV should be less than the maximum flight distance. Constraint (11) indicates that the time consumption in a solution should not exceed the time budget. Constraint (12) ensures that all detecting points of each parking spot are visited. The notation and terminology used throughout the paper are shown in Table 1.

4. Algorithm Design

In this section, we first introduce some challenges encountered in designing the efficient solution. Then, we propose

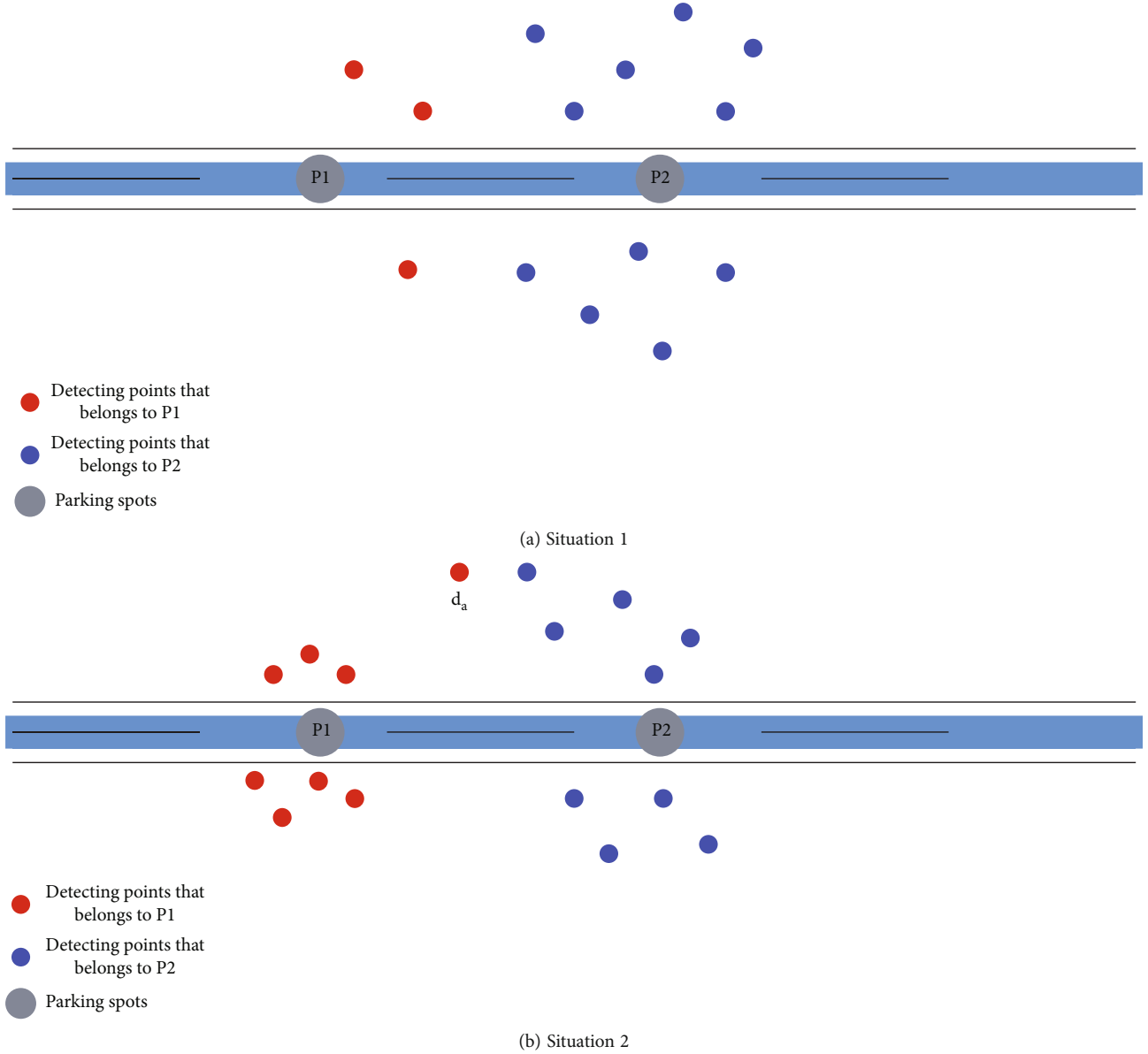(a) Situation 1

(b) Situation 2

FIGURE 2: The situations of allocating detecting points.

MVP to solve these problems. After that, we provide a detailed description of each part of MVP.

4.1. The Challenges. In order to complete the whole sensing mission effectively, we need to solve the following problems:

(1) How to allocate each detecting point to a proper parking spot? In our scenario, the detecting points are randomly distributed in a large target region, and the parking spots are sampled from the points of the road network. To reduce the distance between the detection point and the parking point, for each detecting point, a naive method is to allocate it to the closest candidate parking spot, which is selected every other distance in the roads. However, the shortest distance between parking spots and detecting points does not mean the smallest time cost for

the UAVs to visit those detecting points. It is illustrated by the following examples

First, as shown in Figure 2(a), some parking spots possess few detecting points. When ground vehicles traverse these points, too few detecting points will cause some drones to sit idle. This will incur unnecessary time wastage. Besides, as shown in Figure 2(b), the detecting point d_a is assigned to the parking spot p_1 due to the shortest distance between them. However, other detecting points assigned to the parking spot p_1 are far from d_a. Thus, it will incur a relatively large time cost when a UAV traverses $p_1's$ detecting points.

(2) How to allocate the parking spots to ground vehicles? Unlike previous studies, we employ multiple vehicles in the meantime. We transform the problem of assigning sensing tasks into the parking spot
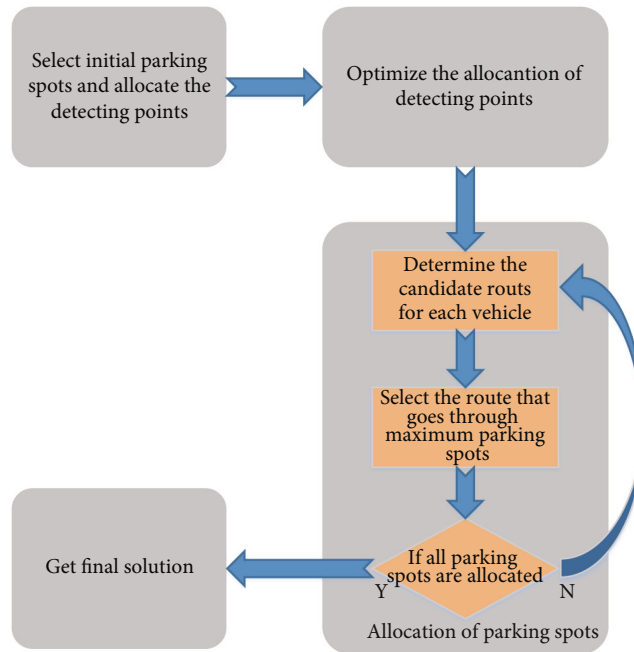
FIGURE 3: The overall architecture of MVP.
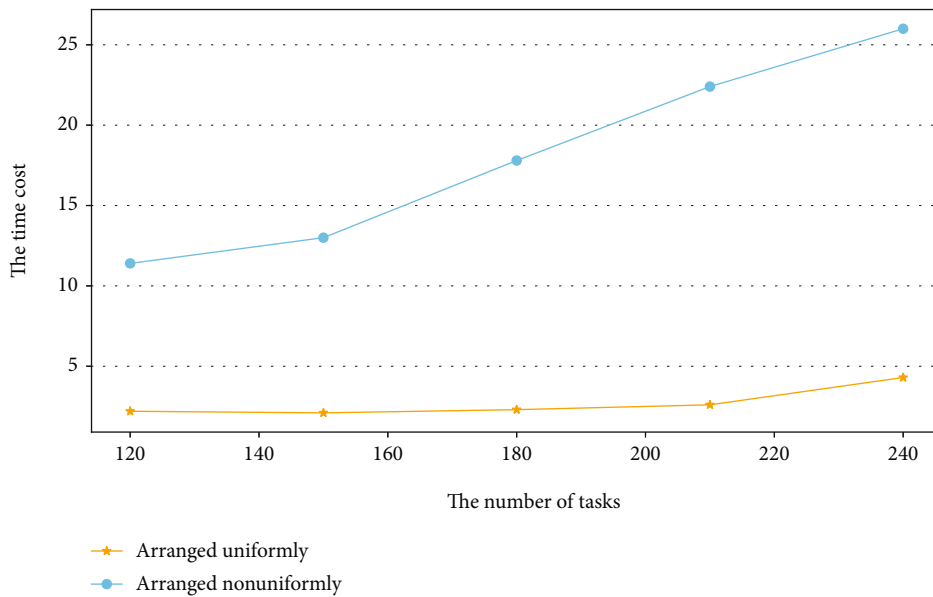
FIGURE 4: The time cost in nonuniform environment.

allocation problem. This problem can be defined as follows: given a set of parking spots, a set of detecting points, and the corresponding relation between them, we need to determine the route for each employed vehicle to minimize the produced incentive rewards with a time budget constraint. Notice that each parking spot can be visited exactly once by only one ground vehicle, and the number of employed ground vehicles is not determined until all parking spots are allocated

(3) How to plan the paths of UAVs when a ground vehicle arrives at a parking spot? After the allocation of the detecting points, we know exactly the corresponding detecting points of each parking spot. When a ground vehicle arrives at a parking spot, we should plan the paths of UAVs. Since every vehicle possesses multiple drones, the problem can be transformed into the multiple travelling salesman problem (MTSP). The MTSP in our scenario is illustrated as follows: given a parking spot and a set of
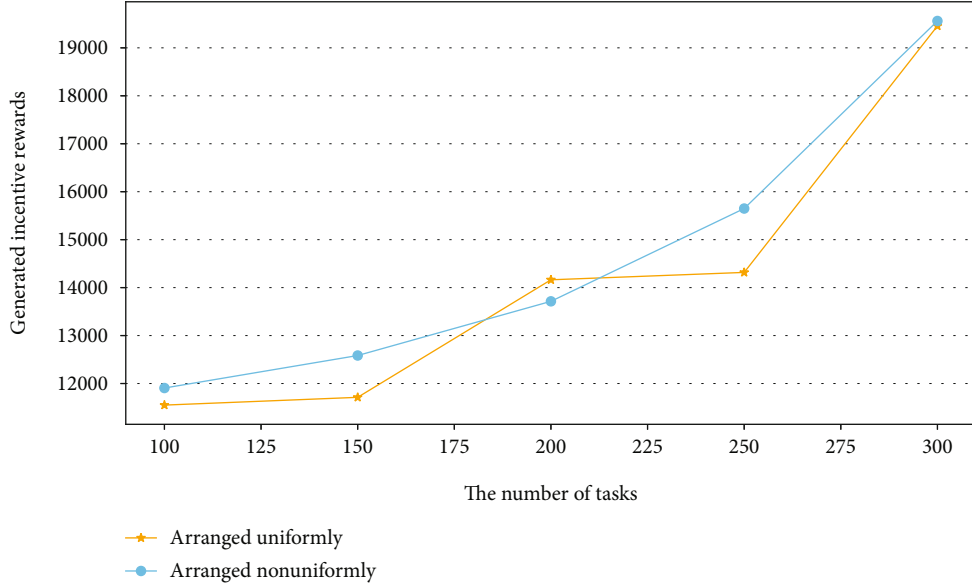
FIGURE 5: The impact of the number of tasks for different methods of selecting candidate parking spots.
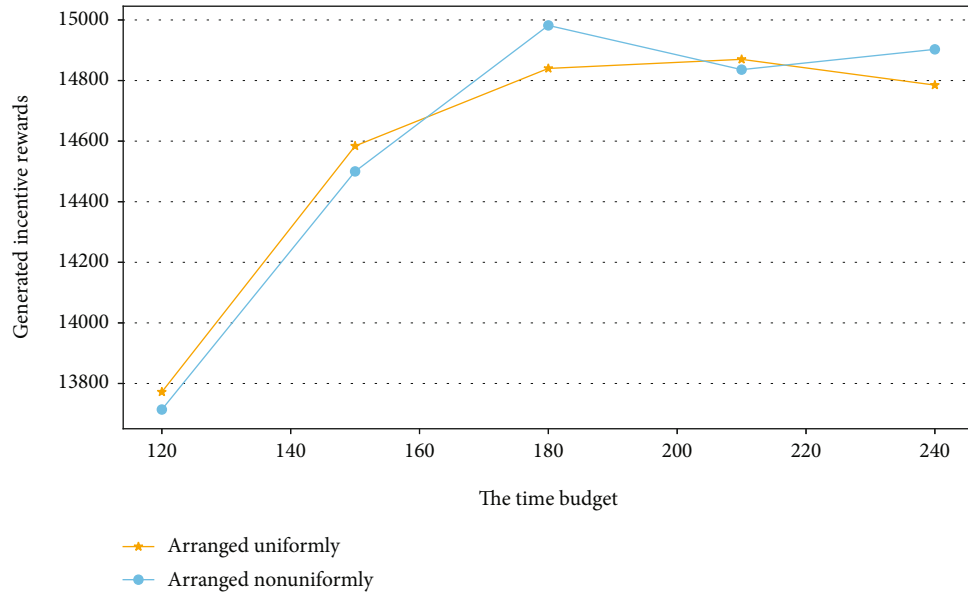
FIGURE 6: The impact of the time budget for different methods of selecting candidate parking spots.

detecting points allocated to it, we need to find out a flight path for each drone such that the total cost of time is minimized and that each detecting point is visited exactly once by only one drone

4.2. The Overall Architecture of MVP. The overall architecture of MVP is shown in Figure 3. First, we mark a point on roads every other distance to construct the set of initial parking spots. After that, the detecting points are clustered by allocating them to different parking spots according to their distance to the parking spots. Then, in order to improve the performance of MVP, several optimizations

are used to reallocate detecting points. Subsequently, parking spots are allocated to ground vehicles in an iterative process. In each iteration, we can determine the route of one ground vehicle $gv_i(gv_i \in GV)$ and the paths of $gv_i's$ UAVs at each parking spot. The route of gv_i is represented as $R_{gv_i} = \{p_{k_1}, p_{k_2}, \cdots, p_{k_i}, \cdots, p_{k_n}\}(p_{k_i} \in V_p)$, and the paths of $gv_i's$ UAVs at parking spot p_i are represented as $FP_{p_j}^{gv_i} = \{R_{p_j}^{u_1}, R_{p_j}^{u_2}, \cdots, R_{p_j}^{u_k}, \cdots, R_{p_j}^{u_{m_i}}\}$, where $R_{p_j}^{u_k}(1 \leq k \leq m_i)$ denotes the flight path of u_k at the parking spot p_j. The ground vehicle gv_i will access the parking spots in the route R_{gv_i} sequentially. Besides, gv_i will release its UAVs to visit the detecting

points along the paths in $\text{FP}_{p_j}^{\text{gv}_i}$ when it arrives at the parking spot p_j. When the iterative process ends, we get the routes of all ground vehicles and the paths of their UAVs at each parking spot, which ensures that all detecting points in the target region have been accessed.

4.3. Parking Spot Selection. The selection of the parking spots for detecting points is divided into two steps: the initialization of the parking spots and their optimization. The details of the steps are described as follows.

4.3.1. Initialization. First, a set of candidate parking spots is determined by sampling points on roads every other distance. Then, for each detecting point, we calculate the distance between it and its nearby candidate parking spot. After that, the nearest candidate parking spot of each detecting point is determined. These parking spots are composed of the initial set of parking spots. Besides, there is another method to mark the candidate parking spots when detecting points are distributed nonuniformly. It arranges the candidate parking spots nonuniformly. The process is described as follows:

(1) For each of the roads, we first mark the endpoint p_1 as a candidate parking spot

(2) Then, we calculate the density of detecting points around p_1. If the density is big, we mark the next candidate parking spot at a location close to the p_1. If the density is small, we mark the next candidate parking spot at a location far from p_1

(3) After that, we calculate the density of detecting points around the second candidate parking spot and repeat the process above to mark all candidate parking spots of the road

We have performed some experiments to compare these two methods. The results of the experiments are shown in Figures 4–6.

4.3.2. Optimization. Choosing the nearest candidate parking spot is not always the best strategy. Therefore, in order to get better performance, we need to optimize the allocation of detecting points.

(a) As shown in Figure 2(a), there are many selected parking spots that have few detecting points. It will incur unnecessary time cost if the ground vehicle parks at these parking spots and releases its UAVs to access corresponding detecting points. Therefore, the detecting points assigned to these parking spots should be reallocated. In detail, for a selected parking spot p_j, if the number of p_j's detecting points is less than a predefined value N_m, we will remove p_j from the set of parking spots and reallocate each detecting point of p_j to the second closest parking spot to it. The procedure will be repeated until all selected parking spots have at least N_m detecting points. In

---

```
Input The set of initial parking spots V_p,
the set of corresponding detecting points V.
Ouput NULL
1  for each p_i ∈ V_p do
2      if |V_{p_i}| < N_m then
3  reallocate each point in V_{p_i} to the second
   nearest parking spot to it;
4  V_p = V_p \ p_i
5      end
6      else
7          for each d_i ∈ V_{p_i} do
8              calculate the distance D_r between d_i
               and its nearest detecting point in V_{p_i};
9              find d_i's second nearest parking spot p_k
10             if ∃d_k ∈ V_{p_k} is inside Cir(d_i, D_r) then
11                 reallocate d_i to p_k;
12             end
13         end
14     end
15 end
```

ALGORITHM 1: Reallocate the detecting points.

---

the experimental part, we will investigate the impact of N_m's value by performing some experiments

(b) As for the situation shown in Figure 2(b), it is obviously a better choice to allocate the detecting point d_a to parking spot P_2 as it avoids the waste of flight time of drones. Therefore, the detecting point in such a situation should be reallocated. We use $\text{Cir}(c, r)$ to denote the circle with c as the center and r as the radius. Besides, V_{p_j} represents the detecting points of the parking spot p_j. For a detecting point d_i of a parking spot p_i, we suppose that d_k is the nearest detecting point to it in V_{p_i} and the distance between d_i and d_k is D_r. Furthermore, p_k is supposed to be the second nearest parking spot to d_i. If there is at least one detecting point in V_{p_k} that is inside the circle $\text{Cir}(d_i, D_r)$, the detecting point d_i will be reallocated to p_k

The pseudocode of the reallocation procedure is shown in Algorithm 1.

4.4. Allocation of Parking Spots. After the selection of parking spots, for each parking spot, we allocate it to a proper ground vehicle. The travel route of each ground vehicle and the flight paths of corresponding drones at each parking spot are determined in the procedure of allocation. In a word, we will get the final solution of RPTSP when the procedure ends. An efficient heuristic allocation algorithm EHA is proposed to effectively allocate the parking spots.

In the procedure of allocation, for a ground vehicle gv_i, we need to find the K nearest neighbor parking spots to g v_i. A naive method is to calculate the distances between gv_i and all parking spots, which obviously incurs a large amount

Input The set of selected parking spots V_p,
the set of corresponding detecting points V,
the set of candidate vehicles GV and its UAVs U
Output The final solution S_{final}
1 $S_{final} \longleftarrow \varnothing$;
2 build R-tree RT using the points in V_p
3 do
4   for $n = 1 \longrightarrow |GV|$
5   select a vehicle gv_i from GV;
6          $R_{gv_i}, R_{gv_i}^{uav} \longleftarrow \varnothing$;
7             $Time_{gv_i} = 0$;
8   do
9   search $gv_i's$ nearby parking spots P according to RT;
10             $IR_{\min} = MaxNumber$;
11             $R_{temp} \longleftarrow \varnothing$;
12 for each $p_j \in P$ do
13 $R_{p_j} \longleftarrow$ utilize GA to plan the paths of U_{gv_i} at p_j;
14 calculate the $l(gv_i, p_j)$ based on R_{p_j};
15 calculate the current $l(gv_i)$ when visit p_j;
16 $IR_{temp} = IR_{base} + \alpha l(gv_i) + \beta \sum_{p_j \in R_{gv_i}} l(gv_i, p_j)$;
17   if $IR_{temp} < IR_{\min}$ then
18             $IR_{\min} = IR_{temp}$;
19 $R_{temp} = R_{p_j}$;
20             $P_{temp} = p_j$;
21             $Time_{temp} = (l(gv_i, p_j)/V_{uav}) + (l(gv_i)/V_{vehicle})$
22 end
23 end
24 $R_{gv_i}^{uav} = R_{gv_i}^{uav} \cup R_{temp}$;
25 $R_{gv_i} = R_{gv_i} \cup p_{temp}$;
26 $Time_{gv_i} = Time_{gv_i} + Time_{temp}$;
27 $Time_{gv_i} = Time_{budget}$;
28       $GV = GV \setminus gv_i$
29   end
30 select the vehicle gv_k with maximum $|R_{gv_k}|$
31 $S_{final} = S_{final} + \{R_{gv_k}, R_{gv_k}^{uav}\}$
32 $V_p = V_p \setminus R_{gv_k}$;
33 while $V_p \neq \varnothing$
34 return S_{final}

ALGORITHM 2: Plan the paths of ground vehicles.

of time consumption. To improve the performance, in EHA, R-tree [19] is introduced to index the locations of all parking spots. After that, we utilize the branch-and-bound R-tree traversal algorithm proposed in [20] to find the K nearest neighbor parking spots to gv_i.

The details of EHA are described in Algorithm 2. EHA starts with building R-tree RT, which utilizes the locations of all parking spots (line 2). Then, it chooses a vehicle gv_i (line 5) and iterates to generate gv_i's candidate routes until the consumed time exceeds the time budget constraint (lines 8-27). In each iteration, we search RT to get $gv_i's$ nearby parking spots P (line 9), from which the parking spot that produces minimum incentive rewards is selected (lines 12-23). The procedure is repeated until all vehicles' candidate

routes have been determined (lines 4-29). Then, we choose the vehicle gv_k with maximum $|R_{gv_k}|$ and add gv_k's corresponding routes $\{R_{gv_k}, R_{gv_k}^{uav}\}$ into the solution S_{final} (lines 30-31). The above process will keep looping until all parking spots have been allocated (lines 3-33).

Algorithm 2 is designed to minimize the generated incentive rewards with a time budget constraint. In the meantime, it minimizes the number of employed ground vehicles.

4.5. Path Planning of UAVs.
When a ground vehicle arrives at a parking spot, the paths of its UAVs need to be planned. Notice that the path planning of UAVs is involved in the

```
Input The parking spot p_j,
the set of corresponding detecting points V_{p_j},
the UAVs U_{t_i}
Output Optimal routes of UAVs routes
1 generate initial population Pop,
|Pop| = populationSize;
2 for n = 1 ⟶ iteration do
3        calculate the fitness of each individual in Pop;
4        newPop ⟵ ∅;
5        for m = 1 ⟶ populationSize do
6            select two individuals from Pop according
to the fitness function
7            if random(0, 1) < P_c perform crossover to generate a child
8            R_{temp}
9        end
10           if random(0, 1) < P_m
11         perform mutation on R_{temp};
12         end
13         newPop = newPop ∪ R_{temp};
14         end
15         pop = newPop;
16 end
17 select the individual routes in pop with maximum fitness;
18 return routes;
```

ALGORITHM 3: Plan the paths of UAVs.

procedure of allocating parking spots for ground vehicles, as shown in Algorithm 2. As mentioned before, this problem can be transformed into the MTSP, which is a typical NP-hard problem. There have been some works that concern on the trajectory scheduling of mobile vehicles [21–23]. In this paper, we adopt the genetic algorithm (GA) and reinforcement learning (RL) to solve MTSP, respectively. For convenience, MVP that uses GA to plan the paths of UAVs is named GA-MVP and MVP that uses RL to plan the paths of UAVs is named RL-MVP.

4.5.1. Genetic Algorithm. GA is a search algorithm used in computational mathematics to solve optimization. And it is a type of evolutionary algorithm. It has been widely used in various combinatorial optimization problems. The procedure of planning paths of UAVs based on GA is illustrated in Algorithm 3.

In the algorithm, one individual of the population is a 2D array, which is the respective routes taken by UAVs. P_c and P_m are the probability of crossover and the probability of mutation, respectively. Besides, the fitness function is defined as the reciprocal of the flight distance of UAVs.

The algorithm first randomly generates some individuals as the initial population (line 1) and then starts an iterative process to evolve the initial population (lines 2-16). In each iteration, the fitness of each individual in the population is calculated (line 3). Besides, we take out two individuals that have the largest fitness iteratively and perform crossover on these two individuals with the probability P_c to generate a new individual (lines 6-9). After that, the mutation is

performed on the new individual with the probability P_m (lines 10-12). When the iteration ends, we get a new population newPop (line 15). Finally, we select the individual with maximum fitness in the newPop as the final routes of UAVs (lines 17-18).

4.5.2. Reinforcement Learning. Reinforcement learning is an area of machine learning that learns what to do in an environment to maximize a numerical reward. Since a traditional heuristic algorithm for solving combinatorial optimization problems may often be suboptimal due to the hard nature of the problems, RL is a good alternative to search the solution. In our work, we adopt the learning-based approach in [24] to optimize the MTSP, i.e., the path planning of UAVs.

4.6. Algorithm Complexity Analysis. In this section, we analyze the time complexity of GA-MVP. GA needs to evolve the population |iteration| times. In each evolving process, it will perform crossover or mutation action to generate a new population that contains |populationSize| individuals. Hence, the running time complexity of GA will be $O(|\text{iteration}| \times |\text{populationSize}|)$. To generate the route of a ground vehicle, GA-MVP needs to generate |GA| candidate routes. For each candidate route, GA-MVP needs to search at most $|V_p|$ parking spots. Then, GA will be used to solve MTSP in each parking spot. Since we will generate at most |GA| routes, the time complexity of GA-MVP is $O(|\text{GA}|^2 \times |V_p| \times |\text{iteration}| \times |\text{populationSize}|)$.
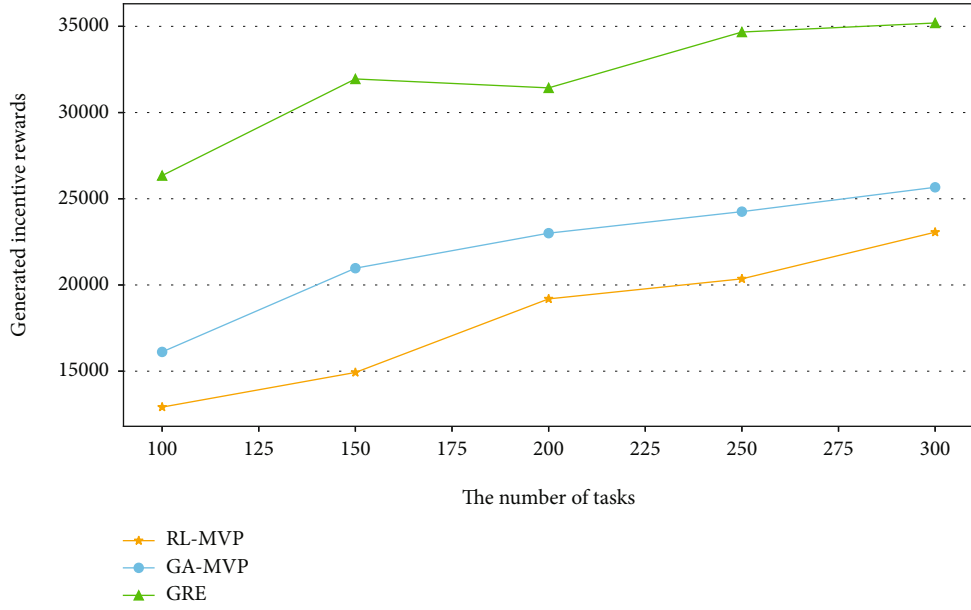
(a) Uniform distribution
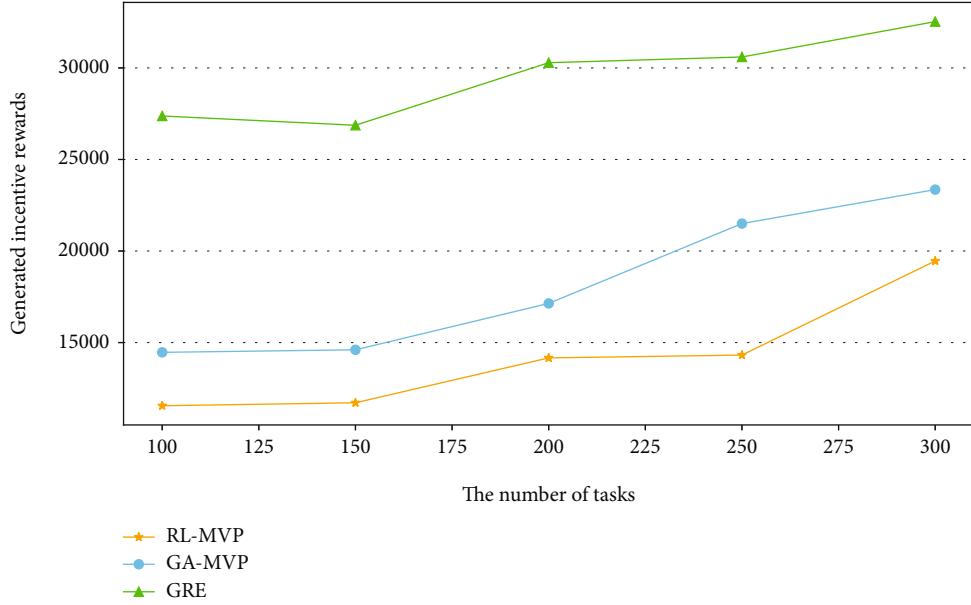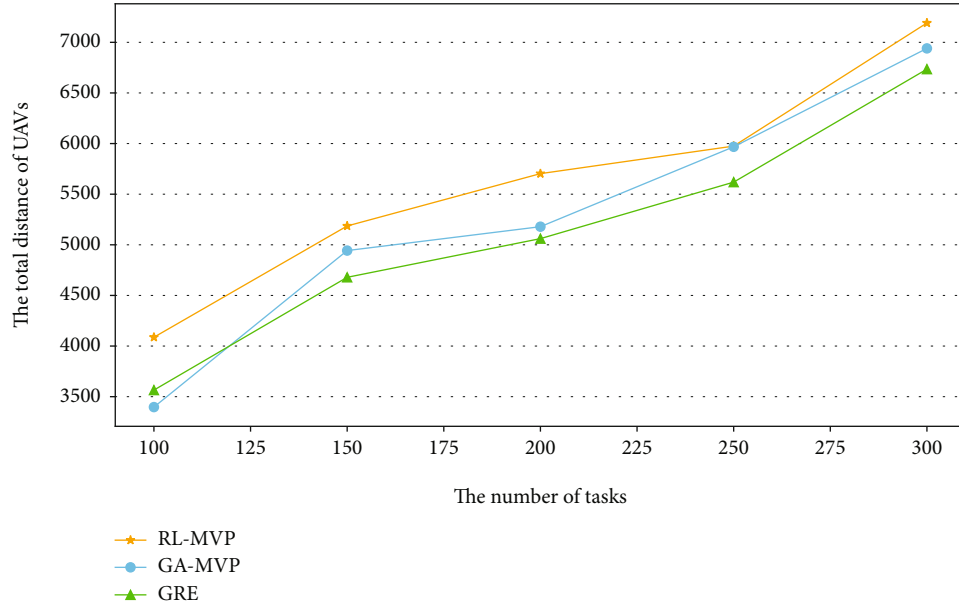

(b) Nonuniform distribution

FIGURE 7: The impact of the number of tasks on the generated incentive rewards in the environment of multiple vehicles.

5. Experimental Simulation

In this section, we evaluate the proposed algorithm through some simulation experiments. We use the simulator implemented in [25]. In our experiments, a number of detecting points are distributed in the 240 units × 240 units region, in which 1 unit represents 50 m in reality. The roads in the region are generated randomly. For detecting points, we consider two types of distribution: uniform distribution and nonuniform distribution. Besides, a set of ground vehicles is distributed randomly in the target region and is waiting to be employed. The hovering time and speed of

all drones possessed by different ground vehicles are identical. However, different ground vehicles may have varying numbers of drones. The speed of drones and ground vehicles are set as 5 m/s and 10 m/s, respectively.

Since we are the first to study the path planning of multi-vehicle-assisted multi-UAVs, there is no existing algorithm that supports employing multiple vehicles. Hence, to evaluate the performance of MVP in the environment of multiple vehicles, we design a naive greedy algorithm (GRE) as the baseline algorithm. In GRE, we utilize the method in VAMU [12] to select parking spots and allocate detecting points. The allocation of parking spots in GRE is greedy as it simply
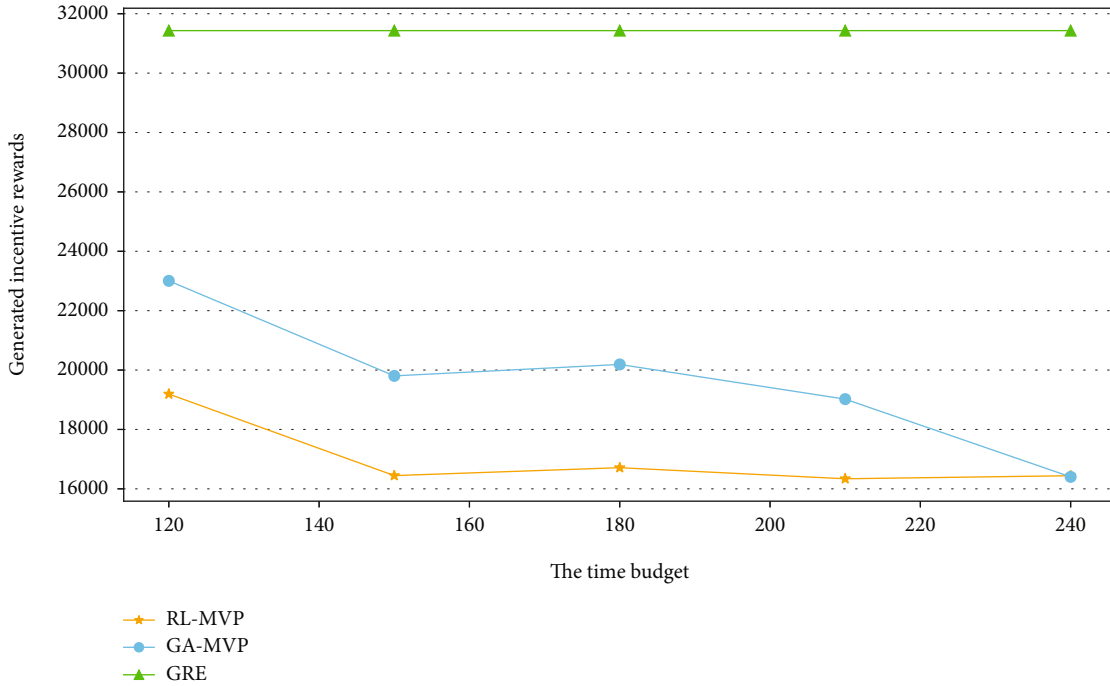
(a) Uniform distribution
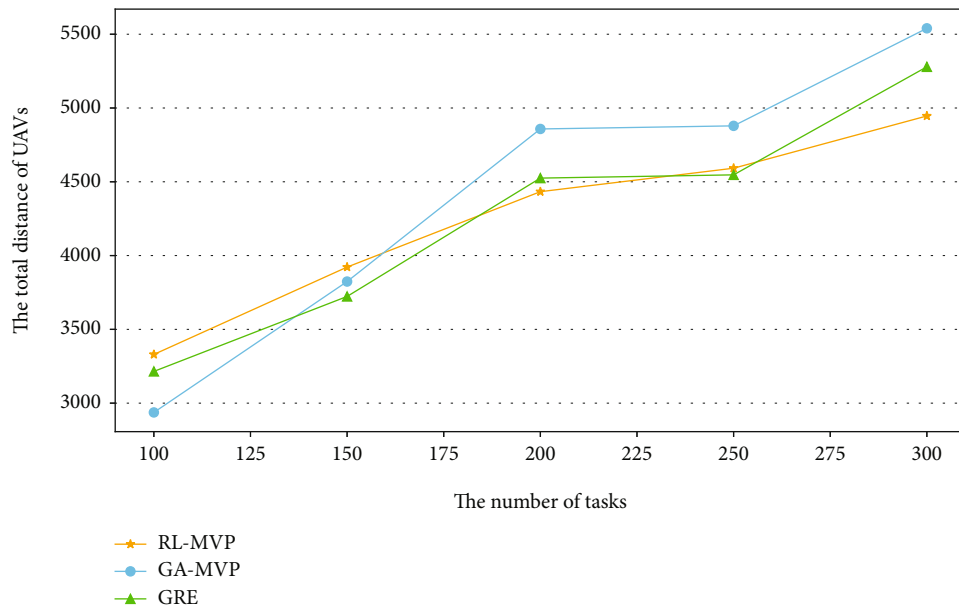
(b) Nonuniform distribution

FIGURE 8: The impact of the number of tasks on the distance of UAVs in the environment of multiple vehicles.

employs all ground vehicles and allocates the closest parking spots to each of them. After that, for each ground vehicle, GRE utilizes GA to plan the path of the ground vehicle and UAVs. Besides, to make the experiments more complete, we compare MVP with VURA [18]. VURA is a vehicle-assisted multi-UAV routing and scheduling algorithm, but it only employs one vehicle. So the number of available vehicles of MVP is limited to 1 when compared with VURA. In a word, we compare MVP with GRE in the environment of multiple vehicles but compare MVP with VURA in the environment of a single vehicle.

In our experiments, we focus on two metrics. The first is the incentive cost of the algorithm. It is defined by the total incentive rewards produced in the whole procedure of performing all sensing tasks. The second metric is the number of employed vehicles. The smaller the number of required vehicles, the better the performance of the algorithm in the situation where vehicles may not be enough.

We designed some experiments to compare the performance of MVP and GRE. First, we varied the number of tasks (i.e., the number of detecting points) to study the impact of the number of tasks. Besides, we also investigated
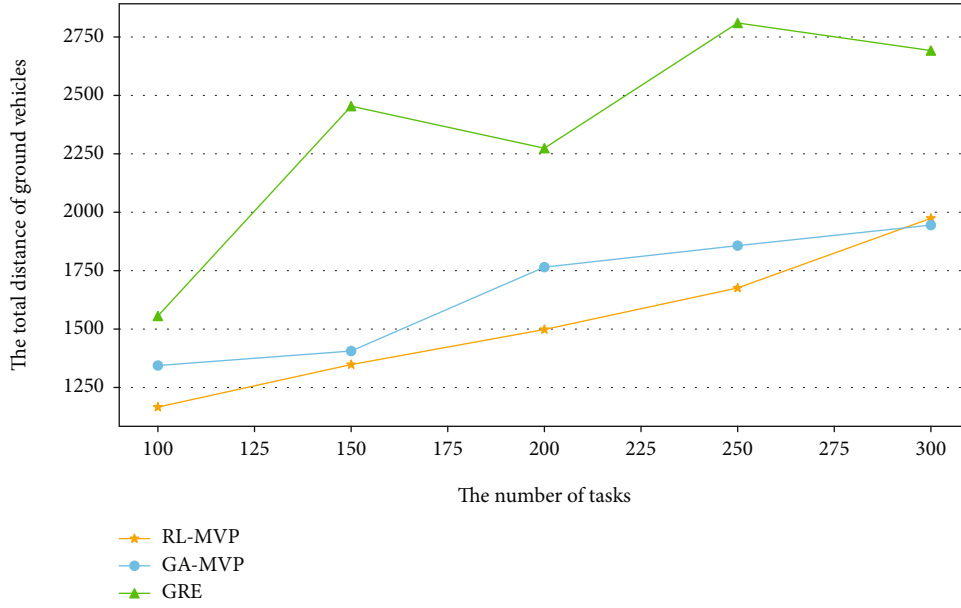
(a) Uniform distribution
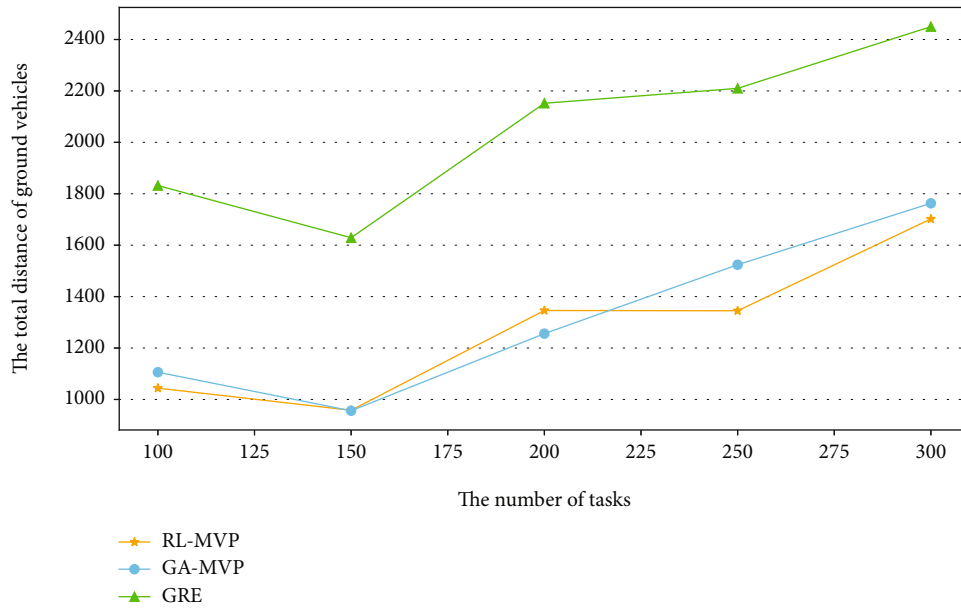
(b) Nonuniform distribution

Figure 9: The impact of the number of tasks on the distance of vehicles in the environment of multiple vehicles.

the impact of the number of tasks on the travel distance of UAVs and vehicles. Then, the time budget is varied to study its impact. After that, we varied the speed of UAVs and the speed of ground vehicles, respectively. Finally, several experiments are performed to investigate the impact of N_m for MVP. For each of the above experiments, we performed it in two environments: (1) uniform environment: detecting points are distributed uniformly, and (2) nonuniform environment: detecting points are distributed nonuniformly.

5.1. The Impact of the Number of Tasks in the Environment of Multiple Vehicles. Figure 7 shows the impact of the num-

ber of sensing tasks on the generated incentive rewards. It can be observed that the incentive rewards generated in all algorithms are positively related to the number of sensing tasks. Moreover, GA-MVP and RL-MVP outperform GRE significantly. Besides, RL-MVP outperforms GA-MVP, which represents that RL performs better than GA in the path planning of UAVs.

Figures 8 and 9 present the impact of the number of tasks on the total distance of drones and vehicles, respectively. Figure 8 shows that the total flight distance of all drones in all algorithms is approximately the same regardless of the varying number of tasks. Details shown in
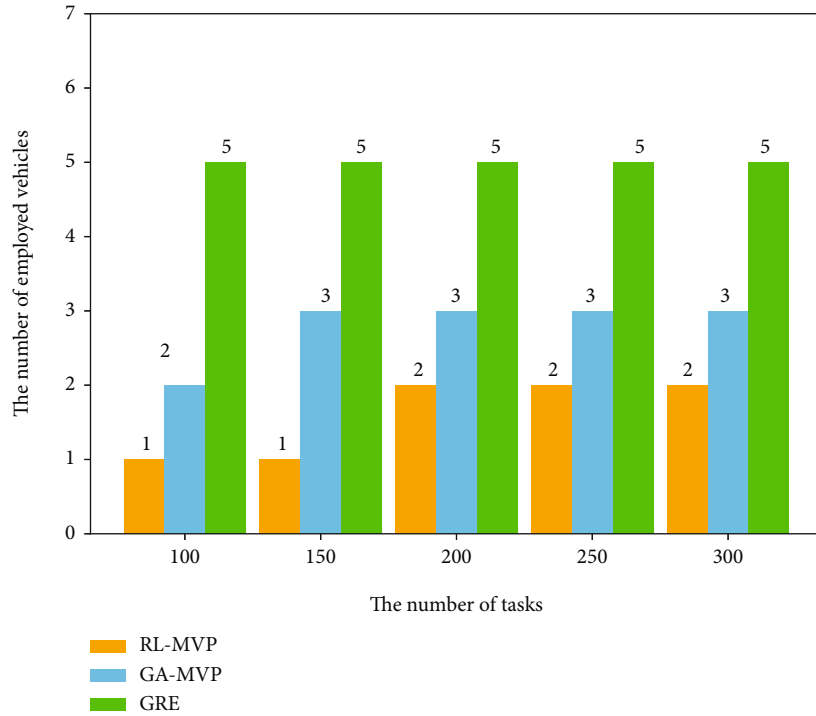
(a) Uniform distribution
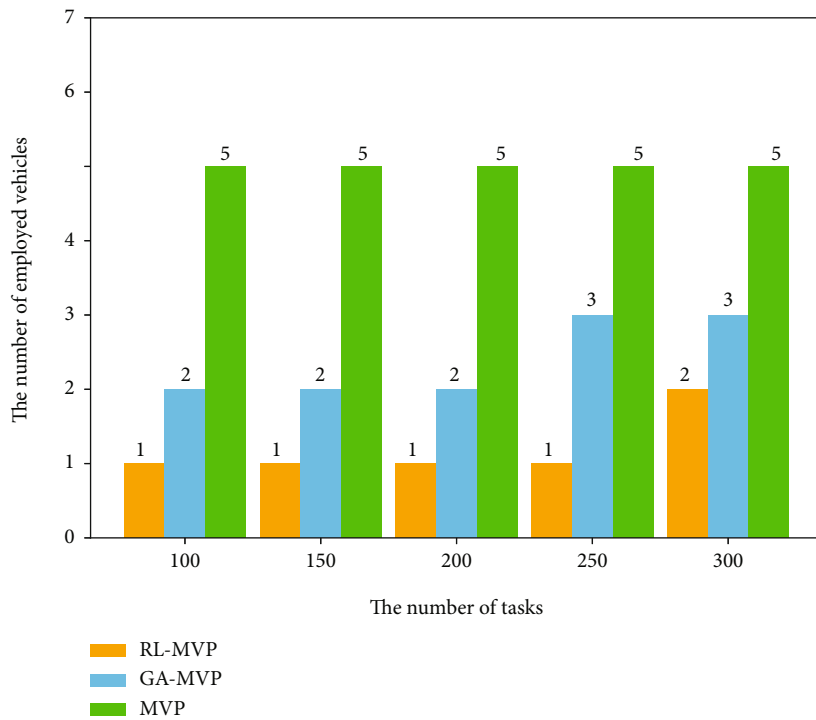
(b) Nonuniform distribution

FIGURE 10: The impact of the number of tasks on the number of employed vehicles in the environment of multiple vehicles.

Figure 9 indicate that the total travel distance of all vehicles in GA-MVP and RL-MVP is smaller than that of GRE, which is contributed by the strategy of allocating parking spots in MVP. Nevertheless, the total travel distance of all vehicles increases as the number of tasks increases.

Figure 10 shows that GA-MVP and RL-MVP perform better than GRE in terms of the number of employed vehicles. The number of employed vehicles in GRE is a constant as GRE simply employs all candidate vehicles to perform tasks. Besides, from an overall perspective, the number of

(a) Uniform distribution
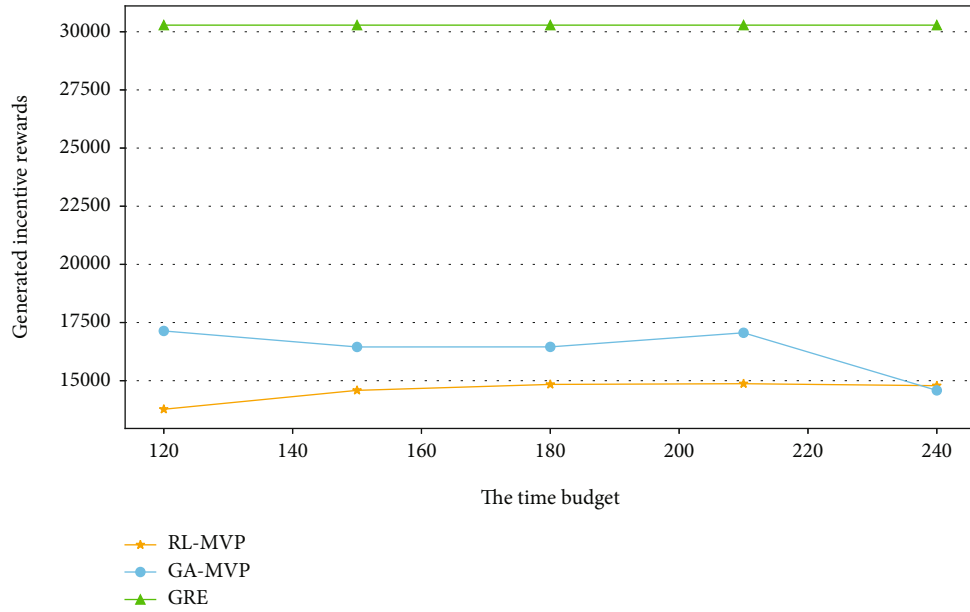
(b) Nonuniform distribution

FIGURE 11: The impact of the time budget on the generated incentive rewards in the environment of multiple vehicles.

employed vehicles in GA-MVP and RL-MVP increases as the number of tasks increases. This is because when the number of tasks increases, more ground vehicles need to be employed due to the fixed time budget.

5.2. The Impact of the Time Budget in the Environment of Multiple Vehicles. Figure 11 indicates that GA-MVP and RL-MVP outperform GRE regardless of the varying time budget. It can be seen that the performance of GRE is not affected regardless of the varying time budget. This is because the time cost of GRE will not exceed the time budget as there are enough ground vehicles. Thus, the time budget does not affect the performance of GRE. Besides, the generated incentive rewards in GA-MVP and RL-MVP decrease as time budget increases in the uniform environment but almost remains unchanged in the nonuniform environment. This is because the number of employed vehicles almost cannot decrease anymore in nonuniform environment.
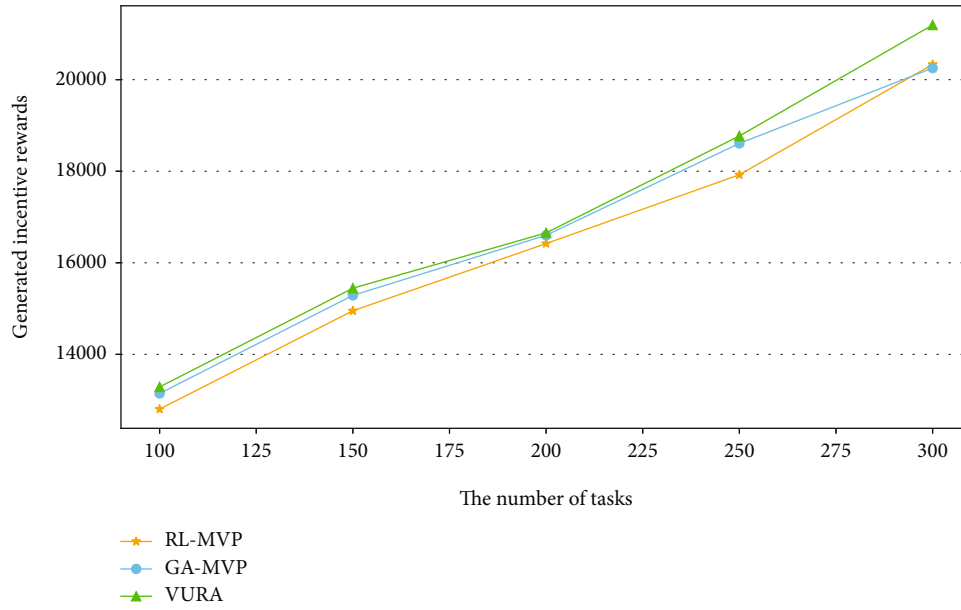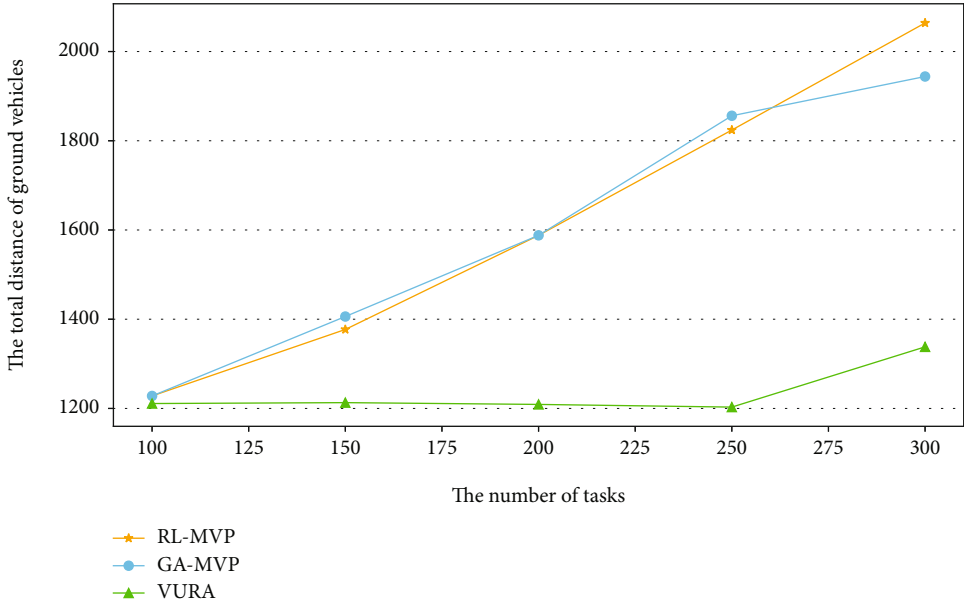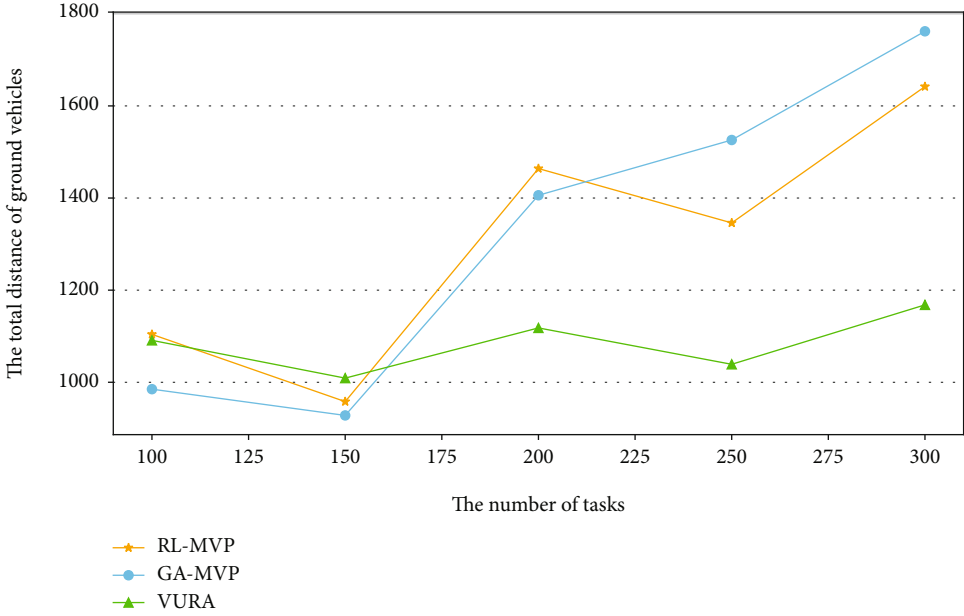
(a) Uniform distribution
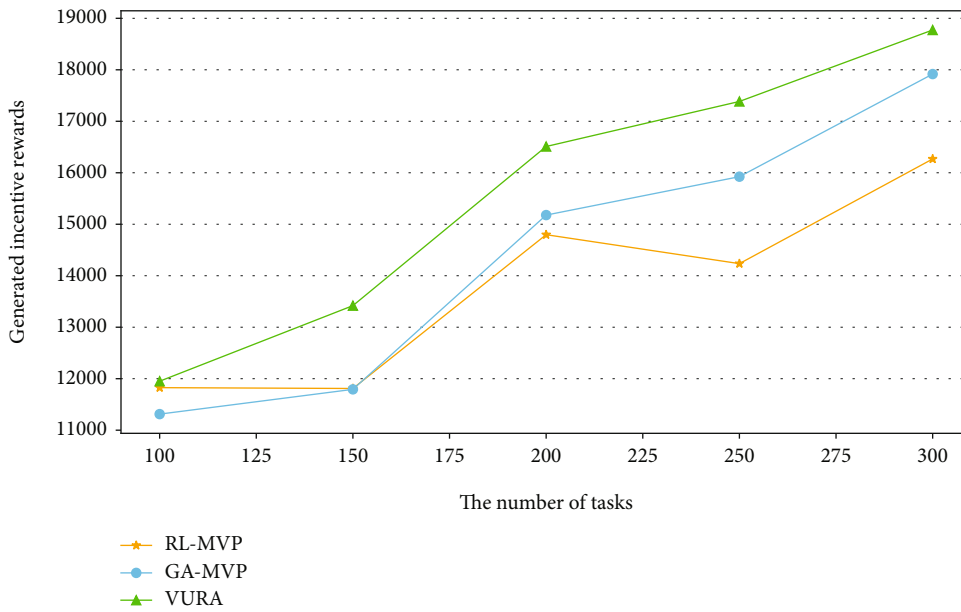
(b) Nonuniform distribution

Figure 12: The impact of the number of tasks on the generated incentive rewards in the environment of a single vehicle.

5.3. The Impact of the Number of Tasks in the Environment of a Single Vehicle. Figures 12–14 compare RL-MVP and GA-MVP with VURA in the environment of a single vehicle. Figure 12 indicates that the incentive rewards generated in all algorithms are positively related to the number of sensing tasks. It can be observed that RL-MVP outperforms other algorithms in both uniform and nonuniform environments. Besides, VURA performs as well as GA-MVP in the uniform environment but does not in the nonuniform environment. Figures 13 and 14 show that GA-MVP and RL-MVP outperform VURA in the path planning of UAVs but are inferior to VURA in the path planning of the vehicle. The results are acceptable for us since MVP is designed to solve the problem in the environment of multiple vehicles rather than in the environment of a single vehicle.

5.4. The Impact of N_m. Figure 15 indicates that the generated incentive rewards in MVP decrease as the value of N_m increases. Besides, we can observe that the generated incentive rewards reduce more gently in the nonuniform environment. This is because when the detecting points are distributed nonuniformly, most parking spots have enough detecting points, which will not cause some drones to sit idle. Finally, as shown in Figure 15, the value of N_m can be set to 6 so that MVP can work well in both uniform environment and nonuniform environment.
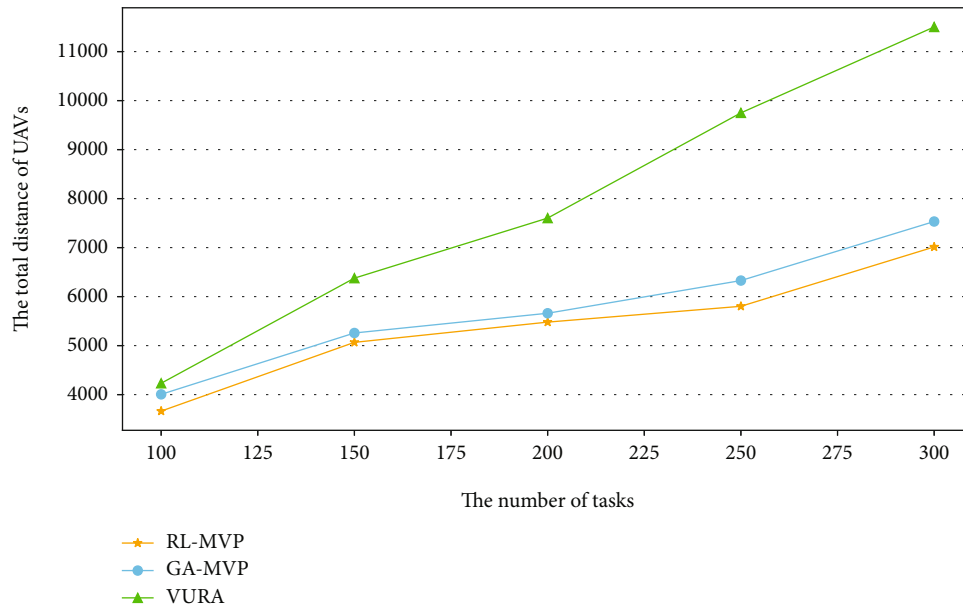
(a) Uniform distribution
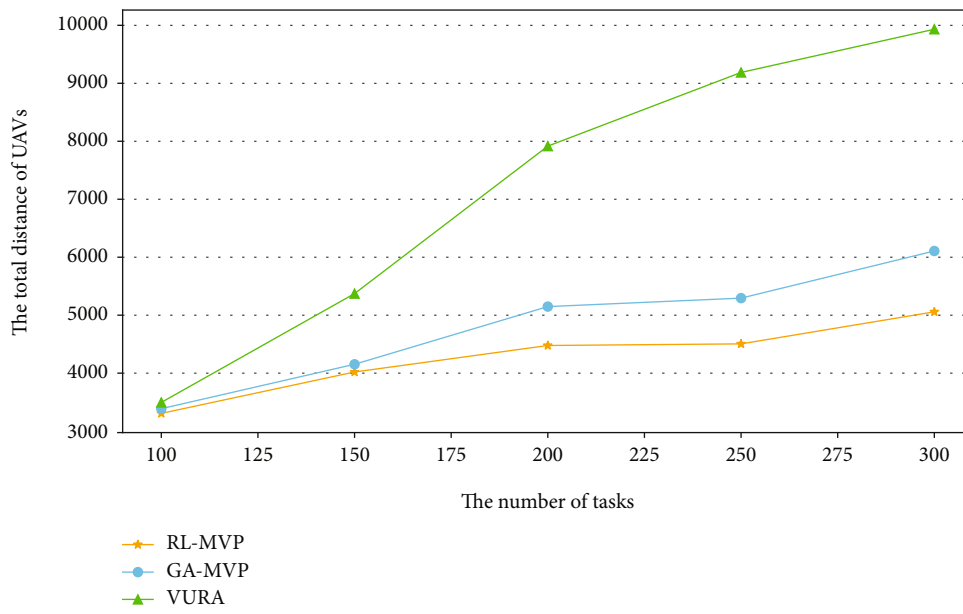
(b) Nonuniform distribution

FIGURE 13: The impact of the number of tasks on the distance of UAVs in the environment of a single vehicle.

(a) Uniform distribution

(b) Nonuniform distribution

FIGURE 14: The impact of the number of tasks on the distance of vehicles in the environment of a single vehicle.
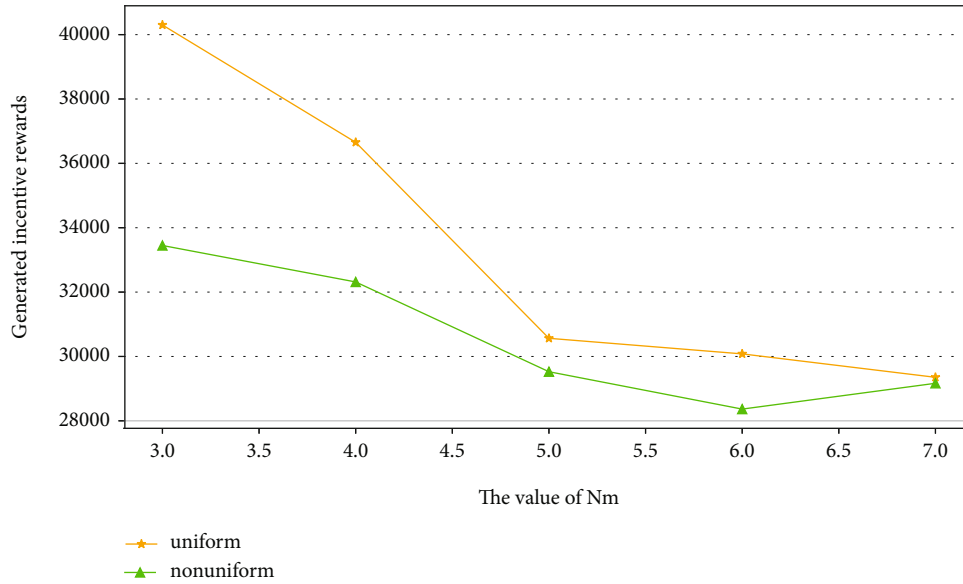
Figure 15: The impact of N_m for MVP.

5.5. The Impact of the Method of Selecting Candidate Parking Spot. Figure 4 presents the total time cost of arranging candidate parking spots, allocating detecting points, and optimizing the allocation in both methods. It can be noticed that the method that arranges candidate parking spots non-uniformly costs more time than the other method. This is because the calculation of density is time-consuming. Besides, Figures 5 and 6 indicate that the generated incentive rewards in both methods are approximately the same.

In a word, RL-MVP always performs better significantly, i.e., generating fewer incentive rewards and requiring fewer ground vehicles when the number of tasks, the time budget, the speed of UAVs, or the speed of ground vehicles varies.

6. Conclusion

In this paper, we propose an efficient algorithm called MVP to address the multi-vehicle-assisted multi-UAVs path planning problem in MCS. To the best of our knowledge, we are the first to take multiple ground vehicles into consideration. In MVP, at first, the detecting points are allocated to proper parking spots. Subsequently, we propose an efficient heuristic allocation algorithm EHA to plan the paths of ground vehicles. Besides, the genetic algorithm and reinforcement learning are utilized to plan the paths of UAVs. Simulation results show that RL-MVP outperforms the other algorithms in terms of the generated incentive rewards in most cases. In the environment of multiple vehicles, GRE produces about 50%-80% more incentive rewards than RL-MVP and GA-MVP produces about 20% more incentive rewards than RL-MVP. In the environment where only one vehicle is available and detecting points are distributed nonuniformly, VURA produces about 15% more incentive rewards than RL-MVP and GA-MVP produces about 7% more incentive rewards than RL-MVP.

In this work, we assume that all UAVs have the same flying speed and hovering time. However, in the reality, one ground vehicle may carry different kinds of UAVs. And different types of UAVs have different flight speeds and hovering time. Hence, as for further work, we will consider the situation where the UAVs carried by one vehicle may be heterogeneous.

Data Availability

The data used to support the findings of this study are included within the article

Conflicts of Interest

The authors declare that they have no conflicts of interest.

Acknowledgments

References

[1] H. Ma, D. Zhao, and P. Yuan, "Opportunities in mobile crowd sensing," *IEEE Communications Magazine*, vol. 52, no. 8, pp. 29–35, 2014.

[2] A. M. A. al-muqarm and F. Rabee, "IoT technologies for mobile crowd sensing in smart cities," *Journal of Communications*, vol. 14, no. 8, pp. 745–757, 2019.

[3] Z. Zhou, J. Feng, B. Ai, and M. Guizani, "Energy-efficient mobile crowd sensing based on unmanned aerial vehicles," in *2018 IEEE global communications conference (GLOBECOM)*, pp. 1–6, Abu Dhabi, United Arab Emirates, 2018.

[4] M. Chen, Y. Hao, M. Qiu, J. Song, D. Wu, and I. Humar, "Mobility-aware caching and computation offloading in 5G

ultra-dense cellular networks," *Sensors*, vol. 16, no. 7, p. 974, 2016.

[5] Y. Yang, Z. Zheng, K. Bian, L. Song, and Z. Han, "Real-time profiling of fine-grained air quality index distribution using UAV sensing," *IEEE Internet of Things Journal*, vol. 5, no. 1, pp. 186–198, 2017.

[6] M. Chen and Y. Hao, "Task offloading for mobile edge computing in software defined ultra-dense network," *IEEE Journal on Selected Areas in Communications*, vol. 36, no. 3, pp. 587–597, 2018.

[7] M. Chen, Y. Tian, G. Fortino, J. Zhang, and I. Humar, "Cognitive internet of vehicles," *Computer Communications*, vol. 120, pp. 58–70, 2018.

[8] C. C. Murray and A. G. Chu, "The flying sidekick traveling salesman problem: optimization of drone-assisted parcel delivery," *Transportation Research Part C: Emerging Technologies*, vol. 54, pp. 86–109, 2015.

[9] A. Ponza, *Optimization of Drone-Assisted Parcel Delivery*, 2016.

[10] S. Mourelo Ferrandez, T. Harbison, T. Weber, R. Sturges, and R. Rich, "Optimization of a truck-drone in tandem delivery network using k-means and genetic algorithm," *Journal of Industrial Engineering and Management (JIEM)*, vol. 9, no. 2, pp. 374–388, 2016.

[11] Z. Luo, Z. Liu, and J. Shi, "A two-echelon cooperated routing problem for a ground vehicle and its carried unmanned aerial vehicle," *Sensors*, vol. 17, no. 5, p. 1144, 2017.

[12] M. Hu, W. Liu, J. Lu et al., "On the joint design of routing and scheduling for vehicle-assisted multi-UAV inspection," *Future Generation Computer Systems*, vol. 94, pp. 214–223, 2019.

[13] S. He, D.-H. Shin, J. Zhang, and J. Chen, "Toward optimal allocation of location dependent tasks in crowdsensing," in *IEEE INFOCOM 2014 - IEEE Conference on Computer Communications*, pp. 745–753, Toronto, ON, Canada, April 2014.

[14] H. Xiong, D. Zhang, Z. Guo, G. Chen, and L. E. Barnes, "Near-optimal incentive allocation for piggyback crowdsensing," *IEEE Communications Magazine*, vol. 55, no. 6, pp. 120–125, 2017.

[15] Z. Shi, H. Huang, Y.-E. Sun, X. Wu, F. Li, and M. Tian, "An efficient task assignment mechanism for crowdsensing systems," *International Conference on Cloud Computing and Security*, 2016, pp. 14–24, Springer, 2016.

[16] Y. Chen, P. Lv, D. Guo, T. Zhou, and M. Xu, "Trajectory segment selection with limited budget in mobile crowd sensing," *Pervasive and Mobile Computing*, vol. 40, pp. 123–138, 2017.

[17] H. Savuran and M. Karakaya, "Route optimization method for unmanned air vehicle launched from a carrier," *Lecture Notes on Software Engineering*, vol. 3, no. 4, pp. 279–284, 2015.

[18] M. Hu, W. Liu, K. Peng et al., "Joint routing and scheduling for vehicle-assisted multidrone surveillance," *IEEE Internet of Things Journal*, vol. 6, no. 2, pp. 1781–1790, 2018.

[19] A. Guttman, "R-trees: a dynamic index for geometric data," in *Proceedings of the ACM SIGMOD International Conference on Management of Data*, pp. 47–57, Brighton, England, 1984.

[20] N. Roussopoulos, S. Kelley, and F. Vincent, "Nearest neighbor queries," in *Proceedings of the 1995 ACM SIGMOD international conference on Management of data*, pp. 71–79, San Jose California USA, 1995.

[21] P. Li and J. Xu, "Fundamental rate limits of UAV-enabled multiple access channel with trajectory optimization," *IEEE Trans-* *actions on Wireless Communications*, vol. 19, no. 1, pp. 458–474, 2019.

[22] Z. Fang, J. Wang, C. Jiang, Q. Zhang, and Y. Ren, "AoI-inspired collaborative information collection for AUV-assisted Internet of underwater things," *IEEE Internet of Things Journal*, vol. 8, no. 19, pp. 14559–14571, 2021.

[23] Z. Fang, J. Wang, J. Du, X. Hou, Y. Ren, and Z. Han, "Stochastic optimization aided energy-efficient information collection in Internet of underwater things networks," *IEEE Internet of Things Journal*, 2021.

[24] Y. Hu, Y. Yao, and W. S. Lee, "A reinforcement learning approach for optimizing multiple traveling salesman problems over graphs," *Knowledge-Based Systems*, vol. 204, article 106244, 2020.

[25] J. Xi, L. Liu, M. Li, X. Li, and J. Peng, "Power-aware path planning for vehicle-assisted multi-UAVs in mobile crowd sensing," in *2021 IFIP/IEEE international symposium on integrated network management (IM)*, pp. 687–691, Bordeaux, France, 2021.

WILEY | Hindawi

Research Article

A Dual-Frequency Miniaturized Frequency Selective Surface Structure Suitable for Antenna Stealth

Wei Zhang, Maojun Li, Mingnan Le [iD], Bin Li, and Jiaqi Wei

School of Information Science and Technology, Northwest University, Xi'an, CO 710127, China

Correspondence should be addressed to Mingnan Le; lemingnan@nwu.edu.cn

A tiny dual-band frequency selective surface structure is proposed in this paper. With dual-band rejection characteristics at the corresponding frequency points of the S-band and C-band, suitable for antenna stealth. To achieve miniaturization, the unit-cell architecture resembles the shape of a "S." First of all, the author describes the parameters of the surface element, and then, the transmission characteristics of the surface element are analyzed by the equivalent circuit method. By maintaining a constant response to TE and TM polarization patterns and oblique incident angles, the suggested device ensures angular independence. The measured findings from the constructed FSS are used to validate the computed results. Finally, a new unit structure is provided for the application of FSS in antenna stealth.

1. Introduction

The traditional structure-type wave-absorbing material Salisbury screen is composed of an impedance layer $\lambda/4$ away from the metal backplane, a space layer, and a connection base plate. The Salisbury screen has a simple structure, but its narrow absorption bandwidth and the need for a larger thickness at low frequencies restrict the application of this structure in practical engineering [1]. The Jaumann absorber is improved on the basis of the traditional Salisbury screen. It is composed of multiple dielectric layers and impedance layers. Although the absorption bandwidth has been greatly improved, the thickness of the absorber is increased, and the structure is also increased. The design difficulty and complexity limit its practical application. In order to improve the comprehensive performance of absorbing materials to meet actual needs, absorbing materials based on frequency-selective surfaces have become the research focus. FSS has a variety of patterns, which can be optimized by loading lumped elements or materials with specific impedance, and the resonance frequency can be modified by controlling the size of the FSS and the loaded resistance. Compared with the Salisbury screen, it can only pass through in terms of adjusting the thickness of the media layer, and the design of the absorber based on the frequency selection surface is more diversified.

An endless periodic array of metal patches or apertures is known as a frequency selective surface. The features of the FSS mainly depend on the shape and dimension of the FSS unit. Common FSS units are square, ring, or crossed dipoles, which are widely used in radome, beam steering, radar cross-section reduction, and wireless security [2–5]. Antenna stealth technology is advancing at a breakneck pace. The frequency selection of the antenna on the drone surface technology has also been widely used. Unmanned aerial vehicles are widely used in air operations due to they do not require combatants to directly face various dangers. At present, there are strong military and political use requirements; in order to meet the needs of these fields, we need to continuously improve its design and performance.

In 2008, Xu and others realized the frequency selection surface of resonance at 2.5 GHz and 3.5 GHz by loading lumped capacitors [6]. Sivasamy and Kanagasabai [7] and Chen et al. [8] led the team and successfully developed a dual-band FSS structure with low-frequency ratio, which was used in practical applications. In order to accommodate more FSS unit structures in a limited space, a miniaturized design of FSS structures will be required. Sheng et al. [9] and Li et al.

[10] have reduced the size of FSS units by designing curved unit structures to achieve the purpose of miniaturization, however, for antenna stealth, miniaturization alone is not enough. We also need to ensure its angular stability. Another frequent way to improve angular performance is to use multilayer technology. The coupling of two meander line resonators separated by an ultrathin substrate results in a compact FSS element [11]. Up to 80 degrees, the FSS can create a consistent angular response. In recent years, the teams of Ghosh and Srivastava [12], Hong Tao et al. [13], and Tong et al. [14] have designed a bent multicurrent path structure to obtain a dual-band frequency selective surface with a compressed cell structure and good angular stability. These studies provide a useful reference for the design of dual-frequency and miniaturized FSS structures.

This paper is mainly for antenna stealth. A new type of miniaturized dual-frequency structure is proposed, which can realize the band rejection characteristics of S-band 3.8 GHz and C-band 5.0 GHz through two dual-frequency points, and the characteristics of FSS are verified through physical tests. The results show that the designed structure not only has two closely adjacent resonance points that can be adjusted independently but also has the advantages of miniaturization and incident angle stability up to $60°$.

2. FSS Design

2.1. Unit-Cell Design. AS we all know, the angular stability of the FSS is affected by both the unit-cell spacing and the element's structure. Generally speaking, the basic element with symmetric structure has better angular stability and smaller cell size than the basic element with asymmetric structure, but the unit structure adopted in this article is asymmetric. The proposed structure is the modification of cross ring, and the improved cross-shaped ring unit is composed of two mutually perpendicular "S"-shaped rings. The "S"-shaped ring is composed of two circular rings with different radii and the same width. The center of the ring unit does not coincide with the center of the upper surface of the dielectric substrate. Figure 1 depicts the unit-cell geometry, the material of the substrate is FR-4 with relative permittivity $\varepsilon_\gamma = 4.4$, loss tangent $\tan \delta = 0.02$, and thickness $h = 2.56$mm. Figure 2 shows the FSS surface shape, and full-wave simulations are implemented using the software HFSS Microwave Studio. Table 1 displays the optimal settings, where D is the length of the unit period, g is the distance between the units, W is the width of the ring, and α is the central angle.

2.2. Analysis Frequency Selection Surface. The analysis method of FSS is an important content of FSS research. At present, the analysis methods of FSS mainly include pattern matching method, spectral domain method, numerical method, and equivalent circuit method. This article mainly uses equivalent circuit method to analyze FSS structure, ignoring the thickness of the metal layer, each metal layer and its underlying dielectric layer can be regarded as an FSS layer, and the bottom metal layer alone is regarded as an FSS layer, then the structure is a two-layer FSS structure.
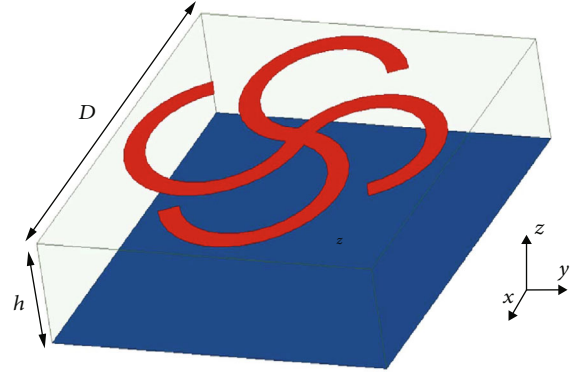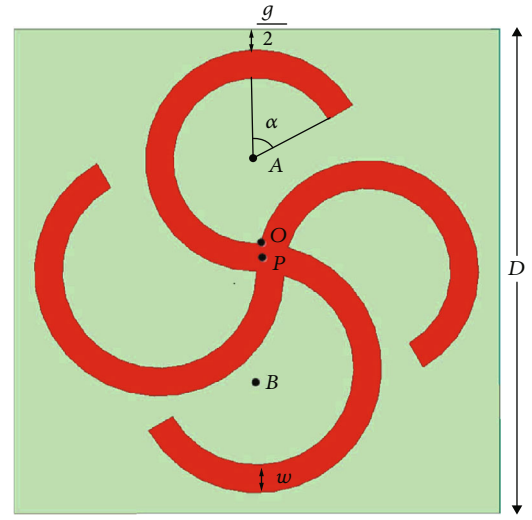

Figure 1: Proposed unit-cell geometry.

Figure 2: Related dimensions of upper surface structure.

According to transmission line theory, the equivalent circuit model for this two-layer FSS structure is shown in Figure 3.

In this circuit, Z_0 and β_0 separately denote the peculiarity impedance and dissemination constant in free space; Z_d and β_d denotes the peculiarity impedance and dissemination constant in the medium; Z_{m1} represents the equivalent impedance of the fss metal layer, Z_{m2} denotes the equivalent impedance of the bottom metal patch. So we can get

$$\beta_0 = \frac{w}{c}, \tag{1}$$

$$\beta_d = \beta_0 \sqrt{\varepsilon_r (1 - j \tan \delta)}, \tag{2}$$

$$Z_0{}^{TE} = \frac{\eta_0}{\cos \theta}, \tag{3}$$

$$Z_0{}^{TM} = \eta_0 \cos \theta, \tag{4}$$

$$Z_d = \frac{\eta_0}{\sqrt{\varepsilon_r (1 - j \tan \delta)}}, \tag{5}$$

where w is the angular velocity, c is the speed of light in vacuum, $\tan \delta = 0.02$ represents the loss tangent of the

TABLE 1: Geometric parameters of the FSS.

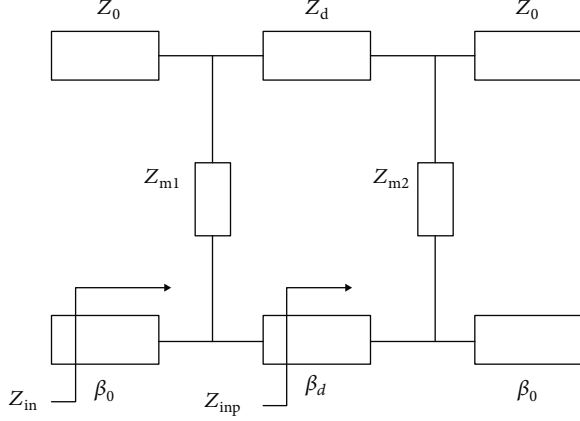| Parameter	D	h	g	w	α	OA	OB
Value	11.2 mm	2.56 mm	0.96 mm	0.64 mm	60°	2.24 mm	2.56 mm

FIGURE 3: Circuit model of transmission line.
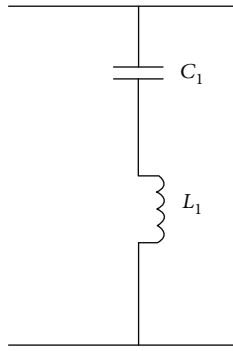
FIGURE 4: Equivalent circuit facsimile of the metal layer.

TE mode

- - - Ang_the = 0°   ⋯ Ang_the = 45°
☐ Ang_the = 15°   - - - Ang_the = 60°
- - - Ang_the = 30°

FIGURE 5: TE wave absorption at different angles of incidence.
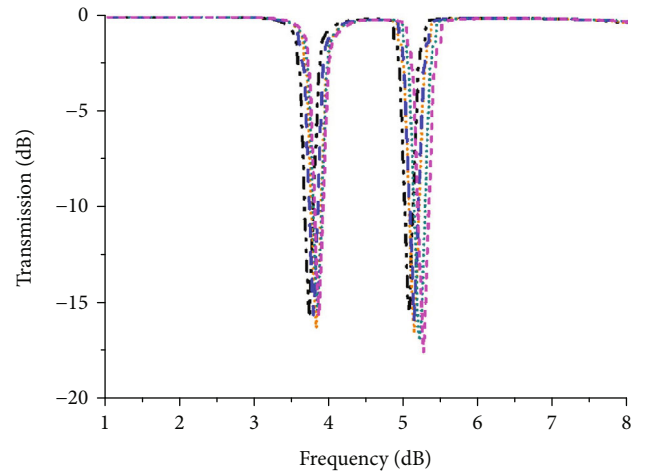
TM mode

- - - Ang_the = 0°   ⋯ Ang_the = 45°
⋯ Ang_the = 15°   - - - Ang_the = 60°
- - - Ang_the = 30°

FIGURE 6: TM wave absorption at different angles of incidence.

dielectric layer, and the wave impedance in open space is represented by η_0.

The equivalent input impedance of the entire two-layer FSS structure can be expressed as

$$Z_{in} = Z_0 \frac{Z_L + jZ_0 \tan(\beta h)}{Z_0 + jZ_L \tan(\beta h)}, \qquad (6)$$

$$\Gamma = \frac{Z_L - Z_0}{Z_L + Z_0}, \qquad (7)$$

$$\tau^2 + \Gamma^2 = 1. \qquad (8)$$

In the formula, h represents the thickness of the medium, and Z_L represents the effective load impedance. The transmission coefficient τ can be calculated.

The metal layer shown in Figure 4 can be equivalent to the form of a series resonant circuit L1-C1 in the transmis- sion line model, and the normalized inductance and capaci- tance of the component are [15]

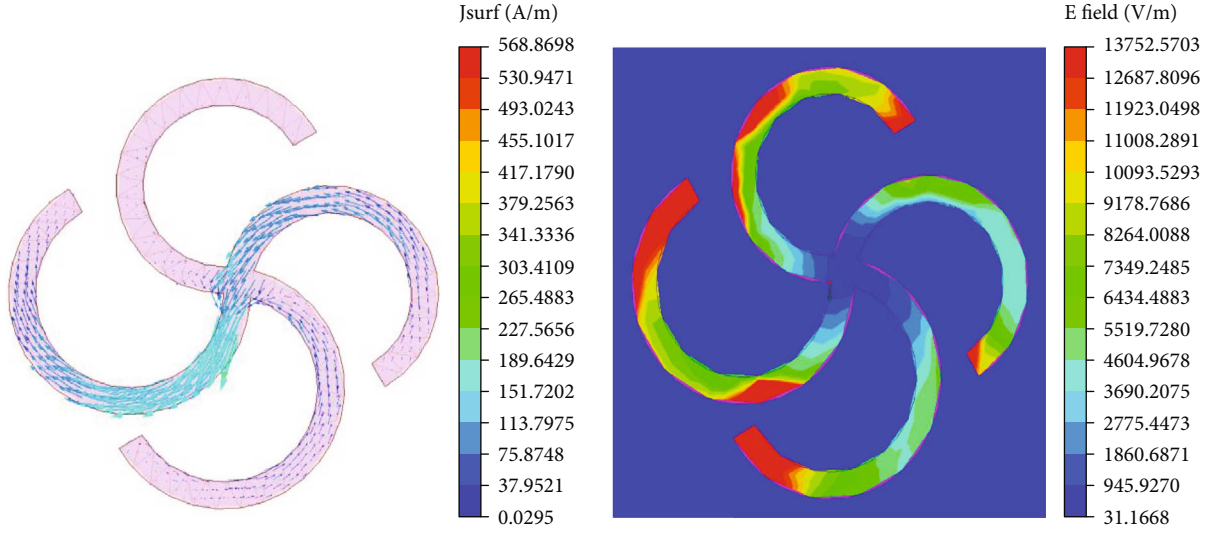$$X_L = \frac{p}{D} F(D, 2w, \lambda), \qquad (9)$$

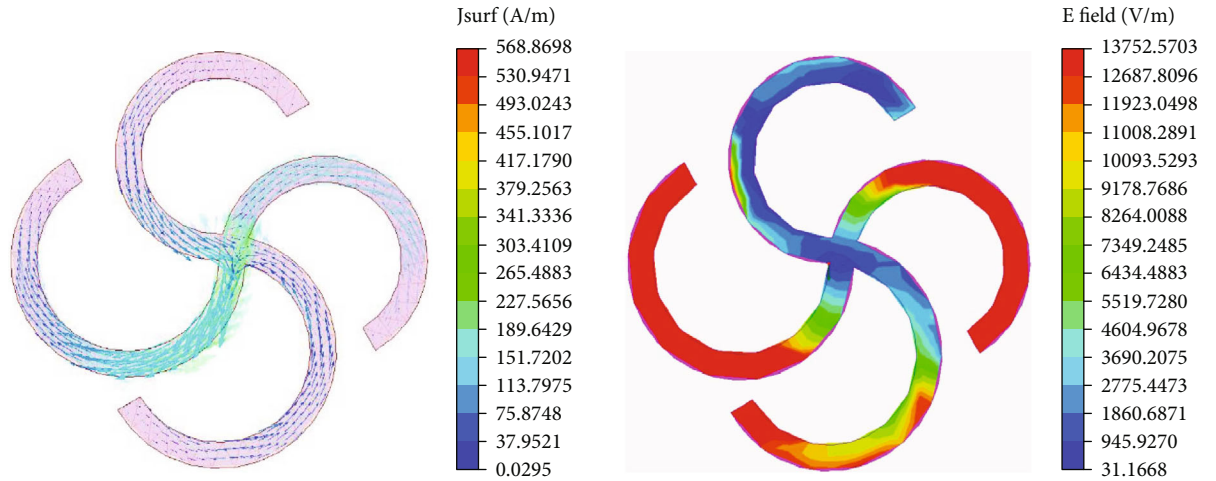FIGURE 7: 3.8 GHz field strength distribution in the metal layer.

FIGURE 8: 5.0 GHz field strength distribution in the metal layer.

$$X_C = \frac{4p}{D} \varepsilon_{eff} F(D, g, \lambda), \tag{10}$$

$$F(D, w, \lambda) = \frac{D}{\lambda} \left\{ \ln \csc \left\{ \frac{\pi w}{2D} \right\} + G(D, w, \lambda) \right\}, \tag{11}$$

$$G(D, w, \lambda) = \frac{1}{2} \frac{(1-\beta^2)^2 \left\{ (1-\beta^2/4)(C_+ + C_-) + 4\beta^2 C_+ C_- \right\}}{(1-\beta^2/4) + \beta^2 (1 + (\beta^2/2) - \beta^4/8)(C_+ + C_-) + 2\beta^6 C_+ C_-}. \tag{12}$$

The capacitive reactance is affected when the frequency selection unit is loaded with a medium. Assume that ε_{eff} is the medium's equivalent relative dielectric constant. When calculating the multilayer structure, $\varepsilon_{eff} = 1 + \varepsilon_r/2$ for the first and last layer, and $\varepsilon_{eff} = \varepsilon_r$ for the middle layer. p represents the side length of the S ring, g represents the cell gap, w represents the width of the ring, D represents the length of the smallest periodic element, and λ is the wavelength of the incident electromagnetic wave.

Where $\quad c_{\pm} = 1/\sqrt{1 \pm 2D \sin \theta/\lambda - (D \cos \theta/\lambda)^2} - 1$ $\beta = \sin \pi w/2D$. The normalized inductive reactance and normalized capacitive reactance of the FSS array can be determined through the calculation of the above formula, and the relevant electromagnetic parameters can be calculated by substituting in the theoretical calculation formula of the transmission line.

Figure 5 is the transmission curve of the FSS absorbing structure, where the minimum period $D = 11.2$mm, the loop width $w = 0.64$mm, and the cell gap $g = 0.96$mm. The material of the substrate is FR-4 with relative permittivity $\varepsilon_{\gamma=4.4}$, loss tangent $\tan \delta = 0.02$, and thickness $h = 2.56$mm. It can be understood from Figure 5 that the transmission coefficient calculated by the equivalent circuit model is basically consistent with the HFSS simulation result, thus verifying the validity of the equivalent circuit model.

The practical implementation of FSS filters and shields needs FSS operation that is angular independent. The first thing we need to understand is that when a beam of light
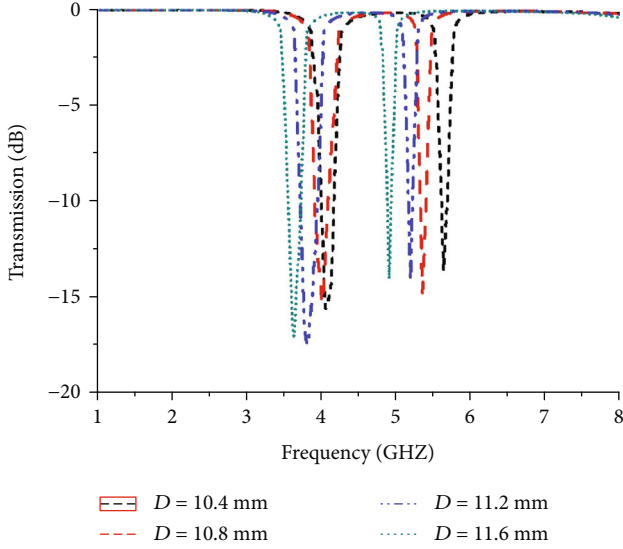
FIGURE 9: Absorption curve for different square ring size.

FIGURE 10: Absorption curves of different unit heights.

FIGURE 11: Absorption curve for different loop width.

is incident on a metal surface, the plane where the incident light and the normal to the metal surface are located is the incident surface. The electric vector of the incident light wave can be decomposed into two polarized light components orthogonal to each other. TE waves are polarized light with a perpendicular electric vector to the incidence plane, whereas TM waves are polarized light with a parallel electric vector to the incident plane. The cells in a unit are illuminated with varying incident angles of 15°, 30°, 45°, and 60° to demonstrate the design's angular stability, and the TM-mode transmission peculiarity is presented in Figure 5.

The design gives a stable response for oblique impact angles, as seen in Figure 5. Similarly, the stability of the TE-mode transmission characteristics is presented in Figure 6. Through the analysis of the figure, we can get that whether in the TM mode or the TE mode, the frequency selection surface has two resonant frequency points $f_1 = 3.8$ GHz, $f_2 = 5.0$ GHz, and at 0 The frequency shift within the incident angle range of 0° ~60° does not exceed 0.5 GHz.

By observing the transmission curve, we can see that the absorber has two resonant frequencies, 3.8 GHz and 5 GHz. When the electromagnetic wave enters the interior of the absorber, the field strength diagrams of the two frequency points are shown in Figure 7. As shown in Figure 8, after electromagnetic waves enter the absorbing body, strong electromagnetic resonance is generated, the energy is converted into heat energy and other forms of energy loss, and this is the absorbing principle of this design.

With the change of the size D of the FSS square ring, the transmission curve of the structure is shown in Figure 9. Obviously as the size of the square ring becomes larger and larger, the longer the current path, the absorption frequency band gradually shifts to low frequency. Therefore, by adjusting the square ring, the size is easy to adjust the absorption band of the structure, and the FSS resonance frequency point has a certain offset as the height h grows, as seen in Figure 10. We set $h = 2.56$mm to ensure resonance at the desired frequency point. Similarly, analyzing the influence
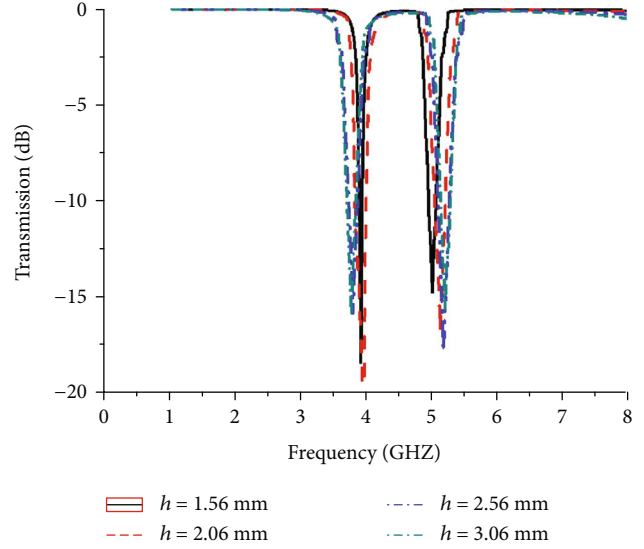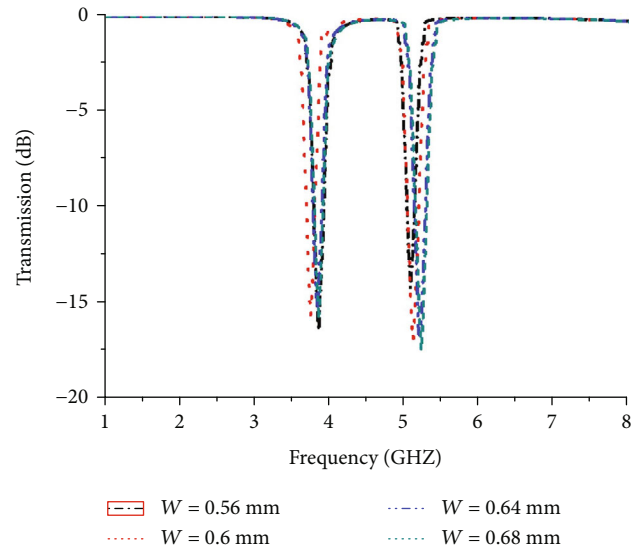
of the loop width w and the unit interval g on the transmission curve, it can be seen from Figures 11 and 12 that the changes of these two parameters have little influence on the transmission.

2.3. Measurement Setup. We measured the free-space transmission of a prototype FSS to confirm the projected FSS performance. As illustrated in Figure 13, a prototype with dimensions of 112 mm is built and gauged in an anechoic enclosures.

Figure 14 depicts the measuring set-up. Use standard horn antennas WR229 and WR187 to connect the vector network subband to test the absorber. The tests were conducted in a semianechoic chamber. The range between the transmitting and receiving antennas and the FSS was
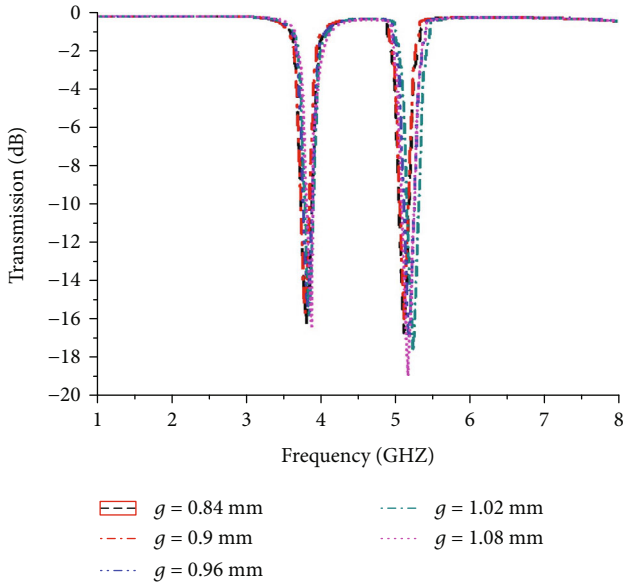
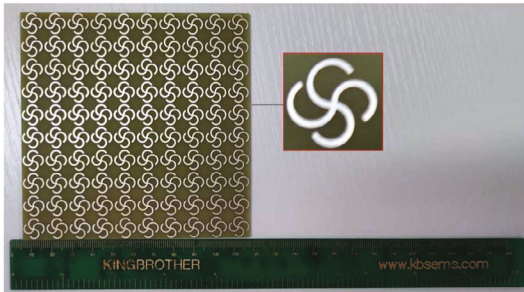FIGURE 12: Absorption curve for different unit interval.
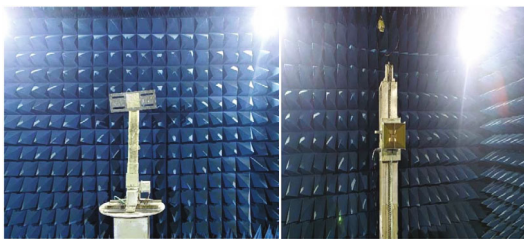

FIGURE 13: Fabricated prototype.

FIGURE 14: Test environment.

restricted to one meter. Absorbers were stored on the floor between the FSS and the transmitting antenna and on the side of the FSS facing the transmitting antenna. Figure 15 shows the measured and simulated values under normal incidence, indicating that the measured and simulated results are not completely coincident, and there is a certain difference, because the thickness of the air spacer is not permanent and is also related to the instability of the relative permittivity of the substrates, we assume that the variations between models and measurements are primarily due to this.
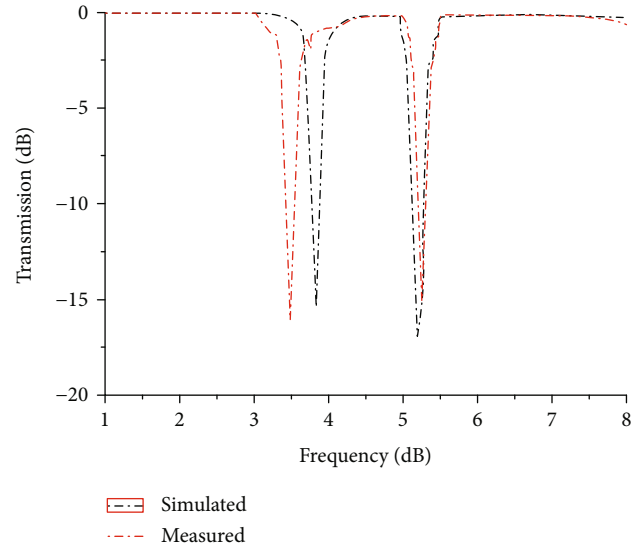

FIGURE 15: Measured and simulated transmissions.

3. Conclusion

A FSS element is proposed in this paper to attain miniaturized angular stability. Simulation and comparable current model analysis are used to investigate the compositional principle. Emulation and measurement are used to analyze FSS's performance. When the incidence angle varies from 0° to 60°, the results demonstrate that steady angular performances are attained and the highest resonant frequency divergence is only 0.5 GHz. This FSS promises to be a viable choice for drone antenna stealth.

Data Availability

The data used to support the finding of this study are included in the article.

Conflicts of Interest

The authors declare that there are no conflicts of interest regarding the publication of this paper.

Acknowledgments

References

[1] K. J. Vinoy and R. M. Jha, *Radar Absorbing Materials from Theory to Design and Characterization*, Kluwer Academic Publishers, Boston, 1996.

[2] B. A. Munk, *Frequency Selective Surfaces: Theory and Design*, Wiley, New York, 2000.

[3] G. H. H. Sung, K. W. Sowerby, M. J. Neve, and A. G. Williamson, "A frequency-selective wall for interference reduction in wireless indoor environments," *IEEE Antennas and Propagation Magazine*, vol. 48, no. 5, pp. 29–37, 2006.

[4] J. Shaker, R. Chaharmir, and H. Legay, "Investigation of FSS-backed reflectarray using different classes of cell elements," *IEEE Trans. Antennas Propag*, vol. 56, no. 12, pp. 3700–3706, 2008.

[5] G. I. Kiani, L. G. Olsson, A. Karlsson, K. P. Esselle, and M. Nilsson, "Crossdipole bandpass frequency selective surface for energy-saving glass used in buildings," *IEEE Trans. Antennas Propag*, vol. 59, no. 2, pp. 520–525, 2011.

[6] R. R. Xu, H.-c. Zhao, Z.-y. Zong, and W. Wu, "Dual-band capacitive loaded frequency selective surfaces with close band spacing," *IEEE Microwave and Wireless Components Letters*, vol. 18, no. 12, pp. 782–784, 2008.

[7] R. Sivasamy and M. Kanagasabai, "A novel dual-band angular independent FSS with closely spaced frequency response," *IEEE Microwave and Wireless Components Letters*, vol. 25, no. 5, pp. 298–300, 2015.

[8] C. Sihong, P. Taisong, and L. Yuan, "Flexible dual-band ultra-thin FSS with ultra-close band spacing," in *2018 International Symposium on Antennas and Propagation*, pp. 1-2, IEEE, 2018.

[9] X. Sheng, J. Ge, K. Han, and X. Zhu, "Transmissive/reflective frequency selective surface for satellite applications," *IEEE Antennas Wirel Propag Lett*, vol. 17, no. 7, pp. 1136–1140, 2018.

[10] W. Li, C. Wang, Y. Zhang, and Y. Li, "A miniaturized frequency selective surface based on square loop aperture element," *International Journal of Antennas and Propagation*, vol. 2014, 6 pages, 2014.

[11] S. N. Azemi, K. Ghorbani, and W. S. T. Rowe, "Angularly stable frequency selective surface with miniaturized unit cell," *IEEE Microw. Wireless Compon. Lett.*, vol. 25, no. 7, pp. 454–456, 2015.

[12] S. Ghosh and K. V. Srivastava, "An angularly stable dual-band FSS with closely spaced resonances using miniaturized unit cell," *IEEE Microwave and Wireless Components Letters*, vol. 27, no. 3, pp. 218–220, 2017.

[13] H. Tao, W. Mengdan, P. Ke et al., "Ultrathin and miniaturized frequency selective surface with closely located dual resonance," *IEEE Antennas and Wireless Propagation Letters*, vol. 18, no. 6, pp. 1288–1292, 2019.

[14] T. Cheng, Z. Jia, T. Hong, W. Jiang, and S. Gong, "Dual-band frequency selective surface with compact dimension and low frequency ratio," *IEEE Access*, vol. 8, pp. 185399–185404, 2020.

[15] R. J. Langley and E. A. Parker, "Double-square frequency-selective surfaces and their equivalent circuit," *Electronics Letters*, vol. 19, no. 17, pp. 675–677, 1983.